Variability and interannual trends in the climatology of radon-222 at two Southern Hemisphere coastal baseline sites.

Ryno Botha

Thesis presented in fulfilment of the requirements for the degree of Doctoral of Physics at the University of the Western Cape.

Supervisors: Prof. R. Lindsay

Department of Physics, University of Western Cape, Private Bag X17 Bellville 7535, South Africa

Dr. A.G. Williams

Australian Nuclear Science and Technology Organisation, Locked bag 2001, Kirrawee DC, NSW 2232, Australia

Mr. C. Labuschagne

South African Weather Service, c/o CSIR, PO Box 320, Stellenbosch, 7599, South Africa

Date 4 November 2020

DECLARATION

I declare that "Variability and interannual trends in the climatology of radon-222 at two Southern Hemisphere coastal baseline sites" is my own work, that it has not been submitted for any degree for examination at any other university, and that all the sources I have used or quoted have been indicated and acknowledge by complete reference.

Full Name: Ryno Botha

Date: 26 March 2021

Signature:  .....

Variability and interannual trends in the climatology of radon-222 at two Southern Hemisphere coastal baseline sites.

Ryno Botha
Department of Physics, University of the Western Cape, Private Bag X17, Bellville, South Africa.
rbotha@caretac.com

ABSTRACT

This thesis characterises and discusses two continuous coastal Southern Hemispheric (SH) atmospheric radon (^{222}Rn) signals. Large-scale atmospheric circulation patterns are important components of the climate system implicated in driving catastrophic events such as extreme droughts and mega-wildfires and radon measurements at coastal sites provide valuable information on interactions of terrestrial and oceanic air masses on regional to hemispheric scales. The main collaborating SH atmospheric observatories in this study are located at Cape Grim (CGO, Tasmania, 1992-2017) and Cape Point (CPO, South Africa, 1999-2017). The radon signal from a high-altitude remote island oceanic site in the Northern Hemisphere Mauna Loa Observatory (MLO, Hawaii, 2004-2015) is also incorporated for comparison purposes. The CGO radon signal is the longest and most sensitive in current existence. A variety of statistical, spectral, trend, back-trajectory and trajectory density methods are utilized in this study to illuminate features of the datasets on multiple scales. Strongly skewed radon distributions occur, with a large number of events falling into a compact range of low values (corresponding to marine air-masses) and a smaller number of events spread over a wide range of high-radon values (continental air-masses). Making use of Fast Fourier Transform power spectral analysis, prominent periodicities are identified on diurnal and annual scales. Inter-annual variations in seasonal and diurnal radon and meteorological characteristics, indicating changes in the continental/oceanic atmospheric mixing state, are evident especially during the period from 2012 to 2017, perhaps associated with the strong El-Niño southern oscillation centred on 2015. A slow but systematic decline in CGO and CPO radon levels is evident over the dataset, associated with fewer continental and more marine air-masses impacting the coastal stations. The long-term trends observed in the atmospheric radon signal may indicate changes in SH circulation patterns over time, perhaps associated with climate change effects.

Keywords**:** Atmospheric Radon-222 Signals; Southern Hemisphere; Characterisation; Seasonal and Inter-Annual Variation; Spectral Analysis; Back-Trajectory Analysis.

ACKNOWLEDGEMENTS

The journey towards this dissertation took momentum after being inspired by reading “die atoom” at some stage during primary school. The journey would not have been achievable without the collective support and mentorship of so many. I would like to take a moment to acknowledge it. Most important is the privilege to study the creation of our God. His favour and blessings are a testament to this dissertation. My parents, your continuous support and motivation especially among the difficult times is the cornerstone which has made this possible. My wife, your listening ear, and words of encouragement are of great motivation. Mike and Trish Daneel, Deon van Zyl, Sylvia and Matthew Hurst your interest and faith are cherished. My dear friend Arnoux Rossouw, it is privilege and honour to have you as a comrade in my corner on this journey and would not have been same without you.

There is no doubt that this achievement is the result of standing on the shoulders of giants. The Australian Nuclear Science and Technology Organisation (ANSTO) it goes without saying without your investment in numerous dimensions, none of this would have been possible. The South African Weather Service (SAWS) and Council for Scientific and Industrial Research (CSIR) is acknowledged for their scientific contributions. The South African National Research Foundation (NRF) and the University of the Western Cape’s Physics Department for the generous scholarship and funding. My supervisors, no words in my vocabulary will be able to encapsulate my gratitude for your contribution and mentorship to achieve this lifelong goal. My colleagues, Scott Chambers, Jagoda Crawford, Gurthwin Bosman your conceptual input have been instrumental in improving the work which is presented.

Ad astra per aspera

CONTENTS

DECLARATION ii
ABSTRACT iii
ACKNOWLEDGEMENTS iv
LIST OF TABLES xiii
1.1 Applications of Radon 14
1.2 Motivation and Aims for this Study 15
CHAPTER 2 Radioactivity Principles 18
2.1 Introduction 18
2.2 Radioactivity 19
2.2.1 Alpha Decay (α) 21
2.2.2 Beta Decay (β) 21
2.2.3 Gamma Decay (γ) 22
2.3 Interaction of Radiation with Matter 23
2.3.1 Interaction of Heavy Charged Particles with Matter 23
2.4 Radon Characteristics 25
2.4.1 Introduction 25
2.4.2 Nuclear Properties of Radon 26
2.4.3 Chemical and physical properties 29
CHAPTER 3 Atmospheric Radon Metrology 30
3.1. **Introduction** 30
3.2. **ANSTO DFLTF Radon Detector** 31
3.2.1 **Introduction** 31
3.2.2 Sampling System 32
3.2.3 Delay System 34
3.2.4 Detector Unit 35
3.2.5 Instrumental Calibration 42
3.2.6 Instrumental Background Measurements 47
3.2.7 Data Acquisition 51
3.2.8 Data Processing 52
3.2.9 Radon Time-series Reconstruction 54
3.3. RAD7 Radon Detector 56
3.3.1 Introduction 56
3.3.2 RAD7 Radon Detector Metrology 57

3.3.3 Radon and Thoron Soil and Rock Emanation Measurements 59
3.4. E-PERM Radon Detector 61
3.4.1 Introduction 61
3.4.2 E-PERM Metrology 61
3.4.3 HYSPLIT: Atmospheric Back-Trajectory Modelling 63
CHAPTER 4 Measurement Locations 67
4.1 Introduction 67
4.2 Cape Grim Meteorological Observatory 69
4.3 Cape Point Meteorological Observatory 73
4.4 Mauna Loa Meteorological Observatory 81
CHAPTER 5 Results and Discussion 83
5.1. Introduction 83
5.2. Atmospheric Radon Signal Characterisation 83
5.2.1. Time-series and Distributions 83
5.2.2. Spectral Analysis 88
5.2.3. Seasonal Characteristics 98
5.2.4. Diurnal Characteristics 103
5.2.5. Meteorological Characteristics 114
5.3. Long-Term Variation Analysis 123
5.3.1. Long-Term Variation and Trend Analysis 123
5.3.2. Analysis of the Wind Direction Sectors 127
5.4. Long-term Atmospheric Air-Masses Back-trajectory Modelling 135
5.4.1. Air-Masses Back-Trajectory – Spatial Analysis 135
5.4.1.1. CGO Air-Masses Back-Trajectory – Spatial Analysis 137
5.4.1.2. CGO Air-Masses Back-Trajectory – Density Analysis 138
5.4.1.3. CPO Air-Masses Back-Trajectory – Spatial Analysis 146
5.4.1.4. CPO Air-Masses Back-Trajectory – Density Analysis 148
5.4.2. Air-Masses Back-Trajectory – Altitude Analysis 155
5.4.2.1. CGO Air-Masses Back-Trajectory – Altitude Analysis 155
5.4.2.2. CPO Air-Masses Back-Trajectory – Altitude Analysis 160
CHAPTER 6 General Conclusion 166
6.1 Discussion and Conclusion 166
6.2 Future Work 173
REFERENCES 174

Appendix 189

LIST OF FIGURES

FIGURE 2-1: TRANSITION CHART FOR NUCLEAR DECAY MODES (A, B^- AND B^+) FOR A SINGLE PARENT ATOM, WITH NEUTRON NUMBER (N), PROTON NUMBER (Z) AND THE MASS NUMBER (A). 22

FIGURE 2-2: ENERGY DISSIPATION OF ^{12}C IONS IN WATER AT VARIOUS ENERGIES WHICH IS ALSO KNOWN AS THE BRAGG CURVE (YUAN ET AL., 2013). 25

FIGURE 2-3: THE ALPHA AND BETA DECAY MODES OF THE URANIUM SERIES. THE CONVENTIONAL ENVIRONMENTAL RADON DECAY CHAIN IS ILLUSTRATED WITH THE DASHED RED ARROWS. 27

FIGURE 2-4: MODELLING OF UNSUPPORTED RADON (UPPER PLOT) AND ASSOCIATED PROGENY (LOWER PLOT) MAKING USE OF THE BATEMAN EQUATIONS FOR THREE CONSECUTIVE DECAY DAUGHTERS (N = 4) WITH 10 000 ^{222}Rn- ATOMS AT t_0 = 0 HOURS (SEE APPENDIX CODE 1). 28

FIGURE 2-5: THORIUM'S ALPHA AND BETA DECAY CHAIN AND ASSOCIATED THORON DECAY PROGENY. THE CONVENTIONAL RADON DECAY CHAIN IS ILLUSTRATED WITH THE DASHED RED ARROWS 29

FIGURE 3-1: SIMPLIFIED BLOCK DIAGRAM ILLUSTRATING THE FOUR PRINCIPAL ELEMENTS OF THE DFLTF RADON DETECTION SYSTEM. 32

FIGURE 3-2: (A) CPO ATMOSPHERIC ALUMINIUM SAMPLING MAST. (B) SAMPLING MAST ON TOP OF THE COASTAL CLIFF AT CAPE POINT NATURE RESERVE. 33

FIGURE 3-3: AN OPERATIONAL STACK BLOWER. THE BLACK PVC 40 MM PIPING IS DIRECTED FROM THE MAST TO THE INLET OF THE STACK BLOWER. THE GREEN OUTLET 19 MM PIPING FLOWS FROM THE STACK BLOWER TO THE DELAY TANKS. 34

FIGURE 3-4: PERCENTAGE OF THORON WITHIN AN ENCLOSED SYSTEM AS A FUNCTION OF TIME (SEE APPENDIX CODE 2) BASED ON THE ASSUMPTION THAT NO ADDITIONAL THORON IS ADDED TO SYSTEM AFTER T = 0. 35

FIGURE 3-5: CPO DFLTF DETECTOR INSTALLED WITHIN A LABORATORY SITUATED BELOW THE SAMPLING MAST. 36

FIGURE 3-6: DETECTION ELECTRONIC HUB: (1) ^{226}Ra CALIBRATION SOURCE, (2) BLOWER ELECTRONICS, (3) DETECTOR HEAD, (4) HV PAD, (5) DATA LOGGER, (6) INLET FILTER, (7) GAS FLOW METER AND (8) POWER SUPPLY. 37

FIGURE 3-7: DFLTF RADON DETECTOR SCHEMATIC ILLUSTRATING THE VARIOUS INTERNAL COMPONENTS (TOP VIEW). 38

FIGURE 3-8: (A) UNASSEMBLED DETECTOR HEAD SHOWING THE SECONDARY MESH FILTER (1) AND INTERNAL SUPPORT FRAMEWORK (2). (B) INTERNAL FRAMEWORK WITH INSTALLED WHITE ZNS (AG) SCINTILLATOR SCREEN (3) AND AN ASSEMBLY WITH BOTH SCINTILLATOR SCREEN AND SURROUNDING SECONDARY FILTER (4). 39

FIGURE 3-9: (A) DETECTOR HEAD ASSEMBLY WITH AN ATTACHED PMT WITHOUT AN ATTACHED EXTERNAL CASING VIEWED FROM THE SIDE. (B) ASSEMBLY VIEWED FROM THE TOP WITH THE PMT VISIBLE AT THE BOTTOM AND THE WHITE SCINTILLATOR SCREEN. (C) A FULLY ASSEMBLED DETECTOR HEAD UNIT VIEWED FROM THE SIDE. (D) AN ASSEMBLY WITH AN EXTERNAL CASING VIEWED FROM THE TOP WITHOUT AN ATTACHED PMT TO ILLUSTRATE THE ENTRY GAP BETWEEN THE SECONDARY FILTER AND VISIBLE SCINTILLATOR SCREEN. 40

FIGURE 3-10: SCHEMATIC OF THE INTERNAL AND EXTERNAL AIRFLOW WITHIN THE RADON DETECTOR (TOP VIEW). 41

FIGURE 3-11: DFLTF RADON DETECTOR SCHEMATICS TO ILLUSTRATE THE INTERNAL COMPONENTS AND THE ASSOCIATED AIRFLOW PATHWAYS. 41

FIGURE 3-12: MODELLING THE BUILD-UP OF ^{222}Rn FROM A KNOWN ^{226}Ra SOURCE (19.85 KBQ) AS A FUNCTION OF THE TIME MAKING USE OF THE BATEMAN EQUATIONS IN AN ENCLOSED ENVIRONMENT (SEE APPENDIX CODE 3). 44

FIGURE 3-13: INTER-ANNUAL CPO RADON DETECTOR CALIBRATION MEASUREMENTS ANALYTICS. MONTHLY CALIBRATION (LEFT-HAND SECTION) IS PERFORMED, INDEXED FROM JANUARY (CR1) TO DECEMBER (CR12). THE CORRESPONDING STANDARD DEVIATION ACCORDING FOR THE TWELVE ANNUAL CALIBRATIONS IS PLOTTED ON THE RIGHT-HAND SECTION. 46

FIGURE 3-14: CPO INTER-ANNUAL RADON CALIBRATION COEFFICIENTS FROM 2011 TO 2018. 47

FIGURE 3-15: INTER-ANNUAL CPO MEAN INSTRUMENTAL BACKGROUND MEASUREMENT ANALYTICS. 49

FIGURE 3-16: MEAN CPO BACKGROUND MEASUREMENT COUNT RATE FROM 2011 TO 2018 AT CPO (N = 30) AND THE LINEAR TRENDLINE FIT THAT IS REPRESENTED BY THE DASHED RED-LINE. 51

FIGURE 3-17: SCHEMATIC OF OFFLINE DFLTF RADON DETECTORS DATA PROCESSING. 54

FIGURE 3-18: CAPTURE EFFICIENCY OF THE CPO AND CGO ANNUAL RADON MEASUREMENTS. 56

FIGURE 3-19: AN ELECTRONIC RAD7 RADON AND THORON DETECTOR UNIT. CREDIT DURRIDGE INC. 57

FIGURE 3-20: (A) RADON AND THORON EMANATION MEASUREMENT SYSTEM MAKING USE OF A RAD7 DETECTOR (1); DRYSTIK ADS-3R ELECTRONIC DEHUMIDIFIER (2), DRYSTIK UPS (3) AND EMANATION CHAMBER (4). (B) EMANATION CHAMBER CONTAINING CPO ROCK SAMPLES WITH THE AIR INLET VISIBLE AT THE TOP. 60
FIGURE 3-21: SCHEMATIC OF RADON AND THORON EMANATION SYSTEM TO ILLUSTRATE THE EXPERIMENTAL SETUP AND AIR FLOW SAMPLING STRUCTURE. 60
FIGURE 3-22: (A) SIDE VIEW SCHEMATIC OF THE E-PERM S-CHAMBER SETUP TO ILLUSTRATE THE INTERNAL METROLOGY. CREDIT RAD ELEC INC. (B) AN S-CHAMBER RADON DETECTOR SETUP TO THE RIGHT WHICH IS ACTIVATED (OPENED) TO PERFORM MEASUREMENTS AND AN ENCLOSED INACTIVE SYSTEM TO THE LEFT. (C) ELECTRET VOLTAGE READER..... 62
FIGURE 3-23: THE THREE E-PERM MEASUREMENT LOCATIONS WITHIN THE CPO RADON LAB. 63
FIGURE 3-24: ILLUSTRATION OF AIR-MASSES BACK-TRAJECTORY DENSITY (CLUSTER) ANALYSIS. THE SIZE OF THE CLUSTER IS DEFINED AS D_1 (LENGTH OF A SINGLE CLUSTER, 11.1 KM) AND THE VARIOUS AIR-MASSES TRAJECTORIES WITH P1 TO P3..... 65
FIGURE 4-1: MAP OF ATMOSPHERIC RADON MEASUREMENT OBSERVATORIES WHICH ARE UTILISED IN THIS STUDY; (1) MAUNA LOA, HAWAII, UNITED STATES; (2) CAPE POINT, WESTERN CAPE PROVINCE, SOUTH AFRICA AND (3) CAPE GRIM, TASMANIA, AUSTRALIA. 68
FIGURE 4-2: MAP OF SOUTHERN HEMISPHERE RADON MEASUREMENT OBSERVATORIES AND METEOROLOGICAL EFFECTS. 69
FIGURE 4-3: SATELLITE IMAGES OF THE COASTAL CAPE GRIM OBSERVATORY (B) ON THE AUSTRALIAN ISLAND, TASMANIA (A). CREDIT GOOGLE EARTH ® 2018. 70
FIGURE 4-4: (A) COASTAL CGO ATMOSPHERIC BASELINE MONITORING LABS AND TELECOMMUNICATION MAST FROM WHICH SAMPLING IS PERFORMED, CREDIT AGAGE. (B) DFLTF RADON DETECTORS INSTALLED OUTSIDE OF THE RADON LABS. CREDIT ANSTO. 70
FIGURE 4-5: MAP INDICATING THE FOUR ANGULAR AIR-MASS FETCH REGIONS RELATIVE TO CGO (CGO-S1 TO CGO-S4)..... 72
FIGURE 4-6: MAP PRESENTING THE MAJOR AUSTRALIAN URANIUM DEPOSITS TAKEN FROM GEOSCIENCE AUSTRALIA (2005). 73
FIGURE 4-7: SATELLITE IMAGES OF THE COASTAL LOW-ALTITUDE CAPE POINT OBSERVATORY (B) ON THE SOUTHERN TIP OF THE CAPE PENINSULA, SOUTH AFRICA, WESTERN CAPE PROVINCE (A). CREDIT GOOGLE EARTH ® 2018. 74
FIGURE 4-8: (A) CPO SAMPLING MAST EQUIPPED WITH METEOROLOGICAL MEASUREMENT INSTRUMENTATION. (B) VIEW FROM THE TOP OF SAMPLING MAST TOWARDS THE TIP OF THE CAPE PENINSULA. (C) NORTH EASTERN VIEW FROM CPO STATION ACROSS FALSE BAY. 75
FIGURE 4-9: MAP INDICATING THE SOUTHERN HEMISPHERE ATMOSPHERIC CPO TWO FETCH REGIONS, CPO-S1 AND CPO-S2. 76
FIGURE 4-10: MAP PRESENTING THE MAJOR SOUTH AFRICAN URANIUM DEPOSITS (KENAN AND CHIRENJE, 2016). 77
FIGURE 4-11: CPO RADON AND THORON EMANATION PROFILE OF SOIL SAMPLES. RADON LINEAR INTERPOLATION (Y = 1.9 X + 73, (HOURS), R-SQUARE: 0.93 AND RMSE: 15.79). THE VERTICAL BARS REPRESENT THE ASSOCIATED MEASUREMENT UNCERTAINTY. 78
FIGURE 4-12: CPO RADON AND THORON EMANATION PROFILE FROM THE ROCK SAMPLES. RADON LINEAR INTERPOLATION (Y = 1.4 X TIME + 140, (HOURS), R-SQUARE: 0.88 AND RMSE: 44.57). THE VERTICAL BARS REPRESENT THE ASSOCIATED MEASUREMENT UNCERTAINTY. 79
FIGURE 4-13: CPO ROCK SAMPLES THORON EMANATION PROFILE (A) AT ASSOCIATED INTERNAL DETECTION CHAMBER AIR TEMPERATURES (B). THE VERTICAL BARS REPRESENT THE ASSOCIATED MEASUREMENT UNCERTAINTY. 79
FIGURE 4-14: INDOOR RADON ACTIVITY CONCENTRATION AT THE CPO RADON LAB MEASURED FOR ABOUT 20 DAYS MAKING USE OF 9 PASSIVE E-PERM DETECTORS AT THREE DIFFERENT LOCATIONS. THE VERTICAL BARS REPRESENT THE ASSOCIATED MEASUREMENT UNCERTAINTY. 80
FIGURE 4-15: SATELLITE IMAGES OF MAUNA LOA OBSERVATORY ON THE ISLAND OF HAWAII (A) WHICH FORMS PART OF THE HAWAI'IAN ISLANDS (B). CREDIT GOOGLE EARTH ® 2018. 81
FIGURE 4-16: (A) MAUNA LOA OBSERVATORY LOCATED IN THE HAWAII VOLCANOES NATIONAL PARK. CREDIT ANSTO (B) MAUNA LOA OBSERVATORY AFTER A SNOWSTORM. CREDIT MARY MILLER, NOAA. 82
FIGURE 5-1: RESPECTIVE CGO, CPO, AND MLO FULL (CUMULATIVE) ATMOSPHERIC RADON SIGNALS. 84
FIGURE 5-2: RESPECTIVE CUMULATIVE CGO (A1), CPO (A3), AND MLO (A5) ATMOSPHERIC RADON SIGNALS AND ASSOCIATED PROBABILITY NORMALIZED COUNTS (NUMBER OF OBSERVATIONS IN BIN / TOTAL NUMBER OF OBSERVATIONS) HISTOGRAMS (A2, A4 AND A6). INDIVIDUAL BIN SIZES AND X-SCALES ARE UTILISED..... 85

FIGURE 5-3: ATMOSPHERIC RADON CONCENTRATION DISTRIBUTIONS FROM CGO (1992 TO 2017), CPO (1999 TO 2017) AND MLO (2004 TO 2016). THE LONG-TERM RADON DISTRIBUTIONS ARE CHARACTERISED BY THE WHISKERS, BARS AND CENTRAL HORIZONTAL LINE WITHIN THE BARS WHICH REFER TO REGIONS OF MOST EXTREME DATA POINTS CONSIDERED OUTLIERS (RED +), 25TH, 75TH, 50TH (MEDIAN) PERCENTILES, RESPECTIVELY. WHISKERS ARE 5THAND 95TH PERCENTILES. 87
FIGURE 5-4: POWER SPECTRUM (AMPLITUDE) FOR THE CUMULATIVE 26-YEAR CGO RADON SIGNAL USING FFT ANALYSIS (CPD, COUNTS PER DAY). THE BLUE-LINE REPRESENTS THE RAW POWER SPECTRUM AND THE RED-LINE THE SMOOTHED SPECTRUM PROCESSED USING SAVITZKY-GOLAY DIGITAL FILTERING. 90
FIGURE 5-5: THE RELATIVE INTER-ANNUAL CGO ATMOSPHERIC RADON POWER SPECTRAL DENSITY (PSD) FROM 1992 TO 2017 (UPPER) AND THE ASSOCIATED AVERAGED PSD FOR THE SAME PERIOD (LOWER) WITH STANDARD DEVIATION. 91
FIGURE 5-6: POWER SPECTRUM (AMPLITUDE) FOR THE CUMULATIVE 19-YEAR CPO RADON SIGNAL USING FFT ANALYSIS (CPD, COUNTS PER DAY). THE BLUE-LINE REPRESENTS THE RAW POWER SPECTRUM AND THE RED-LINE THE SMOOTHED SPECTRUM PROCESSED USING SAVITZKY-GOLAY DIGITAL FILTERING. 92
FIGURE 5-7: THE RELATIVE INTER-ANNUAL CPO ATMOSPHERIC RADON POWER SPECTRAL DENSITY (PSD) FROM 1999 TO 2017 (UPPER) AND THE AVERAGED PSD FOR THE SAME PERIOD (LOWER) WITH ASSOCIATED STANDARD DEVIATION. 93
FIGURE 5-8: POWER SPECTRUM (AMPLITUDE) FOR THE CUMULATIVE 12-YEAR MLO RADON TIME-SERIES USING AN FFT ANALYSIS (CPD, COUNTS PER DAY). THE BLUE-LINE REPRESENTS THE RAW POWER SPECTRUM AND THE RED-LINE THE SMOOTHED SPECTRUM PROCESSED USING SAVITZKY-GOLAY DIGITAL FILTERING. 94
FIGURE 5-9: THE RELATIVE INTER-ANNUAL MLO ATMOSPHERIC RADON POWER SPECTRAL DENSITY (PSD) FROM 2004 TO 2015 (UPPER) AND THE AVERAGED PSD FOR THE SAME PERIOD (LOWER) WITH ASSOCIATED STANDARD DEVIATION. 95
FIGURE 5-10: (A) CGO INTER-MONTHLY ATMOSPHERIC RADON ACTIVITY CONCENTRATION DISTRIBUTIONS FROM 1992 TO 2017. THE LONG-TERM RADON DISTRIBUTIONS ARE CHARACTERISED BY THE WHISKERS, BARS AND CENTRAL HORIZONTAL LINE WITHIN THE BARS WHICH REFER TO REGION OF MOST EXTREME DATA POINTS CONSIDERED OUTLIERS (RED+), 25TH/75TH, 50TH (MEDIAN) PERCENTILES, RESPECTIVELY. (B) SELECTED INTER-MONTHLY PERCENTILE REGION OF INTEREST ZOOMED IN FROM (A). 99
FIGURE 5-11: (A) CPO INTER-MONTHLY ATMOSPHERIC RADON CONCENTRATION DISTRIBUTIONS FROM 1999 TO 2017. THE LONG-TERM RADON DISTRIBUTIONS ARE CHARACTERISED BY THE WHISKERS, BARS AND CENTRAL HORIZONTAL LINE WITHIN THE BARS WHICH REFER TO REGION OF MOST EXTREME DATA POINTS CONSIDERED OUTLIERS (RED+), 25TH/75TH, 50TH (MEDIAN) PERCENTILES, RESPECTIVELY. (B) SELECTED INTER-MONTHLY PERCENTILE REGION OF INTEREST ZOOMED IN FROM (A). 101
FIGURE 5-12: (A) MLO INTER-MONTHLY ATMOSPHERIC RADON CONCENTRATION FROM 2004 TO 2016. THE LONG-TERM RADON DISTRIBUTIONS ARE CHARACTERISED BY THE WHISKERS, BARS AND CENTRAL HORIZONTAL LINE WITHIN THE BARS WHICH REFER TO REGION OF MOST EXTREME DATA POINTS CONSIDERED OUTLIERS (RED+), 25TH/75TH, 50TH (MEDIAN) PERCENTILES, RESPECTIVELY. (B) SELECTED INTER-MONTHLY PERCENTILE REGION OF INTEREST ZOOMED IN FROM (A). 102
FIGURE 5-13: CGO, CPO AND MLO ATMOSPHERIC RADON DIURNAL CYCLE COMPOSITE ANALYSIS MAKING USE OF THE CUMULATIVE SIGNALS. THE NOCTURNAL SECTIONS OF THE DAY ARE INDICATED WITH A BLACK SHADE (A), HOURS WHICH CAN BE EITHER DAY OR NIGHT DEPENDING ON SEASON WITH AN ORANGE SHADE (B), AND THE HOURS REPRESENTING DAY ARE IN YELLOW (C). THE COMPOSITE ANALYSIS IS PERFORMED FOR THE 25TH, 50TH (MEDIAN), AND 75TH PERCENTILES. 105
FIGURE 5-14: CGO, CPO AND MLO ATMOSPHERIC RADON COMPOSITE DIURNAL DIFFERENCES FOR THE CUMULATIVE TIME-SERIES FILTERED ACCORDING TO DAYTIME OR NIGHT-TIME. THE COMPOSITE ANALYSIS IS PERFORMED FOR THE 25TH, 50TH (MEDIAN), AND 75TH PERCENTILES COMBINED WITH DAY-NIGHT DIFFERENCE STATISTICS. 106
FIGURE 5-15: C CGO INTER-ANNUAL ATMOSPHERIC RADON COMPOSITE DIURNAL ANALYSIS. AVERAGE VALUES ACROSS THE NOCTURNAL (N) AND DAY-TIME (D) COMPOSITE WINDOWS ARE SHOWN FOR THE 25TH, 50TH (MEDIAN), AND 75TH PERCENTILES. (B) THE ASSOCIATED DAY-TIME VERSUS NOCTURNAL RADON COMPOSITE DIFFERENCES (DIURNAL RESIDUAL) MAKING USE OF THE RESULTS OF (A). 107
FIGURE 5-16: CPO INTER-ANNUAL ATMOSPHERIC RADON COMPOSITE DIURNAL ANALYSIS. AVERAGE VALUES ACROSS THE NOCTURNAL (N) AND DAY-TIME (D) COMPOSITE WINDOWS ARE SHOWN FOR THE 25TH, 50TH (MEDIAN), AND 75TH PERCENTILES. (B) THE ASSOCIATED DAY-TIME VERSUS NOCTURNAL RADON COMPOSITE DIFFERENCES (DIURNAL RESIDUAL) MAKING USE OF THE RESULTS OF (A). 108
FIGURE 5-17: MLO INTER-ANNUAL ATMOSPHERIC RADON COMPOSITE DIURNAL ANALYSIS. AVERAGE VALUES ACROSS THE NOCTURNAL (N) AND DAY-TIME (D) COMPOSITE WINDOWS ARE SHOWN FOR THE 25TH, 50TH (MEDIAN), AND 75TH

PERCENTILES. (B) THE ASSOCIATED DAY-TIME VERSUS NOCTURNAL RADON COMPOSITE DIFFERENCES (DIURNAL RESIDUAL) MAKING USE OF THE RESULTS OF (A). 109
FIGURE 5-18: CUMULATIVE CGO AND CPO SEASONAL ATMOSPHERIC RADON COMPOSITE DIURNAL ANALYSIS RESULTS (A AND C). THE TOTAL SEASONAL RADON COMPOSITE DAY-NIGHT DIFFERENCES ARE ILLUSTRATED ON B AND D. NOCTURNAL (NIGHT, N) AND DAYTIME (D) COMPOSITE ANALYSIS ARE PERFORMED FOR THE 25TH, 50TH, AND 75TH PERCENTILES. 110
FIGURE 5-19: CUMULATIVE MLO SEASONAL ATMOSPHERIC RADON COMPOSITE DIURNAL ANALYSIS (A). THE TOTAL SEASONAL RADON COMPOSITE DIFFERENCE BETWEEN DAY AND NIGHT ARE ILLUSTRATED ON B NOCTURNAL CONDITIONS (NIGHT, N) AND DAYTIME (D) COMPOSITE ANALYSIS ARE PERFORMED FOR THE 25TH, 50TH (MEDIAN), AND 75TH PERCENTILES. 111
FIGURE 5-20: (A) CGO INTER-ANNUAL DIURNAL RADON COMPOSITE RESIDUAL ANALYSIS FROM 1992 TO 2017 ACCORDING TO SUMMER (DJF, A), AUTUMN (MAM, B), WINTER (JJA, C) AND SPRING (SON, D). 112
FIGURE 5-21: (A) CPO INTER-ANNUAL DIURNAL RADON COMPOSITE RESIDUAL ANALYSIS FROM 1999 TO 2017 ACCORDING TO SUMMER (DJF, A), AUTUMN (MAM, B), WINTER (JJA, C) AND SPRING (SON, D). 113
FIGURE 5-22: (A) MLO INTER-ANNUAL DIURNAL RADON COMPOSITE RESIDUAL ANALYSIS FROM 2004 TO 2015 ACCORDING TO SUMMER (DJF, A), AUTUMN (MAM, B), WINTER (JJA, C) AND SPRING (SON, D). 114
FIGURE 5-23: WD-DEPENDENCE OF CGO AND CPO ATMOSPHERIC RADON DISTRIBUTION CHARACTERISED BY 5TH, 25TH, 50TH (MEDIAN), 75TH AND 95TH PERCENTILES WITHIN CONTINENTAL (C1 = AUSTRALIAN MAINLAND, C2 = TASMANIA, AND C3 = AFRICA MAINLAND) AND MARINE (O1 = SOUTHERN OCEAN; O2 = BASS STRAIT, AND O3 = ATLANTIC AND INDIAN OCEAN). SEE ALSO FIGURE 4-5. 116
FIGURE 5-24: CGO SEASONAL ATMOSPHERIC RADON DISTRIBUTION CHARACTERISED BY 5TH, 25TH, 50TH (MEDIAN), 75TH AND 95TH PERCENTILES WITHIN CONTINENTAL (C1 = AUSTRALIAN MAINLAND, C2 = TASMANIA), AND MARINE (O1 AND O2 = INDIAN OCEAN) ACCORDING TO THE WD. 117
FIGURE 5-25: CPO SEASONAL ATMOSPHERIC RADON DISTRIBUTION CHARACTERISED BY 5TH, 25TH, 50TH (MEDIAN), 75TH AND 95TH PERCENTILES WITHIN CONTINENTAL (C3 = AFRICAN MAINLAND, C2 = TASMANIA), AND MARINE (O3 = ATLANTIC AND INDIAN OCEAN) ACCORDING TO THE WD. 118
FIGURE 5-26: (A & C) CGO AND CPO SEASONAL ATMOSPHERIC FREQUENCY OF RADON OCCURRENCE (EVENTS) ACCORDING TO THE LOCALLY OBSERVED WIND SPEED FROM 1999 TO 2017. (A) CGO SECTORS INCLUDE THE CONTINENTAL (C1 = AUSTRALIAN MAINLAND, C2 = TASMANIA), AND MARINE (O1 AND O2 = INDIAN OCEAN). (C) CPO SECTORS CONTINENTAL (C3 = AFRICAN MAINLAND, C2 = TASMANIA), AND MARINE (O3 = ATLANTIC AND INDIAN OCEAN). (B & D) ASSOCIATED MEAN IN-SITU WIND SPEED ACCORDING TO THE WIND DIRECTION (WD). 120
FIGURE 5-27: (A AND C) CGO AND CPO ATMOSPHERIC RADON LEVELS AS FUNCTION OF THE ON-SITE RECORDED AMBIENT AIR TEMPERATURE. RADON-TEMPERATURE REGIONS WHICH OCCUR AT BOTH CGO AND CPO (YELLOW DOTS), ONLY AT CGO (PURPLE DOTS), AND ONLY AT CPO (GREEN DOTS) ARE INDICATED. (B AND D) CGO AND CPO AIR TEMPERATURE FREQUENCY DISTRIBUTIONS. 121
FIGURE 5-28: (A AND C) CGO AND CPO ATMOSPHERIC RADON LEVELS AS A FUNCTION OF THE ON-SITE RECORDED AMBIENT AIR PRESSURE. (B AND D) CGO AND CPO AIR PRESSURE FREQUENCY DISTRIBUTIONS. NOTE THAT DIFFERENT BIN SIZES ARE UTILIZED FOR HISTOGRAM B (N = 1000) AND D (N = 100). 122
FIGURE 5-29: CGO, CPO, MLO INTER-ANNUAL ATMOSPHERIC RADON CONCENTRATION PERCENTILE DISTRIBUTIONS. THE LONG-TERM RADON DISTRIBUTIONS ARE CHARACTERISED BY THE WHISKERS, BARS AND CENTRAL HORIZONTAL LINE WITHIN THE BARS WHICH REFER TO REGIONS OF MOST EXTREME DATA POINTS CHARACTERISED AS OUTLIERS (RED+), 25TH/75TH, 50TH (MEDIAN) PERCENTILES, RESPECTIVELY. 125
FIGURE 5-30: CGO, CPO AND MLO INTER-ANNUAL ATMOSPHERIC RADON PERCENTILE COMPOSITES. THE ASSOCIATED LINEAR TRENDLINE (BLACK LINE) COMBINED WITH GOODNESS OF FIT (R-SQUARE) AND MK-TEST (P_i-VALUES WHERE I REPRESENTS THE ASSOCIATED PERCENTILE) ARE PRESENTED. THE LINEAR TRENDLINE COEFFICIENTS ARE GIVEN IN TABLE 5-5. 126
FIGURE 5-31: CPO ATMOSPHERIC RADON PERCENTILE DISTRIBUTION COMPOSITES AND TREND ANALYSIS EXPRESSED ACCORDING TO MARINE (O3) AND CONTINENTAL (C3) WD-SECTORS FROM 1999 TO 2017. THE ASSOCIATED LINEAR TRENDLINE (BLACK LINE) GRADIENT COEFFICIENTS AND MK-TEST (P-VALUES) ARE PRESENTED. 129
FIGURE 5-32: CPO ATMOSPHERIC RADON PERCENTILE DISTRIBUTION COMPOSITES AND TREND ANALYSIS EXPRESSED ACCORDING TO MIXING (M2) AND DEEP BASELINE (D) WD-SECTORS. THE ASSOCIATED LINEAR TRENDLINE (BLACK LINE) GRADIENT COEFFICIENTS AND MK-TEST (P-VALUES) ARE PRESENTED. 131

FIGURE 5-33: CGO ATMOSPHERIC RADON PERCENTILE DISTRIBUTION COMPOSITES AND TREND ANALYSIS EXPRESSED ACCORDING TO CONTINENTAL (C1 – AUSTRALIAN MAINLAND AND C2 - TASMANIA) WD-SECTORS FROM 1999 TO 2017. THE ASSOCIATED LINEAR TRENDLINE (BLACK LINE) GRADIENT COEFFICIENTS AND MK-TEST (P-VALUES) ARE PRESENTED. 132
FIGURE 5-34: CGO ATMOSPHERIC RADON PERCENTILE DISTRIBUTION COMPOSITES AND TREND ANALYSIS EXPRESSED ACCORDING TO MARINE (O1 AND O2, INDIAN OCEAN) WD-SECTORS FROM 1999 TO 2017. THE ASSOCIATED LINEAR TRENDLINE (BLACK LINE) COEFFICIENTS AND MK-TEST (P-VALUES) ARE PRESENTED. 133
FIGURE 5-35: CGO ATMOSPHERIC RADON PERCENTILE DISTRIBUTION COMPOSITES AND TREND ANALYSIS EXPRESSED ACCORDING TO MIXED (M3, M4 AND M5) AND DEEP BASELINE (DD) WD-SECTORS FROM 1999 TO 2017. THE ASSOCIATED LINEAR TRENDLINE (BLACK LINE) GRADIENT COEFFICIENTS AND MK-TEST (P-VALUES) ARE PRESENTED. 134
FIGURE 5-36: ILLUSTRATION OF ABOUT TWO DECADES OF CGO AND CPO AIR-MASSES BACK-TRAJECTORIES COMPUTED ON AN HOURLY RESOLUTION PROJECTED UP TO 60 HOURS BACK IN TIME. THE VARIOUS COLOURED LINES REPRESENT THE VARIOUS BACK-TRAJECTORIES..... 136
FIGURE 5-37: CGO ATMOSPHERIC AIR-MASSES BACK-TRAJECTORIES COMPUTED AT VARIOUS DURATIONS BACK IN TIME (T). THE GRID DOMAINS FOR BACK-TRAJECTORIES ARE INDICATED BY THE DASHED RED LINE WHILE THE RED DOT REPRESENTS THE LOCATION OF THE CGO. 138
FIGURE 5-38: (A) CGO CUMULATIVE TRAJECTORY DENSITY (CLUSTER) ANALYSIS MAKING USE OF AIR-MASSES BACK-TRAJECTORIES UP TO T = 60 H. THE UPPER LAND MASS REPRESENTS THE SOUTHERN AUSTRALIA AND THE LOWER LAND MASS TASMANIA. (B) CONTRAST FILTERED CUMULATIVE TRAJECTORY DENSITY PLOT WITH CLUSTERS ASSOCIATED WITH COUNTS GREATER THAN 250, REMOVED..... 139
FIGURE 5-39: PERCENTAGE SPLIT OF INTER-ANNUAL CGO CONTINENTAL AND MARINE (CM) AIR-MASSES FROM 1999 TO 2017 ACCORDING TO VARIOUS HOURS BACK IN TIME UP TO T = 60 H. 141
FIGURE 5-40: MONTHLY CGO CONTINENTAL TO MARINE (CM) AIR-MASSES SPLITS FROM 1999 TO 2017 ACCORDING TO VARIOUS HOURS BACK IN TIME UP TO T = 60 H..... 142
FIGURE 5-41: (A) CGO INTER-ANNUAL CUMULATIVE NUMBER OF CONTINENTAL (C) AND MARINE (M) AIR-MASSES MAKING USE OF BACK-TRAJECTORY TIME UP TO T= 60 H FROM 1999 TO 2017 AND ASSOCIATED LINEAR INTERPOLATION TREND ANALYSIS. (B) PERCENTAGE OF CGO OBSERVED CONTINENTAL AND MARINE AIR-MASSES AND ASSOCIATED LINEAR INTERPOLATION TREND ANALYSIS. (C) THE PERCENTAGE OF CONTINENTAL AIR-MASSES AND (D) THE PERCENTAGE OF MARINE AIR-MASSES BASED ON THE TOTAL ANNUAL NUMBER OF AIR-MASSES..... 144
FIGURE 5-42: INTER-ANNUAL PERCENTAGE OF TASMANIAN AND AUSTRALIAN AIR-MASSES OBSERVED AT CGO MAKING USE OF DENSITY ANALYSIS WITH BACK-TRAJECTORIES UP TO T = 60 H FROM 1999 TO 2017..... 145
FIGURE 5-43: CUMULATIVE CGO SEASONAL INCIDENCE PERCENTAGE OF CONTINENTAL AND MARINE AIR-MASSES MAKING USE OF BACK TRAJECTORIES UP TO T = 60 H FROM 1992 TO 2017..... 146
FIGURE 5-44: CPO ATMOSPHERIC AIR-MASSES BACK-TRAJECTORIES COMPUTED AT VARIOUS DURATIONS (T) BACK IN TIME. THE GRID DOMAINS FOR BACK-TRAJECTORY DENSITY COMPUTATIONS ARE INDICATED BY THE DASHED RED LINE AND THE RED DOT REPRESENTS CPO'S LOCATION..... 147
FIGURE 5-45: (A) CPO CUMULATIVE TRAJECTORY DENSITY (CLUSTER) ANALYSIS MAKING USE OF AIR-MASSES BACK-TRAJECTORIES UP TO T = 60 H. THE UPPER LAND MASS REPRESENTS THE SOUTHERN TIP OF SOUTH AFRICA. (B) CONTRAST FILTERED CUMULATIVE TRAJECTORY DENSITY PLOT WITH CLUSTERS ASSOCIATED WITH COUNTS GREATER THAN 250, REMOVED..... 149
FIGURE 5-46: INTER-ANNUAL CPO CONTINENTAL AND MARINE (CM) AIR-MASSES CONTRIBUTION RESULTS FROM 1999 TO 2017 COMPUTED ACCORDING TO VARIOUS HOURS BACK IN TIME UP TO T = 60 H. 150
FIGURE 5-47: MONTHLY CPO CONTINENTAL TO MARINE (CM) AIR-MASSES CONTRIBUTIONS FROM 1999 TO 2017 ACCORDING TO VARIOUS HOURS BACK IN TIME UP TO T = 60 H. 151
FIGURE 5-48: (A) INTER-ANNUAL CUMULATIVE NUMBER OF CONTINENTAL (C) AND MARINE (M) AIR-MASSES MAKING USE OF BACK-TRAJECTORY TIME UP TO T = 60 H FROM 1999 TO 2017 OBSERVED AT CPO AND ASSOCIATED LINEAR INTERPOLATION TREND ANALYSIS. (B) PERCENTAGE OF CPO OBSERVED CONTINENTAL AND MARINE AIR-MASSES AND ASSOCIATED LINEAR INTERPOLATION TREND ANALYSIS. (C) THE PERCENTAGE OF CONTINENTAL AIR-MASSES AND (D) THE PERCENTAGE OF MARINE AIR-MASSES BASED ON THE TOTAL ANNUAL NUMBER OF AIR-MASSES..... 153
FIGURE 5-49: CUMULATIVE CPO SEASONAL INCIDENCE PERCENTAGE OF CONTINENTAL AND MARINE AIR-MASSES MAKING USE OF BACK TRAJECTORIES UP TO T = 60 H FROM 1992 TO 2017..... 154

FIGURE 5-50: CGO AIR-MASSES BACK-TRAJECTORY ALTITUDE HISTOGRAM COMPUTED FOR VARIOUS DURATIONS BACK IN TIME UP TO T = 60 H. 156
FIGURE 5-51: CGO INTER-ANNUAL AIR-MASSES ALTITUDE DENSITIES. KEY REGIONS OF INTEREST ARE INDICATED: (A1) LOW-ALTITUDE AIR-MASSES (< 1000 M), (A2) STEADY CONTINUOUS LOW-ALTITUDE STATES FOR THE ENTIRE BACK-TRAJECTORY, (A3) HIGH-ALTITUDE (< 7000 M), AND (A4) RAPIDLY DECREASING HIGH-ALTITUDE AIR-MASSES. 157
FIGURE 5-52: INTER-ANNUAL CGO AIR-MASSES BACK-TRAJECTORIES MEAN ALTITUDE ABOVE SEA LEVEL TEMPORAL EVOLUTION FROM 1999 TO 2017. 158
FIGURE 5-53: INTER-ANNUAL CGO AIR-MASSES BACK-TRAJECTORIES ALTITUDE ABOVE SEA LEVEL PERCENTILE COMPOSITE DISTRIBUTIONS ANALYSIS (0 H ≤ T ≤ 60 H) CHARACTERISED BY 5TH, 25TH, 50TH (MEDIAN), 75TH AND 95TH PERCENTILES FROM 1999 TO 2017. 159
FIGURE 5-54: MONTHLY CGO AIR-MASSES BACK-TRAJECTORIES ALTITUDE ABOVE SEA LEVEL PERCENTILE COMPOSITE DISTRIBUTIONS ANALYSIS (0 H ≤ T ≤ 60 H) CHARACTERISED BY 5TH, 25TH, 50TH (MEDIAN), 75TH AND 95TH PERCENTILES COMPUTED UP TO 60 H BACK IN TIME FROM 1999 TO 2017. 160
FIGURE 5-55: CPO AIR-MASSES BACK-TRAJECTORY ALTITUDE ABOVE SEA LEVEL HISTOGRAM COMPUTED FOR VARIOUS DURATION BACK IN TIME UP TO T = 60 H. 161
FIGURE 5-56: CPO INTER-ANNUAL AIR-MASSES ALTITUDE DENSITIES RESULTS. KEY REGIONS OF INTEREST ARE INDICATED: (A1) LOW-ALTITUDE AIR-MASSES (< 1000 M), (A2) STEADY CONTINUOUS LOW-ALTITUDE STATES FOR THE ENTIRE BACK-TRAJECTORY, (A3) REGIONS OF LONG LOW-ALTITUDE POCKETS, (A4) HIGH-ALTITUDE (< 8000 M) AIR-MASSES. 162
FIGURE 5-57: INTER-ANNUAL CPO AIR-MASSES BACK-TRAJECTORIES MEAN ALTITUDE TEMPORAL EVOLUTION FROM 1999 TO 2017. 163
FIGURE 5-58: INTER-ANNUAL CPO AIR-MASSES BACK-TRAJECTORIES ALTITUDE PERCENTILE COMPOSITE DISTRIBUTION ANALYSIS (0 H ≤ T ≤ 60 H) FOR 5TH, 25TH, 50TH (MEDIAN), 75TH AND 95TH PERCENTILES FROM 1999 TO 2017. 164
FIGURE 5-59: MONTHLY CPO AIR-MASSES BACK-TRAJECTORIES ALTITUDE PERCENTILE COMPOSITE DISTRIBUTIONS (0 H ≤ T ≤ 60 H) CHARACTERISED BY 5TH, 25TH, 50TH (MEDIAN), 75TH AND 95TH PERCENTILES FROM 1999 TO 2017. 165

LIST OF TABLES

TABLE 2-1: TABLE OF RADON ISOTOPES (133 ≤ N ≤ 136) WITH ASSOCIATED NUCLEAR PROPERTIES (NNDC, 2018; WIESER, 2006). 26
TABLE 3-1: DFLTF RADON DETECTORS CHARACTERISTICS AT THE THREE MAIN MEASUREMENT LOCATIONS USED IN THIS STUDY. 42
TABLE 3-2: CPO DFLTF RADON DETECTOR TOTAL BACKGROUND MEASUREMENT RESULTS FROM 2011 TO 2015. 50
TABLE 4-1: CGO, CPO AND MLO ALTITUDE ABOVE SEA LEVEL AND SAMPLING ALTITUDE. 68
TABLE 5-1: STATISTICAL ANALYSIS OF THE CUMULATIVE CGO, CPO AN MLO RADON SIGNALS. 86
TABLE 5-2: CGO, CPO AND MLO CUMULATIVE ATMOSPHERIC RADON SIGNALS PERCENTILE COMPOSITES ANALYSIS. 87
TABLE 5-3: COLLECTIVE RESULTS OF THE DIURNAL AND ANNUAL PERIODICITY STRUCTURES IDENTIFIED AT CGO, CPO AND MLO. THE PRESENCE OF THE SPECIFIED PERIODICITY STRUCTURE IS MARKED BY A X. 97
TABLE 5-4: TEMPORAL FILTERS WHICH ARE APPLIED TO GENERATE THE DIURNAL ATMOSPHERIC RADON TIME-SERIES. *HOURS OF THE DAY SELECTED TO GENERATE THE DIURNAL DATASETS. THE TIME PRESENTED IS IN THE VARIOUS LOCAL TIMES. 103
TABLE 5-5: TREND ANALYSIS (GRADIENT IN MBQ/M^3) RESULTS OF CGO, CPO, AND MLO INTER-ANNUAL RADON SIGNAL PERCENTILE COMPOSITES DISTRIBUTIONS. 126
TABLE 5-6: CGO AND CPO STATISTICAL ANALYSIS OF ATMOSPHERIC RADON LEVELS FOR SPECIFIED WD-SECTORS (1999 TO 2017). 128

CHAPTER 1 Introduction

1.1 Applications of Radon

Radon (^{222}Rn) is one of the most useful naturally occurring radionuclide tracers in nature (Csondor et al., 2017; Kikaj et al., 2019; Utkin and Yurkov, 2010; Zhang et al., 2018). Elevated radon levels (> 1000 Bq/m^3 in-air or > 200 Bq/L in-water) can be found in various places within nature for instance in caves (Nemangwele, 2005) and hot springs (Botha et al., 2016; Song et al., 2011; Vogiannis, et al., 2004). Nonetheless, the isotope can be found within soil (Zhuo et al., 2006), water (Botha et al., 2019; WHO, 2011), rocks (Garver and Baskaran, 2004; Ongori et al., 2015), and atmosphere (Podstawczyńska and Chambers, 2018). Being a noble gas, radon does not chemically react with other atmospheric components and its relatively low solubility makes radioactive decay the predominant factor of reduction in the atmosphere. Radon is an isotope with a specific expiration date (half-life) making it ideal for researching a wide range of meteorological events (Kikaj et al., 2019; Williams et al., 2013; Zahorowski et al., 2004). The first qualitative atmospheric radon measurement in history was performed around 1902 by Elster and Geitel making use of charged wire screens (Qureshi et al., 2000) and since then vast technological improvements have been accomplished.

Radon has proven to be a versatile isotopic-tracer in numerous research fields including; hydrology (Botha et al., 2019; Bouchaou et al., 2017; Santos & Eyre, 2011); seismology (Deb et al., 2018; Kuo et al., 2018; Nevinsky et al., 2018); pollution and environmental studies (Chambers et al., 2015; Crawford et al., 2017; Florea & Duliu, 2012; Kikaj et al., 2020; Kikaj et al., 2019; Zhu et al., 2012); health physics (Botha et al., 2017; Griffiths et al., 2010; NNR, 2013; Nonka et al., 2017; Szabó et al., 2014) and atmospheric physics (Chambers et al., 2016; Kikaj et al., 2019;Williams et al., 2013). It is utilised as a natural tracer in hydrology to study groundwater discharge, geochemical exploration, the interaction between deep and shallow groundwater systems, and physical geological systems (Nevinsky et al., 2018; Swana, 2016; Vinson et al., 2018). Radon measurements are also utilised in seismology to investigate the correlation with seismic activity potential applications such as precursor system (Barman et al., 2016; Zhang et al., 2017; Nevinsky et al., 2018).

1.2 Motivation and Aims for this Study

Long-term (> 10 years) continuous atmospheric radon measurement projects especially those spanning decades are rare. Numerous atmospheric radon measurements studies have been performed to date, however, most rarely exceeded 2 years of continuous measurement (Gäggeler et al., 1995; Magalhães et al., 2003; Pereira, 1990; Sesana et al., 2003; Vargas et al., 2015; Zhang et al., 2009; Zhu et al., 2012). Consequently, to conduct a long-term (climatic) atmospheric radon study an extensive continuous radon time-series (signal) will be required. The other key element essential for performing coastal (land-based) radon monitoring is a detection system with an ultra-low detection level (see Section 3.2). Marine air-masses contain considerably lower levels of radon compared to continental air-masses (Botha et al., 2018; Kikaj et al., 2020). Coastal atmospheric radon observatories are prone to be subjected to both marine and continental air-masses or a mixture of the two. The ANSTO atmospheric radon detector has some of the lowest lower detection levels (Chambers et al., 2017; Griffiths et al., 2016; Xia et al., 2010).

To the best of our knowledge, the longest (1992 to present) and most comprehensive continuous ground-based atmospheric radon measurement project in the world is at Tasmania, Cape Grim. This program at Cape Grim Observatory (CGO, see Section 4.2) has been pioneered by Australia's Nuclear Science and Technology Organisation (ANSTO). The ANSTO dual-flow loop two-filter (DFLTF) radon detector system (see Section 3.2) is the globally leading instrument to perform consistent ultra-low (< 50 mBq/m^3) atmospheric radon measurements with a high temporal resolution (≤ 1 h). The CGO radon time-series will form a major part of this thesis.

The historic CGO atmospheric radon signal presents a unique research opportunity to systematically characterise the most detailed time-series in current existence. About 30 DFLTF radon detectors are currently active around the world and are increasing. The two other land-based observatories which conduct continuous atmospheric radon measurements that will be part of this thesis are Cape Point Observatory (CPO, see Section 4.3) and Mauna Loa Observatory (MLO, see Section 4.4). A research paper was published in 2018 (Botha et al., 2018), "Characterising fifteen years of continuous atmospheric radon activity observations at Cape Point (South Africa)" which will form part of this thesis and will be expanded on. CGO, CPO, and MLO are part of the Global Atmospheric Watch (GAW) network of baseline stations, functioning under the auspices of the World Meteorological Organization (WMO).

In this thesis, an emphasis will be placed on the Southern Hemisphere radon signals (CGO and CPO). Nonetheless, a radon signal from the Northern Hemisphere (MLO) is included to a limited degree for comparison purposes. CGO and CPO (S 34° – 40°) have analogous climatologically and geographical conditions (see Section 4.1). One of the biggest motivational factors for focusing particularly on the Southern Hemisphere is the extensive variations in the associated tropospheric circulation trends in which changes in the mid-latitude jet stream is noted (Banerjee et al., 2020; Swart, 2012). Signatures of these variations are identified in our findings as presented in our article, Botha et al., 2018. This thesis will follow on from the publication. In conjunction with the above-mentioned, it should be noted from 2015 onwards a strong El-Niño southern oscillation occurred (Baudoin et al., 2017; Richman and Leslie, 2018). South Africa experienced a record national drought in 2015 and 2017 Cape Town became the first metropolitan city getting within days ("day-zero[1]") of running out of fresh water supply (Baudoin et al., 2017; Richman and Leslie, 2018).

By studying the atmospheric radon signals, insights into the associated Southern hemispheric and regional meteorological events such as transport pathways; temporal periodicity structures; atmospheric stability; seasonal and long-term variations; baseline conditions; local nocturnal terrestrial build-up, the interaction between mesoscale marine and continental breezes and finally climate change related phenomena will be gained.

The objectives of this thesis will be presented in the following section. The main focal point of this thesis is to comprehensively analyse the complex long-term austral atmospheric radon time-series. A collective 45 years' (394 200 h) of Southern Hemisphere atmospheric radon signal will be analysed, discussed and interpreted (see Chapter 5). Of these collective 45 years of radon measurements 26 are from CGO and 19 from CPO. The analysis will consist of several data, statistical and back-trajectory methods.

The aim is to perform the characterization analysis on various temporal scales. By performing the analysis on different temporal scales a range of elements will be studied. On a cumulative level (entire time-series), long-term trends can be investigated, on an inter-annual scale it will be plausible to track variations from year-to-year bases, an inter-monthly scale will provide insights on seasonality variations, and lastly on an hourly scale will unlock the ability to conduct diurnal analysis. Each of the above-mentioned temporal scale analysis will be of value

[1] Day-zero is defined as the day when the taps will be without water supply for the estimated four million residents.

to study the radon signals based on hemispheric circulations variations (seasonal) and interaction between mesoscale marine and continental breezes (hourly - diurnal) and semi-climatological variations (cumulatively).

Power spectral Fast Fourier Transformation (FFT) analysis will be applied to identify radon periodicity structures. The aim is to use the spectral analysis to identify diurnal periodicity groups to extend the diurnal analysis. Diurnal analysis is a powerful tool for studying atmospheric stability and air-quality (Kikaj et al., 2020; Podstawczyńska & Chambers, 2018; Victor et al., 2016). A key element which will be analysed is the long-term; inter-annual, periodicity, seasonal, diurnal radon variations making use of trend, statistical significance and trajectory density (cluster) analysis methods.

The atmospheric radon signals characterisation will be extended by analysing it in conjunction with two main sets of observations namely on-site measured metrological parameters and high-quality air-mass back-trajectory modelling. The aim will be to use the back-trajectory analysis to independently verify the main findings made from characterising the Southern Hemispheric radon signals. For instance, if a decrease is observed within the higher radon percentiles (> 2000 mBq/m^3) does it correspond with the expected circulation decrease of air-masses originating from a continental origin? The back-trajectory analysis will not just be applicable for tracking where the air-masses originates from but also for providing the associated altitudes. This will present an opportunity to characterise the radon signals based on the altitude that it originates from.

CHAPTER 2 Radioactivity Principles

2.1 Introduction

Utilising the nuclear properties of radon is instrumental in performing ultra-low continuous radon-in-air activity concentration measurements especially with a high temporal resolution. Radioactivity was first discovered by Henry Becquerel in 1896 (Radvanyi and Villain, 2017). Nuclear decay or radioactivity is defined at the microscopic level by which an unstable nucleus of an unstable atom that dissipates energy by emitting radiation. The different radiation types include fast electrons (β-decay, internal conversion and Auger electrons); heavy charged particles (α-decay and spontaneous fission); electromagnetic radiation (γ-rays, annihilation, Bremsstrahlung, synchrotron radiation, and characteristic X-rays); and neutrons.

Radioactive isotopes also referred to as radionuclides can be characterised according to two main groups, primordial or anthropogenic. Primordial radionuclides are known to have originated before the creation of the Earth (Sheppard et al., 2008) which was about 4.543 x 10^9 years ago (Allègre et al., 1995). Primordial nuclides are known as nucleogenesis radionuclides. Consequently, they were not synthesised by mankind however within the Big Bang or stars (Valković, 2000). The primordial radionuclides such as ^{232}Th ($t_{1/2}$ = 1.41 x 10^{10} years), ^{238}U ($t_{1/2}$ = 4.47 x 10^9 years), ^{40}K ($t_{1/2}$ = 1.25 x 10^9 years) and ^{235}U ($t_{1/2}$ = 7.04 x 10^8 years) have radiological half-lives ($t_{1/2}$) comparable to the age of the universe. The age of the universe is estimated at a minimum of 9.5 x 10^9 years (Chaboyer, 1998). It is generally accepted to be 13.5 x 10^9 years which is based on Jordan-Brans-Dicke theory of a scalar field φ[2] (Moffat, 1995). The calculated age of the universe is consistent with the age determined by making use of globular clusters observations (Krauss, 2000). The radionuclide of great importance in this thesis will be radon (^{222}Rn), which is a naturally occurring radioactive material (NORM) that occurs in a primordial decay sequence (see Figure 2-3). A more detailed description of radon will be presented in Section 2.4. The primordial radionuclides decay series (see Figure 2-3) on Earth can be found in nature within the atmosphere, soil, rocks and groundwater.

[2] The solution of an evolutionary differential equation for the scalar field φ drives the vacuum energy towards a cosmological constant at the present epoch that can give for the age of the universe, t = 13.5 Gyr for $\Omega_0 = 1$.

Radionuclides synthesised by humans are defined as anthropogenic for example ^{90}Sr ($t_{1/2}$ = 28.8 years), ^{129}I ($t_{1/2}$ = 1.47 x 10^7 years), and ^{239}Pu ($t_{1/2}$ =2.411 x 10^4 years). The main sources of anthropogenic radionuclides found in the environment are from:

(1) nuclear weapon programs,

(2) nuclear weapons testing,

(3) nuclear power plants,

(4) commercial fuel reprocessing; geological repository of high-level nuclear wastes that include radionuclides that might be released in the future,

(5) production of nuclear medicine, and

(6) nuclear accidents (Hu et al., 2010).

2.2 Radioactivity

In Section 2.2 the fundamental concepts of nuclear decay applicable to this thesis will be presented and discussed. The topics include the following; the exponential decay law; different types of radiation; radiation interaction with matter; and an in-depth overview on the characteristic of radon (nuclear properties, chemical properties, and transport mechanisms). The specific activity concentration of a radionuclide can be quantitatively determined by measuring the associated characteristic radiation. The main modes of nuclear decay include the following: alpha decay (α-decay); beta decay (β-decay); and gamma decay (γ-decay). A full description of the various nuclear decay mechanisms can be found in several textbooks (e.g. Knoll, 2010; L'Annunziata, 2003) and only those of particular importance to this thesis will be presented and discussed.

The following first-order differential equation is used to express the nuclear mechanism of a single decay chain for an unstable radionuclide X1 that decays to another X2:

$$A = -\frac{dN}{dt} = \lambda N \qquad \text{(Equation 2-1)}$$

where N is the number of particles; dt an increment of time; λ the decay constant, and A the total activity (i.e. the number of nuclear decays per second). The International System of Unit

(SI) for an activity of one decay per second is the Becquerel (Bq). The alternative internationally accepted unit is the (Ci)[3].

A solution to the first-order differential equation 2-1 is:

$$N(t) = N_o e^{-\lambda t} \quad \text{(Equation 2-2)}$$

where N_o is the number of radioactive nuclei at t = 0 ($N_o = N_{X1,t=0}$). The following assumptions must hold for all times (t):

$$N_{X_1} + N_{X_2} = N_{total} \quad \text{(Equation 2-3)}$$

and it can be shown that:

$$N_{X2} = N_{X1,t=0}(1 - e^{-\lambda t}) \quad \text{(Equation 2-4)}$$

A prominent radionuclides characteristic is the radiological half-life ($t_{1/2}$). The nuclear half-life for a specific nuclide is defined as the time elapsed for a number of particles to decay to precisely half of its initial value. The half-life equation for a single decay sequence is the following:

$$t_{1/2} = \frac{\ln(2)}{\lambda} \quad \text{(Equation 2-5)}$$

Radionuclides can decay via multiple decay modes (see Figure 2-3). The ratio of the exact number of nuclei that decay via a specific decay mode to the total amount of atoms decayed is referred to as the branching ratio (BR).

Bateman's equations (see Equation 2-8 and 2-9) presents a multiple consecutive decay chain (D > 2):

$$R_1 \rightarrow R_2 \rightarrow \cdots \rightarrow R_i \rightarrow \cdots \rightarrow R_D \quad \text{(Equation 2-6)}$$

will generate the following first-order differential equation:

$$\frac{dN_i}{dt} = \lambda_{i-1} N_{i-1} - \lambda_i N_i \ (i = 2, D) \quad \text{(Equation 2-7)}$$

The general solution to this recursive first-order differential equation is given by Bateman's equation:

[3] The conversion factor between Curie and Becquerel is defined by 1 Ci = 3.7 x 10^{10} Bq.

$$N_D(t) = \frac{N_1(0)}{\lambda_D}\sum_{i=1}^{D} \lambda_i c_i e^{-\lambda_i t} \quad \text{(Equation 2-8)}$$

with the expansion coefficient of:

$$c_i = \prod_{j=1, i\neq j}^{D} \frac{\lambda_j}{\lambda_j - \lambda_i} \quad \text{(Equation 2-9)}$$

2.2.1 Alpha Decay (α)

Alpha decay (α-decay) is one of the modes (see Figure 2-3) utilised to perform ^{222}Rn (radon) and ^{220}Rn (thoron) measurements (Bigu, 1986; L'Annunziata, 2003). The detection of α-particles with particular energy (α-spectrometry) proves to be an efficient method for measuring isotopes of radon (De Felice and Myteberi, 1996; Liang et al., 2018; Picolo, 1996; Topin et al., 2017). The fundamental α-decay of a radionuclide can be expressed as follow:

$${}^{V}_{Z}X \rightarrow {}^{4}_{2}He + {}^{V-4}_{Z-2}X' \quad \text{(Equation 2-10)}$$

where a helium atom also known as an α-particle ($^{4}_{2}He$) is discharged (see Figure 2-1). Unstable heavy isotopes with V > 150 are prone to undergo α-decay. Almost all α-particle energies (E_α) associated with the decay of NORM radionuclides are limited to between 3 and 7 MeV (Environmental Measurements Laboratory, 1997). There is a strong correlation between the α-particle energy (E_α) and the associated radiological half-life ($t_{1/2}$) for a specific radionuclide[4]. Alpha particles with a greater E_α exhibit shorter half-lives (Environmental Measurements Laboratory, 1997). The penetration power of α-particles within matter is extremely low[5].

2.2.2 Beta Decay (β)

For beta decay (β-decay), the nucleus of a radionuclide emits an electron or a positron or captures one of its atomic electrons. In beta minus decay (β^-), a neutron in the nucleus is converted via the weak interaction to a proton. Based on the charge and mass conversation principles the emission of an electron and antineutrino proceed (see Figure 2-1). Beta minus decay generally is more likely to occur in neutron-rich radionuclides. In beta plus decay (β^+), a proton is converted to a neutron and in the process, a positron and neutrino are emitted, also known as positron emission (see Figure 2-1). The process during which a nucleus captures one

[4] For instance, ^{232}Th has a half-life of 1.405 x 10^{10} years with an associated E_α = 3.947 MeV (BR = 21.7 %) and 4.012 MeV (BR = 78.2 %) compared to the shorter half-life of the radon progeny nuclide, ^{218}Po with a higher E_α = 6.002 MeV (99.79%).

[5] α-particles range in-air under standard temperature and pressures is about 2 to 10 cm

of its atomic electrons resulting in the emission of a neutrino is known as electron capture. In the event that a nucleus undergoes beta plus decay, consequently, electron capture is also permitted.

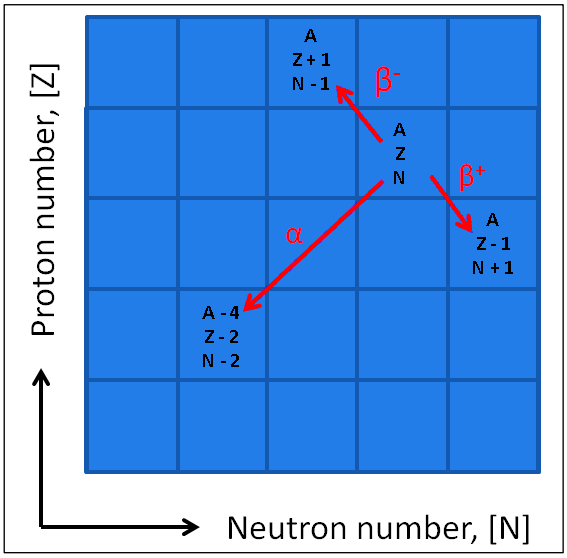

Figure 2-1: Transition chart for nuclear decay modes (α, β^- and β^+) for a single parent atom, with neutron number (N), proton number (Z) and the mass number (A).

2.2.3 Gamma Decay (γ)

Gamma decay (γ-decay) is the emission of a short wavelength photon from a nucleus as the result of the de-excitation of an excited nuclear state. Gamma radiation and X-rays are fundamentally different from alpha and beta radiation based on properties such as charge and penetration power. Gamma rays are electromagnetic ionizing radiation with zero charge. Gamma ray energies range from 70 keV to 8 MeV (McLaughlin et al., 2005). These γ-rays can be seen as energetic photons which are emitted when excited atomic nuclei undergo transitions to a lower nuclear energy state. Gamma radiation can be produced as a secondary reaction of β-decay (or electron capture), for example, that of; ^{22}Na, ^{57}Co, ^{60}Co and ^{137}Cs.

The decay of radon can be measured by making use of γ-spectroscopy utilizing a typical γ-detector such as a High-Purity Germanium (HPGe) detector. Radium (^{226}Ra) decays to ^{222}Rn via α-decay, with an associated 186 keV γ-decay that also occurs in the process. The generation of radon activity concentration can be calculated by performing a sensitive measurement of the ^{226}Ra 186 keV γ-decays. Similarly, ^{222}Rn nuclei are prone to undergo α-decay (BR = 99.92%). However, 510 keV γ-decays do occur rarely making it possible to perform radon activity

concentration measurements via γ-spectroscopy. Using γ-spectroscopy for measuring ultra-low atmospheric radon levels (see Chapter 3), will not be practical. However, γ-spectroscopy is effective for aerial surveys to map NORM (radium) activity concentrations across large areas from the gamma emitters in the decay chain.

2.3 Interaction of Radiation with Matter

The radiation interaction with matter physics principles underpins the fundamental laws to design modern radiation detection systems. The various interaction of radiation with matter are well studied and reported. An exclusive elaboration will be made on the interaction of heavy charged particles (α-particles) with matter applicable to this thesis.

2.3.1 Interaction of Heavy Charged Particles with Matter

Positively charged particles, such as α-particle, predominantly interact with matter and undergoes energy loss based on the following two mechanisms; ionization or collisional losses and radiative losses or Bremsstrahlung (Dance et al., 2014). The first mechanism involves collisions between charged particles moving through matter and excites the electrons from atoms which are part of the material. The ionization mass stopping power is a measure of the charged particles energy loss per unit path length divided by the density of the penetrated material. The ionization mass stopping power, S_{ion}/ρ (MeV.cm^2.g^{-1}) was derived by Bethe-Bloch and extended by Sternheimer in the early part of the 20th century (Dance et al., 2014; Paul and Sánchez-Parcerisa, 2013):

$$\frac{S_{ion}}{\rho} = 2\,\pi\, r_0^2 N_e \frac{\mu_0}{\beta^2}\left[\ln\frac{T^2(T+2\mu_0)}{2\mu_0 I^2} + \frac{\frac{T^2}{8} - (2T+\mu_0)\mu_0 \ln 2}{(T+\mu_0)^2} + 1 - \beta^2 - \delta\right] \qquad \text{(Equation 2.11)}$$

- r_0: classical electron radius
- $N_e = N_A\left(\frac{Z}{A_r}\right)$: N_A is the Avogadro constant
- Z: is the atomic number
- A_r: atomic weight
- $\mu_0 = m_0c^2$: rest mass of an electron multiplied by the speed of light squared
- T: kinetic energy
- β : ratio of the speed of the electron to that of light
- δ : density correction term

- I: mean excitation energy

The second mechanism occurs when a charged particle such as an electron passes in close proximity to the positive nucleus subjecting it to the Coulomb force (Coulomb interaction). During Coulomb interaction, the charged particle will be decelerated, and electromagnetic radiation will be radiated, also known as Bremsstrahlung. The approximate radiative mass stopping power, S_{rad}/ρ (MeV.cm^2.g^{-1}) with approximations of energies in the diagnostic range can be expressed as (Dance et al., 2014):

$$\frac{S_{rad}}{\rho} = \sigma_0 \frac{N_A}{A_r} Z^2 \left(T + \mu_0\right) \overline{\beta} \qquad \text{(Equation 2-12)}$$

- N_A is the Avogadro constant
- Z: is the atomic number
- A_r: atomic weight
- $\mu_0 = m_0 c^2$: rest mass of an electron multiplied by the speed of light squared
- $\sigma_0 = \frac{1}{137}\left(\frac{\varepsilon}{\mu_0}\right)^2 = 0.580 \text{ barn/nucleus}$
- ε: charge on the electron
- T: kinetic energy
- $\overline{\beta} = 5.33$: coefficient, (non-relativistic energies)

For both mechanisms, see Equation 2-11 and 2-12, the energy loss due to the interaction of charged particles (electron) with matter is strongly dependent on the atomic number (Z) of a specific material. The charged particles travel only a finite range within matter (Bragg curve). More specifically α-particles from natural radioactivity do not travel more than a few μm in matter (see Figure 2-2). The energy loss of α-particles in matter can be characterised by a gradual build-up until the Bragg ionization peak is reached followed by a sharp decrease (see Figure 2-2). The α-energy deposition characteristic of naturally occurring radioactive materials (NORM) within the air will be of significant metrological importance within this study (see Section 3.2).

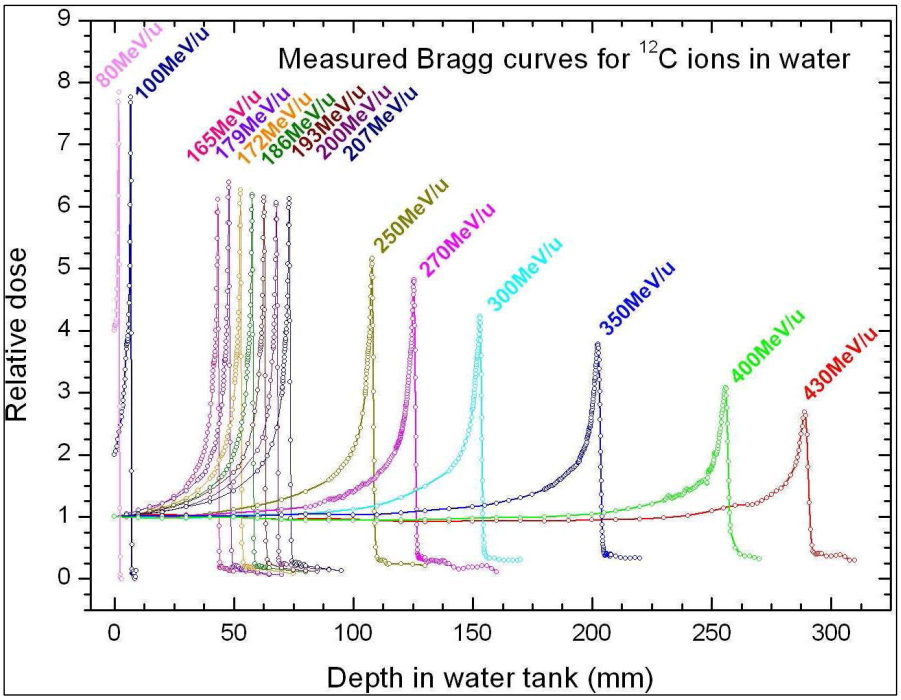

Figure 2-2: Energy dissipation of ^{12}C ions in water at various energies which is also known as the Bragg curve (Yuan et al., 2013).

2.4 Radon Characteristics

2.4.1 Introduction

Radon was first observed by the pioneering radioactivity scientists Pierre and Marie Curie in 1899 as a by-product of their isolation of radium compounds (Radvanyi and Villain, 2017). It was noticed that radium (^{226}Ra) emanated a radioactive gas of which little was known about before 1899 and as a result, it received its first name, radium emanation. The discovery of radon is historically reported to be made by Ernest Rutherford and Robert Owens (Partington, 1957).

The three of the 38 radon isotopes that occur naturally are; ^{219}Rn ($t_{1/2}$ = 3.96 s) known as actinon since it is part of the actinium series; ^{220}Rn ($t_{1/2}$ = 55.6 s) known as thoron; and ^{222}Rn ($t_{1/2}$ = 3.8235 d) known as radon (see Table 2-1). Hereinafter, radon or Rn will refer to the radionuclide ^{222}Rn.

Isotope	Historic Name	Atomic Number, [Z]	Neutron Number, [N]	Isotopic mass, [u]	Half-life, [$t_{1/2}$]	Decay Modes	Daughter Isotope
^{219}Rn	Actinon, Actinium emanation	86	133	219.00948 02 (27)	3.96 (1) s	α	^{215}Po
^{220}Rn	Thoron, Thorium emanation	86	134	220.01139 40 (24)	55.6 (1) s	α	^{216}Po
						$\beta^-\beta^-$ (rare)	^{220}Ra
^{221}Rn		86	135	221.01553 7 (6)	25.7 (5) mi n	β^- (78%)	^{221}Fr
						α (22%)	^{217}Po
^{222}Rn	Radon, Radium emanation, Emanation , Emanon, Niton	86	136	222.01757 77 (25)	3.8235 (3) d	α	^{218}Po

Table 2-1: Table of radon isotopes ($133 \leq N \leq 136$) with associated nuclear properties (NNDC, 2018; Wieser, 2006).

2.4.2 Nuclear Properties of Radon

The nuclear properties of radon will be discussed in this section. The fundamental design principles of modern radon metrology are based on nuclear properties. The isotopes of radon ranging from ^{193}Rn to ^{231}Rn (NNDC, 2018) have predominantly α-, β^-- and β^+ decay modes. The half-lives for these isotopes range from an extremely short 245 ns (^{214m}Rn) up to 3.82 days for ^{222}Rn (NNDC, 2018). Radon is part of the primordial transuranium group (see Figure 2-3) which is produced by the decay chain series originating from uranium (^{238}U). Radon undergoes predominantly α-decay with E_α = 5.59 MeV and BR = 99.92% to ^{218}Po. For practical environmental radioactivity metrology purposes, the decay modes with ultra-low BRs (< 0.01%) will not be taken into consideration in this thesis. By making use of this assumption the following decay scheme of radon (Figure 2-3, red dashed sequence) and thoron (Figure 2-4,

red dashed sequence) will be utilised. In the atmosphere radon decay daughter products (RnDP) initially exist as positively charged free ions. Nano-sized clusters of both unattached RnDP (> 10 nm) and RnDP attached to aerosols (10 to 1000 nm) could be produced (Butterweck et al., 1992; Trassierra et al., 2016; Vaupotič, 2008).

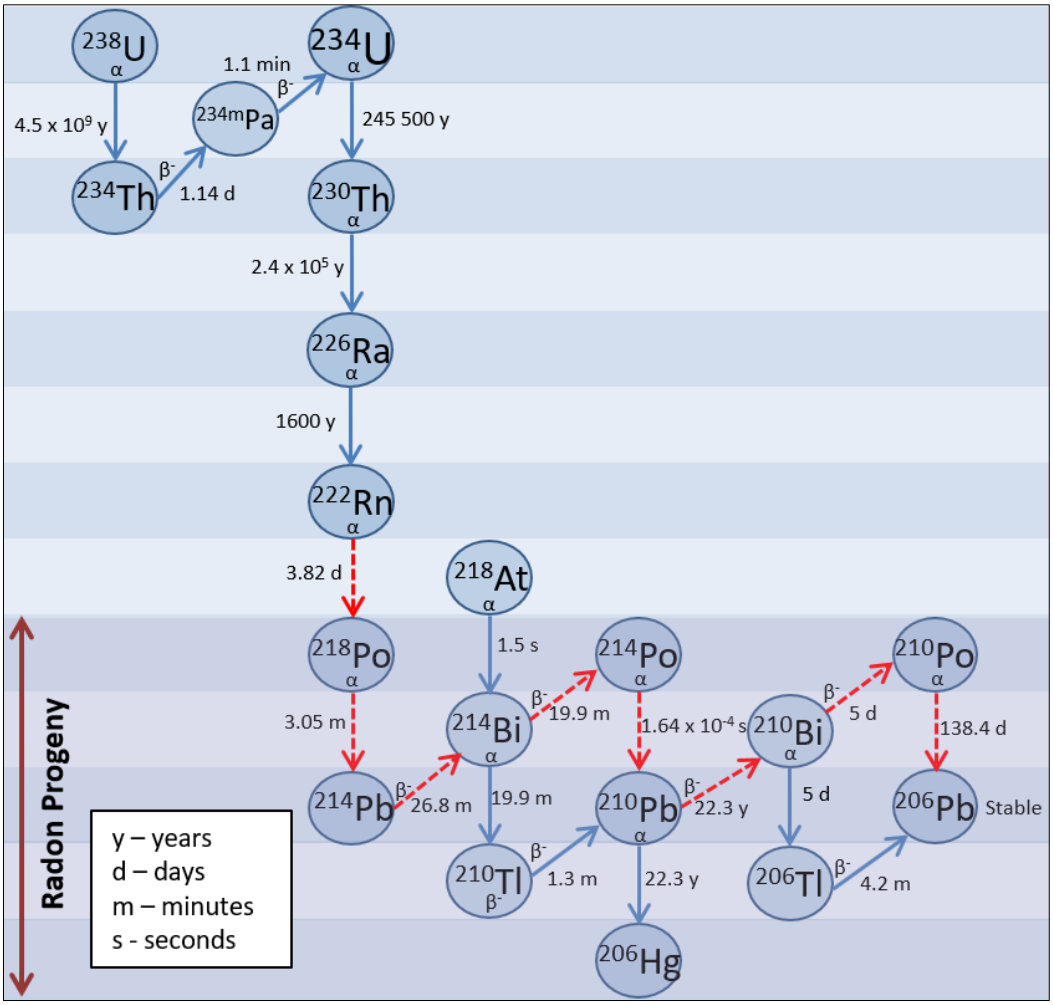

Figure 2-3: The alpha and beta decay modes of the uranium series. The conventional environmental radon decay chain is illustrated with the dashed red arrows.

The ratio between the activity concentration of equilibrium equivalent (EC) radon progeny (^{218}Po, ^{214}Bi, and ^{214}Po) and radon (^{222}Rn) is known as the equilibrium factor (F). An equilibrium factor of F = 1 implies that radon and its associated progeny activity concentrations in a specified space-time are equal (in equilibrium). In forced ventilated regions a typical value of F = 0.2 is expected. The ICRP recommends general indoor and outdoor equilibrium factors of 0.4 and 0.8, respectively (ICRP, 2014). Within natural systems such as the atmosphere, the activity concentrations of radon and its progeny vary significantly with space and time due to

factors such as surface characteristics, altitude above sea level, aerosol concentration (including cloud condensation nuclei), ventilation and humidity (Ali et al., 2018; Jamil et al., 1997). As a result, the equilibrium factor (F) for a dynamic environment can range from 0.19 – 0.90 (Lee & Lee, 2013; Yu et al., 2008). By making use of the processed Bateman's equations (see Equation 2-7 and 2-8) the temporal nature of unsupported (see Section 2.4.4.4) radon and associated decay progeny (n = 4) is simulated (see Figure 2-4 and Appendix Code 1). The assumption in the model is introduced that no ventilation occurs or rather it can be considered to be a closed system. It can be seen that the equilibrium factor is a time-dependent parameter (see Figure 2-4). At t = 0 it is transparent that the F = 0, the equilibrium factor will increase to a maximum at about 3 minutes and will then gradually decrease onwards (see Figure 2-4) for this particular model.

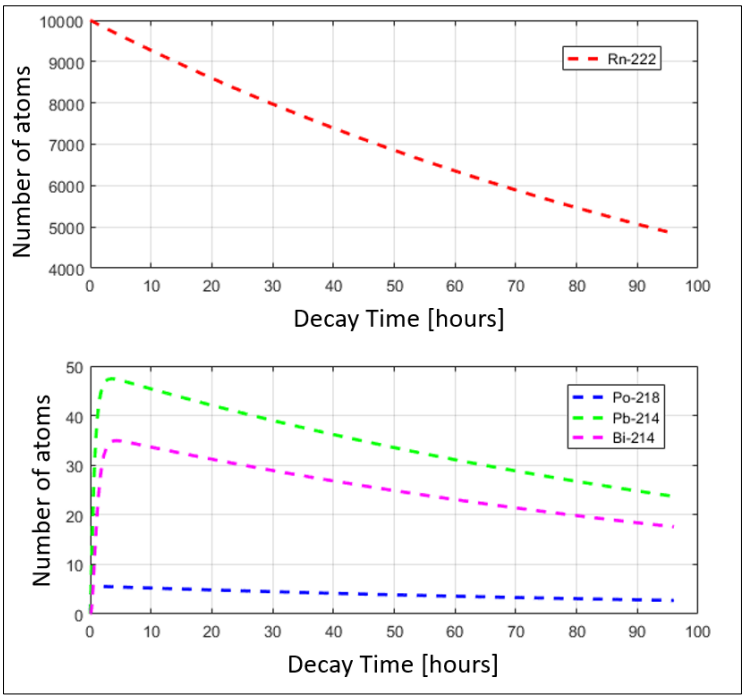

Figure 2-4: Modelling of unsupported radon (upper plot) and associated progeny (lower plot) making use of the Bateman equations for three consecutive decay daughters (n = 4) with 10 000 ^{222}Rn- atoms at t_0 = 0 hours (see Appendix Code 1).

Thoron (^{220}Rn) is an isotope of radon (see Table 2-1) in the ^{232}Th decay chain. ^{220}Rn ($t_{1/2}$ = 55.6 s) undergoes α-decay (E_α = 6.28 MeV) to ^{216}Po ($t_{1/2}$ = 0.14 s) which α-decays (E_α = 6.77 MeV) to ^{212}Pb ($t_{1/2}$ = 10.6 h) and further β-decays to ^{212}Bi (see Figure 2-5). ^{212}Bi ($t_{1/2}$ = 60.6 min) undergoes both α-decay (E_α = 6.21 MeV, BR = 36%) to ^{208}Tl ($t_{1/2}$ = 3.1 min) and β-decay (E_β

= 2.25 MeV, BR = 64%) to ^{212}Po ($t_{1/2}$ = 0.2 µs) which decays to the stable isotope ^{208}Pb (see Figure 2-5).

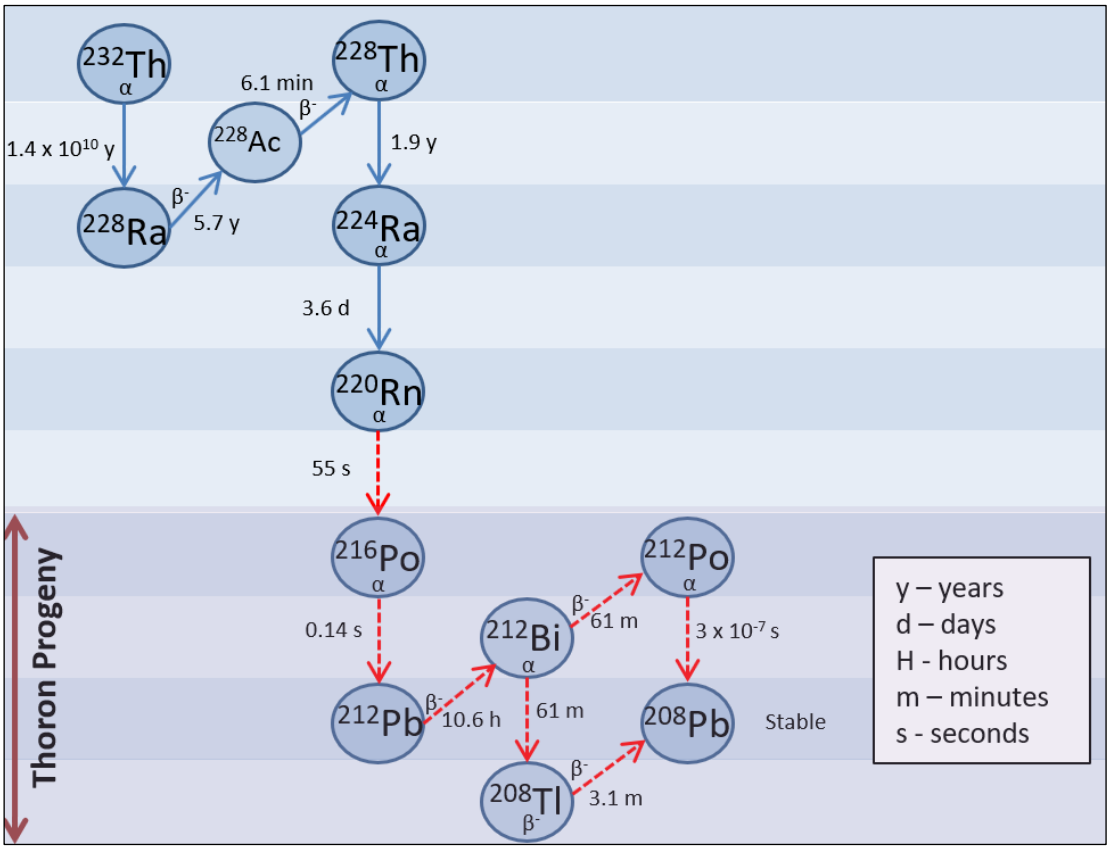

Figure 2-5: Thorium's alpha and beta decay chain and associated thoron decay progeny. The conventional radon decay chain is illustrated with the dashed red arrows

2.4.3 Chemical and physical properties

Radon is a noble gas, and therefore chemically unreactive; attributable to its valence electron structure ($1s^2\ 2s^2 2p^6\ 3s^2 3p^6 3d^{10}\ 4s^2 4p^6 4d^{10}\ 5s^2 5p^6 5f^{14} 5d^{10}\ 6s^2 6p^6$) being completely occupied. As a result, it is a versatile natural tracer for atmospheric studies.

Radon is colourless, tasteless, and odourless. As an element, it exhibits characteristics of both true metals and non-metals. The non-magnetic monatomic gas with a boiling point of -61.7 °C has a density of about 9.73 kg/m^3 at STP. This makes radon one of densest gases at room temperature. When radon is cooled below its freezing point of -71.6 °C it emits a bright radioluminescence.

CHAPTER 3 Atmospheric Radon Metrology

3.1. Introduction

The emphasis of Chapter 3 will be on discussing the atmospheric radon metrology applicable to this thesis. The dual-flow loop, two-filter DFLTF ANSTO atmospheric radon system is considered to be the leading detector within its class (ANSTO, 2016; Griffiths et al., 2016). The ANSTO radon detector has demonstrated the ability for the past 3 decades to achieve ultra-low atmospheric radon activity concentration measurements (< 50 mBq/m^3). The ANSTO radon detector's design, functioning, calibration, background monitoring, data acquisitioning, and processing will be presented and discussed.

Marine air-masses are prone to have a 10 to 1000 times less radon compared to continental masses (Chambers et al., 2014; Zahorowski et al., 2004). As a result, when performing a study of atmospheric radon associated especially with marine air-masses a radon detector capable of ultra-low detection sensitivity will be required. Leading commercial radon detectors like the AlphaGuard or RAD7, are not capable of performing accurate continuous ultra-low radon measurements which requires a high temporal resolution (< 1 hour). The ANSTO DFLTF radon detector is designed to meet the following requirements; remotely controllable automatic operation; minimum maintenance; low power consumption, reliability; and high-temporal resolution ultra-low radon sensitivity. However, it should be noted that there are subtle differences with respect to components of the three ANSTO radon detectors such as delay tank volume (see Table 3-1), flow rates, and the number of detector heads.

The other two radon-in-air detectors used for supplementary measurements were the electret ion chamber (EIC) E-PERM (see Section 3.4.2) and α-spectroscopy RAD7 detector (see Section 3.3.2). EIC E-PERM detectors were deployed to conduct passive ambient radon-in-air level monitoring within the CPO ANSTO detector laboratory. The ambient laboratory radon-in-air level is of use as an indicator of the surrounding radon which can act as a contaminant in the event of a leak. The RAD7 detector was utilised to perform radon and thoron emanation measurements from soil and rocks samples (see Section 3.3.4) and the ANSTO thoron background signal.

3.2. ANSTO DFLTF Radon Detector

3.2.1 Introduction

In Section 3.2, the innovative radon detection technology of the ANSTO DFLTF detector will be discussed. The DFLTF detector is based on a direct radon detection approach. A direct radon detector in principle is based on filtering out existing radon progeny and sample only the radon which will be determined by measuring the associated decay progeny. The direct radon detection approach is unaffected by the degree of ambient disequilibrium between radon and associated progeny (Griffiths et al., 2016). The DFLTF detector is additionally referred to as the HURD, HUge Radon Detector. The primary radon detector currently operating at CGO is called the HURD3 (the 3rd HUge Radon Detector), on account of its 5000 L delay tank volume. The auxiliary (backup) detector at CGO is called BHURD. HURD3 is a unique DLFTF detector on account of its large volume and 8 detector heads, giving it a superior sensitivity of 1.53 cps/Bq.m^{-3} or lower level of detection of 9 mBq/m^3 (see Table 3-1). For comparison, the leading commercial electronic radon detectors such as the RAD7, RTM-2100 or AlphaGUARD have a lower level of detection (LLD_1) of about 0.6 Bq/m^3 based on an hourly temporal resolution (Lin et al., 2013; Topin et al., 2017).

To perform ideal continuous radon measurements of deep baseline air-masses an LLD_1 ranging from 10 to 100 mBq/m^3 is a minimum prerequisite. Ultra-low atmospheric radon measurements are almost exclusively used at coastal and high-altitude observatories and marine research vessels (RV). Observatories situated inland will be susceptible to predominant continental air-masses associated with higher radon activity concentrations which will not require a detection system with such a low LLD_1. The core components of the DFLTF radon detection system are illustrated in Figure 3-1. It should be noted that the external delay tank can be technically regarded to be part of the sampling system and likewise the internal delay tank part of the radon detector.

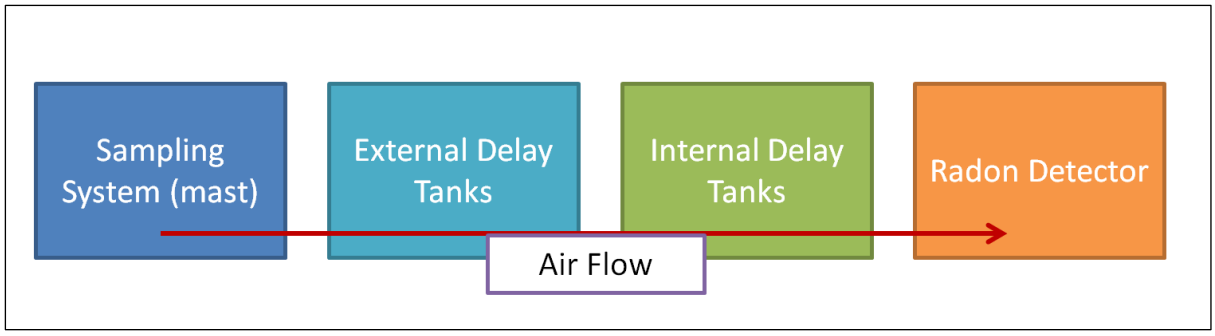

Figure 3-1: Simplified block diagram illustrating the four principal elements of the DFLTF radon detection system.

3.2.2 Sampling System

The first section of the DFLTF radon detection system is the ambient air sampling system (see Figure 3-1). The sampling system consists of a mast and intake line (see Figure 3-2), stack blower (see Figure 3-3), and water trap. Atmospheric radon measurement starts with ambient air being sampled from the top of a mast. To reduce unwanted sampling of regional thoron emanation, it is ideal to sample air from high above the surface source (see Figure 3-2). The CGO, CPO and MLO sampling heights above ground level (a.g.l.) is 70 m, 30 m and 38 m, respectively.

The half-life of thoron is 55.6 s. By making use of this nuclear property, it is assumed a large amount of thoron would have decayed by the time elapsed by travel from potential local emanation spots towards the sampling inlet near the top of the mast. Nonetheless, fast-moving local winds could shorten the travelling time. The DFLTF detector technically cannot distinguish between radon and thoron decays. Consequently, it is of importance to eliminate potential ambient thoron intake into the detection chamber (see Figure 3-1). The importance of removing thoron is most directly associated with the variable influence such as the progeny (see Figure 2-5), ^{212}Pb ($t_{1/2}$ = 10.6 h) on the background α-decay rate of the second filter (see Figure 3-11).

Noteworthy design features are implemented to avoid potential ambient thoron contamination (Brunke et al., 2002). A “gooseneck” inlet is used to minimising the intake of precipitation and a water trap remove condensation forming within the sampling lines (particularly at night). In sub-zero climates, the aim is to avoid sampling of precipitation based on the risk of it being frozen which could result in a blockage. A water trap is becoming of great use if the ambient

relative humidity (RH) is high (> 95%). The water trap is installed at a low point between the inlet and stack blower. The piping system consists of two main sections; inlet to the stack blower (40 mm) and from the stack blower to the radon detector (19 mm). The sampling system is considerably less critical for a direct radon measurement method approach compared to the indirect approach when tube loss comes into effect (Chambers et al., 2019, 2018; Levin et al., 2017).

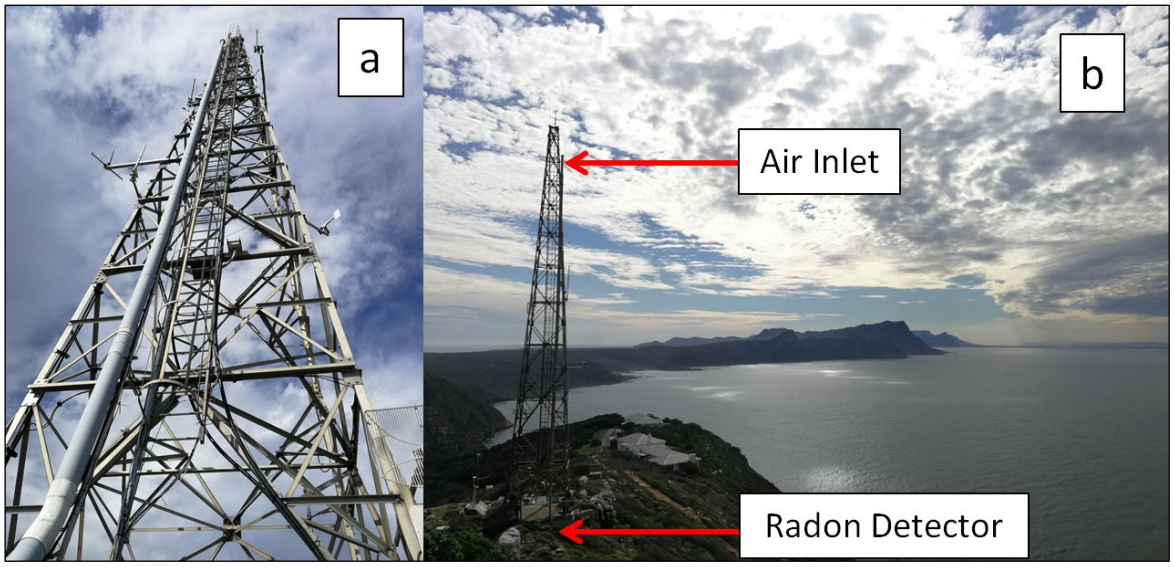

Figure 3-2: (a) CPO atmospheric aluminium sampling mast. (b) Sampling mast on top of the coastal cliff at Cape Point nature reserve.

A stack blower (see Figure 3-3) is installed when ambient air sampling is performed from masts with a height a.g.l. of 10 m or more (when flow impedance becomes large) otherwise the blower within the detector is sufficient. The stack blower's function is pumping air from the inlet line to the delay tanks and lastly to the radon detector (see Figure 3-1). The stack blower's continuous pumping rate is adjusted by means of a flow bypass system to be between 80 to 100 L/min in 1500 L detectors. The flowrate was selected based on balancing the ratio between the detector volume to flow rate in order to achieve a flush time of around 15-20 min (sufficient time for some of the newly sampled radon to decay inside the detector). Ensuring a high flow rate in the sampling system for the purpose of avoiding radon decay is not of importance since it has a half-life of 3.82 d. The system is kept at a positive pressure of 80-120 Pa relative to the ambient conditions. The internal positive pressure feature reduces the possibility even further

of accidental regional (< 850 m) radon or thoron sampling that may inadvertently occur as a result of leaks in the detector delay volume or inlet line plumbing.

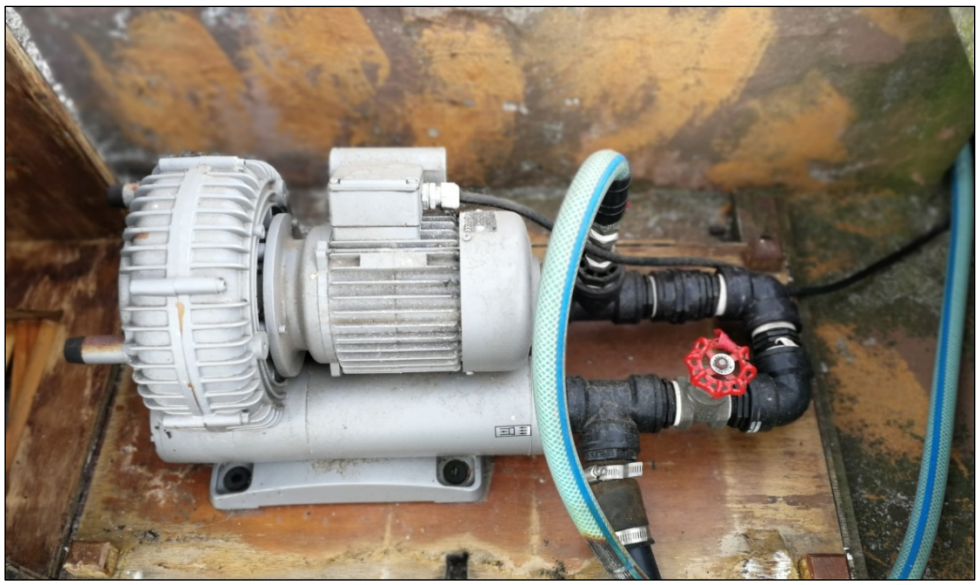

Figure 3-3: An operational stack blower. The black PVC 40 mm piping is directed from the mast to the inlet of the stack blower. The green outlet 19 mm piping flows from the stack blower to the delay tanks.

3.2.3 Delay System

Delay tanks have been installed for the primary purpose of reducing thoron concentrations to < 2% of their ambient values. This is performed by delaying the sampled air within tanks in order for the sampled thoron ($t_{1/2}$ = 55.6 s) to undergo decay. Thoron progeny within the sampling line is subsequently removed by the primary filter. As discussed, the external delay tanks can be regarded as part of the sampling system. Injecting and removing ambient air from the opposite ends of the delay barrels minimises the chance of the flow bypassing most of the barrel volume in order to optimize mixing. The CPO delay system, for example, consisted of the following components:

a) Piping Line One (40 mm): 44 L
b) Piping Line Two (19 mm): 4 L
c) External Delay Tanks (Two Plastic Bins): 400 L
d) Detector Delay Tank: 1500 L

The total delay volume of the DFLTF radon detectors used in this thesis range from about 2000 L (CPO and MLO) to 5000 L (CGO-BHURD3, see Table 3-1). It should be noted the volume of the sampling line controls thoron decay (to minimise instrumental background influences), the volume of the detector controls radon decay (for sampling). The estimated traveling time from the mast inlet to the radon detector chamber using a pumping rate of 90 L/min will be about 6 min. By making use of the 6 min traveling time the percentage thoron which decayed is calculated (see Figure 3-4). This calculation shows that only 1 % of the initial thoron has the potential to be detected assuming no mixing occurred, or leaks are present (see Figure 3-4).

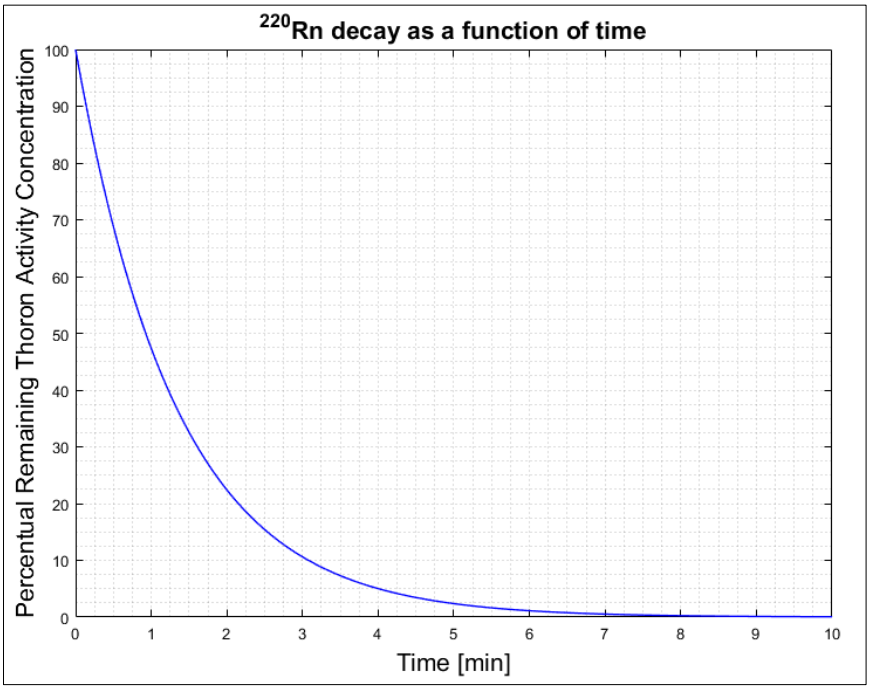

Figure 3-4: Percentage of thoron within an enclosed system as a function of time (see Appendix Code 2) based on the assumption that no additional thoron is added to system after t = 0.

3.2.4 Detector Unit

The detector unit consists of two main sections (see Figure 3-5); detector delay tank (1500 L) and detection electronics hub (see Figure 3-6). The radon detector is designed as a dual-flow loop two-filter (DFLTF) system. The dual-flow loop refers to internal and external flow loops within the detector unit (see Figure 3-10). The internal flow loop is defined as the flow of ambient air passing through the homogenising screen directed to the detector head to flow through the secondary filter (see Figure 3-11) into the external flow loop. The external flow loop can be described as the flow of air through the inlet filter (see Figure 3-10) to the internal delay tank.

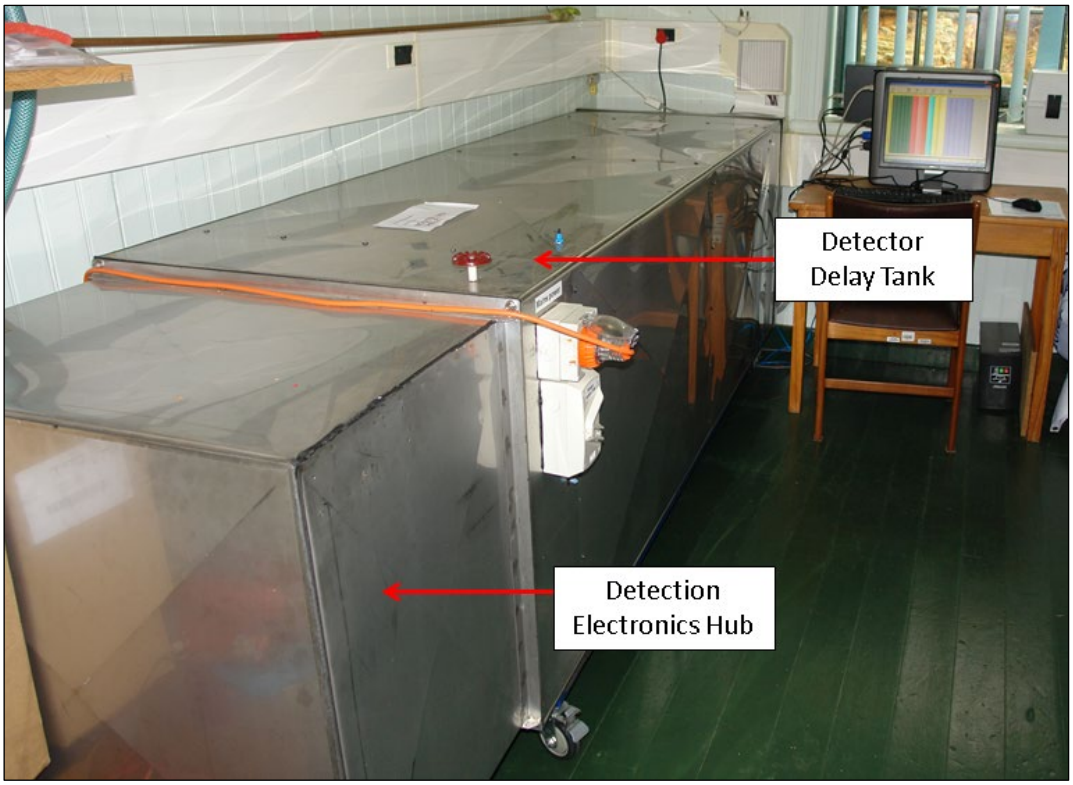

Figure 3-5: CPO DFLTF detector installed within a laboratory situated below the sampling mast.

The dual-flow loop will be discussed in further detail in the following section. Ambient air is pumped from the external delay tanks to the primary inlet filter also referred to as the first filter. The inlet filter removes aerosols combined with ambient radon and thoron progeny (see Figure 3-7). It is essential to ensure that the detector unit remains aerosols free to prevent the formation of attached radon progeny (plating). The first filter is installed inside the electronic hub (see Figure 3-6, 6) and the secondary filter is located within the detector head (see Figure 3-6, 3). The sampled air is injected through the inlet filter into the gas flow meter (see Figure 3-10). A domestic gas meter is installed to measure the flow rate of air which surpasses through the external flow loop (see Figure 3-10). A domestic gas meter is chosen for its simplicity and reliability.

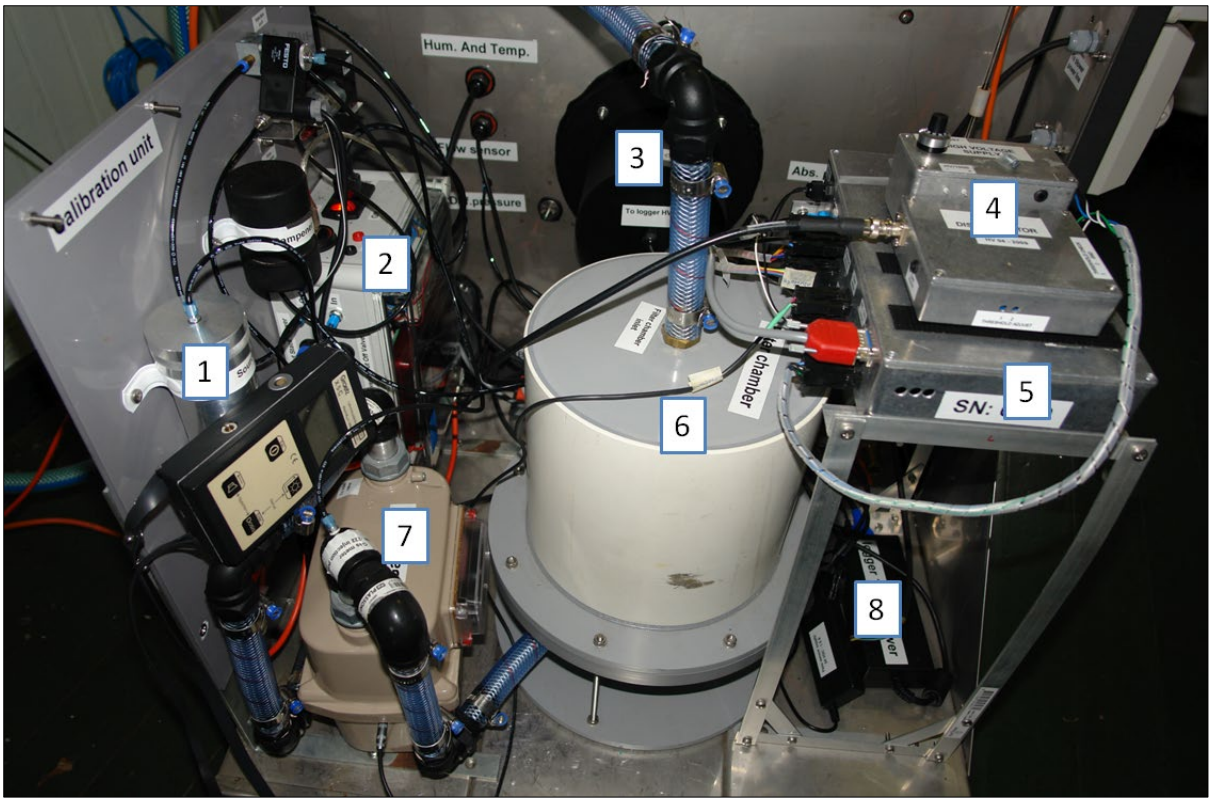

Figure 3-6: Detection electronic hub: (1) ^{226}Ra calibration source, (2) blower electronics, (3) detector head, (4) HV pad, (5) data logger, (6) inlet filter, (7) gas flow meter and (8) power supply.

Two identical radial blowers are installed within the internal delay tank (see Figure 3-7). The EBM-PAPST blower is highly efficient based on low power consumption and an operational lifespan of 10 to 15 years when continuously operated. The first blower's function is to move ambient air through the detector (the external flow loop; see Figure 3-10). The second blower's purpose is for circulating air within the detector's main volume, through the measurement head. A flow homogenising denim screen is installed within the detector delay tank to minimize turbulent flow in the main delay volume (see Figure 3-10). The homogenising screen is installed about 30 cm from the one end of the detector to create non-turbulent air flow through the majority of the delay volume (see Figure 3-7). The denim screen creates a penetrative inlet barrier between the external and internal flow loop. The flow homogenising assists with reducing plate-out of newly generated unattached progeny on the walls of the detector or internal plumbing. High flow rates from the internal blower are of importance ensuring unattached radon progeny is filtered out of the system by the secondary filter (see Figure 3-8) before it decays (Whittlestone and Zahorowski, 1998). Additionally, the entire volume of

sampled air within the detector needs to pass through the detector head in less time than the specified half-life of most of the α-emitting radon progeny (see Figure 2-3).

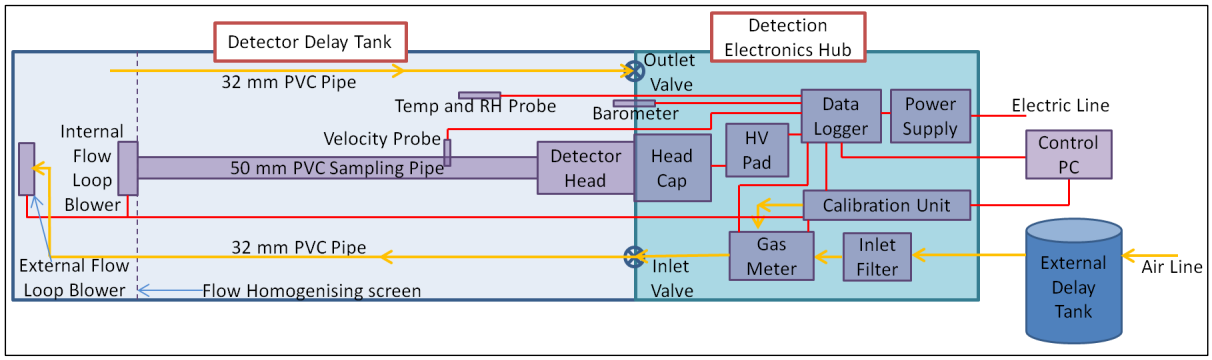

Figure 3-7: DFLTF radon detector schematic illustrating the various internal components (top view).

The heart of the DFLTF detector unit is considered to be the detector head (see Figure 3-7 and 3-9). The detector head contains the key components (see Figure 3-11) for detecting the α-decays (^{218}Po and ^{214}Pb) to determine the atmospheric radon activity concentrations. These components consist of; a PMT (see Figure 3-9, b and c) which is designed to detect the photons generated from the interaction between the α-decays and the ZnS (Ag) coated scintillator screen (Figure 3-8, b), secondary filter (see Figure 3-8, b and Figure 3-9, a), and an optic reflector for increasing the PMT photon detection (see Figure 3-11).

The decay modes (see Figure 2-3) of the radon progeny are predominantly short travelled α- and β-decay as discussed in Section 2.4.2. The α-decays energy deposition range in the air (STP) based on energies ranging from 4 MeV to 9 MeV is in the order of 2 cm to 10 cm. Therefore, to detect the unattached radon progeny, the sampled air must be in a close proximity (see Figure 3-9, d) to the ZnS (Ag) scintillator screen (see Figure 3-11).

Figure 3-8: (a) Unassembled detector head showing the secondary mesh filter (1) and internal support framework (2). (b) Internal framework with installed white ZnS (Ag) scintillator screen (3) and an assembly with both scintillator screen and surrounding secondary filter (4).

The DFLTF detector is designed in such a manner to achieve maximum airflow across the scintillator screen (see Figure 3-10 and Figure 3-11). This is achieved by concentrating the flow pathways across the scintillator (see Figure 3-11). The secondary filter is a 20-micron stainless steel filter with very low flow impedance. The rapid flow of air through the second filter is important due to the short half-life of ^{218}Po ($t_{1/2}$ = 3.05 m). For this reason, it is required for most of the air within the 1500 L internal delay tank to pass through the detector head in less than three minutes. Consequently, to promote detection efficiency it is important to position the unattached decay progeny as fast as possible within the detection range of the scintillator screen. The secondary filter also acts as a filter for reducing unattached radon

progeny circulating between the internal and external flow loops (see Figure 3-10). For the secondary filter to be effective at capturing radon progeny it is required to be in an unattached state. As discussed, the ambient aerosols are removed by the first filter to reduce the formation of attached radon progeny.

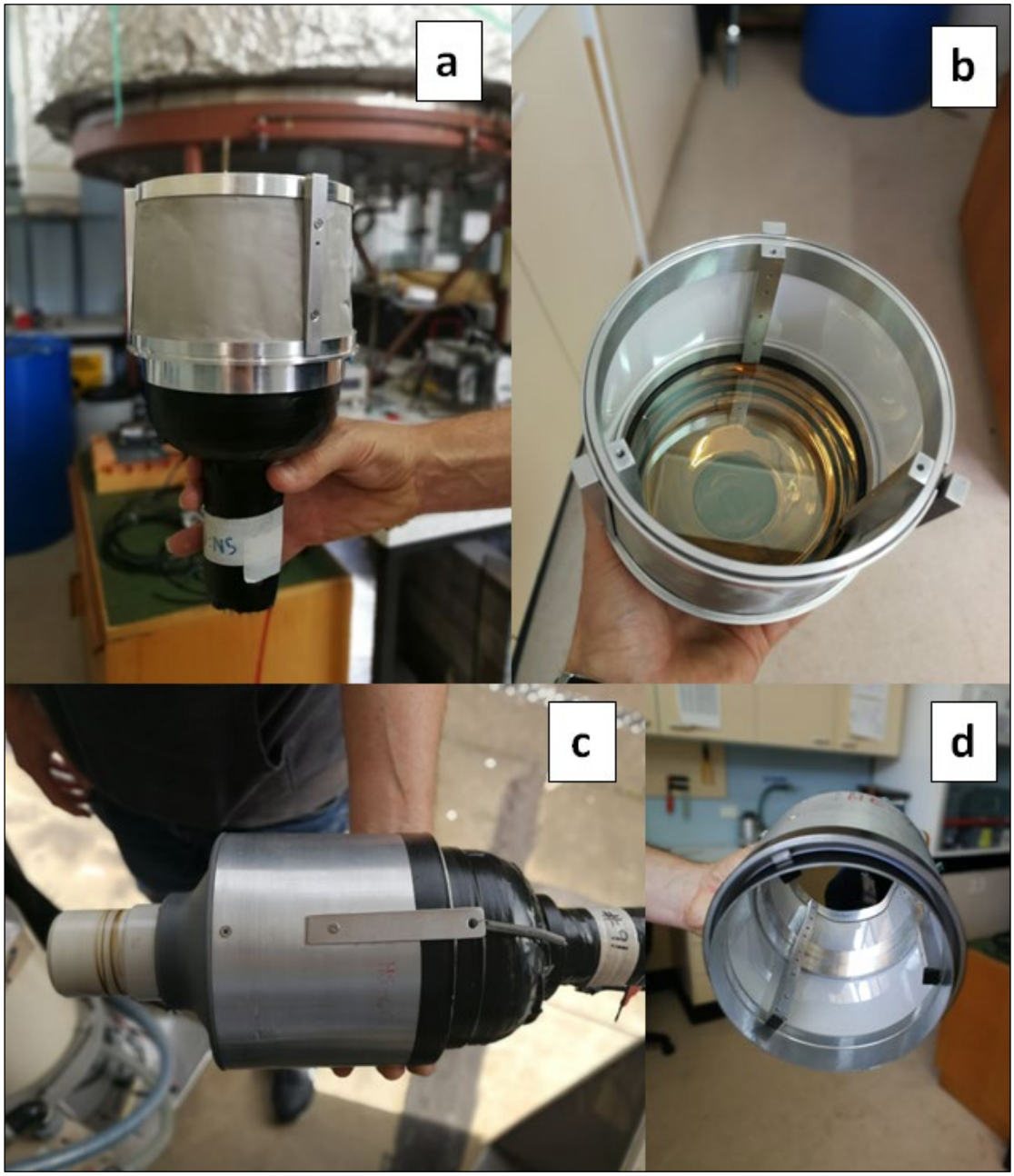

Figure 3-9: (a) Detector head assembly with an attached PMT without an attached external casing viewed from the side. (b) Assembly viewed from the top with the PMT visible at the bottom and the white scintillator screen. (c) A fully assembled detector head unit viewed from the side. (d) An assembly with an external casing viewed from the top without an attached PMT to illustrate the entry gap between the secondary filter and visible scintillator screen.

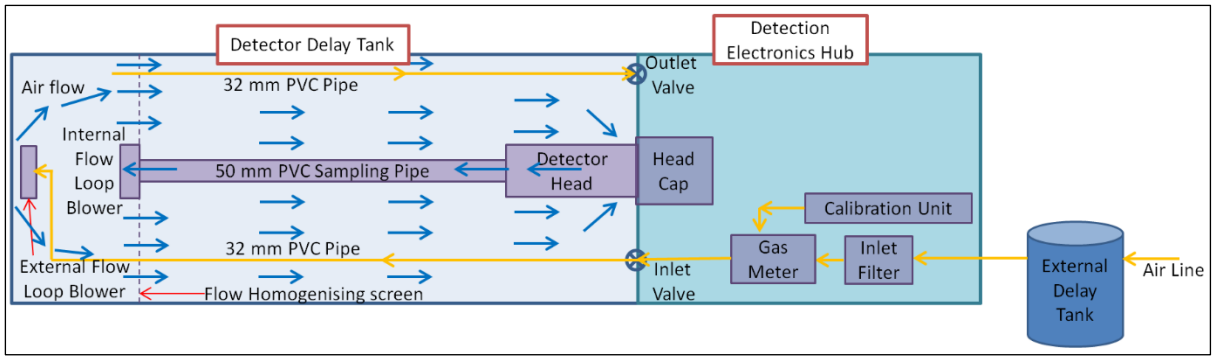

Figure 3-10: Schematic of the internal and external airflow within the radon detector (top view).

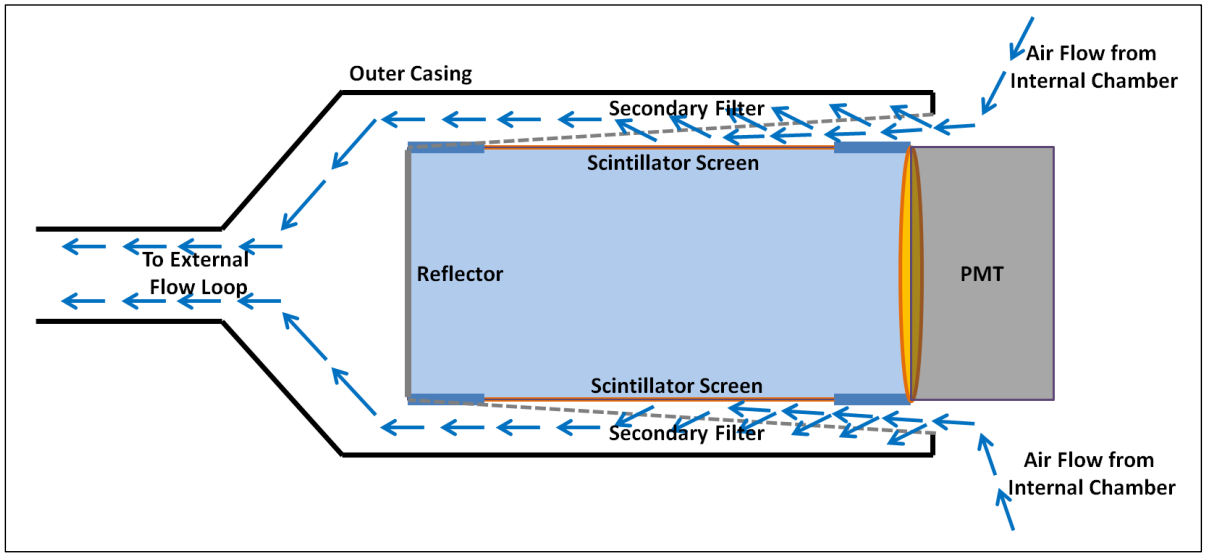

Figure 3-11: DFLTF radon detector schematics to illustrate the internal components and the associated airflow pathways.

The CGO, CPO and MLO DFLTF radon detector design is fundamentally identical. However, some components do vary between the three DFLTF detectors. The most significant differences are the delay volume capacity and number of detector heads (see Table 3-1). It should be noted that two DFLTF detectors are operating simultaneously (see Table 3-1) at CGO compared to only one radon detector at CPO and MLO. The primary CGO detector is the HURD3 and the supporting detector (backup) is referred to as the BHURD. The CGO HURD3 is an advanced DFLTF detector with superior sensitivity which is operating by making use of eight detector heads and an internal delay volume of 5000 L (see Table 3-1).

Location	Detector Heads Units	Internal Delay Volume, [L]	Sensitivity, [cps/Bq.m^{-3}]	Background, [cph]	LLD$_1$, [mBq/m^3]
CPO	1	1500	0.34 (01-01-2018)	86 (14-03-2018)	33 (28-05-2018)
CGO - BHURD	1	1500	0.38 (14-03-2018)	32 (21-09-2017)	24 (25-12-2015)
CGO - HURD3	8	5000	1.53 (28-05-2018)	249 (02-02-2017)	9 (02-04-2016)
MLO	1	1500	0.35 (01-05-2004)	-	27 (01-05-2004)

Table 3-1: DFLTF radon detectors characteristics at the three main measurement locations used in this study.

The CPO DFLTF radon detector has received upgrades in 2001 and 2011. The 2001 and 2011 upgrades reduced the hourly temporal LLD$_1$ from 42 ± 13 mBq/m^3 to 33 ± 10 mBq/m^3 and 33 ± 10 mBq/m^3 to 25 ± 8 mBq/m^3, respectively. The upgrades include; installation of an automated calibration system (PYLON), newly upgraded photomultiplier tubes (PMT), improved detector head design, thoron elimination installations and indoor housing. The most significant of these upgrades were performed in 2011.

3.2.5 Instrumental Calibration

Rigorous metrology quality assurance (QA) and quality control (QC) are applied. One of the processes by which this accomplished is by performing automated calibration. The selected calibration data from CPO will be presented to discuss the calibration process. The fundamental calibration process at CGO and CPO are identical.

The primary purpose of monthly calibrations is to configure the PMT count rate to a standard specific radon activity concentration and tracking the gradual degradation in performance of the detector head. The calibration coefficients (CF) are utilised to calculate the representative atmospheric radon activity concentration based on the PMT count rate. The calibration coefficient is also of great use to monitor the long-term change in the performance of the detector head/s (see Section 3.2.4).

The physical calibration process is where a quantified (controlled) amount of radon is injected into the detection chamber combined with a controlled measurement to determine the calibration coefficient. Radon (^{222}Rn) is generated from the decay of radium (^{226}Ra, $t_{1/2}$ = 1600 years, see Figure 2-3). The radium source installed has a specific activity of 19.85 kBq. It is utilised to generate standard radon flux during calibration. Radium (^{226}Ra) is an ideal calibration source based on the long half-life of 1600 years. Monthly accumulation of radon (19.77 kBq) is purged from the system prior to calibration (see Figure 3-12). The specified ^{226}Ra source (see Figure 3-6, 1) generates radon at a rate of 2.5 Bq/min. During calibration, radon is injected via an injection line with an internal diameter of 3 mm into the gas meter inlet (see Figure 3-7). At the typical sampling rate of 90 L/min, the radon for calibration purposes is circulated within the detector delay tank. The calibration sequence takes about 12 hours to complete. Six hours in total is utilised to purge the system from ambient radon conditions and the elevated radon generated from the post-calibration process.

Autonomous remote calibration is an important element of operation since it will not be practical to ship the radon detector periodically to a calibration facility in most situations like for instance Antarctica. The following reasons make it unpractical to ship the detector for calibration purposes; the radon detector could be installed at a distant location; the detector is not accessible due to extreme weather conditions during certain times of the year (Antarctica); the system is large; valuable measurement time will be lost while the system is in transit and will increase operational expenses.

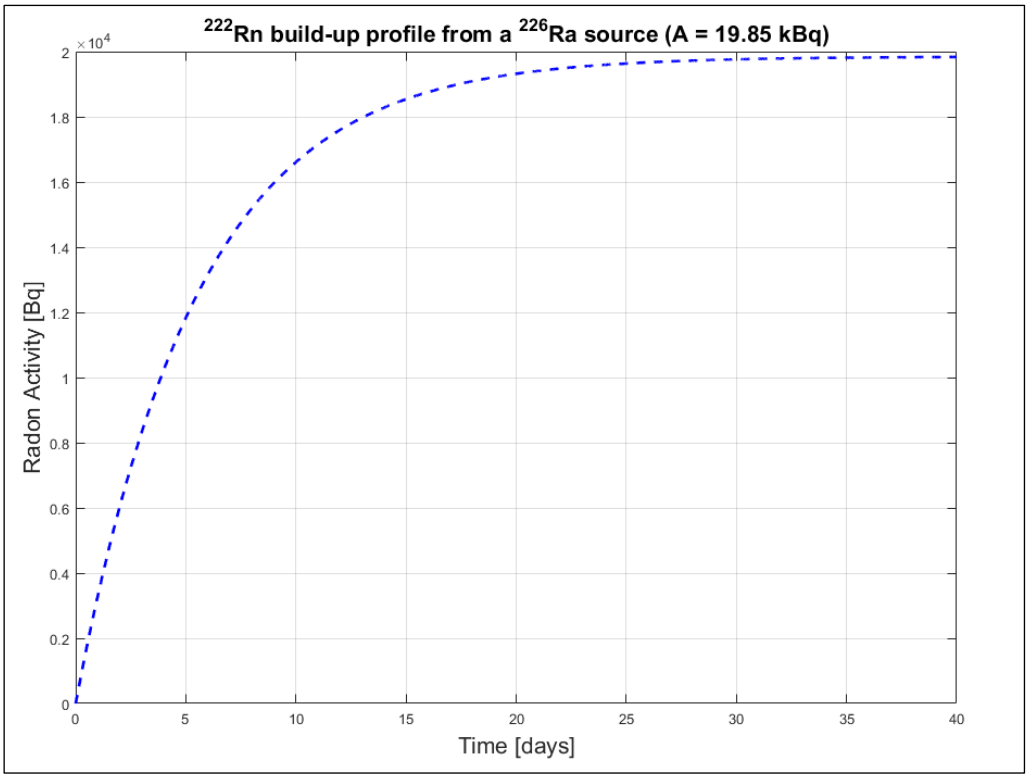

Figure 3-12: Modelling the build-up of ^{222}Rn from a known ^{226}Ra source (19.85 kBq) as a function of the time making use of the Bateman equations in an enclosed environment (see Appendix Code 3).

The calibration factor (CF) is determined from each calibration run (see Figure 3-13). The calibration factor is applied during offline processing when computing the atmospheric radon activity concentration (see Section 3.2.8). Ideally, the calibration should be as stable and consistent with small to no fluctuations. However, as indicated making use of CPO DFLTF calibration data (see Figure 3-14), minor fluctuations are observed. The following factors contribute to fluctuations during calibration:

a) Temperature sensitivity of the electronic components (see Figure 3-6) such as the high-voltage (HV) supply unit. Diurnal temperature changes can result in fluctuation of HV supply to the PMT of up to 10 V.

b) Unconditioned air utilised or calibration (see Figure 3-10). Ambient air is being used as a transport medium to transfer ^{222}Rn generated from the ^{226}Ra calibration source to the detection chamber. If the air which is utilised for this process fluctuates in ambient radon levels, it will result in unsystematic calibration errors being introduced.

c) The RH of the ambient air utilised for calibration can influence calibration stability. High levels of RH can condensate on the ^{226}Ra matrix which will result in a decrease in ^{222}Rn being generated.

d) Variations in sampling flow rate which could be due to ageing pumps or stack blowers.

e) Insufficient flow through the calibration source. Active calibration sources require higher flow rates compared to passive (100 – 130 cc/min).

f) Changes in the ambient radon levels between the start and end of the calibration sequence (see Figure 3-15).

The CPO inter-annual LLD_1[6] monthly calibration results are illustrated in Figure 3-13. A typical radon calibration curve can be characterised by the following regions; a build-up phase for the first 4 hours, steady state (plateau) from the 4th to 7th hour and purging for the remaining 5 hours (see Figure 3-14). The mean radon level during the steady state (equilibrium state) is about 15 000 counts/30 min (see Figure 3-13, left hand section).

During 2011 and 2012 elevated standard deviations are detected during some calibration events (see Figure 3-13). The reason for these outliers was due to airflow decreasing to below 75 L/min possibly due to technical difficulties. As discussed, in 2011 an upgraded version of the DFLTF radon detector was installed at CPO. The elevated unsteady standard deviation calibration radon levels (see Figure 3-13, top-right) can be attributed to the commissioning phase of 2011. Thereafter stable standard deviation calibration LLD_1 profiles were obtained. It was observed that the first three calibration events since the commissioning of the CPO radon detector produced CFs considerably higher than the norm (see Figure 3-14). The CPO CF standard deviation is 0.015 and a mean of 0.347.

[6] The LLD_1 is defined as the radon detector's lower limit of detection (LLD_1) associated with the statistical measurement uncertainty of 30% at "working voltage" conditions.

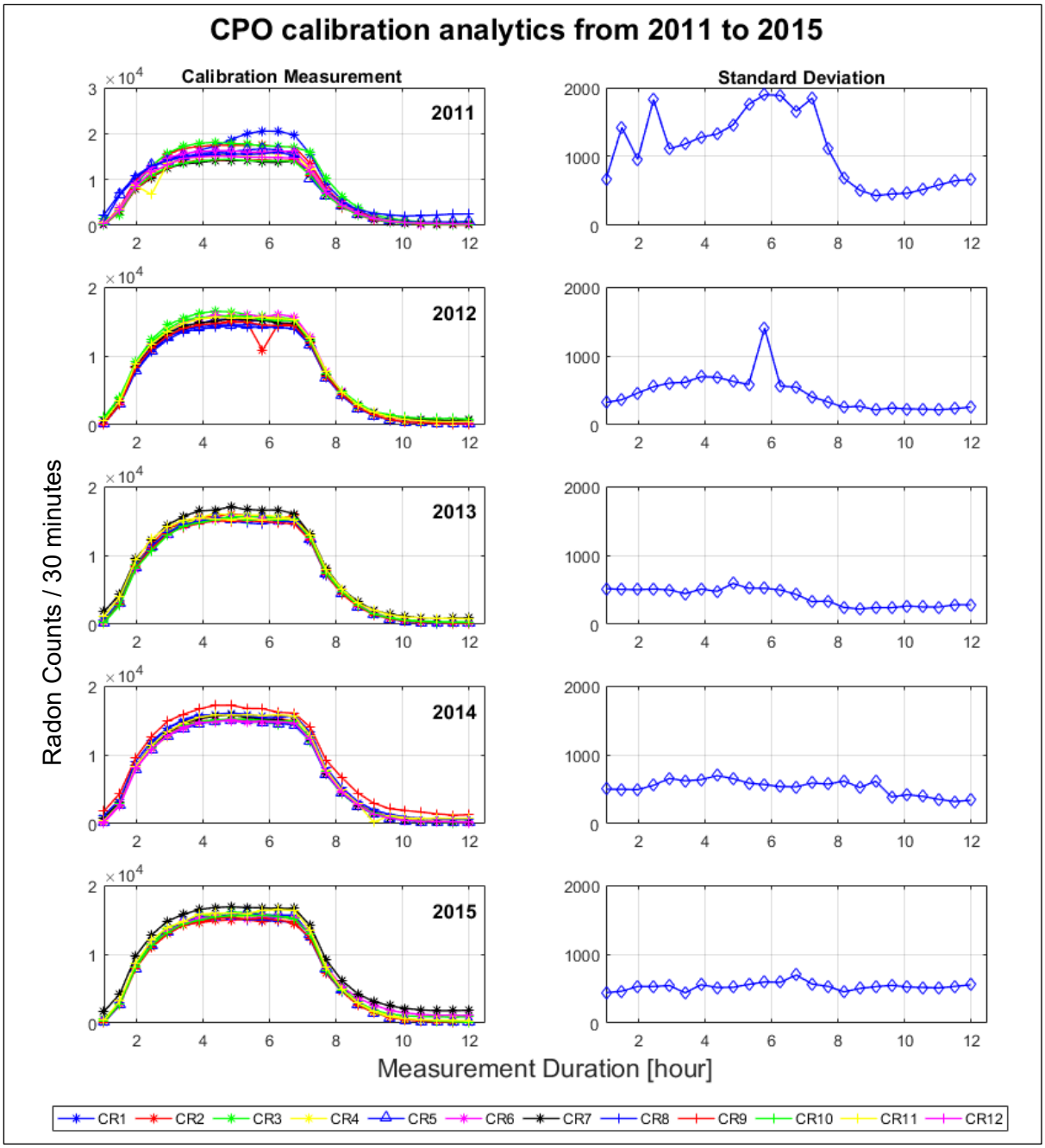

Figure 3-13: Inter-annual CPO radon detector calibration measurements analytics. Monthly calibration (left-hand section) is performed, indexed from January (CR1) to December (CR12). The corresponding standard deviation according for the twelve annual calibrations is plotted on the right-hand section.

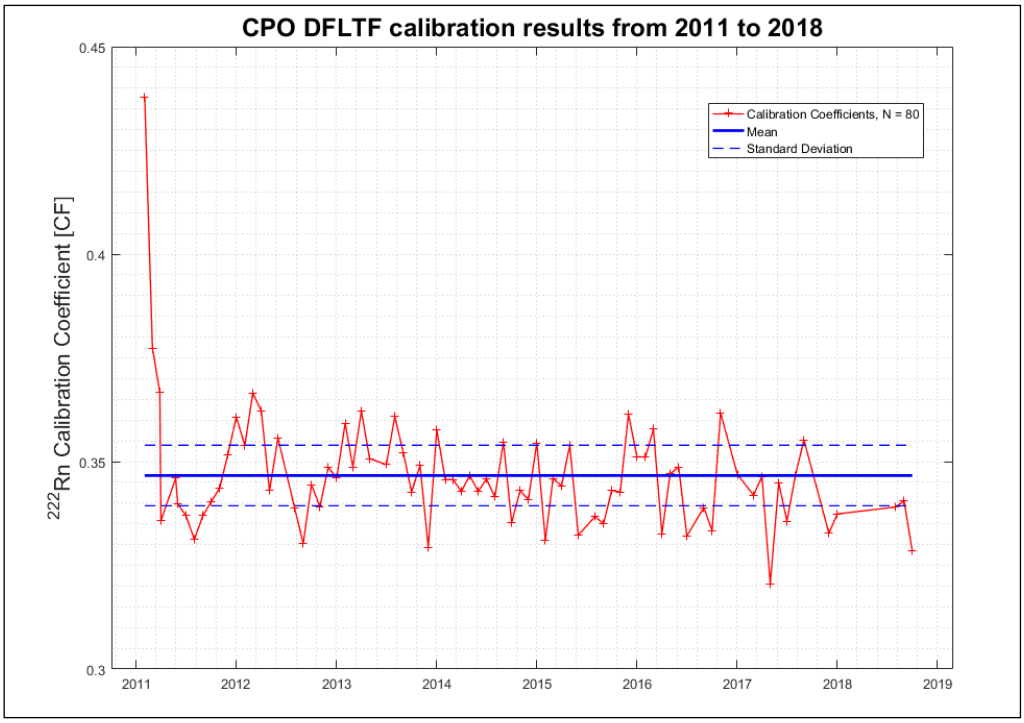

Figure 3-14: CPO inter-annual radon calibration coefficients from 2011 to 2018.

3.2.6 Instrumental Background Measurements

Instrumental background measurements are an important metrology element to monitor, especially since a dynamic background is applicable (see Table 3-2). Unattached radon progeny, specifically the long-lived nuclides such as ^{210}Pb ($t_{1/2}$ = 22.3 years) accumulate on the secondary filter (mesh screen) over time (see Figure 3-11). The accumulation of radon progeny will subsequently increase the instrumental background count rate gradually over time (see Table 3-2). Apart from the main radon progeny contribution to the background, the following factors could also potentially contribute to instrumental background:

a) NORM nuclides (^{40}K and ^{226}Ra) gamma radiation exposure contained in the surrounding building materials or materials from which the detector was constructed. The ZnS (Ag) coated scintillator screen is also susceptible to detection of background gamma radiation and it is not possible to distinguish between alpha or gamma radiation detection,
b) Alpha radiation associated with thoron progeny (contamination),
c) Cosmic rays,
d) PMT bias voltage.

Of these above-mentioned factors influencing the instruments background measurement. The NORM nuclides in the building material and the detector's material can be assumed to be constant. Background originating (radon) from the radium (^{226}Ra) within the detectors' materials is considered to be highly unlikely (low activity levels). Cosmic rays are expected to exhibit stochastic and diurnal temporal variations (Stozhkov et al., 2009). Background detections are interpreted as a false positive radon detection event; therefore, it is measured and corrected (see Equation 3-1).

An automated background (BG) measurement sequence is performed routinely every three months. The background measurement duration ranges from 24 to 100 h. At sites suspected of higher thoron contamination, the background measurement durations are extended up to 3 - 5 days. When background measurements are performed the blowers are switched off (see Figure 3-10). The aim is to measure the background generated from the trapped long-lived radon progeny (^{210}Pb) on the secondary filter (see Figure 3-8, a).

The mean CPO instrumental monthly background signal from 2011 to 2015 is presented in Figure 3-15. The background activity increased as expected from 2011 to 2015 (see Figure 3-15). The background signal results from Figure 3-15 were further processed to determine the total background (see Table 3-2). An increase in the total background activity (BG) from July 2011 to July 2015 of 59 mBq/m^3 is observed (see Table 3-2). An annual total[7] background increase between 10 and 15 mBq/m^3 can be expected for the CPO DFLTF detector. Although for the consecutive three calibration measurements starting from 17 October 2012 the total background remained almost unchanged (see Table 3-2). A decrease in the instrumental background occurred between 15 July 2015 and 15 October 2015 (see Table 3-2). The relatively long half-life radon progeny, ^{210}Pb ($t_{1/2}$ = 22.3 years) and ^{210}Po ($t_{1/2}$ = 133 days) accumulate on the secondary filter. Consequently, it is recommended to replace the secondary filter every 3 to 5 years depending on atmospheric radon levels. The stainless-steel mesh could also deteriorate (corrosion) due to exposure to conditions such as high relative humidity.

[7] The total background (activity concentration) is defined as the cumulative activity concentration determined making use of the entire background measurement duration.

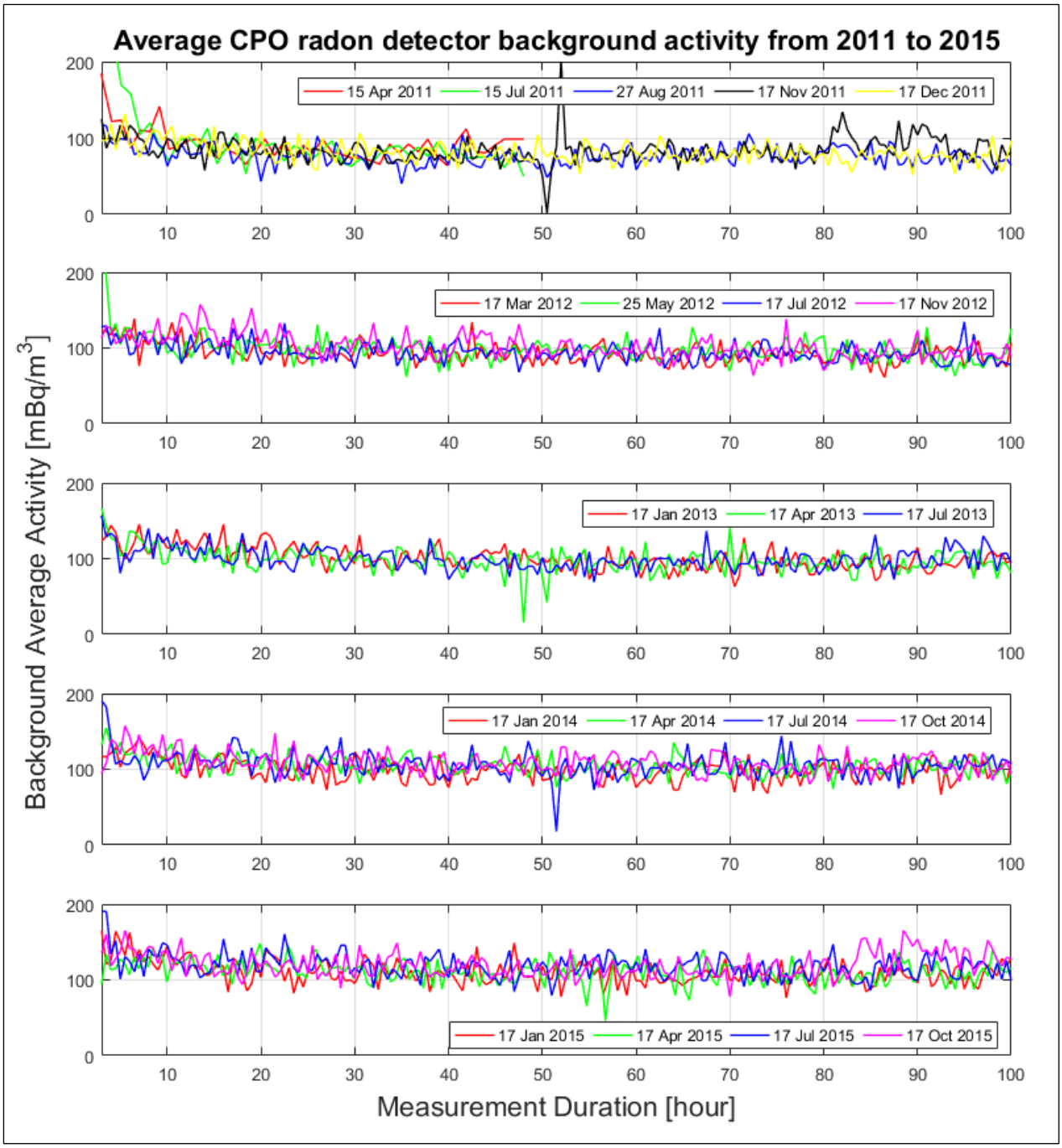

Figure 3-15: Inter-annual CPO mean instrumental background measurement analytics.

Date	Total Background Activity, [mBq/m^3]
2011-07-15	82 ± 12
2011-08-27	76 ± 10
2011-11-17	83 ± 12
2011-12-17	81 ± 11
2012-03-17	92 ± 14
2012-05-25	97 ± 13
2012-07-17	94 ± 13
2012-10-17	101 ± 15
2013-01-17	100 ± 15
2013-04-17	101 ± 15
2013-07-17	97 ± 13
2013-10-17	100 ± 15
2014-01-17	98 ± 13
2014-04-17	105 ± 15
2014-07-17	105 ± 15
2014-10-17	108 ± 15
2015-01-15	113 ± 16
2015-04-15	113 ± 16
2015-07-15	141 ± 18
2015-10-15	121 ± 16

Table 3-2: CPO DFLTF radon detector total background measurement results from 2011 to 2015.

The instrumental background count rate can be accurately represented by a linear increase over time (see Figure 3-16). A linear trendline fitting of the CPO background measurements (N = 30) is performed and a $R^2 = 0.89$ was computed which can be considered a good fit (see Figure 3-16). An instrumental background increase will consequently result in a decrease in detection sensitivity. Assuming the detector is operating as expected the CPO's detector background count rate will increase on average at about 10 counts per hour (CPH) per annum.

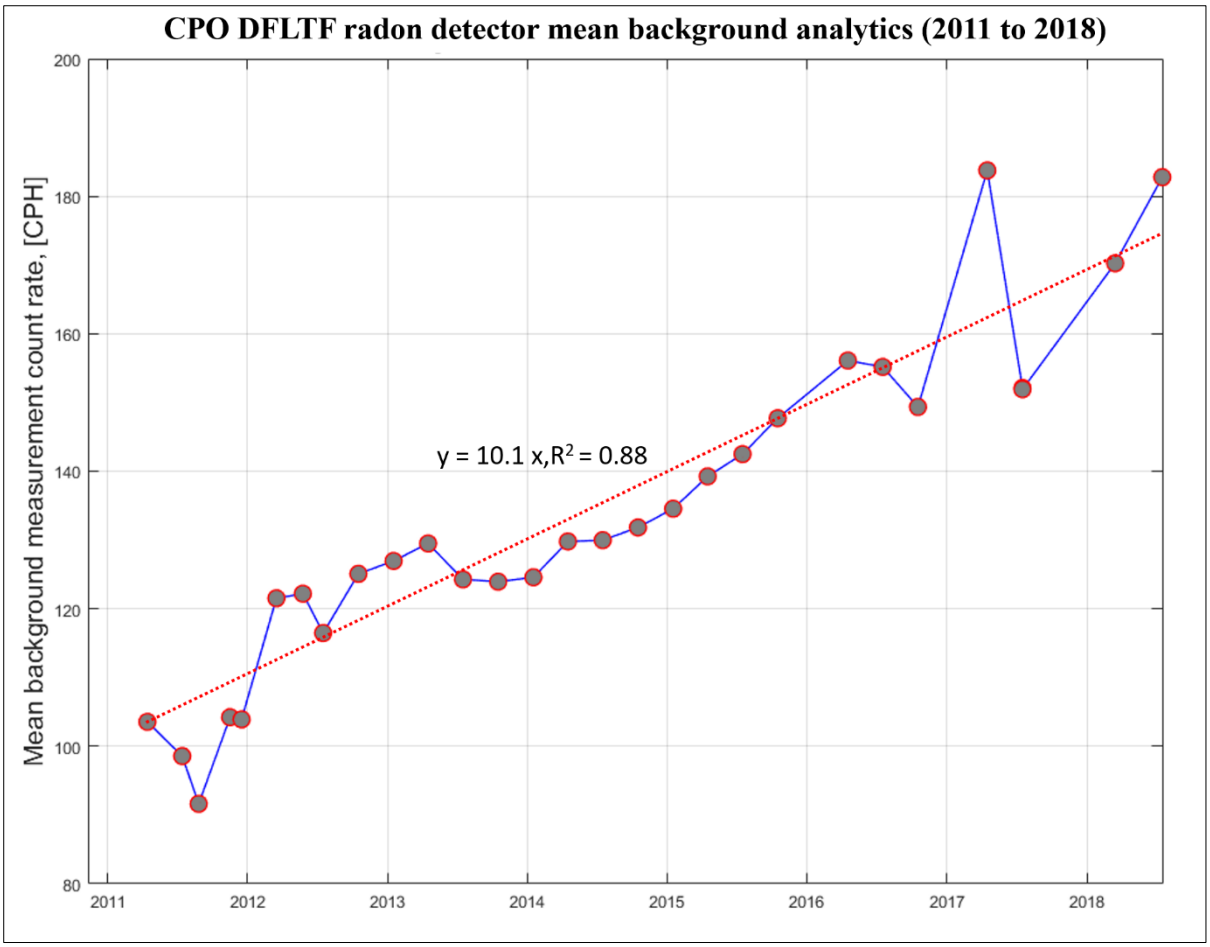

Figure 3-16: Mean CPO background measurement count rate from 2011 to 2018 at CPO (N = 30) and the linear trendline fit that is represented by the dashed red-line.

3.2.7 Data Acquisition

Data acquisition is performed with a CR800 series data logger manufactured by Campbell Scientific and a Windows-based PC (see Figure 3-6). The detector control software developed by ANSTO, "Radon Detector Monitor" (RDM), commands the downloads from the CR800 logger on a 30-minute interval. The data from the logger is accessed from the control computer making use of USB or RS232 signal cable. The following channels are stored on the data logger at a 10-second sampling rate:

a) Time of day and date

b) External flow loop rate (L/min), ExFlow

c) External flow loop from the gas meter, GM

d) Internal flow loop air pipe velocity (m/s), InFlow

e) PMT voltage (V), HV

f) Calibrated radon activity concentration (mBq/m^3), Spare

g) Counts per half hour at the lower threshold setting, LLD_2

h) Counter per half hour at the higher threshold setting, ULD

i) Delay tank average pressure (mV/Pa), TankP

j) Data logger's temperature (°C), Temp

k) Detector's Data Logger (°C), AirT

l) Ambient RH inside detector (%), RelHum

m) Absolute pressure inside the detector (hPA), Pres

n) DC Power supply voltage (V), Batt

The external flow loop rate, spare and, counts at the lower threshold setting are used to calculate the radon-in-air activity concentration. Air temperature and pressure measurements are utilised during offline data analysis if STP related corrections are required. The remaining parameters are measured and recorded for instrumental diagnostics purposes.

3.2.8 Data Processing

The first data set, also referred to as the raw data set (CSV file) contains the unprocessed data described in Section 3.2.7 (see Figure 3-17). The raw data set is analysed (QC) to identify potential anomalies, spikes or potential technical instrumental difficulties. Data anomalies are flagged for further investigation. The raw data set is binned according to active measurements, instrumental background measurement (BG) or calibration process (CF). The DFLTF detector has a 30 min temporal measurement resolution. However, the radon signal is processed to an hourly temporal resolution by averaging the two half-hour radon measurements. The response time of the 700 L DFLTF radon detector occurs with 40% of the signal arriving more than an hour after a radon pulse is detected (Griffiths et al., 2016). The detector's time response can be corrected by making use of a Markov chain Monte Carlo sampler to achieve a deconvolved radon time-series. However, for this study, such corrections are not applicable. Nonetheless, for studies in which a radon time-series is measured in conjunction with fast fluctuating trace gases such as CO_2, time response correction becomes important (Brunke et al., 2004; Crawford et al., 2016, 2017).

The next phase of the data processing is computing the hourly "representative" atmospheric radon activity concentration (see Figure 3-17, set 2). The hourly representative atmospheric radon activity concentration, Rn (Bq/m^3) is calculated by making use of the following equation:

$$\mathrm{Rn} = \left(\frac{\mathrm{LLD_2} - \mathrm{BG}}{3600 \times \mathrm{CF}}\right) \qquad \text{(Equation 3-1)}$$

In Equation 3-1 LLD_2 is defined as the counts from the lower-level discriminator which adjustable (voltage) at the HV/discriminator unit (see Figure 3-6); the background coefficient as BG and the calibration coefficient as CF. The LLD_2 should not be confused with the defined LLD_1 (see Section 5.2.5). The LLD_1 for the DFLTF radon detectors at CPO and CGO respectively are; 25 ± 8 mBq/m^3 and 10 ± 3 mBq/m^3 (Zahorowski et al., 2004). The percentage of detected events below the specified LLD_1 for the CPO and CGO radon time-series are 0.8% and 1.1%, respectively. The third data processing phase (see Figure 3-17, set 3) involves combining auxiliary data and air-masses back-trajectory data (HYSPLIT modelling) to the radon time-series. The auxiliary data consists predominantly of meteorological data such as wind speed (WS), ambient air temperature (T) and wind direction (WD).

Secondary filtering (QC) is performed (CPO) on data fields with wind speeds below 5 m.s^{-1}. This reduces the likelihood further of adding regional radon and thoron emanations (contamination) to the atmospheric radon signal. This is most likely to occur under calm and wind still conditions. The WS filtering results in the removal of about 15% of the CPO radon time-series. However, based on the fact that the radon signal is 19 years long a vast amount of quality data will still be at hand for analysis. Applying the low WS filter on the radon signals is referred to as data set 3 (see Figure 3-17).

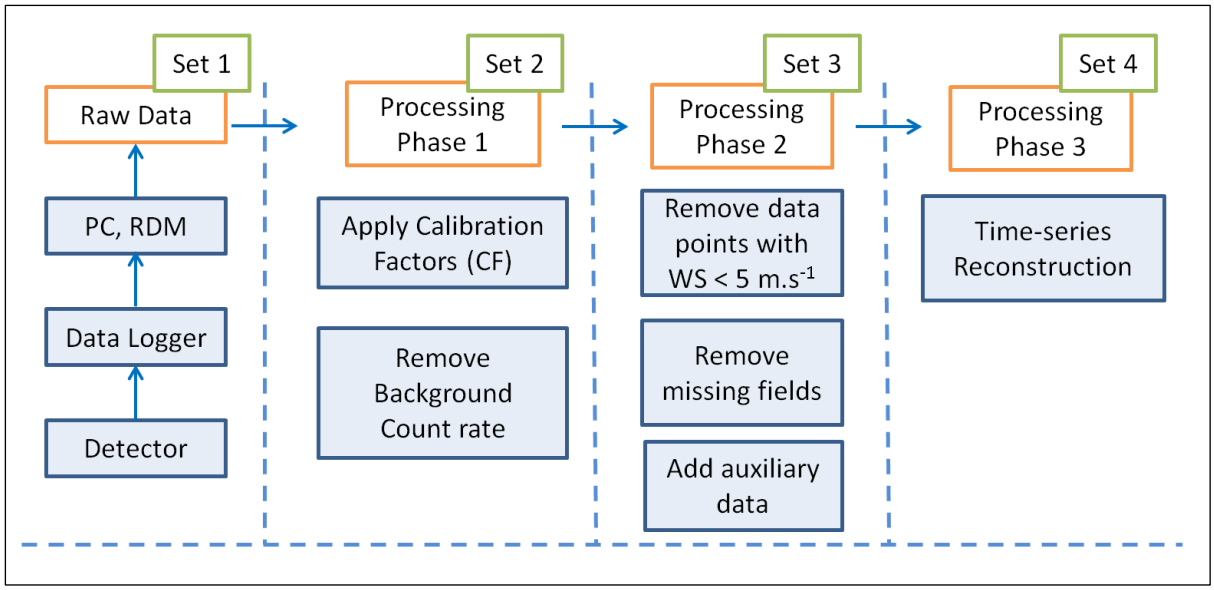

Figure 3-17: Schematic of offline DFLTF radon detectors data processing.

3.2.9 Radon Time-series Reconstruction

Under certain controlled and uncontrolled conditions radon measurement data-loss will occur. It is ideal to aim for achieving a 100% measurement efficiency (N = 8760 data points per annum). Even with the most advanced version of the DFLTF detector, it will be technically challenging to achieve such a goal, especially when making use of only one detector. The following five factors affect the radon measurement capturing efficiency:

a) Instrumental calibrations are performed on a monthly basis (see Section 3.2.5). Calibration is one of those critical processes to perform sustainable quality radon measurements. Annually calibration will consume about 144 hours of measurement time which accounts for a data loss of about 1.6%. Calibration is a planned and controlled instrumental process.

b) Background measurements are performed for a duration of about 24 hours, routinely every three months (see Section 3.2.6). It will require 96 hours which translates to about 1% loss of the total annual hourly radon measurement time. Background measurements are planned and controlled metrological process.

c) The ANSTO designed DFLTF is currently a world-leading detector based on continuous ultra-low atmospheric radon measurements. Nevertheless, the scenario will occur in which the radon sampled are below the detector's LLD_1 and consequently

cannot be detected. These events are predominantly associated with rare deep-baseline air-masses. This radon measurement loss factor cannot be controlled nor planned for apart from R&D to further improve detection sensitivity.

d) The DFLTF detector is remarkably reliable and stable. However, technical breakdowns do occur. Breakdowns become a possibility especially for detectors in service for 10 years or more which has not received the required maintenance or is exposed to extreme environments. The system is monitored remotely. Consequently, operational stability indicators are analysed frequently. Preventative routine maintenance should be performed to reduce critical breakdowns. Not all malfunctions can be prevented thus to a degree it can be characterised as uncontrolled if the necessary maintenance is provided.

e) The last factor which can result in the capturing loss is the scenario in which radon is sampled, however, the decay occurs outside the detection range of the detector head (see Figure 3-10).

The radon signals from 2018 onwards are not included in this thesis. When analysis commenced the 2017 data set was the latest set available. The respective CGO and CPO total annual measurements efficiency is 94% and 84% (see Figure 3-18). Data loss of up to 2.6% due to calibration and background measurements can occur. The CGO annual capture efficiency during some years is 100% (see Figure 3-18). This can technically be achieved since CGO has two detectors operating simultaneously (see Section 3.2.4). By having two or more operational detectors, missing data can be minimised. For instance, when the one detector is performing routine maintenance tasks (calibration) and the other can proceed with standard measurements. The present CPO detector was installed in 2011 which resulted in a capture efficiency increase (see Figure 3-18). The lowest annual measurement capture efficiency for CGO and CPO is 68% (2008) and 71% (2003), respectively.

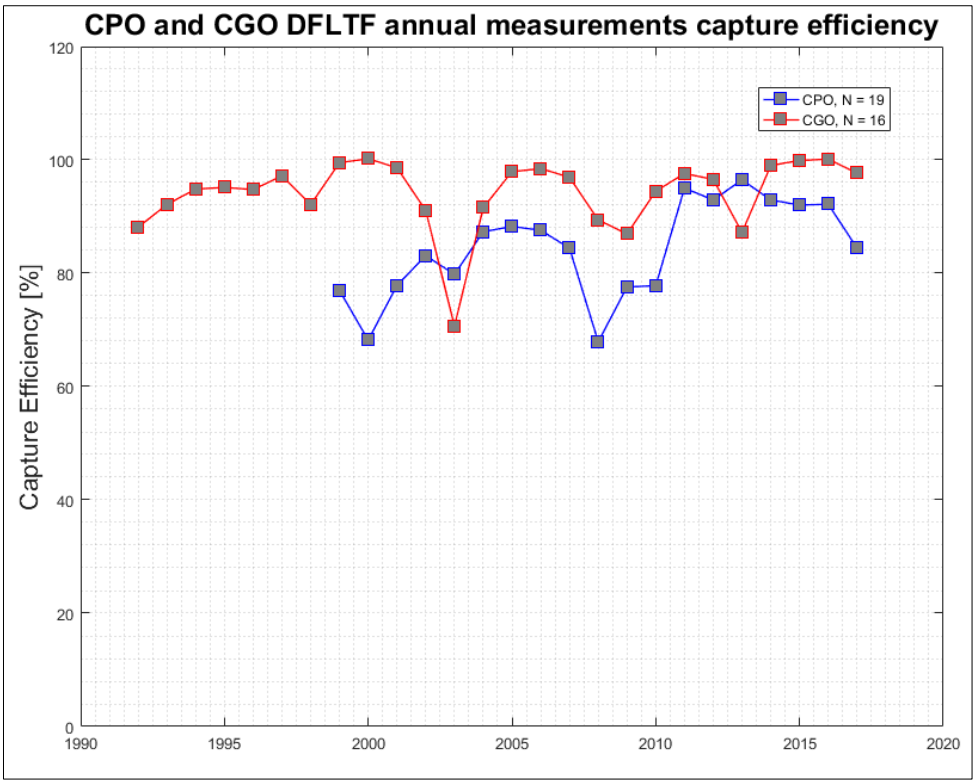

Figure 3-18: Capture efficiency of the CPO and CGO annual radon measurements.

Data loss creates the prerequisite for utilizing modern methods such as machine learning (neural networks) to restore missing data points in an incomplete data set. A machine learning approach for restoring missing data in radon signals has proven to be highly efficient (Janik et al., 2018). Due to data-rich radon signals measured over many years used in this thesis, CGO (N_{CGO} = 215 882) and CPO (N_{CPO} = 107 805), the data losses sustained will not have an impact to perform the required analysis.

3.3. RAD7 Radon Detector

3.3.1 Introduction

The RAD7, electronic continuous radon and thoron detector manufactured by DURRIDGE (see Figure 3-19) was utilised to perform supplementary measurements. These measurements included radon and thoron emanation from soil and rock samples collected at CPO (see Figure 3-20). The results of the radon and thoron emanation from soil and rock samples collected at CPO will be presented in Section 4.3.

3.3.2 RAD7 Radon Detector Metrology

Several commercial electronic radon detectors brands are available on the market. Most of these electronic radon detectors are based on α-spectroscopy detection technology. The RAD7 radon detector has a 0.7 L internal chamber coated with an electrical conductor fitted with a solid-state planar silicon detector strip. Ion-implantation technology is applied by accelerating the unattached radon progeny (^{218}Po and ^{214}Po) or thoron progeny (^{216}Po and ^{212}Po) onto the solid-state planar silicon detector via an induced electromagnetic field. A carrier medium of ambient air with a reduced relative humidity (RH) of below 10% is used to pump the radon into the detection chamber while external decay progeny is stopped by a filter before entering the detector.

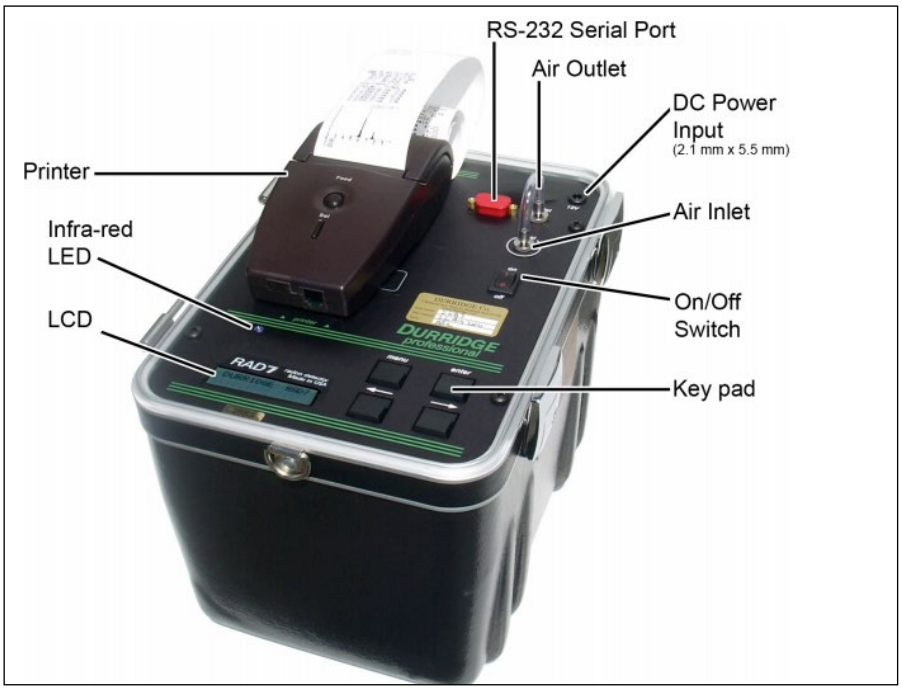

Figure 3-19: An electronic RAD7 radon and thoron detector unit. Credit DURRIDGE INC.

The RAD7 detector modes utilised in this study:

a) **Sniff mode**: This mode is intended to achieve a swift response time ideal for real-time fast-changing radon-in-air activity concentration measurements; however, it in general compromises on statistical accuracy by measuring only the ^{218}Po decays (E_α = 6.00 MeV).

b) **Normal mode:** The ^{218}Po (E_α = 6.00 MeV) and ^{214}Po (E_α = 7.69 MeV) radon progeny are counted to determine the radon activity concentration with superior statistical accuracy. This mode is applicable for measurement times larger than three hours since establishing the equilibrium of longer-lived radon progeny is essential.

c) **Auto mode:** Both the Sniff and Normal mode are utilised when using the Auto mode. The Auto mode measurement is started with the Sniff mode and switches to the Normal mode after three hours of continuous measurements.

A customised Auto Mode is used for measurements in this thesis. Purging is an important operational element when making use of the RAD7 detector. Two different purging approaches can be followed: a closed-loop method or an open-loop method. With an open-loop purging configuration, the air outlet or exhaust port flows into the atmosphere and recirculation is not applicable. When the air outlet or exhaust port is connected to the system's inlet port, it is referred to as closed-loop purging setup.

In the event of high radon activity concentration (> 100 Bq/m^3) measurements, radon and associated progeny will remain active within the detection chamber either until it decays or is removed (purged). To perform quality radon measurements, one has to remove potential ^{222}Rn ($t_{1/2}$ = 3.82 days, E_α = 5.590 MeV), ^{218}Po ($t_{1/2}$ = 3.05 min, E_α = 6.00 MeV), and ^{214}Po ($t_{1/2}$ = 164 μs, E_α = 7.69 MeV) isotopes from previous measurements within the detection system. By making use of open-loop purging, the instrumental α-signature background will be reduced as a function of time. In reality, both nuclear decay and open-loop purging are applied after a radon measurement is performed. An open-loop purge is performed for a minimum of ten minutes before and after each measurement. Before every measurement, the efficiency of the open-loop purge is verified by real-time analysis of the ^{218}Po and ^{214}Po count rates. The intrinsic instrumental background of the long-lived radon daughter isotopes (^{210}Pb, $t_{1/2}$ = 22.3 years) should also be taken into consideration. The long-lived isotope ^{210}Pb undergoes β-decay to ^{210}Bi ($t_{1/2}$ = 5 days) which undergoes β-decay to ^{210}Po ($t_{1/2}$ = 138 days, E_α = 5.30 MeV). However, the β- or γ-decaying radon progeny will not affect the radon measurements when making use of the RAD7 detector since the energies of the alpha particles are used to separate the decays form different progeny.

The other functional aspect of purging is to reduce the RAD7's internal RH. Since the positively charged radon progeny need to move to the negatively charged detector, the water content in the air will affect measurement performance by neutralising the ions. Therefore,

relative humidity (RH) inside the detection chamber should be maintained below 10% during measurements. RH corrections can be applied by making use of DURRIDGE Capture software. Nonetheless, it was not applied since the operational internal RH was maintained below 10%. The closed-loop purging method is highly efficient in reducing RH; however not for removing radon and associated progeny.

A microprocessor onboard the RAD7 detector performs the data acquisition. Real-time data analysis of measurement results can be viewed either on the RAD7 display unit or on a control PC by operating an installed version of the Capture software. The signals generated from the detection of α-decays are binned into 200 channels grouped according to the α-energies. The α-energy (E_α) range for the system is 0.00 to 10.00 MeV (E_α = 0.05 MeV per channel). The relevant α-energy range for detection of radon and also thoron is from 6.00 to 9.00 MeV.

3.3.3 Radon and Thoron Soil and Rock Emanation Measurements

At CPO an experimental setup (RAD7) is utilised to estimate the radon and thoron emanation levels from soil and rocks. The experimental setup is the starting point of further work. The nearby local ambient radon and thoron within a radius of 840 m (see Figure 4-7, b) is of interest. Under certain conditions, it becomes challenging to differentiate between atmospheric radon and radon produced within the nearby region. These conditions include when strong surface winds are not present, that is under calm conditions.

An enclosed chamber will not be as ideal an experimental environment as for instance the natural environment. The internal volume of the chamber ranges between 6 to 9 L, depending on the volume of the samples The RAD7 detection system requires to be operated under low RH conditions (< 10%). As a result, RH reducing instruments (DRYSTIK) will constantly reduce the enclosed ambient RH. The variability in soil and atmospheric RH are the parameters that influence the radon and thoron soil flux rates (Grossi et al., 2011; Tchorz-Trzeciakiewicz et al., 2017). More advanced in-situ environmental radon and thoron emanation monitoring devices do exist which unfortunately were not available during the time of this study at CPO. Nonetheless, the aim is to obtain a simple indicator of radon and thoron levels which are produced within the proximity of the CPO mast. Three hours of measurement (cycle) is selected and repeated 32 times (recycle). The DRYSTIK unit furthermore acts as a secondary pump. It

was set to a duty cycle of 100% to reduce internal RH (< 10%) to circulate the carrier medium (air). The radon and thoron emanation measurements results will be discussed in Section 4.3.

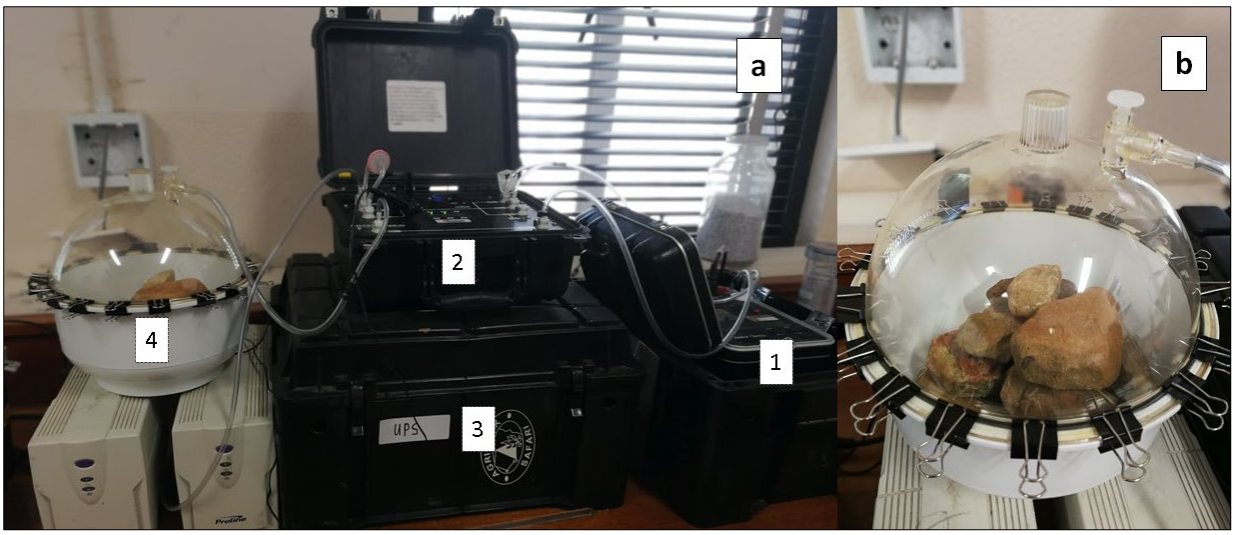

Figure 3-20: (a) Radon and thoron emanation measurement system making use of a RAD7 detector (1); DRYSTIK ADS-3R electronic dehumidifier (2), DRYSTIK UPS (3) and emanation chamber (4). (b) Emanation chamber containing CPO rock samples with the air inlet visible at the top.

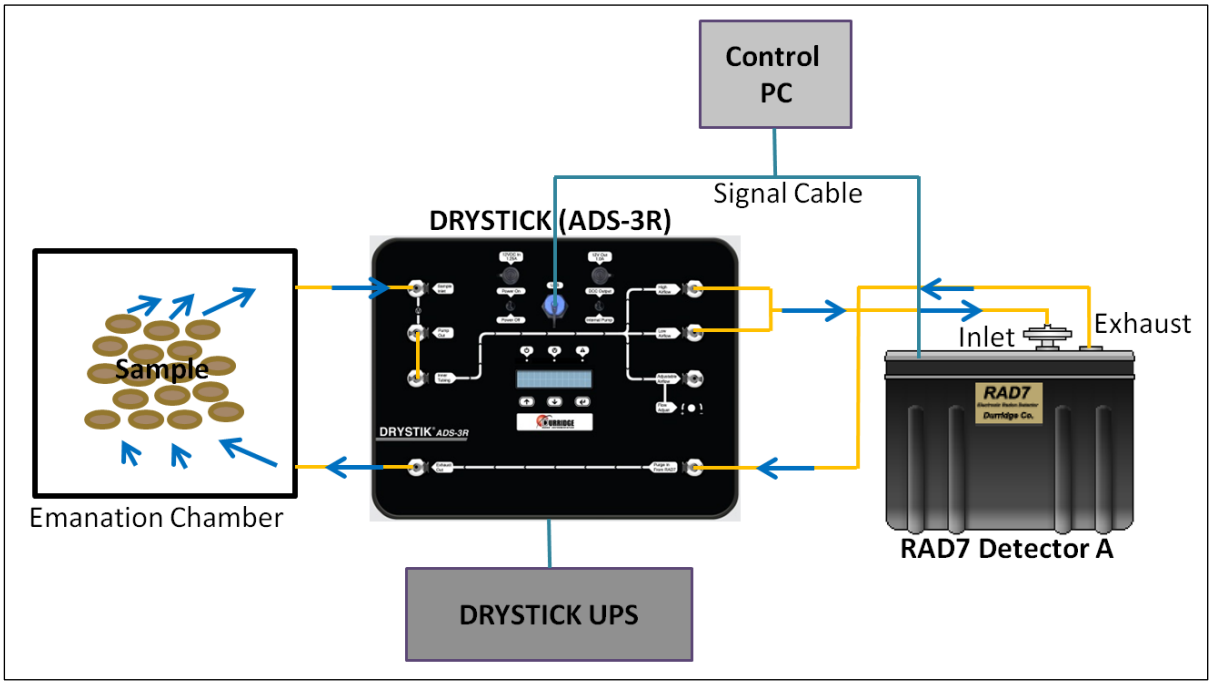

Figure 3-21: Schematic of radon and thoron emanation system to illustrate the experimental setup and air flow sampling structure.

3.4. E-PERM Radon Detector

3.4.1 Introduction

The E-PERM detector system manufactured by Rad Elec is a passive indirect radon measurement method utilised to perform supplementary measurements at the CPO radon lab. Indoor ambient radon can accumulate from sources such as building materials, soil, radium calibration sources, and from the atmosphere. The CPO radon lab is poorly ventilated which makes it prone to radon build-up. In the event that the DFLTF radon detector (see Figure 3-5) develops a leak the ambient radon could lead to contamination, especially if the levels are elevated.

3.4.2 E-PERM Metrology

The E-PERM detector is a passive radon measurement technique which is most favourable to determine the mean radon in-air activity concentrations at multiple locations. The E-PERM detection system cannot be used when any type of temporal resolution is required. These radon detectors are economical, robust and can operate in high RH and dust environments without requiring a power supply. The S-chamber, 210 mL combined with the SST electret variant are utilised (see Figure 3-22, b). The passive E-PERM radon detector functions as follows. Ambient air flows into the chamber by diffusion. The chamber's inlet contains a filter to prevent radon progeny from entering. Within the detection chamber, radon decays and the ions generated by the charged decay progeny are accelerated onto a positively charged electret (see Figure 3-22, a). The unattached radon progeny is accelerated through the Lorentz Force of the electrostatic field created by the conductive plastic Faraday cage acting progeny ions (see Figure 3-22, a & b). The electret mounted at the S-chamber's bottom is an electrostatically charged Teflon® disk. By measuring the decrease of the electret's voltage (see Figure 3-22, c) from the start (I) of the measurement and end (F) a mean radon-in-air activity concentration (RnC) can be determined (see Equation 3-3).

To promote measurement quality and consistency, three E-PERM detectors are placed at a single measurement location (see Figure 3-23). Studies indicate good agreement with the measurement results (within measurement uncertainty) for the different detector units within fixed locations (Botha et al., 2017, 2016). The radon-in-air activity concentration is calculated (see Equation 3-2) by making use of the parameters (A, B and G) which were retrieved from

the E-PERM System User's Manual (Version 2.231b). The calibration factor (CF) can be expressed by:

$$CF = A + B\left(\frac{I+F}{2}\right) \qquad \text{(Equation 3-2)}$$

where A = 1.69776 and B = 0.0005742 are given calibration coefficients applicable to the SST electret and the S-chamber configuration. The initial electret voltage was labelled as I and the final as F. The calibration factor (CF) is utilised to calculate the mean radon-in-air activity concentration (RnC, pCi/L) by making use of:

$$RnC = \frac{(I-F)-(0.066667\ X\ D)}{(CF\ x\ D)} - (BG\ \times\ G)\ \times Elev\ Cf \qquad \text{(Equation 3-3)}$$

where BG is the measured γ-background (μR/hr), D the measurement duration (days) and G the γ conversion constant given as 0.087. Since the CPO's altitude above sea level is below the prescribed 1219 m (4000 ft), the elevation correction factor (Elev CF) is taken to be 1, as recommended in the E-PERM System User's Manual (Version 2.231b).

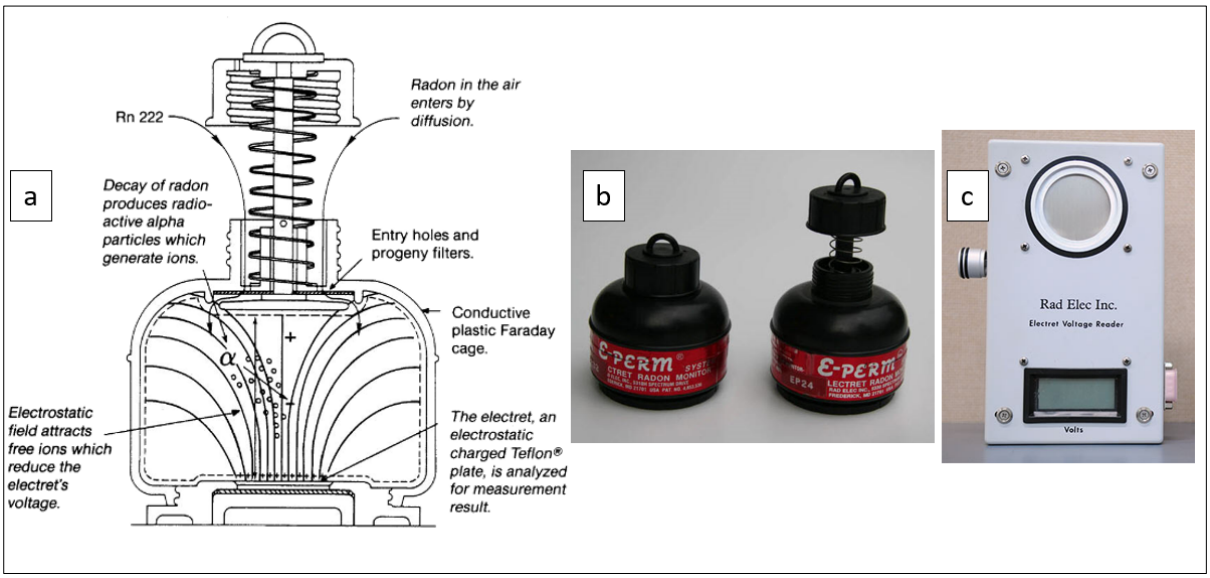

Figure 3-22: (a) Side view schematic of the E-PERM S-chamber setup to illustrate the internal metrology. Credit Rad Elec Inc. (b) An S-chamber radon detector setup to the right which is activated (opened) to perform measurements and an enclosed inactive system to the left. (c) Electret voltage reader.

Three E-PERM measurement locations (see Appendix Table 1) were chosen inside the CPO's radon lab (see Figure 3-23). These measurement locations are strategically chosen to near the DFLTF detector. Location one was on the floor next to the electronics Hub. Location two and

three were chosen on-top of the DFLTF detector. The indoor radon measurement was conducted from the 13-12-2018 to the 02-01-2019 making use of the E-PERM detectors. The measurement was performed during the 2019 December holiday period. The lab's doors were closed most of the time which result in ideal conditions to measure a build-up of indoor radon. The CPO's radon lab ambient radon-in-air measurement results will be discussed in Section 4.3.

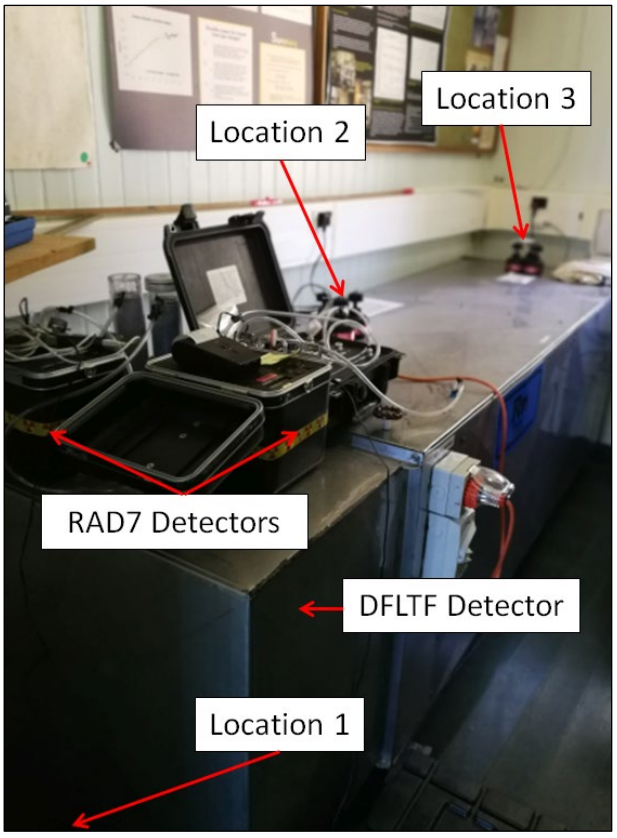

Figure 3-23: The three E-PERM measurement locations within the CPO radon lab.

3.4.3 HYSPLIT: Atmospheric Back-Trajectory Modelling

The Hybrid Single-Particle Lagrangian Integrated Trajectory Model known as HYSPLIT developed in 1982 by the National Marine and Atmospheric Administration (NOAA) and Australia's Bureau of Metrology is one of the most used models for computing air parcel trajectories, atmospheric volcanic ash tracking, tracking pollutants from wildfires, air quality, complex atmospheric transport systems, and radiological or chemical dispersion/deposition (Ngan & Stein, 2017; Ravindra et al., 2019; Rolph et al., 2014, 2017; Stein et al., 2015).

The HYSPLIT modelling inputs are a combination of user's input parameters and meteorological datasets (GFS, HRRR, and NAM). HYSPLIT 4 uses a hybrid algorithm which is a combination of Lagrangian and Eulerian approaches.

The Lagrangian method (ideal for a single point source) uses a moving frame of reference for the diffusion and advection as the trajectories move from their initial location. For the Eulerian method (ideal for multiple sources) a fixed three-dimensional spatial grid is used as a frame of reference to compute the particulate air concentrations.

In this thesis, HYSPLIT will be used to compute (CGO and CPO) high spatial resolution air-mass back-trajectories on an hourly temporal resolution. The back-trajectory analysis is defined as the process of tracking an air parcel (mass) back in time. The back-trajectory will be utilised to track a selected air-mass in three-dimensional space (latitude, longitude and altitude above sea level (a.s.l.)). By performing the high-resolution trajectory analysis, the CPO and CGO air-masses can be analytically characterised according to marine, continental, baseline, and mixed (a combination of marine and continental) and its origin (flightpath).

The atmospheric back-trajectories are computed from 1999 to 2017 to a final a.s.l. of 300 m (e.g., Figure 5-36). An assumption is introduced that the variation between the sampling altitude (see Table 4-1) and final air-mass back-trajectory altitude (300 m) does not unduly affect the conclusions of the analysis. The back-trajectories are computed for each hour of the day 100 hours back in time (T). It was noted that a number of air-masses trajectories (latitude and longitude data) illustrated abnormal behaviour after about T = 65 h back in time. Consequently, the analysis is performed only up to T = 60 h back in time when making use of the spatial coordinates. This should be taken into consideration when reading Section 5.4. The abnormal behaviour is not identified for the air-masses altitude parameter. Thus, in some cases altitude analysis is performed up to T = 100 h back in time. The computation is performed according to the observatories' Coordinated Universal Time (UTC). Local time zone corrections for CGO (UTC+10) and CPO (UTC+2) are applied where applicable.

Trajectory density (cluster) analysis is an analysis method used to track and analyse air-mass back-trajectories within specified sets of two-dimensional spatial (longitude and latitude) finite horizontal grid cells (cluster). A cluster is defined as a spatial grid (see Figure 3-24) with a specified spatial resolution (D_i). The aim is to set the spatial resolution for a cluster as high as technically achievable ($D_{max} = 0.01°$). A high spatial resolution cluster is especially of value at the coastline when trying to distinguish between the contact strip of the land and ocean

(coastline). The disadvantage of a high temporal resolution is that more computational time will be required. The computation and analysis time for a large trajectory dataset of several years becomes extensive, even when making use of a high-end GPU and CPU desktop. Taking that into account the spatial resolution is set at $D_i = 0.1°$ (11.1 km). The cluster analysis is performed only at Southern Hemisphere observatories (CGO and CPO). Computational optimization is applied by doing computations only in regions in which the trajectories will occur (see Figure 5-33). Now that the cluster is defined computations are made to count the number of times an air-mass trajectory moves through a specific cluster. This method will be referred to as cluster analysis in this thesis. In the future, the two-dimensional cluster algorithm can be improved by performing three-dimensional cluster analysis (adding the altitude parameter).

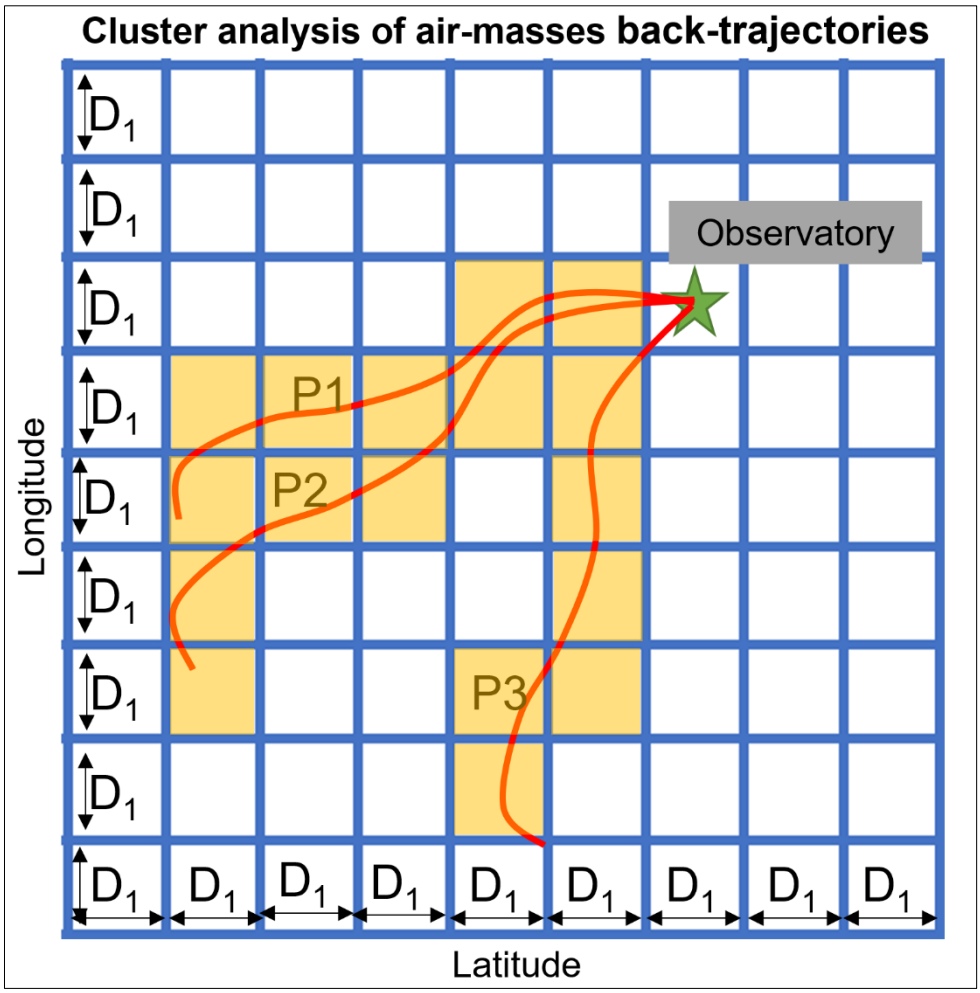

Figure 3-24: Illustration of air-masses back-trajectory density (cluster) analysis. The size of the cluster is defined as D_1 (length of a single cluster, 11.1 km) and the various air-masses trajectories with P1 to P3.

Atmospheric radon measurements are characterised into two distinct air-masses groups, continental (C, higher radon levels) or marine (M, lower radon levels). In this thesis, this will be referred to as CM identification analysis, in other words, continental (C) or marine (M) identification. Making use of the current CM identification algorithm the only large body of water applicable for analysis will be the ocean. Refinements will be introduced in the future to account for identification of rivers, dams and lakes.

The CM identification algorithm is developed in MATLAB and a range of internal functions ("coast = load ('coast.mat')") are utilised. The MATLAB coast function is a matrix containing the coordinates of the global coastline. The back-trajectory (coordinates) are characterised as either marine (output = 1) or continental (output = 0) by making use of the above-mentioned geological matrix. The advantages of this approach are that it can be computed fast with a relatively high spatial resolution of $D_l = 0.1°$ (11.1 km). The most prominent limitation, as discussed, is obtaining a higher spatial resolution (smaller clusters) that will result in more accurate identification. This spatial resolution becomes especially important nearby the coastlines when the difference between land or sea is within a short distance. Future improvements will include obtaining a more powerful computation system. Nonetheless, the algorithm, even taking the limitations into account, has proven to be a good analysis tool.

CHAPTER 4 Measurement Locations

4.1 Introduction

In Chapter 4, a description and discussion will be provided on the observatories which are used in this thesis. As discussed, the primary focus of this study is predominantly on the Southern Hemisphere (see Chapter 1). The main reasons for selecting CPO and CGO are:

a) Analogous geographical position (S 34° - 40°) with continental semi-arid regions to the North and ocean to the South West (see Figure 4-1). The observatories are situated at low-altitude coastal locations (see Table 4-1).

b) A downward limb of the Hadley cell which is driven by convection in the tropics that brings surface air down from the northern regions (see Figure 4-2).

c) The westerly flow of air-masses with embedded synoptic frontal systems (see Figure 4-2).

d) Continuous radon, trace gas, and metrological measurements have been conducted for a minimum of 19 years at each of these individual sites.

e) Subjected to the exposure of marine (deep baseline) and continental (pollution prone) air-masses.

f) Similar climatologically conditions.

g) Both measurement stations are subjected to air-masses originating from the Indian and Southern Ocean (See Figure 4-1).

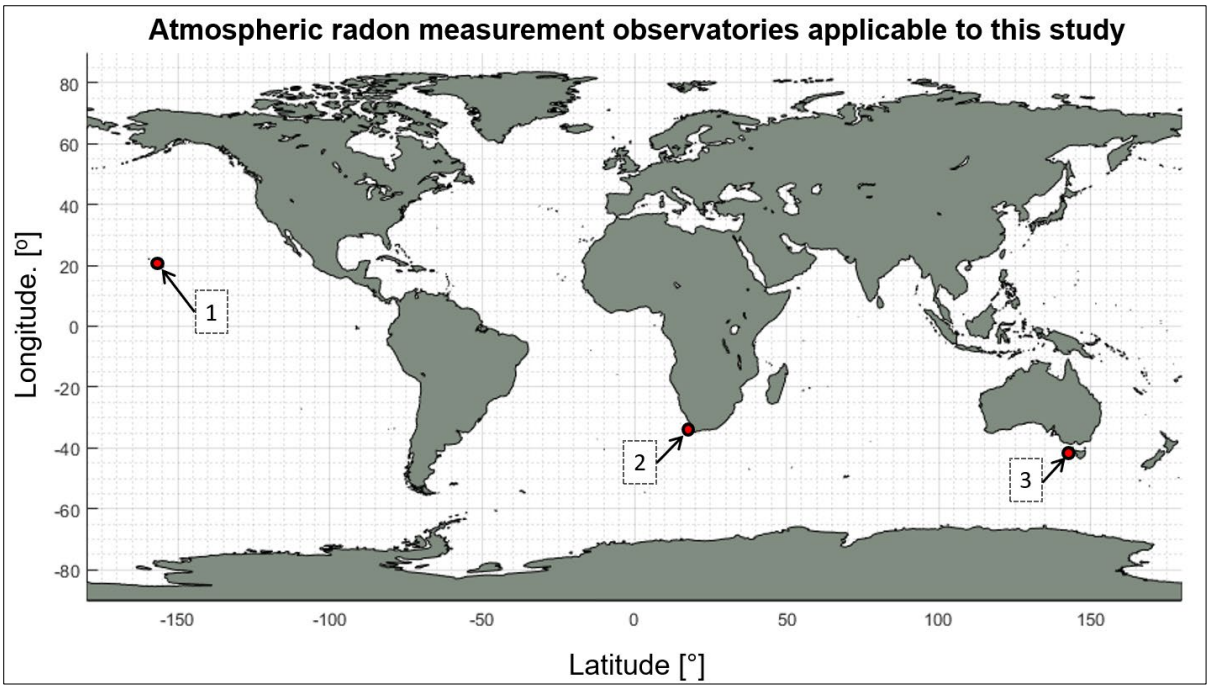

Figure 4-1: Map of atmospheric radon measurement observatories which are utilised in this study; (1) Mauna Loa, Hawaii, United States; (2) Cape Point, Western Cape Province, South Africa and (3) Cape Grim, Tasmania, Australia.

Radon measurement results from a third additional location are included in this study, Mauna Loa Observatory (see Section 4.4) situated in Hawaii (see Figure 4-1). The purpose of adding the Mauna Loa atmospheric radon time-series is to extend the analysis by comparing the Southern Hemisphere results to that of a Northern Hemisphere site.

Location	Site Altitude Above Sea Level, (a.s.l.), [m]	Sampling Altitude Above Ground Level, (a.g.l.), [m]	Sampling Altitude Above Sea Level, (a.s.l.), [m]
CGO	97	70	167
CPO	230	30	260
MLO	3397	38	3435

Table 4-1: CGO, CPO and MLO altitude above sea level and sampling altitude.

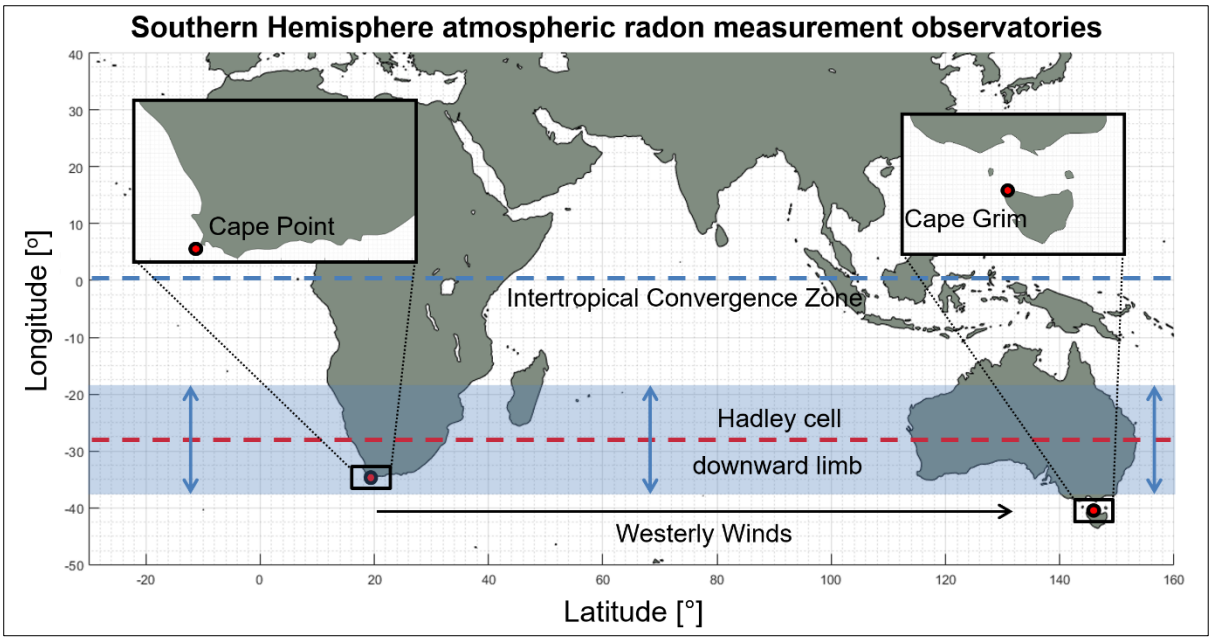

Figure 4-2: Map of Southern Hemisphere radon measurement observatories and meteorological effects.

4.2 Cape Grim Meteorological Observatory

Atmospheric radon measurements have been active at Cape Grim Observatory (CGO) since the 1980s. CGO is also known as the Cape Grim Baseline Air Pollution Station (CGBAPS). CGO (see Figure 4-3, and Figure 4-4, a) is located on a coastal cliff that is 97 m above sea level on the northern tip of Tasmania Island, S 40.683 256° and E 144.689 997° (see Figure 4-2). Tasmania is one of the six states of Australia located about 260 km south of the Australian mainland (see Figure 4-2). Tasmania is promoted as a natural state of which 42% is committed as a protected nature conservation area. The area surrounding CGO consists mainly of farmlands used for agriculture purposes (see Figure 4-3, b). CGO is utilised as one of the global baseline stations collaborating in the World Meteorological Organization (WMO) Global Atmosphere Watch (GAW) program (see Chapter 1). Ambient radon sampling is performed from a telecommunication tower at a height above ground level (a.g.l.) of 70 m (see Figure 4-4, a).

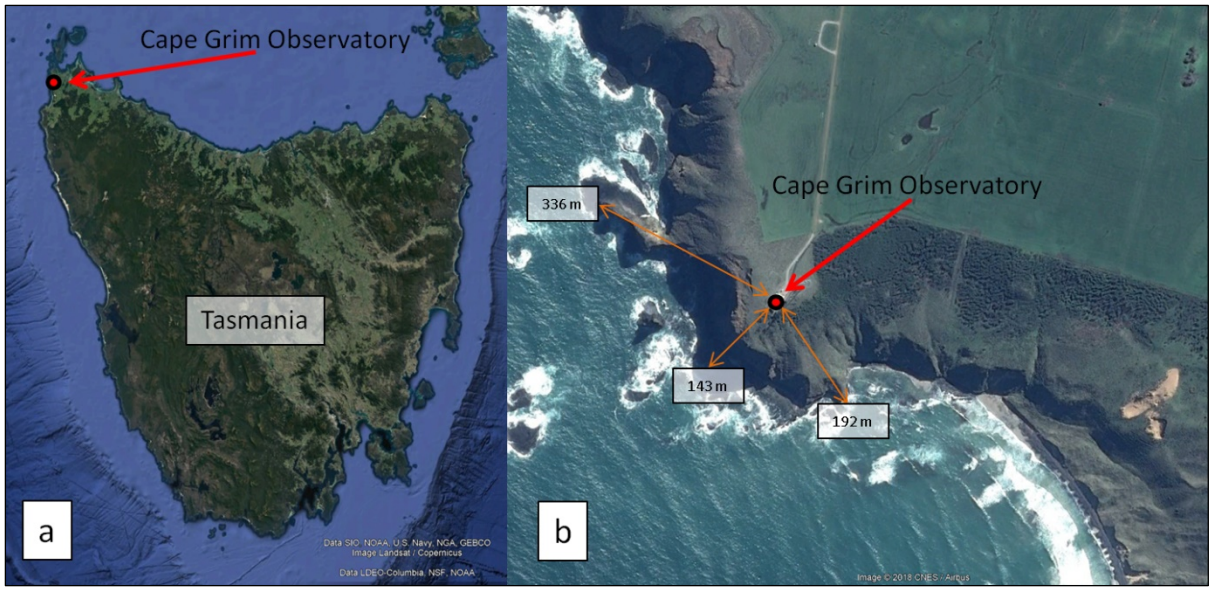

Figure 4-3: Satellite images of the coastal Cape Grim Observatory (b) on the Australian island, Tasmania (a). Credit Google Earth ® 2018.

Figure 4-4: (a) Coastal CGO atmospheric baseline monitoring labs and telecommunication mast from which sampling is performed, Credit AGAGE. (b) DFLTF radon detectors installed outside of the radon labs. Credit ANSTO.

Most air pollution is known to originate from a continental anthropogenic origin (Kelly and Fussell, 2015; SOGA, 2018; Williams et al., 2016). As a result, the "cleanest air" also referred to as baseline air-masses are prone to originate from marine fetch regions. Baseline air-masses are identified by radon levels below 100 mBq/m^3. To conduct advanced atmospheric pollution studies, it is critical to identify and measure the composition of the associated air-masses (A. D. Griffiths et al., 2016). The location of the CGO has been chosen on the northern coastal section of Tasmania (see Figure 4-3). This site is subject to baseline air-masses. CGO can be considered as a true coastal station (see Figure 4-3, b). Nonetheless, it should be taken into

consideration that small strips of surrounding land masses (< 336 m, see Figure 4-3, b) could potentially produce unwanted radon and thoron fluxes. Radon contamination becomes more probable during wind still days in combination with surface winds coming from the local terrestrial regions (see Figure 4-3, b). The land surface length from the ocean to the CGO ranges from 143 to 336 m (see Figure 4-3, b). For instance, for a surface wind (CGO-S1) with a speed of 5 $m.s^{-1}$, the exposure time with the ground during which locally emanated radon and thoron could be fetched can be up to 67 s. This could result in the potential accidental measurement of regional emanated radon. However, as discussed, several design features have been implemented as discussed to counter this (see Section 3.2).

Detection of continental air-masses at GCO is expected from angular sectors; CGO-S4 and CGO-S2 (see Figure 4-5). These continental sectors comprise the angular distribution between the contact line A1 clockwise to A4 (275° to 54°) which is the Australian mainland and A3 clockwise to A2 (90° to 167°) which represents Tasmania. Air-masses originating from continental sectors can contain from 10 to 1000 time higher radon levels compared to marine sectors (Williams et al., 2016, 2009). A comprehensive study to obtain a time-dependent radon flux map of the Australian mainland surface has been performed which indicate weighted arithmetic mean flux over 30 year period to be 23.4 ± 2.0 $mBq/m^2.s$ (Griffiths et al., 2010).

Marine air-masses detected at CGO are associated with the following angular sectors, CGO-S1 and CGO-S3 (see Figure 4-5); A4 clockwise to A3 which represents the Tasmania Sea within the South Pacific (54° to 90°) and A2 clockwise to A1 which represents the Indian Ocean (167° to 275°). The marine sector, CGO-S3, however, does have relatively small geological landmasses including; Flinders Island (1 367 km^2); Hunter Island (73.3 km^2), Robbins Island (99 km^2), Clarke Island (82 km^2), and Cape Barren Island (478 km^2).

It should be noted that marine and continental air-masses mixing zones are expected to be angularly (± 10°) distributed around the contact lines (see Figure 4-5). Nonetheless, air-masses in nature flow in time-dependent non-linear spatial pathways and more advanced back-trajectory modelling (HYSPLIT) will be utilised as an additional tool to track the flow more precise (see Section 3.4.3).

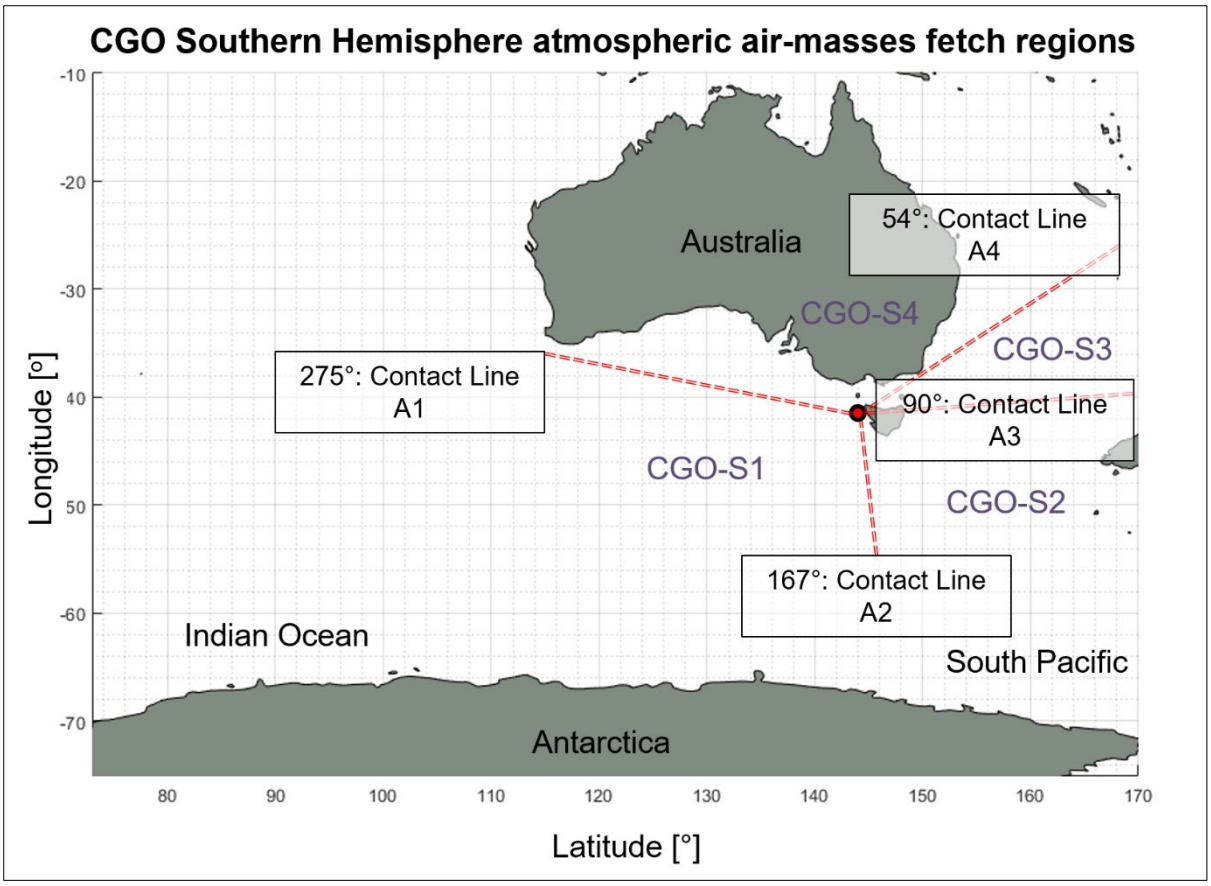

Figure 4-5: Map indicating the four angular air-mass fetch regions relative to CGO (CGO-S1 to CGO-S4).

The major identified uranium deposits in Australia are illustrated in Figure 4-6. The four uranium provinces in the Southern regions of Australia will be a prominent source of radon being observed at CCO. The air-masses incident to CGO from the Australian mainland will rarely originate from the Northern mainland (see Figure 5-37). The closest uranium province to CGO will be Stuart Shelf about 1100 km in the North Western direction (see Figure 4-6).

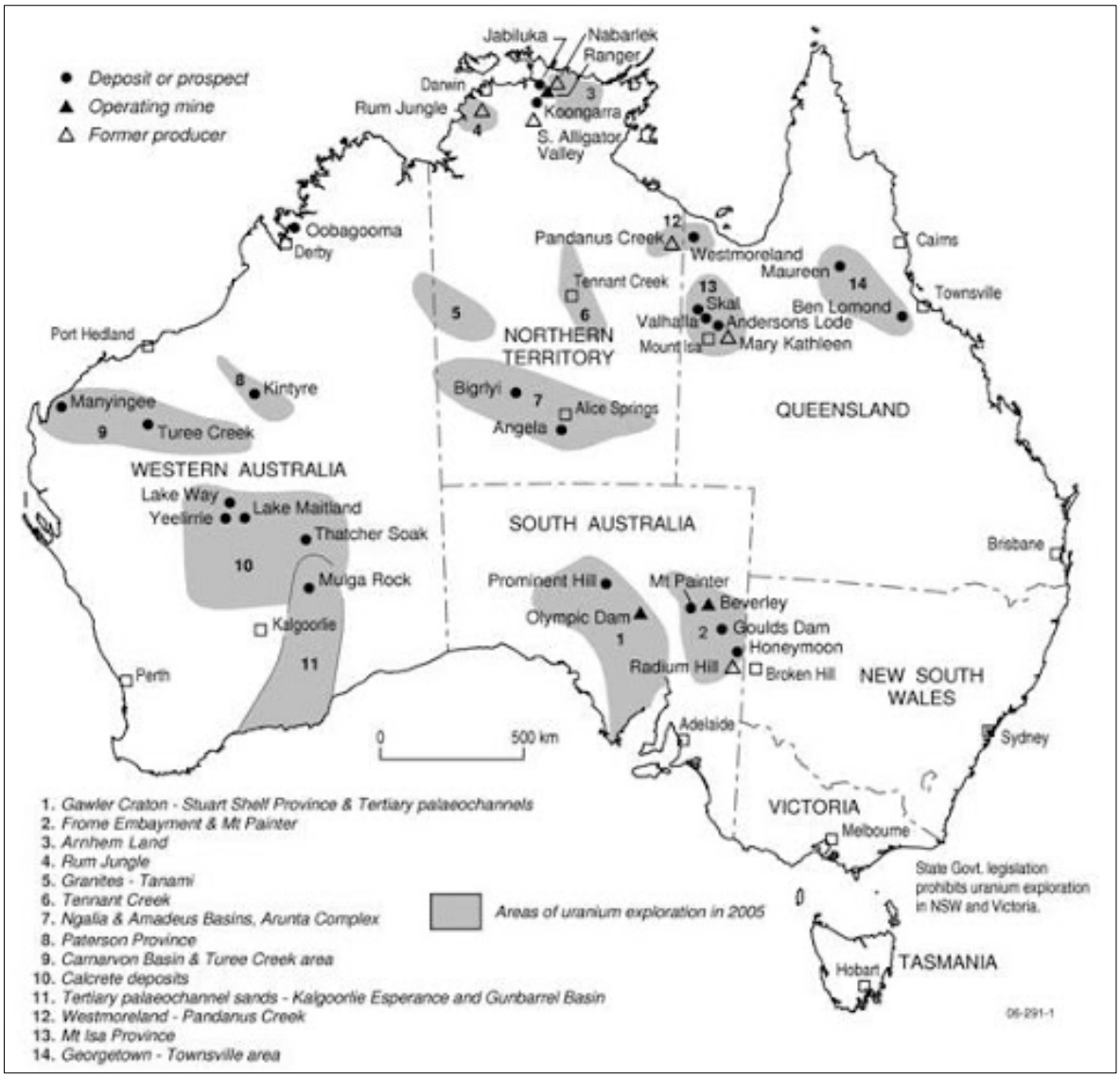

Figure 4-6: Map presenting the major Australian uranium deposits taken from Geoscience Australia (2005).

4.3 Cape Point Meteorological Observatory

Cape Point Observatory (CPO) is at the Southern tip of the Cape Peninsula in the Western Cape Province of South Africa (see Figure 4-2). CPO is approximately 60 km from Cape Town in the renowned Cape of Good Hope Nature Reserve which receives an estimated 1 million annual visitors. One of the first human activities in the area was the construction of "old lighthouse" in 1859 (see Figure 4-8, b). The region is known for its diverse range of unique flora also referred to as fynbos. CPO is a low-altitude coastal baseline atmospheric GAW and SAWS research facility (see Chapter 1). It is positioned at 230 m a.s.l. on a coastal cliff (S 34.353 211° and E 18.489 683°). The CPO atmospheric radon measurements commenced in 1999. The

DFLTF detector designed by ANSTO is being used to perform atmospheric radon measurements at CPO (see Section 3-2). A collection of continuous trace-gas (CO, CO_2, CH_4, O_3, N_2O, and halocarbons) measurements have been performed at the site for the last four decades (Brunke et al., 2004; Labuschagne et al., 2018). Additional continuous gaseous elemental mercury (GEM) measurements have been conducted for the past two decades (Brunke et al., 2010; Slemr et al., 2013). Similar to the Australian CGO, CPO is strategically positioned to conduct baseline atmospheric monitoring (see Section 4.2). As described in Section 3.2.2, ambient air is sampled from a 30 m a.g.l. aluminium mast (see Figure 4-8, a). In the event that ambient air is sampled originating from a surface wind with a heading of about 120 ± 10°, contact with the land surface of up to 840 m could be encountered (see Figure 4-7, b). Consequently, if these angular surface winds are flowing relatively slowly (< 5 $m.s^{-1}$) across the micro-terrestrial strip (< 840 m) it could be expected that local radon could be in the air-masses. For this reason, a radon and thoron emanation experiment from soil and rocks in the surrounding area is performed as described in Section 3.3.2.

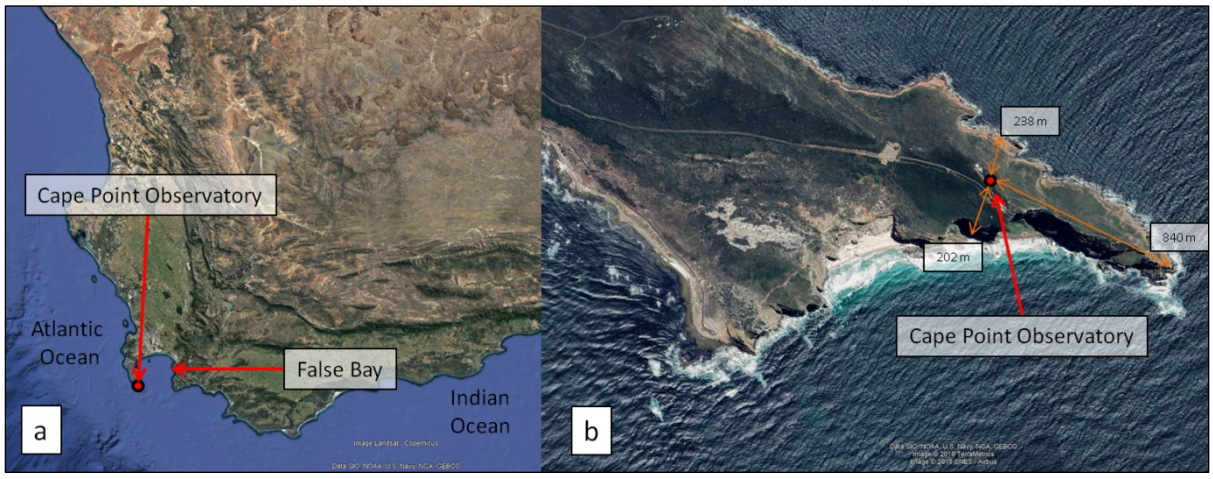

Figure 4-7: Satellite images of the coastal low-altitude Cape Point Observatory (b) on the southern tip of the Cape Peninsula, South Africa, Western Cape Province (a). Credit Google Earth ® 2018.

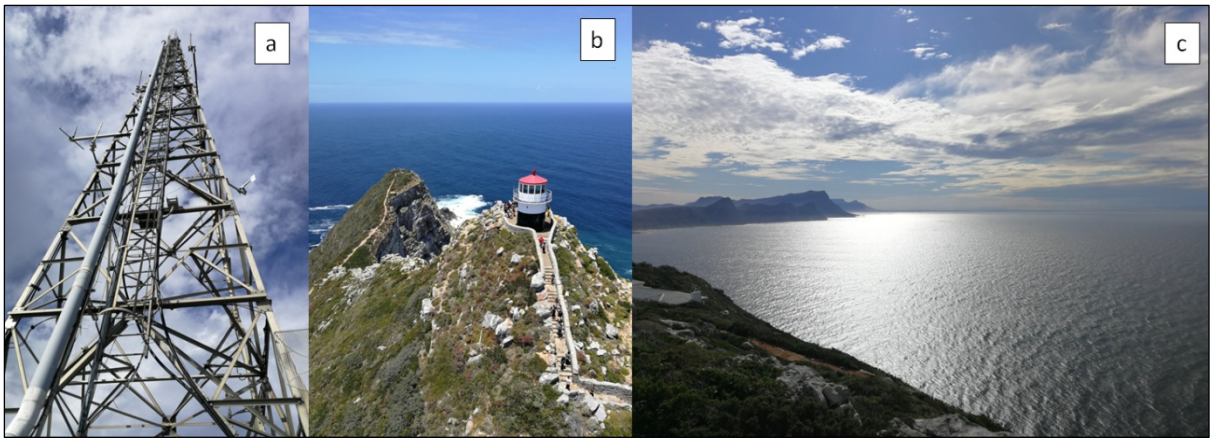

Figure 4-8: (a) CPO sampling mast equipped with meteorological measurement instrumentation. (b) View from the top of sampling mast towards the tip of the Cape Peninsula. (c) North Eastern view from CPO station across False Bay.

CPO is subjected both to continental and marine air-masses. At CPO continental air-masses is predominantly observed during the winter and marine during the summer seasons. The marine air-masses detected at CPO (see Figure 4-9) are prone to originate from the angular sector CPO-S2; B2 (115°) clockwise to B1 (339°). The continental air-masses at CPO, on the other hand, are prone to come from the angular sector CPO-S1, B1 (339°) clockwise to B2 (115°). Both CPO (see Figure 4-9, CPO-S2) and CGO (Figure 4-5, CGO-S1) are subjected to air-masses originating or back-tracking across the Indian Ocean and Southern Ocean.

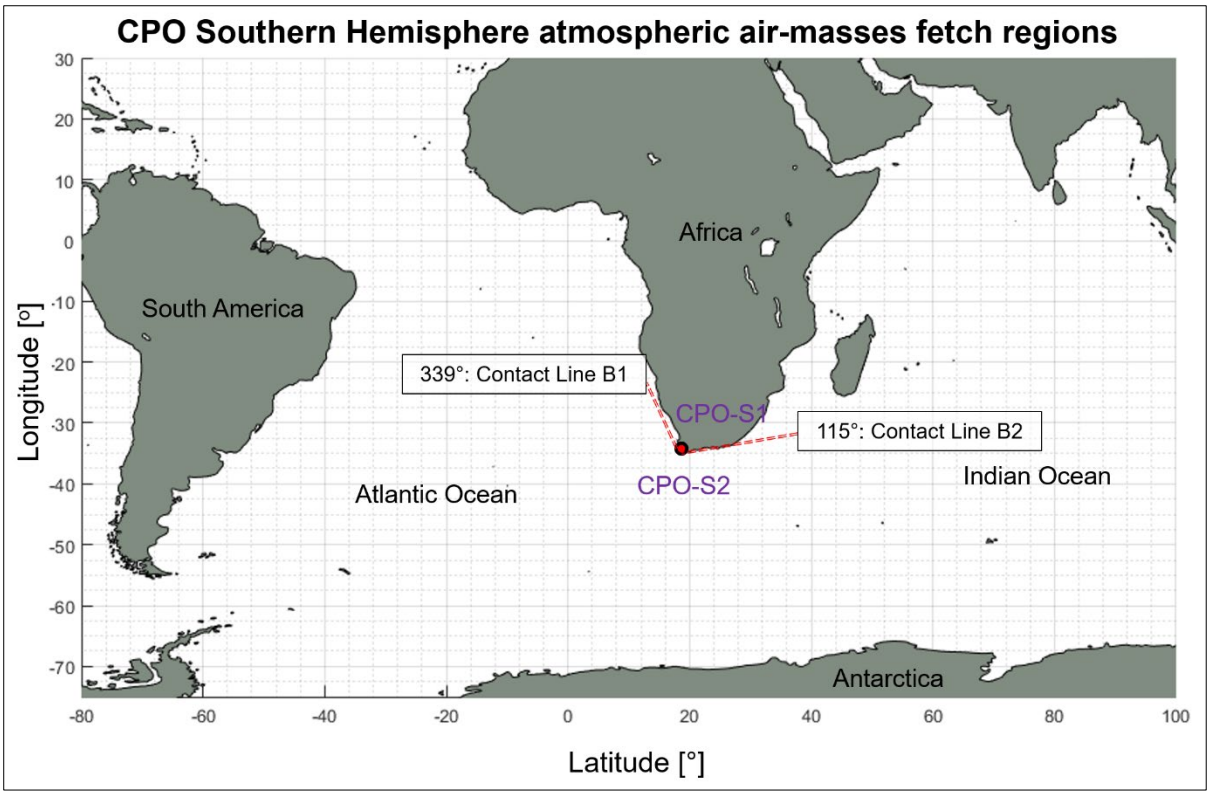

Figure 4-9: Map indicating the Southern Hemisphere atmospheric CPO two fetch regions, CPO-S1 and CPO-S2.

Four distinct uranium deposit regions have been identified in South Africa (Kenan and Chirenje, 2016). It is expected that these regions will be prone to contain elevated concentrations of NORM such as radium (^{226}Ra). Uranium provinces (see Figure 4-10) can be considered a region which produce a higher flux of soil radon emission (Griffiths et al., 2010). The closest two uranium regions to the CPO, Karoo and Namaqualand, will be of particular interest.

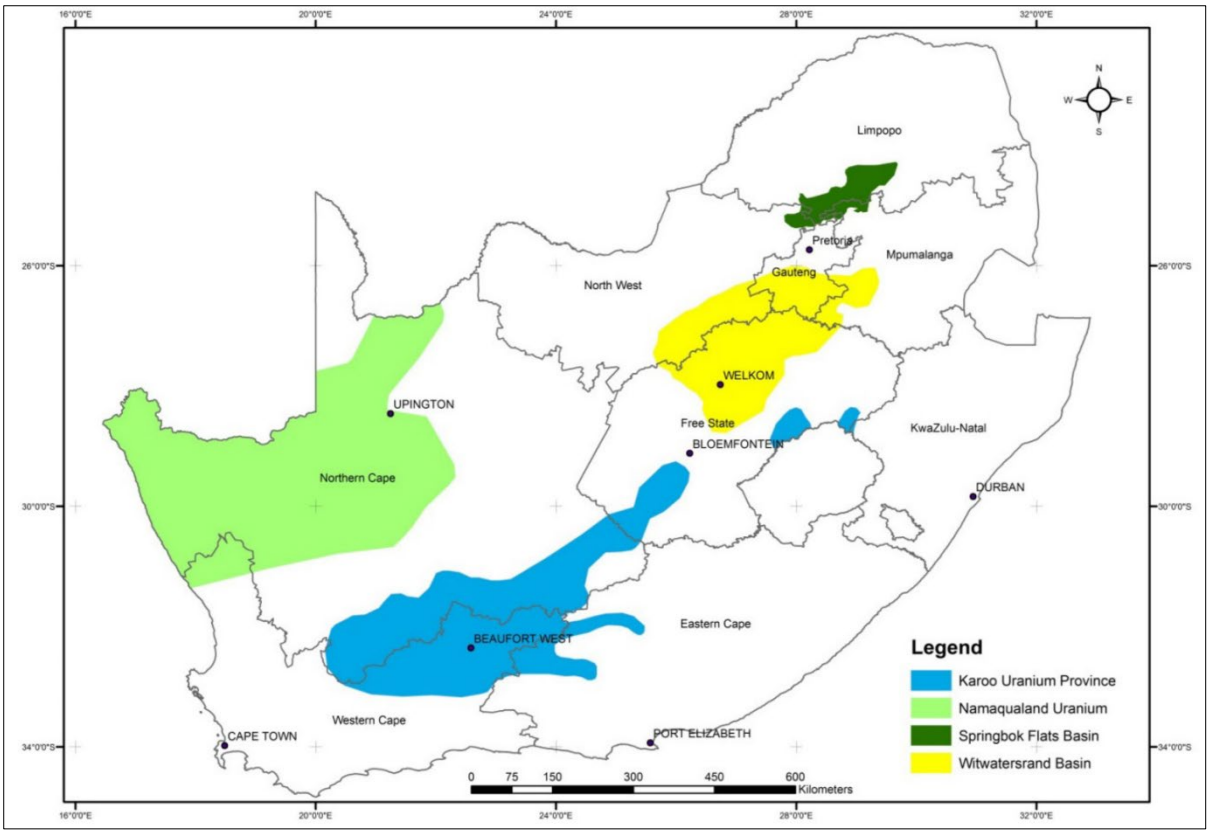

Figure 4-10: Map presenting the major South African uranium deposits (Kenan and Chirenje, 2016).

A simplified local radon and thoron emanation survey was performed from soil and rock samples collected at CPO (see Section 3.3.2). The results presented here are the starting point of further work with the view to estimating the local outdoor contamination. Similar measurements will possibly be performed at CGO and MLO in the future; nonetheless, with the difficulty of travelling to those locations, it has not been conducted. A combined soil sample of 337 g was created by mixing different soil samples from around the sampling mast. Both radon and thoron emanations are observed from the soil samples (see Figure 4-11). The radon generated from the soil samples increased linearly to about 242 ± 23 Bq/m^3 (see Figure 4-11). The radon-in-soil flux rate is estimated to be approximately 5.6 ± 0.6 Bq/m^3.g.h by making use of the radon slope (see Figure 4-11). The soil thoron emanation profile, on the other hand, does not undergo a build-up period, due to thoron ($t_{1/2}$ = 55.6 s) having a significantly shorter half-life compared to radon ($t_{1/2}$ = 3.82 days). For the soil samples a mean of thoron-in-air activity concentration of 177 ± 7 Bq/m^3 is observed during the 96 hours of measurement (see Figure 4-11).

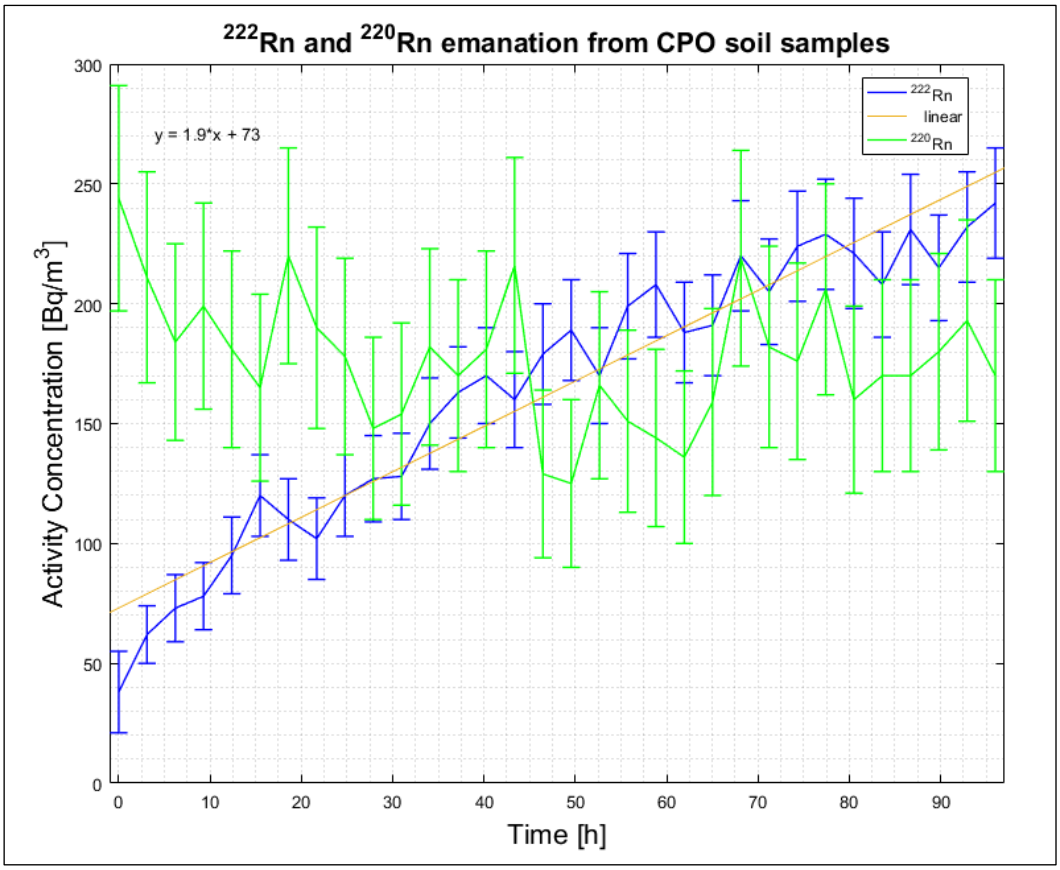

Figure 4-11: CPO radon and thoron emanation profile of soil samples. Radon linear interpolation (y = 1.9 x + 73, (hours), R-square: 0.93 and RMSE: 15.79). The vertical bars represent the associated measurement uncertainty.

Various size rocks (see Figure 3.20, b) with a total mass of 3463 g were collected at close proximity to the sampling mast. The rock samples were measured for a longer duration with 99 cycles and 3 hours measurement duration compared to the soil sample. The longer measurement times is needed since these rock samples (see Figure 4-11) requires about three times as much time to complete the build-up phase compared to the soil sample (see Figure 4-10). This can be expected because the rocks are denser and less porous compared to the soil. After approximately 207 hours the equilibrium build-up from the soil sample with a mean of 458 ± 5 Bq/m^3 for radon and 1680 ± 20 Bq/m^3 for thoron are observed (see Figure 4-11). The radon flux rate from the rocks is estimated to be in the order of 0.40 ± 0.03 mBq/m^3.g.h (see Figure 4-12. Extensive temporal fluctuations (diurnal) are observed (see Figure 4-12). It has been noted that an increase in air temperature coincides to an increase in the levels of thoron detected (see Figure 4-13).

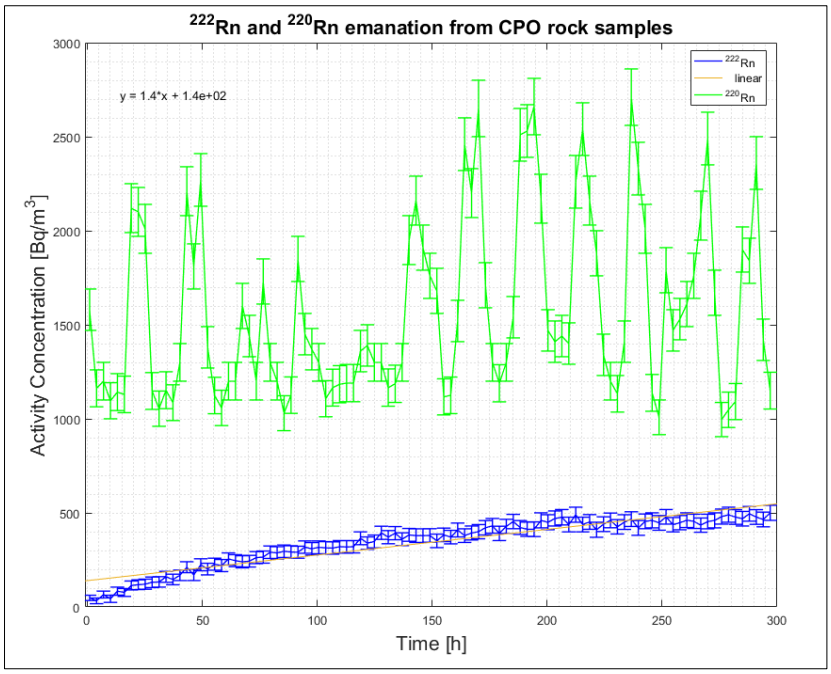

Figure 4-12: CPO radon and thoron emanation profile from the rock samples. Radon linear interpolation (y = 1.4 x Time + 140, (hours), R-square: 0.88 and RMSE: 44.57). The vertical bars represent the associated measurement uncertainty.

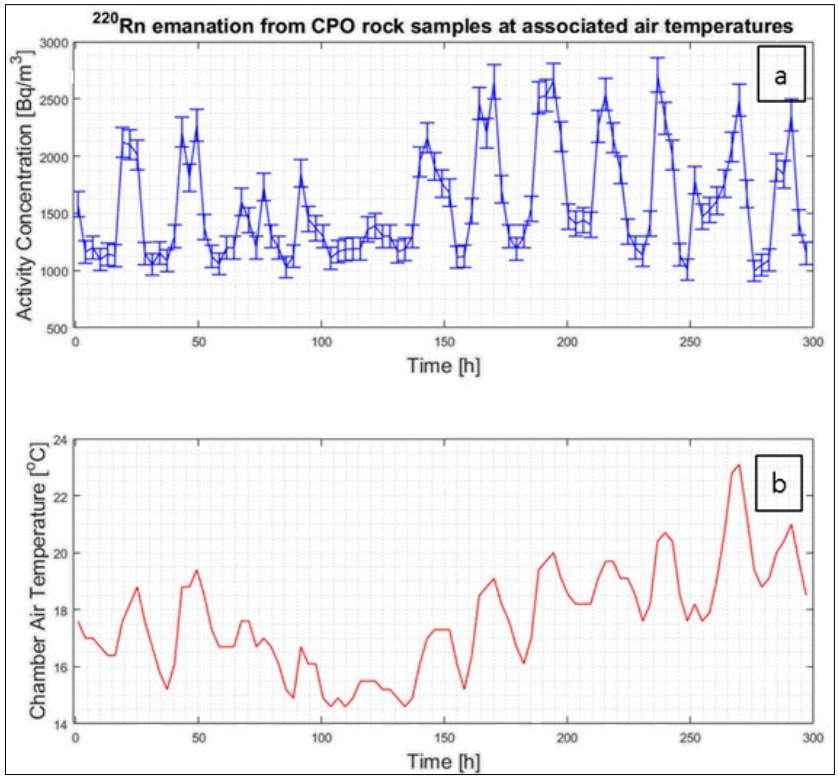

Figure 4-13: CPO rock samples thoron emanation profile (a) at associated internal detection chamber air temperatures (b). The vertical bars represent the associated measurement uncertainty.

The experimental radon and thoron emanation flux setup can be improved as discussed in Section 3.3.2, nonetheless, these additional measurements serve as an indicator of what emanation flux rate levels can be expected in the CPO area. The soil and rocks within the proximity of CPO sampling mast do emanate radon and thoron as mentioned. The radon emanation flux rate for soil (5.6 ± 0.6 mBq/m^3.g.h) is higher compared to that of rocks (0.40 ± 0.03 mBq/m^3.g.h). Within the experimental setup (see Figure 3-20) soil and rock thoron levels of up to 244 ± 47 Bq/m^3 (see Figure 4-10) and 2710 ± 150 Bq/m^3 (see Figure 4-11) are detected, respectively.

The CPO radon lab indoor ambient radon signature is characterised as described in section 3.4.2. The mean radon-in-air levels detected from the 3 indoor locations (see Figure 3-23) are 38 ± 8 Bq/m^3 (see Figure 4-13). The indoor radon signature correlates with a typical worldwide indoor average of 39 Bq/m^3 (WHO, 2009) and the indoor geometric mean of 45 Bq/m^3 (UNSCEAR, 2008).

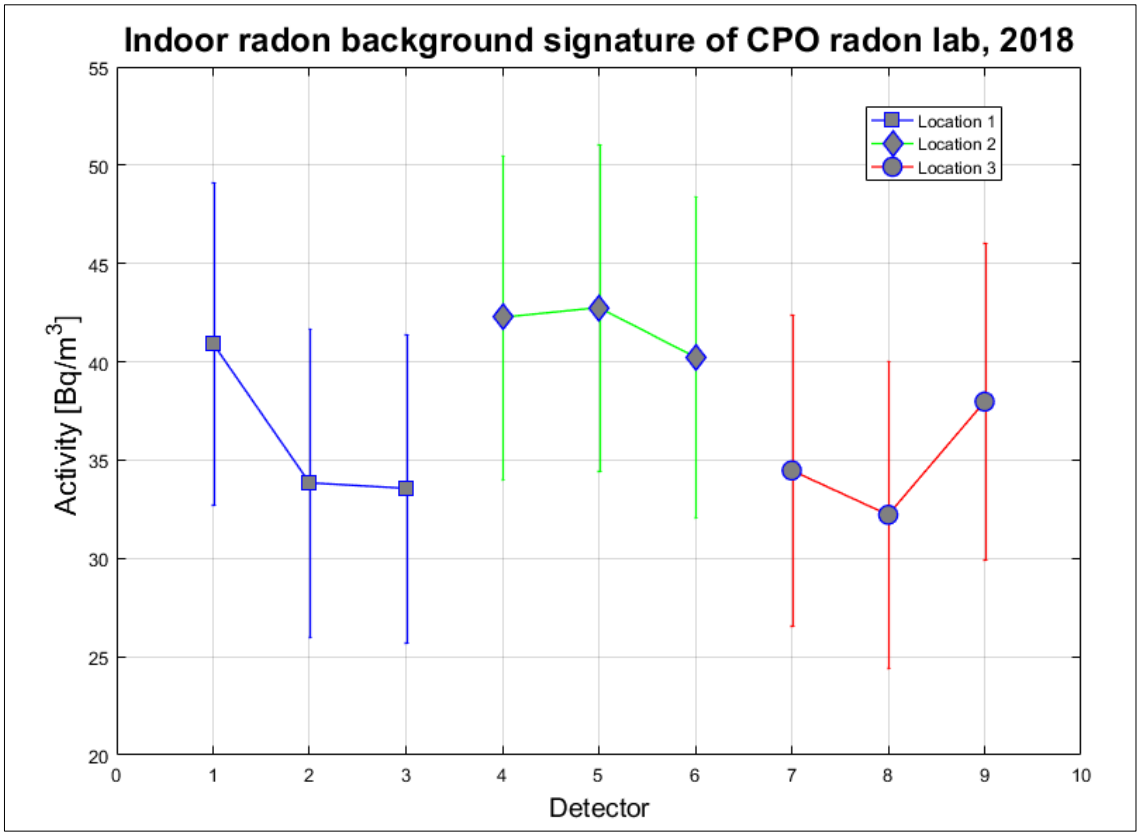

Figure 4-14: Indoor radon activity concentration at the CPO radon lab measured for about 20 days making use of 9 passive E-PERM detectors at three different locations. The vertical bars represent the associated measurement uncertainty.

4.4 Mauna Loa Meteorological Observatory

MLO is a Northern Hemisphere high-altitude ground based atmospheric observation station (see Figure 4-15, a). MLO (N 19.520 103°, S 155.554 105°) located on the upper northern flank of the Mauna Loa mountain at an altitude above sea level of 3397 m (Chambers et al., 2013). The MLO serves as a crucial northern Pacific (see Figure 4-1) basin baseline station (Chambers et al., 2013) able to monitor ever-increasing anthropogenic pollution generated from the central and southern East Asia (Kim et al., 2011; Ohara et al., 2007).

Mauna Loa is one of five volcanoes which create the Hawai'ian Islands (see Figure 4-15, b). The active Mauna Loa volcano is considered to be the largest sub-aerial volcanoes on Earth both in mass and volume (Rhodes and Lockwood, 1995). MLO is located on the summit of the Hawaii Volcanoes National Park (see Figure 4-15, a). The first atmospheric radon measurements at Mauna Loa Observatory (MLO) began in 1989 by Stewart Whittlestone to explore the possibility of using the ANSTO single flow-loop and two-filter (SFLTF) detector (Whittlestone et al., 1992). Atmospheric radon monitoring commenced in 1991, however, metrological improvements were required. In December 2003 a new 1500 L DFLTF radon detector was installed (Williams et al., 2016). "Gooseneck" mast sampling is performed at 38 m a.g.l. (see Figure 4-16).

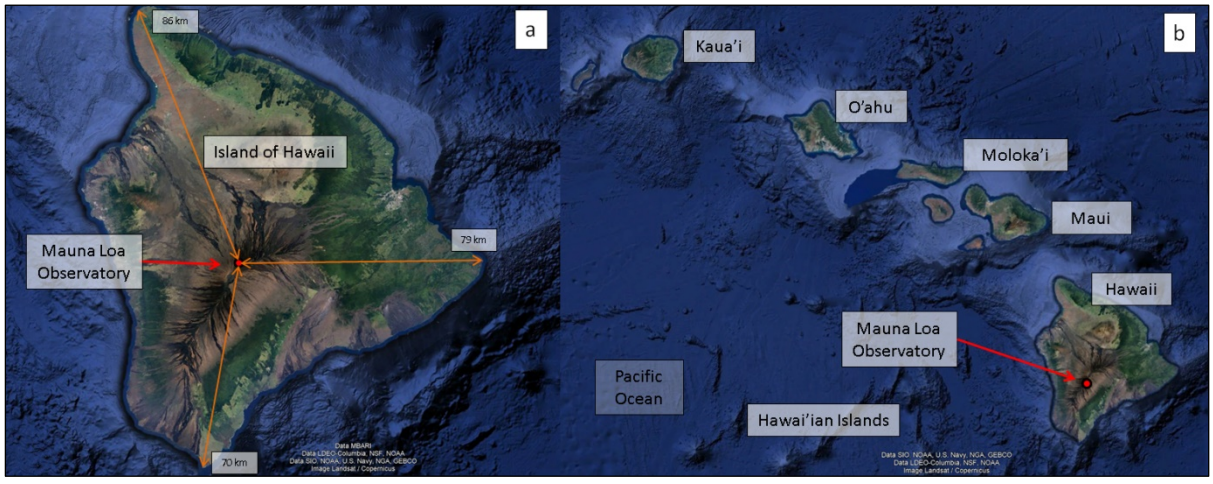

Figure 4-15: Satellite images of Mauna Loa Observatory on the Island of Hawaii (a) which forms part of the Hawai'ian Islands (b). Credit Google Earth ® 2018.

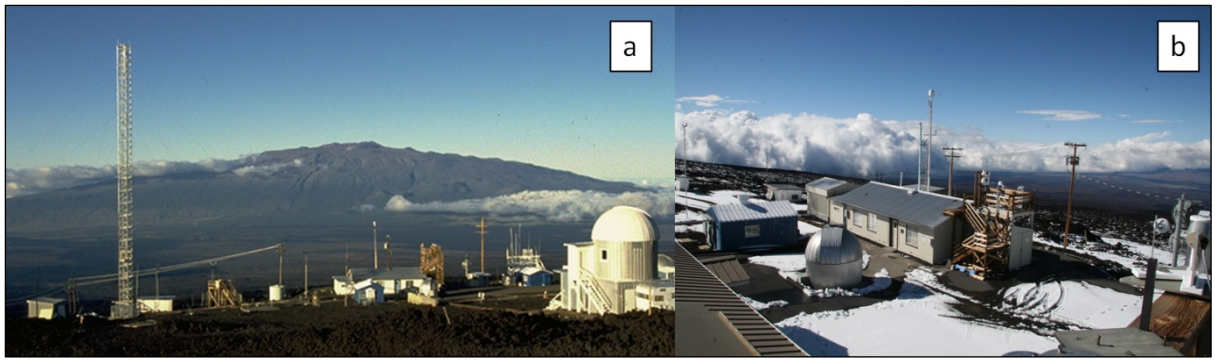

Figure 4-16: (a) Mauna Loa Observatory located in the Hawaii Volcanoes National Park. Credit ANSTO (b) Mauna Loa Observatory after a snowstorm. Credit Mary Miller, NOAA.

CHAPTER 5 Results and Discussion

5.1. Introduction

In Chapter 5, the main analysis results will be presented, discussed and interpreted. The complex radon time-series will be studied on various temporal scales making use of statistical, spectral, trend, back-trajectory and trajectory density (cluster) analysis. By examining air-mass back-trajectory analysis insights into the radon time-series such as fetch regions, boundary layer mixing, temporal evolution will be made. The characterisation of the Southern Hemisphere atmospheric radon time-series will highlight diurnal, monthly, seasonal and interannual periodicities and trends (see Section 5.2) that will then be interpreted in terms of various atmospheric processes.

5.2. Atmospheric Radon Signal Characterisation

5.2.1. Time-series and Distributions

The inter-annual atmospheric radon time-series at CGO, CPO, and MLO are presented in Figure 5-1. The cumulative atmospheric radon (signal) from here on in the thesis will be defined as all of the hourly measurements (time-series) conducted at CGO (1992 to 2017), CPO (1999 to 2017) and MLO (2004 to 2016), respectively. A total of 57 years' high-resolution atmospheric radon time-series measurements are presented in Figure 5-1. It should be noted that temporal overlap for the three radon signals occurs between 2004 to 2016. However, for the austral sites, the temporal overlap is 19 years starting from 1999 to 2017.

A distinctive annual periodic time-series is observed for the coastal CGO and CPO (see Figure 5-1). The atmospheric radon maxima occur during the austral winters and minima during the summers. This is a direct result of a higher incidence of continental air-masses during the winter where for the summer a higher incidence of marine air occurs. The cyclic CGO and CPO atmospheric radon time-series are synchronised in time (see Figure 5-1). The distinctive Southern Hemisphere annual radon periodicity structures are not so transparent for the Northern Hemisphere high-altitude site at, MLO (see Figure 5-1 and 5-2, A5). The temporal atmospheric radon periodicity will be analysed and discussed in greater detail in Section 5.2.2.

By making use of the cumulative radon signals (see Figure 5-1), it can be established that the overall atmospheric levels for CGO (blue) are the highest (Figure 5-1), CPO (red) is lower compared to CGO and MLO (green) has the lowest levels (see Figure 5-1). The annual maxima of CGO appear to decrease over time compared to the steady maxima of CPO (see Figure 5.1).

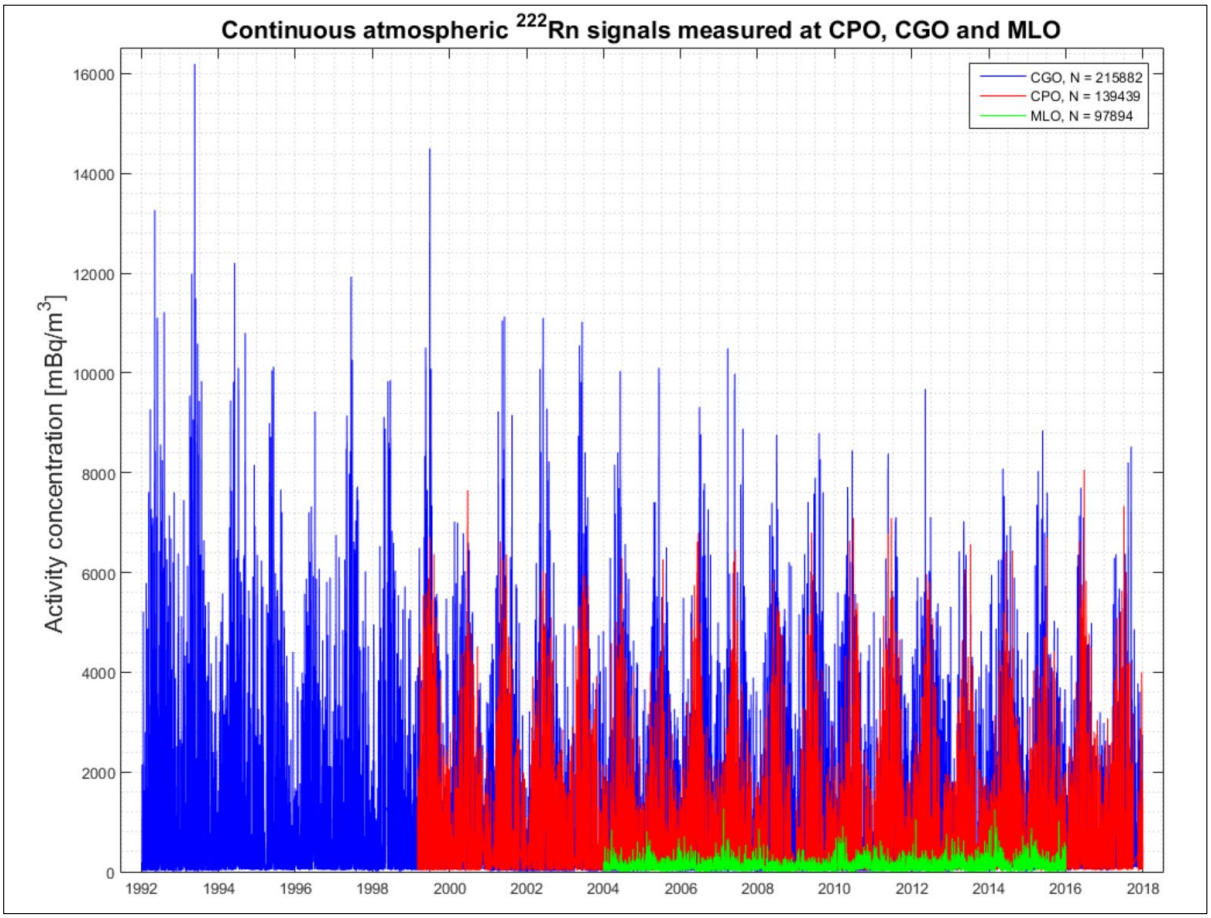

Figure 5-1: Respective CGO, CPO, and MLO full (cumulative) atmospheric radon signals.

The normalized CPO and CGO of atmospheric radon histograms show a predominant number of measurements (events) at the relatively lower activity concentration range of < 400 mBq/m^3 (see Figure 5-2, A2 and A4). This is followed by a sharp decrease in the number of measurements as the radon levels increase. A long "tail" corresponding to a small number of high radon values (> 1000 mBq/m^3). CPO exhibits a second, smaller peak in the range of 300 - 500 mBq/m^3 (A4). The CPO (see Figure 5-2, A2) histogram is wider compared to CGO (see Figure 5-2, A4). It will become evident making use of the back-trajectory analysis that CPO (see Figure 5-38, B) is subjected to larger amount of continental air-masses than CGO (see

Figure 5-44, B). CGO is subjected to a higher number of deep baseline air-masses, resulting in a sharp peak centred around 75 mBq/m^3. Comparing these austral histogram profiles (see Figure 5-1, A2 and A4) with that of MLO (see Figure 5-2, A6), a key difference becomes apparent. For MLO, most radon levels occur within the range 30 –120 mBq/m^3 (see Figure 5-2, noting the different x-scales, A6), and the long "tail" is absent.

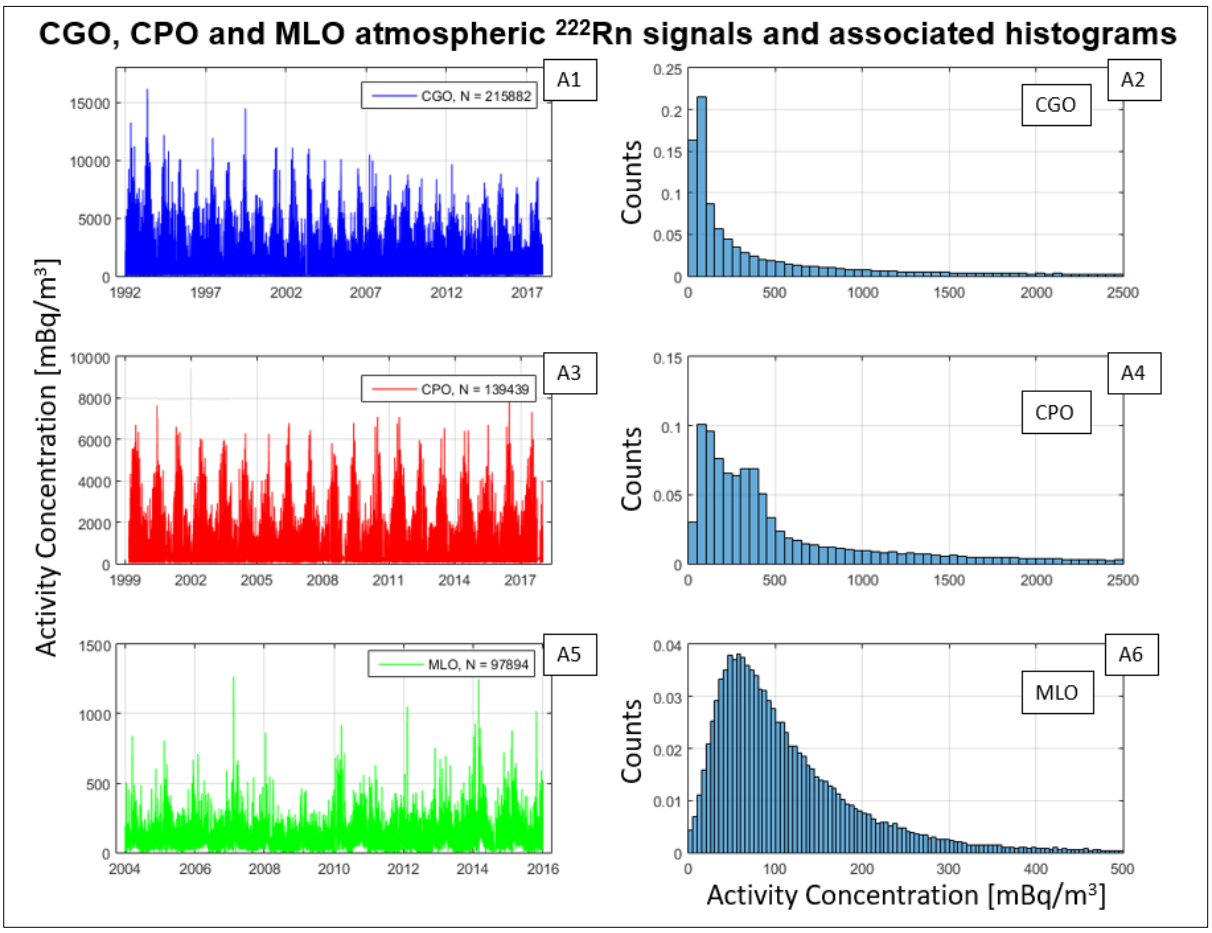

Figure 5-2: Respective cumulative CGO (A1), CPO (A3), and MLO (A5) atmospheric radon signals and associated probability normalized counts (number of observations in bin / total number of observations) histograms (A2, A4 and A6). Individual bin sizes and x-scales are utilised.

The statistical analysis of the fundamental atmospheric radon signals statistical summarised in Table 5-1. The annual maximum atmospheric radon levels observed respectively at CGO, CPO and MLO are, 16 196 ± 809 mBq/m^3 (21 May 1993), 8060 ± 484 mBq/m^3 (23 June 2016) and 1267 ± 139 mBq/m^3 (12 February 2007). For instance, compared to the global indoor geometric

mean radon-in-air level of 39 000 mBq/m^3 (Chambers & Zielinski, 2011; Gaskin et al., 2018), it is relatively low.

The total average MLO atmospheric radon level is about a factor 6 lower compared to CGO or CPO (see Table 5-1). The total median for CPO, 348 mBq/m^3, is about twice that of CGO, 177 mBq/m^3 (see Table 5-1 and Figure 5-3). The greater CPO median preludes to it being exposed to a larger incidence of continental air-masses. The total average of CGO is slightly (4.8%) higher than CPO (see Table 5-1), due to a slightly longer "tail" at CGO. This is related to the wider CPO (double-peaked) histogram and may indicate the effects of mesoscale coastal circulations that are absent or insignificant at Cape Grim. These observations will be explored further later on.

Location	Measurement Time Frame	Median ^{222}Rn Activity Concentration, [mBq/m^3]	Average ^{222}Rn Activity Concentration, [mBq/m^3]	Standard Deviation ^{222}Rn Activity Concentration, [mBq/m^3]	Maximum ^{222}Rn Activity Concentration, [mBq/m^3]
CGO	1992 – 2017	177	708	1 274	16 196
CPO	1999 – 2017	348	674	861	8 060
MLO	2004 – 2016	90	115	92	1 267

Table 5-1: Statistical analysis of the cumulative CGO, CPO an MLO radon signals.

The atmospheric radon distributions observed at CPO and CGO are greatly skewed and exhibits a large number of events falling into a compact range of low values (corresponding to marine air masses), and a smaller number of events with high radon values spread over a wide range (corresponding to continental air masses, see Figure 5-2 and 5-3). For CGO and CPO from the 5th to the 50th percentiles exhibit a range of 149 mBq/m^3 and 287 mBq/m^{3}m, respectively. Whereas those between the 50th and 95th percentile have a range of 3301 mBq/m^3 and 2236 mBq/m^3, respectively (see Table 5-2). A moderately skewed MLO atmospheric radon distribution is observed compared to that of CGO and CPO. The MLO data points from the 5th

to 50th percentile exhibit a range of 67 mBq/m^3, whereas those between 50th and 95th have a range of 201 mBq/m^3 (see Table 5-2).

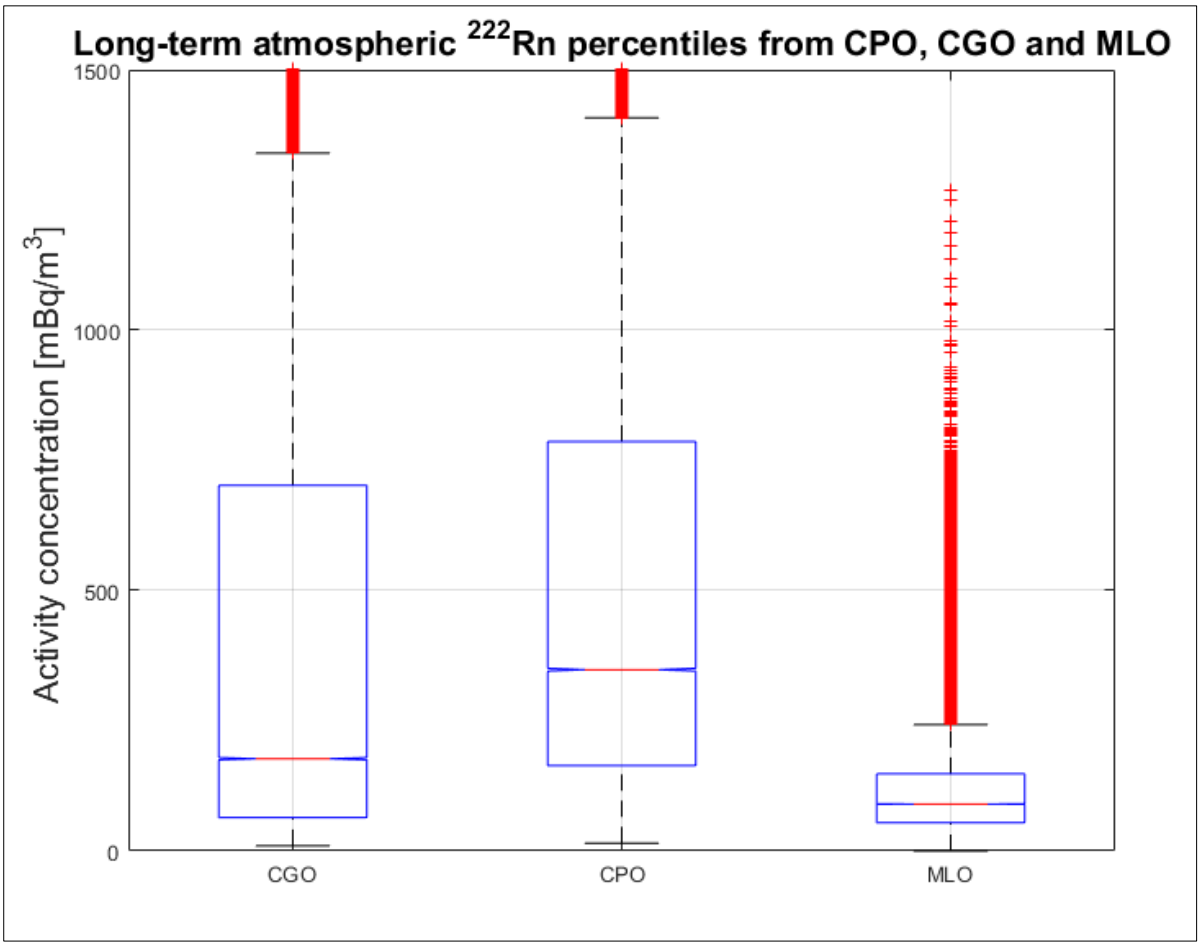

Figure 5-3: Atmospheric radon concentration distributions from CGO (1992 to 2017), CPO (1999 to 2017) and MLO (2004 to 2016). The long-term radon distributions are characterised by the whiskers, bars and central horizontal line within the bars which refer to regions of most extreme data points considered outliers (red +), 25th, 75th, 50th (median) percentiles, respectively. Whiskers are 5thand 95th percentiles.

Composites analysis: CGO, CPO and MLO cumulative atmospheric radon signals					
Location	**5th Percentile, [mBq/m^3]**	**25th Percentile, [mBq/m^3]**	**50th Percentile, [mBq/m^3]**	**75th Percentile, [mBq/m^3]**	**95th Percentile, [mBq/m^3]**
CGO	28	64	177	702	3478
CPO	61	164	348	786	2584
MLO	23	54	90	148	291

Table 5-2: CGO, CPO and MLO cumulative atmospheric radon signals percentile composites analysis.

The differences in overall statistical characteristics (see Table 5-2) between the three sites can be attributed to variations in their geographical positions adjacent to large bodies of land (radon source) and marine. Numerous studies have shown that air-masses associated with continental origin are likely to contain 10 - 1000 times more radon compared to marine air-masses (Chambers et al., 2016; Crawford et al., 2016; Florea & Duliu, 2012; Williams et al., 2011). Consequently, it can be generally accepted that higher atmospheric radon levels are associated with continental air-masses and lower levels by marine air-masses. Therefore, in the scenario that a large decrease is observed at a coastal location, it can be attributed to either an increase in the incidence of marine air-masses, or a decrease in the incidence of continental air-masses. The atmospheric radon levels at specific time and spaced depend on the elements such as the following:

(1) Air-masses altitude (Chambers et al., 2019; Griffiths et al., 2013). By default, it is expected the radon-in-air levels to be the highest the closer it is to the source (^{226}Ra), in other words, the surface and decrease with an increase in altitude. A detailed altitude analysis is performed in Section 5.4.2.

(2) Surface radon flux (Goto et al., 2008). A higher surface radon flux will consequently result in higher regional radon-in-air levels. Anthropogenic events such as mining (open dumps) will contribute to a larger radon flux in some instances (Ongori et al., 2015).

(3) Air-masses travelling distance (Gupta et al., 2004). When radon is transported across longer distances it will have a longer time to decay.

5.2.2. Spectral Analysis

From the atmospheric radon time-series analysis (see Section 5.1.1) it became evident that the signals have an inherent periodic temporal nature. The aim of this section will be to characterise the periodic temporal structures embedded in the radon signals. The analysis will be performed by making use of power spectral Fast Fourier Transform (FFT) analysis. The first approach is performed by analysing the cumulative atmospheric radon signals. Secondly, the atmospheric radon signals are binned into annual data sets and investigated. The objective will be to identify and focus on inter-annual cyclic radon atmospheric occurrences on shorter timescales. On an

annual temporal scale, it has been seen that no periodicity signals are evident for timescales larger than a week.

The CGO radon signal FFT-analysis results are presented in Figure 5-4. The variance grows steadily up to about 10 days. No statistically significant diurnal (1 day) or sub–diurnal peaks are identifiable in the power spectrum (see Figure 5-4). A long plateau of high variance is visible from 10 to about 300 days, likely a result of synoptic and seasonal circulations that direct mixtures of continental and marine air to the station. Medium size peaks are visible from which quarterly-annual (91.3 days), third-annual (121.7 days), half-annual (182.5 days) and strong annual (365 days) temporal periodicity structures are evident.

A large peak can be identified centred on 365 days (see Figure 5-4). The annual (365 days) periodicity signature is visible in the CGO radon time-series (See Figure 5-1). It reflects the reoccurring annual maxima during the austral winter and minima during summer. Consequently, the 365 days CGO peak is associated with the annual cycle of regional and hemispheric seasonal atmospheric circulations due to seasonal changes in the associated patterns of offshore versus onshore flow. The existence of a family of peaks at integer fractions of the main annual cycle within the CGO radon time-series (quarterly-annual, third-annual, half-annual and annual) likely indicates a composite seasonal pattern of radon concentrations which departs from a simple sinusoid (skewed seasonal distribution). Seasonal atmospheric radon patterns and diurnals will be further investigated.

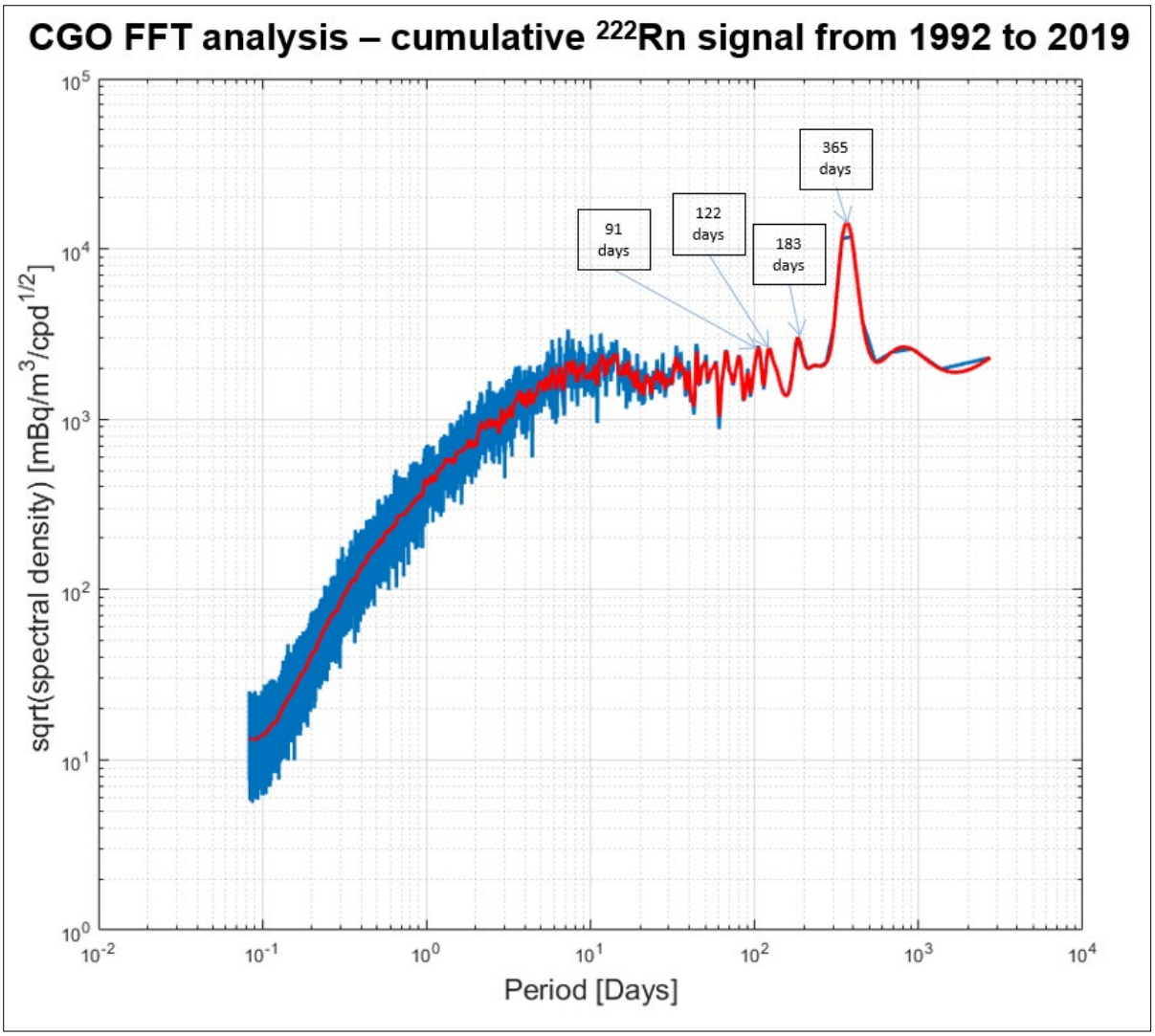

Figure 5-4: Power spectrum (amplitude) for the cumulative 26-year CGO radon signal using FFT analysis (cpd, counts per day). The blue-line represents the raw power spectrum and the red-line the smoothed spectrum processed using Savitzky-Golay digital filtering.

The inter-annual CGO power spectral density plot focusing on shorter timescales (see Figure 5-5) confirms the non-existent diurnal or sub-diurnal periodicity structures. The relative power spectral density (PSD) plots are limited to a frequency between 0.5 and 3 day^{-1} (x-axis). The reason for applying the scaling (removing frequencies below 0.5 day^{-1} and above 3 day^{-1}) is that no periodicity structures can be identified in the remaining regions, on average or in any individual years (see Figure 5-7).

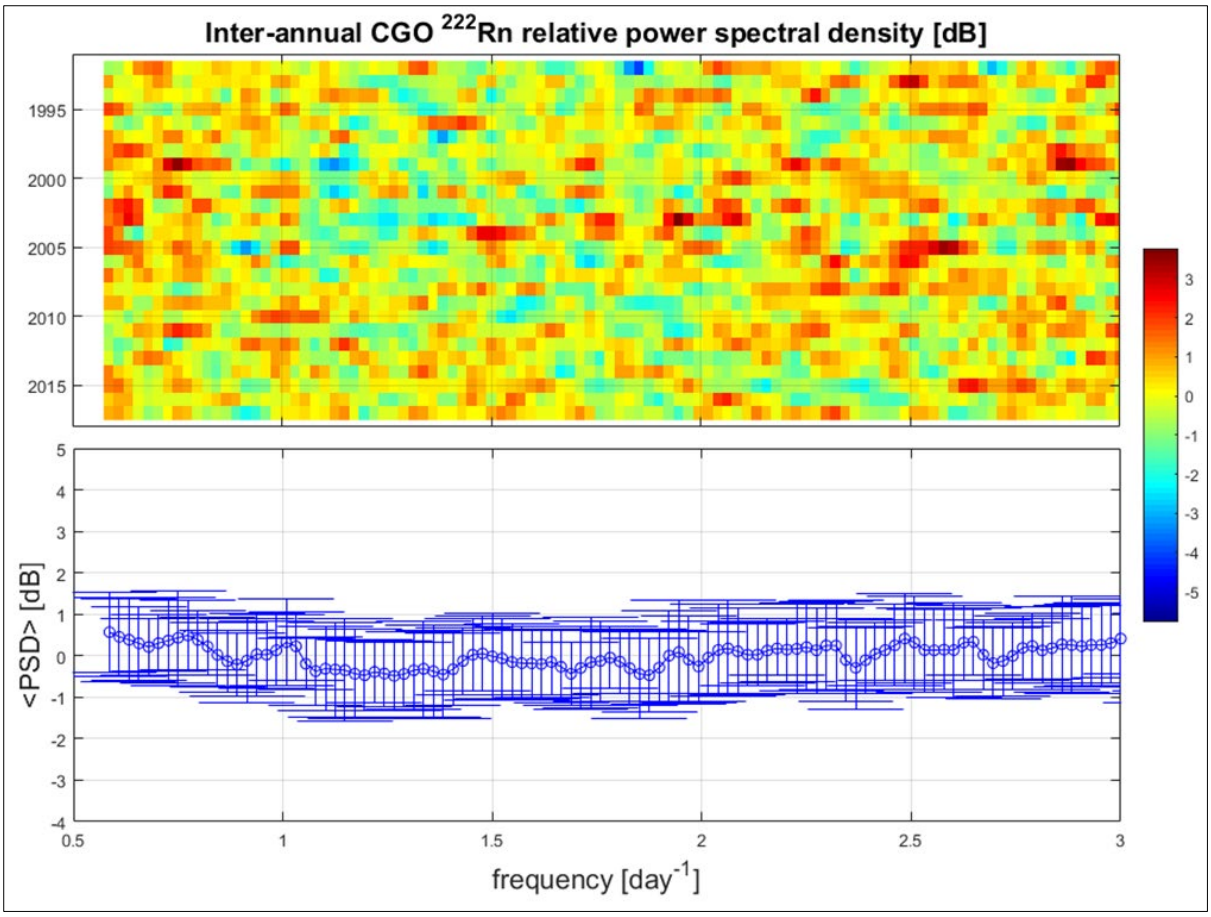

Figure 5-5: The relative inter-annual CGO atmospheric radon power spectral density (PSD) from 1992 to 2017 (upper) and the associated averaged PSD for the same period (lower) with standard deviation.

The cumulative CPO radon signal FFT-analysis results are illustrated in Figure 5-6. Modest diurnal and half-diurnal peaks are distinguishable in the power spectrum (see Figure 5-6). Apart from this, the overall variance pattern is similar to that observed at CGO (see Figure 5-4). The variance grows steadily up to about 10 days and then has a long plateau to about 300 days. The power spectral density of the plateau is lower compared to CGO (see Figure 5-4).

A distinctive strong annual (365 days) radon peak is identifiable in the power spectrum (see Figure 5-6), together with smaller peaks at quarter-annual (122 days) and half-annual (182.5 days) timescales. As discussed, the annual periodicity (365 days) occurs as a result of regional and hemispheric atmospheric circulations. During the austral winters, the atmospheric radon is at its annual maximum (see Figure 5-1) as a result of a higher incidence of continental air-masses flowing across CPO, whereas a minimum is observed during the austral Summer seasons due to a higher incidence of marine air-masses. The spectral analysis provides further

confirmation of an annual radon periodicity with a skewed distribution at both Southern Hemisphere stations which will be investigated further in the section below.

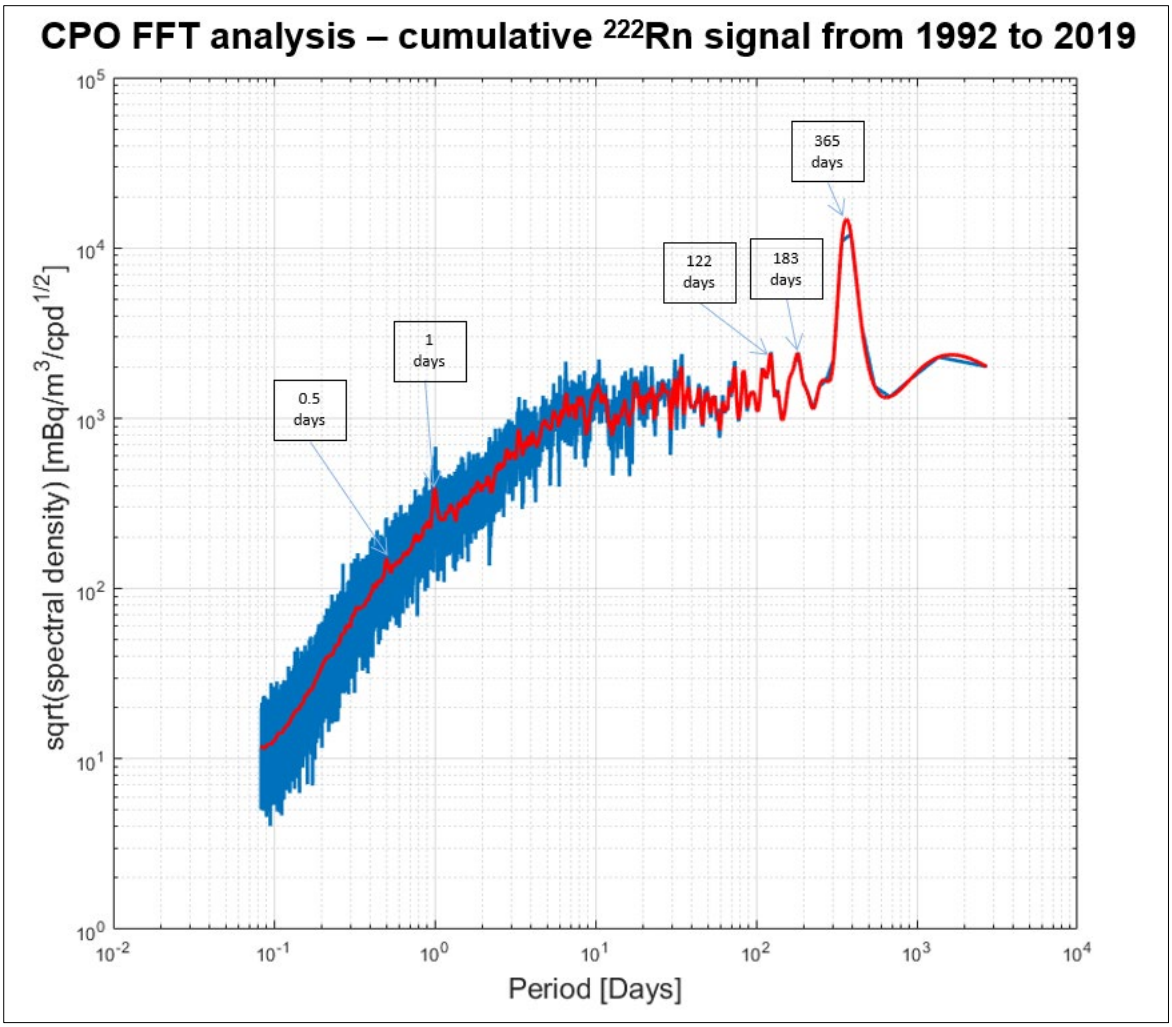

Figure 5-6: Power spectrum (amplitude) for the cumulative 19-year CPO radon signal using FFT analysis (cpd, counts per day). The blue-line represents the raw power spectrum and the red-line the smoothed spectrum processed using Savitzky-Golay digital filtering.

The inter-annual power spectrum density (PSD) plot focusing on multi-day timescales (see Figure 5-7) conclusively confirms the diurnal and half-diurnal spectral peaks. The strong inter-annual diurnal signal, 1.03 ± 0.04 day^{-1}, is evident for all of the years in the CPO radon time-series (1999 to 2017) apart from 1999 and 2008 (see Figure 5-7, upper). It is probable that during 2008 a drifting of about 0.3 day^{-1} for the diurnal and half-diurnal occurred. The half-diurnal peak, 2.07 ± 0.15 day^{-1}, is not as strong as the diurnal amplitude; but its existence is evident. The dual diurnal (0.5 and 1 day) periodicity peaks jointly reflect the effect of local

nocturnal terrestrial radon build-up, potentially modulated by the interplay between mesoscale marine/continental breezes. It has been established that the nocturnal terrestrial radon build-up leads to a ramp-shaped diurnal radon structure (Chambers et al., 2011; Williams et al., 2009). The occurrence of ramp-shaped structure in the diurnal radon signals is confirmed in Figure 5-7 by the presence of secondary peaks at integer fractions of the main peak. Interestingly, when a skewed sine wave of period 1-day pattern is repeated frequently enough in a radon signal (see Figure 5-1), the results of performing an FFT analysis will be spectral peaks at multiplies of the diurnal periodicity.

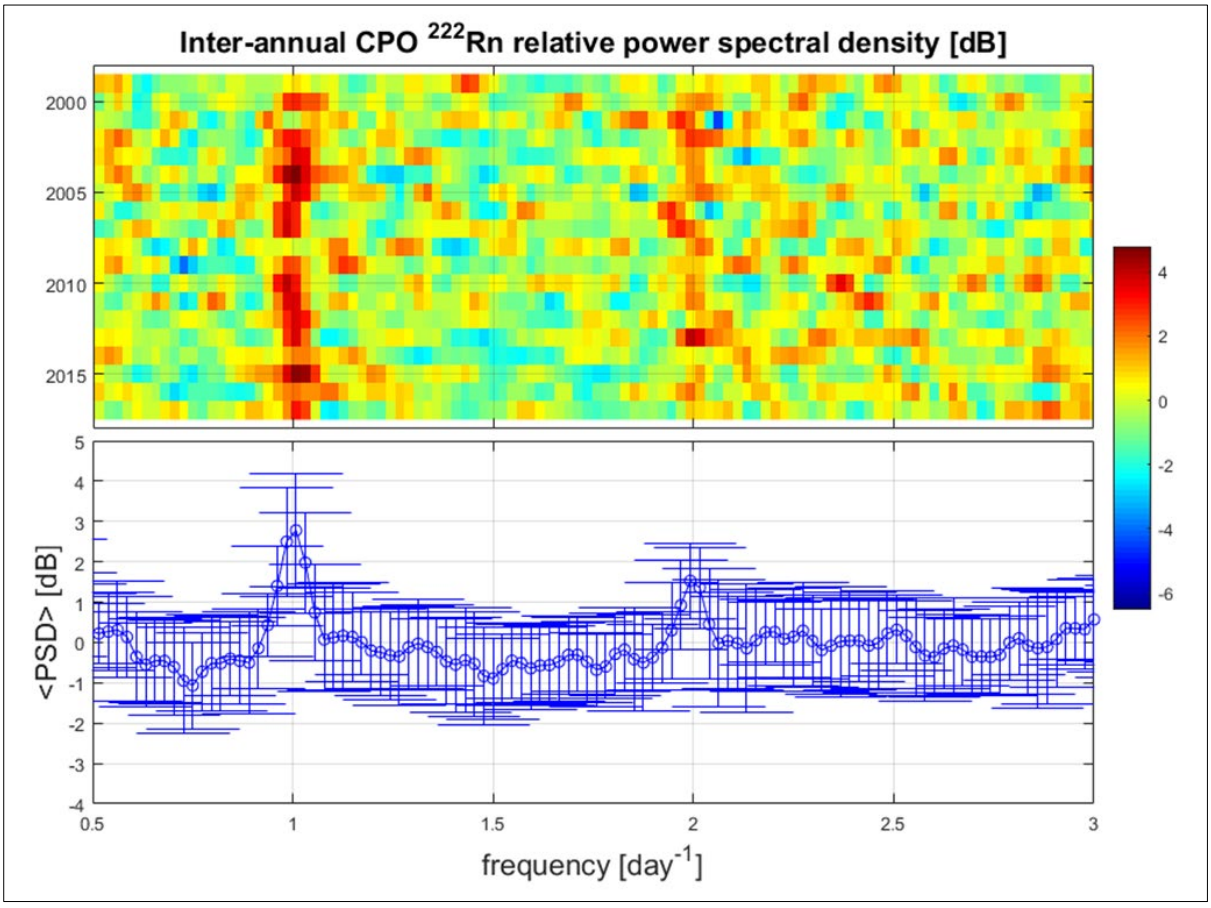

Figure 5-7: The relative inter-annual CPO atmospheric radon power spectral density (PSD) from 1999 to 2017 (upper) and the averaged PSD for the same period (lower) with associated standard deviation.

By making use of the FFT analysis results performed on the cumulative MLO radon signal multiple diurnal and annual periodicity peaks are identified (see Figure 5-8). The four diurnal periodicity peaks identified are the quarter-diurnal (0.25 day), third-diurnal (0.33 day), half-

diurnal (0.5 day), and, finally the diurnal (1 day, See Figure 5-8). An annual periodicity integer group is visible. The annual amplitude (365 day) is weaker compared to the half-annual amplitude (183 day) which is different compared to the results of both CGO (see Figure 5-4) and CPO (see Figure 5-6). Although the overall MLO radon variance pattern is similar in shape to both CGO (see Figure 5-4) and CPO (see Figure 5-6) it is much weaker in amplitude across the whole spectrum (a factor of 10), likely due to the geographical position of MLO in the lower troposphere (high altitude) on a remote island in the tropics, a long distance from any nearby continental land mass. It is challenging to qualitatively identify the annual periodicity by searching for the cyclic inter-annual maxima and minima in the MLO radon time-series plots (see Figure 5-1 and Figure 5-2, A5). This emphasises the usefulness of making use of FFT analyses to identify obscured atmospheric radon periodicity structures. A full family of the low variance annual periodicity structures can be identified in the MLO power spectrum, namely the quarterly-annual, third-annual, half-annual and annual (see Figure 5-8).

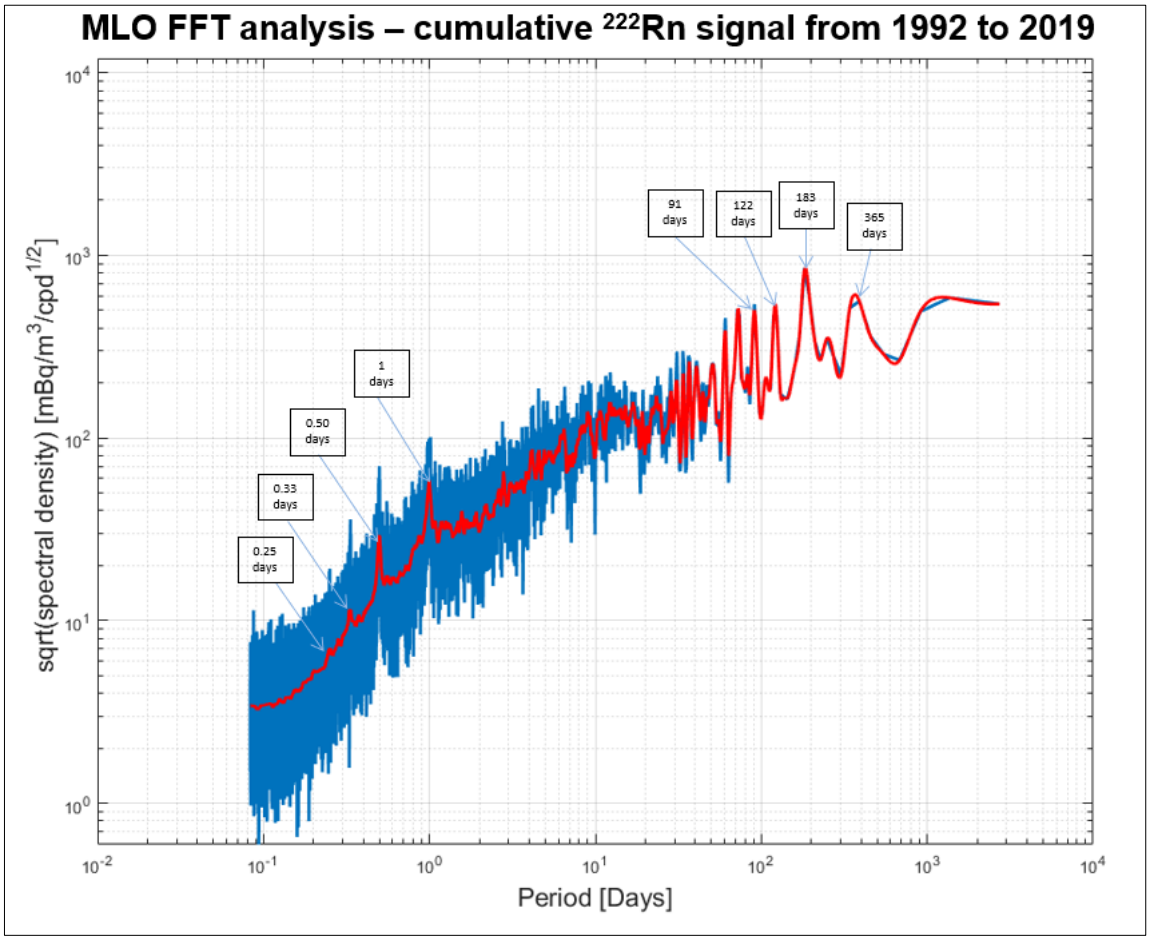

Figure 5-8: Power spectrum (amplitude) for the cumulative 12-year MLO radon time-series using an FFT analysis (cpd, counts per day). The blue-line represents the raw power spectrum and the red-line the smoothed spectrum processed using Savitzky-Golay digital filtering.

A comprehensive range of strong diurnal periodicity peaks are observed in the inter-annual MLO PSD results (see Figure 5-9). The periodicity signals detected beyond the measurement uncertainty band are the quarter-diurnal (4.01 ± 0.21 day^{-1}), third-diurnal (3.01 ± 0.11 day^{-1}), half-diurnal (2.01 ± 0.07 day^{-1}), and diurnal (1.01 ± 0.01 day^{-1}). The diurnal, half-diurnal and third-diurnal periodicity peaks are strong (see Figure 5-9, lower) and consistent with almost no inter-annual drifting (see Figure 5-9, upper). There is also some evidence of smaller quarter-diurnal (4 day^{-1}) and fifth-diurnal (5 day^{-1}) peaks, although the latter cannot be conclusively identified above the measurement uncertainty (see Figure 5-9).

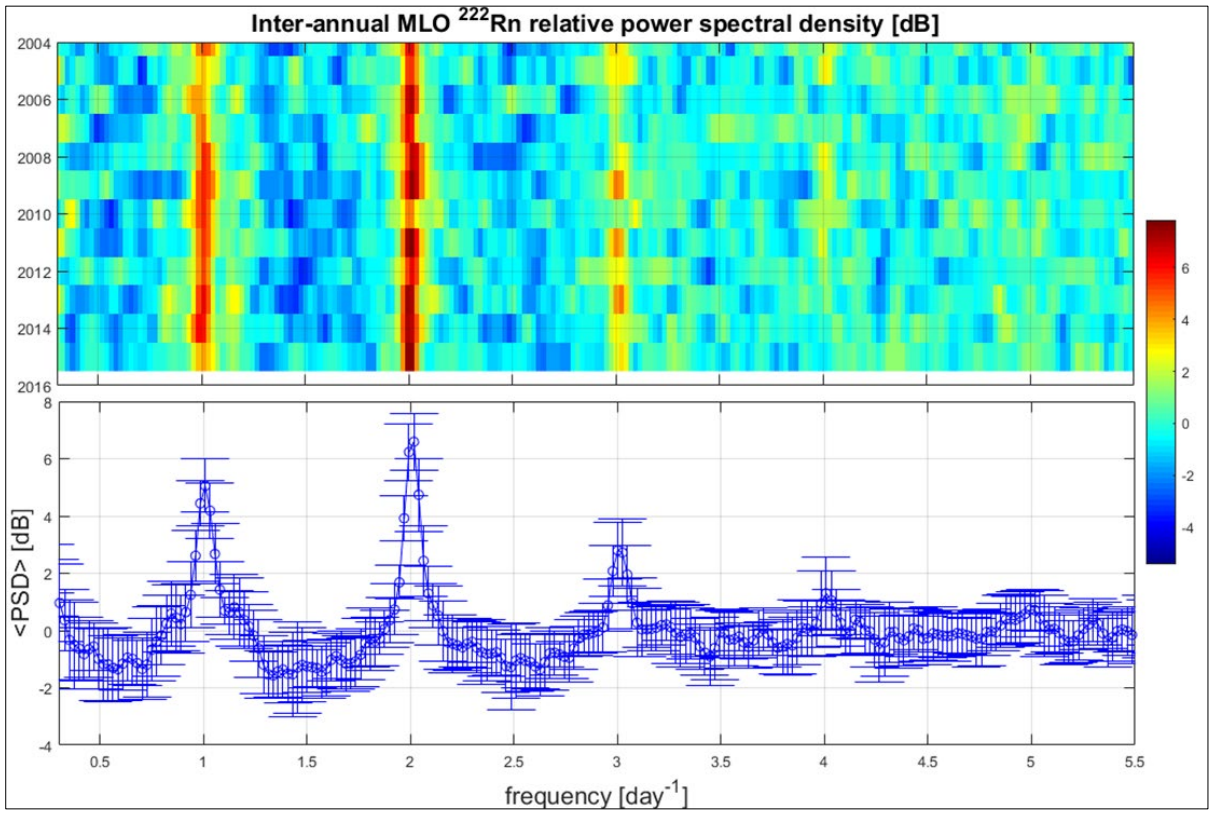

Figure 5-9: The relative inter-annual MLO atmospheric radon power spectral density (PSD) from 2004 to 2015 (upper) and the averaged PSD for the same period (lower) with associated standard deviation.

The differences in spectral analysis results between the two Southern Hemisphere (SH) sites (CGO and CPO) will be discussed in further detail. Most prominent is the family of diurnal periodicities that are identified at CPO but not at CGO (see Table 5-3). It is improbable that the radon signal will be a pure sine function and is one of the key reasons why the family of diurnal periodicities (specifically the harmonic peaks at 2 and 3 day^{-1}) appear in the FFT signal. The diurnal CPO peaks are due to the combined effects of nocturnal terrestrial radon build-ups

and interactions between mesoscale marine/continental breezes. Other key points to take into consideration are the difference in climatology and terrestrial fetch regions between these two stations (see Figure 4-2). The important terrestrial fetch regions at CGO are, directly, the island of Tasmania (see Figure 4-5, SGO – S2) and, indirectly, the Australian continental mainland (see Figure 4-5, SGO – S4), with the latter being separated from the station by a significant body of water (Bass Strait). Cape Grim's location with the ocean on 3 sides (170° - 360° and 0° - 90°), combined with its latitudinal positioning in strong westerly winds for much of the year, results in very few local influences associated with the Tasmanian landmass which manifest the diurnal timescales (such as sea/land breezes and nocturnal stable boundary layers). On the other hand, CPO has a direct single terrestrial fetch region (see Figure 4-9, CPO – S2), the continent of Africa, and is strongly influenced by coastal sea-breezes and downslope mountain flows. Furthermore, CPO is positioned in a mid-latitude belt characterised by strong synoptic weather systems. This produces a large variability in the wind direction and strength experienced at the station, allowing the opportunity for mesoscale flows to developing when synoptic winds are favourable.

In contrast to the lack of a diurnal component of variability at CGO, it is noted that CGO displays more seasonal variability compared to CPO. By comparing Figures 5-6 and 5-8, it can be seen that, although the annual (365 days) peak is the strongest at both CGO and CPO, the spectral density is generally higher at CGO for all timescales >10 days. In addition, CPO does not exhibit the decisive quarter-annual peak seen at CGO (Figs 5-6, 5-8 and Table 5-3), and the overall maxima and standard deviation statistics are greater for CGO than CPO (Table 5-1). These differences may be attributed to a number of factors, including:

(1) The exact positioning of the two stations to the south of longitudinally wide (CGO) and narrow (CPO) major landmasses. In the presence of synoptic variability, the position of CGO allows for a greater opportunity for the air-masses incident at the station to have travelled over the Australian continental mainland in their recent history. In contrast, the African mainland subtends a much smaller angle to CPO.

(2) Variations in the regional and hemispheric seasonal atmospheric circulations leading to seasonal changes in offshore (higher in atmospheric radon) versus onshore flow (lower atmospheric in radon) incident at the two stations. The variation in seasonal circulations are due to influences of ocean currents on the regional meteorology and south Atlantic pressures systems driving local meteorology

(3) Possible differences in radon emissions from the different continental regions such as Tasmania, Australian mainland, Southern Africa.

Further, it is evident that there is a difference for the radon periodicity structures when comparing the results of CPO and CGO to MLO (see Table 5-3). The most notable difference is that MLO, in general, has several more periodicity structures. Of these structures, the third-diurnal and quarter-diurnal occur only at MLO. These variances may be attributed to a number of factors, including:

(1) MLO is a high-altitude mountainous station, (see Table 4.1) which is about 3100 m higher than CPO or CGO.

(2) MLO is located inland, almost central on the Mauna Loa island on an upper mountain flank (see Figure 4-14) and as a result, it is subjected to stronger daily mesoscale offshore (land breeze occurring during the night, katabatic wind) and onshore (sea breeze occurring during the day, anabatic winds) flow. At island altitude sites, anabatic (upslope) winds and a sea breeze combine to bring air from the lower levels up to the observatory, and the inverse occurs at night, bringing free tropospheric air from aloft after the inland residual layer has been flushed (Lesouëf et al., 2011). The diurnal effect has been investigated and will be discussed in further detail in Section 5.3.2.

Collective FFT analysis: full CGO, CPO and MLO radon signal								
Location	**Multiples of the diurnal periodicity structures**				**Multiples of the annual periodicity structures**			
	1/4 Diurnal, [4 days^{-1}]	**1/3 Diurnal, [3 days^{-1}]**	**1/2 Diurnal, [2 days^{-1}]**	**Diurnal, [1 day^{-1}]**	**1/4 Annual, [91 days]**	**1/3 Annual, [122 days]**	**1/2 Annual, [183 days]**	**Annual, [365 days]**
CGO					X	X	X	X
CPO			X	X		X	X	X
MLO	X	X	X	X	X	X	X	X

Table 5-3: Collective results of the diurnal and annual periodicity structures identified at CGO, CPO and MLO. The presence of the specified periodicity structure is marked by a X.

5.2.3. Seasonal Characteristics

In Section 5.2.3 the atmospheric radon signals are analysed on a monthly timescale. From analysing the radon signals on shorter timescales, it provides the advantages of being able to notice seasonal effects and to identify micro-temporal signatures. The first analysis step is to filter the entire radon signal into the 12 individual months of the year. This temporal filtering represents a cumulative overview of the radon distributions for a specific month of the year making use of the entire signal (see Figure 5-10 to Figure 5-12).

The inter-monthly CGO radon distributions are symmetrically arranged centred around June (see Figure 5-10). The distributions can be characterised by the annual maxima occurring during the turn of the austral Autumn to Winter, Jun (median: ~ 300 mBq/m^3), and minima during the turn of the austral Spring to Summer, December (median: ~ 100 mBq/m^3). The individual CGO monthly radon percentile distributions profile is strongly negatively skewed (see Figure 5-10). The data points between the 25th and 50th percentile have an average range of 276 mBq/m^3 (47 mBq/m^3 to 323 mBq/m^3) across all months. However, between 50th and 75th radon percentile the range is about 1178 mBq/m^3 (323 mBq/m^3 to 1501 mBq/m^3).

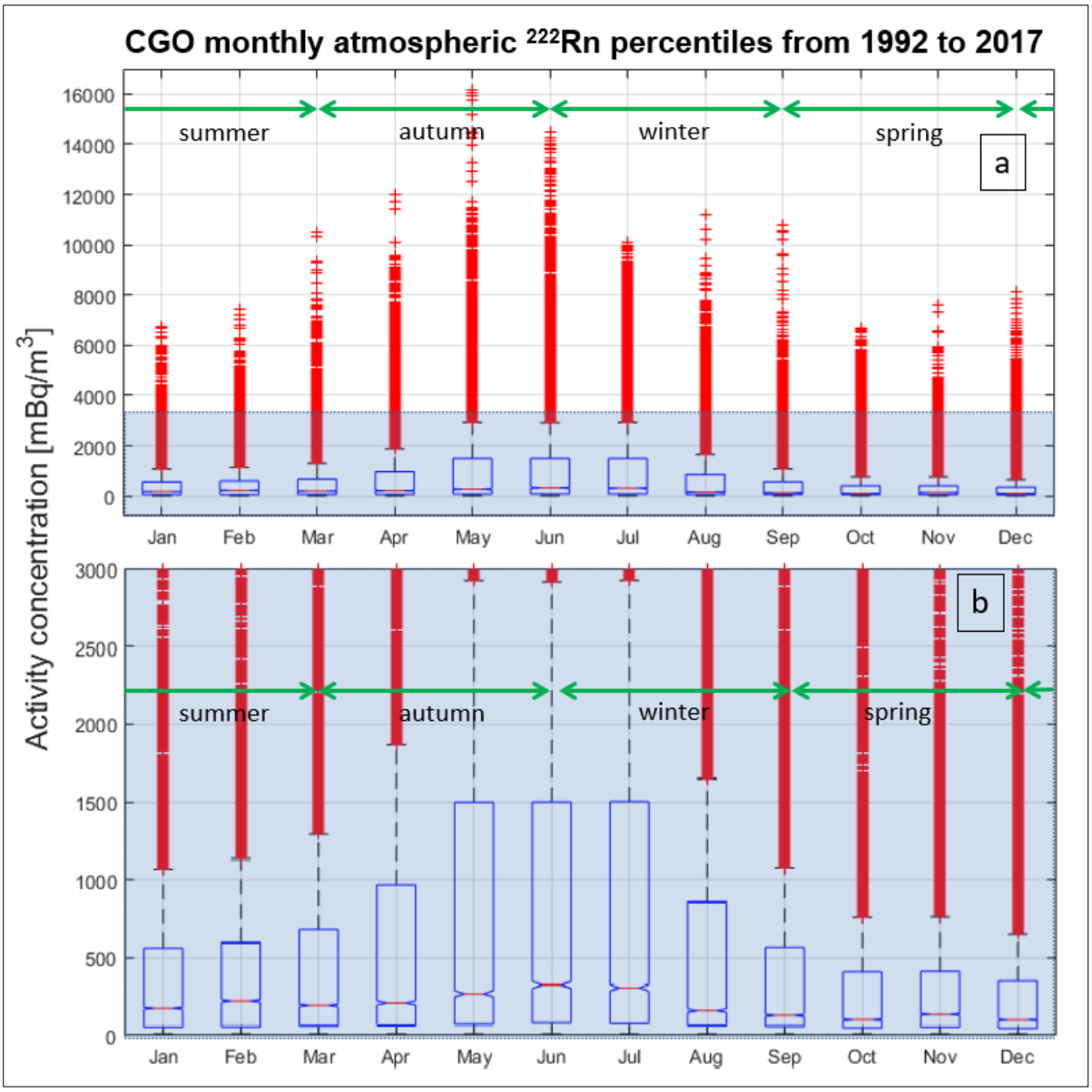

Figure 5-10: (a) CGO inter-monthly atmospheric radon activity concentration distributions from 1992 to 2017. The long-term radon distributions are characterised by the whiskers, bars and central horizontal line within the bars which refer to region of most extreme data points considered outliers (red+), 25th/75th, 50th (median) percentiles, respectively. (b) Selected inter-monthly percentile region of interest zoomed in from (a).

The CPO monthly atmospheric radon profile (see Figure 5-11, b) are similar to the CGO profile (see Figure 5-10, b) in several ways. The CPO inter-monthly radon percentiles composites are symmetrically distributed around June. The CPO inter-annual atmospheric radon composites are systematically the highest during the austral winter and the lowest from the end of Spring to the beginning of Summer (see Figure 5-11, b). The overall highest radon levels are associated with the month of July (median: 446 mBq/m^3) and lowest in January (median: 341 mBq/m^3).

During most of the months, the CPO atmospheric radon percentile distributions are strongly negatively skewed (March to October). For instance, the June radon levels between the 25th and 50th percentiles have a range of 352 mBq/m^3 (112 mBq/m^3 to 464 mBq/m^3) as opposed to between the 50th and 75th that has a range of 1165 mBq/m^3 (352 mBq/m^3 to 1517 mBq/m^3). However, the CPO radon percentiles become almost equally distributed for the months from November to January. It is noticed for both CPO and CGO that the monthly percentiles become more skewed as the atmospheric radon levels (median) increase. For instance, during the months (May to July) when the highest radon levels occur, the monthly distributions are correspondingly also the most skewed (see Figure 5-10, b and Figure 5-11, b). The higher radon levels are evident during the austral winter coinciding with the larger incidence of air-masses originating from a continental origin. The lower radon levels coinciding with summer is as a result of a higher incidence of marine air-masses. If the inter-monthly CPO radon distribution analysis is not performed (see Figure 5-11) and observations were made only from the cumulative radon signal (see Figure 5-3), the equal monthly distributions occurring from Nov to Jan would not have been transparent (see Figure 5-11).

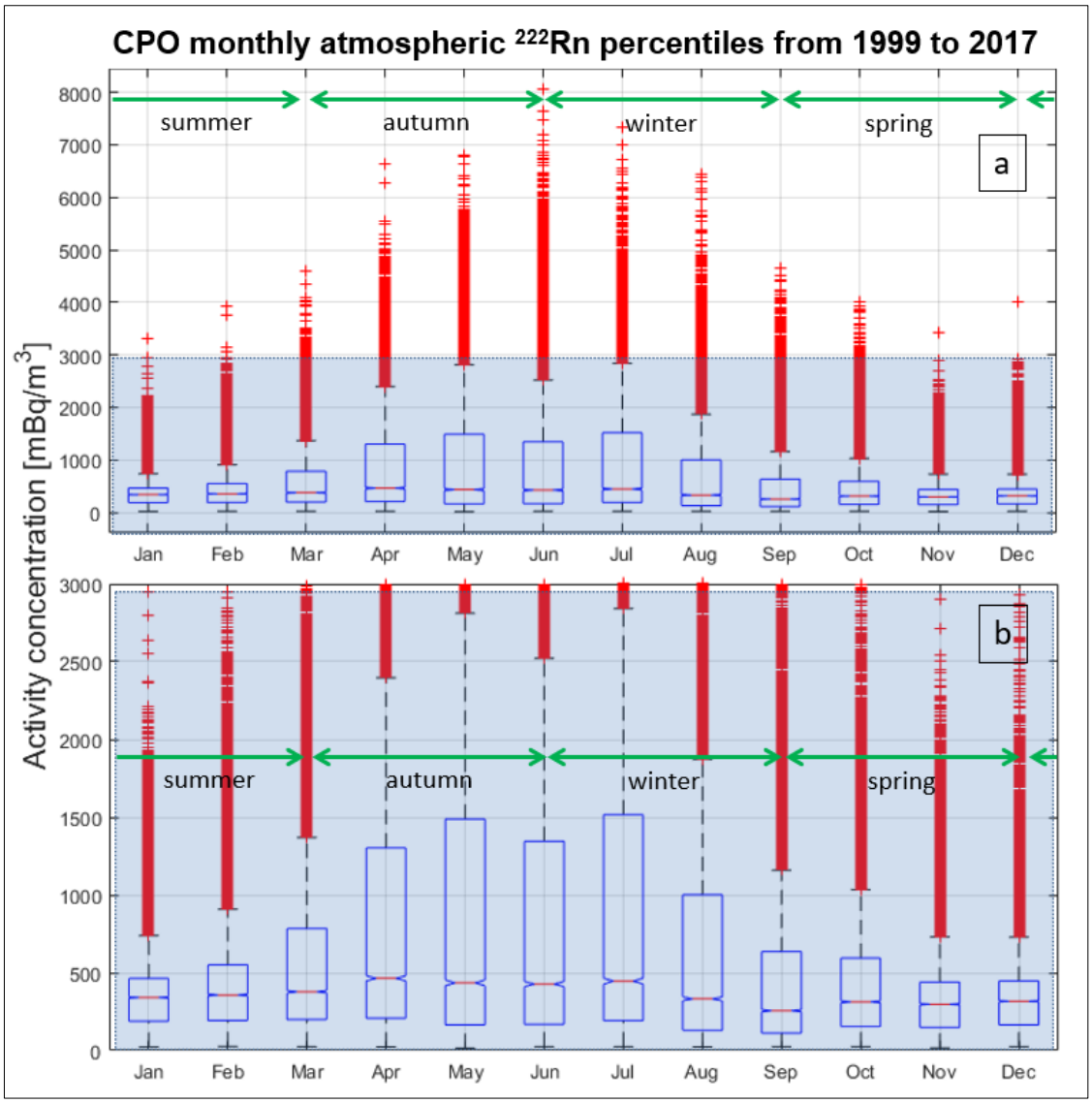

Figure 5-11: (a) CPO Inter-monthly atmospheric radon concentration distributions from 1999 to 2017. The long-term radon distributions are characterised by the whiskers, bars and central horizontal line within the bars which refer to region of most extreme data points considered outliers (red+), 25th/75th, 50th (median) percentiles, respectively. (b) Selected inter-monthly percentile region of interest zoomed in from (a).

The MLO monthly radon distributions show higher levels during the Northern Hemisphere winter and lowest during summer (see Figure 5-12, b). March is the month with the highest radon distribution (median: 135 mBq/m^3) and the lowest in June (median: 62 mBq/m^3). In general, the monthly radon distributions for MLO are systematically lower and less negatively skewed compared to that of CGO (see Figure 5-10, b) and CPO (see Figure 5-11, b). The symmetric distribution and lower radon percentile results from a higher incidence of marine air-masses (deep baseline).

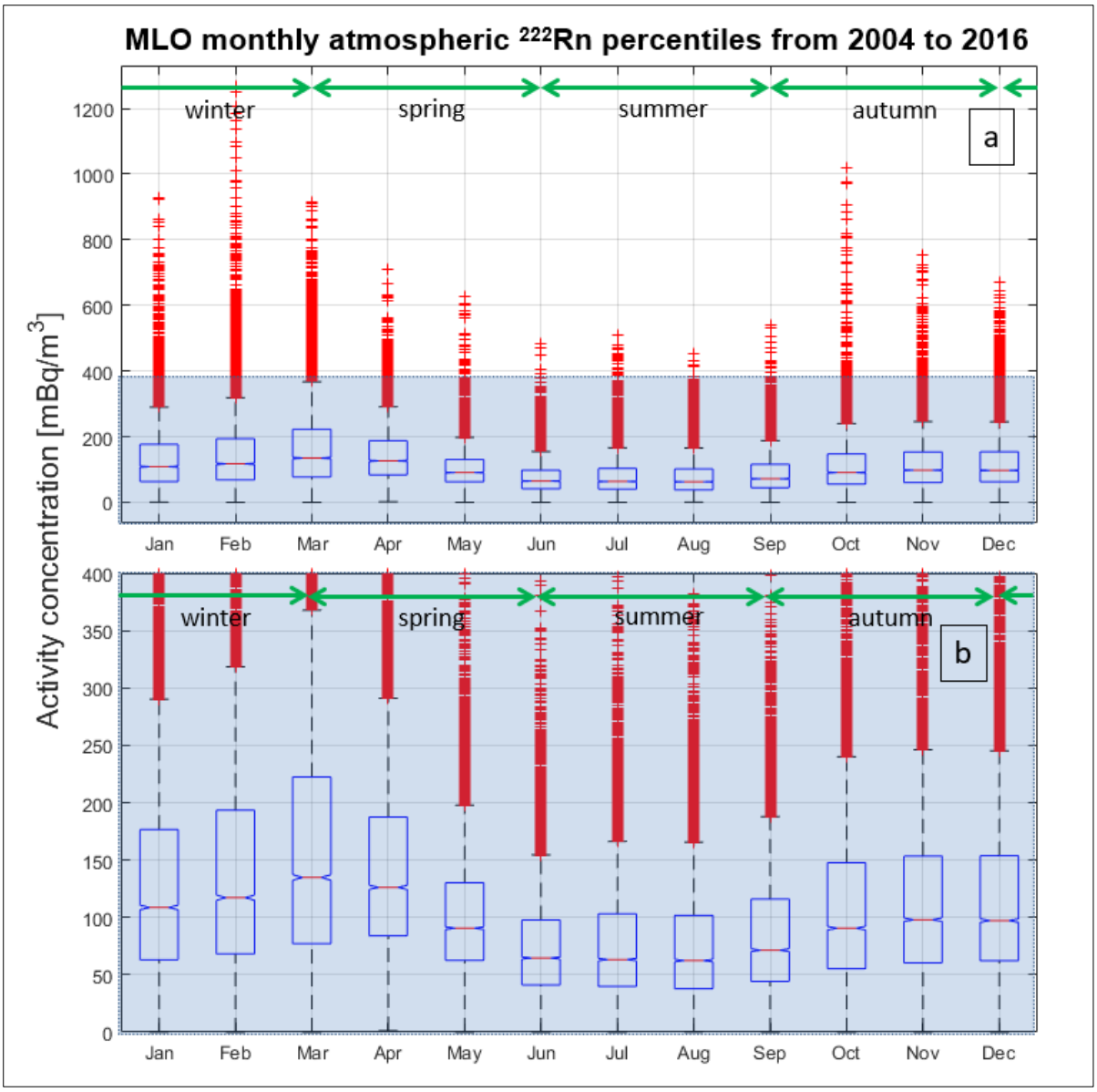

Figure 5-12: (a) MLO inter-monthly atmospheric radon concentration from 2004 to 2016. The long-term radon distributions are characterised by the whiskers, bars and central horizontal line within the bars which refer to region of most extreme data points considered outliers (red+), $25^{th}/75^{th}$, 50^{th} (median) percentiles, respectively. (b) Selected inter-monthly percentile region of interest zoomed in from (a).

The atmospheric radon distribution analysis is extended to an inter-annual monthly timescale (see Appendix Figure 8 to Figure 19). By performing the above-mentioned analysis, it enables one to observe how the atmospheric radon distributions temporally evolve inter-annually for a particular month. In general, for all the months the inter-annual variations are the most significant for the higher percentiles (see Appendix Figure 8 to Figure 19). The analysis will be utilised in conjunction with analysis yet to be presented.

5.2.4. Diurnal Characteristics

The diurnal radon characteristics are studied in Section 5.2.4. The aim of performing the diurnal analysis is to comprehensively analyse the radon signals' daytime vs night (nocturnal) variations. Radon diurnal signatures were first identified in Section 3.2.2 making use of spectral analyses methods. This finding shows the need for extending the diurnal analysis to greater detail. Diurnal radon analysis is utilised extensively to outline the atmospheric mixing state, which is closely related to atmospheric thermal stability (Chambers et al., 2015; Podstawczyńska & Chambers, 2018). Diurnal radon analysis distinguishes subtle changes in atmospheric mixing that makes it a powerful tool for studying air quality (Kikaj et al., 2020). Diurnal mixing patterns, as seen in the radon cycles, are directly linked to the capability of the atmosphere to dilute pollutants (Chambers et al., 2016).

The radon signals are transformed into daytime and nocturnal datasets by applying the following temporal filter (see Table 5-4). By using the Gregorian calendar, summer and winter solstice combined with sunlight refraction corrections the particular hours throughout the year which will be day or night depending on the time of year are identified (see Table 5-4). These temporal filters are utilised to generate the diurnal atmospheric radon signals. As mentioned previously, the radon measurement temporal resolution is hourly, and this was synchronised to the different hours of the day.

Location	Selected Annual Daylight Hours*	Selected Annual Night Hours*	Winter Solstice	Summer Solstice
CGO	08:00 - 17:00	21:00 - 05:00	22 June, 07:45 – 17:00	22 Dec, 5:47 – 20:53
CPO	08:00 - 18:00	20:00 - 05:00	22 June, 07:51 – 17:45	22 Dec, 5:32 – 19:57
MLO	07:00 - 18:00	19:00 - 05:00	22 Dec, 5:45 – 19:03	22 June, 06:52 – 17:50

Table 5-4: Temporal filters which are applied to generate the diurnal atmospheric radon time-series. *Hours of the day selected to generate the diurnal datasets. The time presented is in the various local times.

The cumulative CGO, CPO and MLO radon signals are presented according to the different hours of the day in Figure 5-13. The respective daytime and nocturnal radon signal will be generated from the regions of interest (ROI) in Figure 5-13, C and A. The diurnal radon signal (amplitude) for this thesis will be defined as the difference between the daytime and nocturnal radon signals. The hourly CGO and CPO radon signals are both characterised by a minimum during the early evening (18:00 – 20:00) when the lower atmosphere is most deeply mixed, and a maximum during late morning (10:00 to 11:00) when the lower atmosphere is likely at its shallowest. For the CPO and CGO 50th percentile (median), it is seen that CPO (~ 356 mBq/m^3) exhibits a larger diurnal amplitude range compared to CGO (~ 181 mBq/m^3) and an earlier morning maximum. These differences are likely related to geographical effects, as discussed in the spectral analysis (Section 5.2.2) which reported a strong CPO PSD diurnal peak (see Figure 5-7, lower) compared to the small peak of CGO (see Figure 5-5, lower).

In contrast to the two coastal stations, at the high-altitude northern hemisphere MLO island site, the diurnal radon cycles can be characterised by a minimum during the late morning (09:00 – 11:00) and a maximum during the late hours of the afternoon (16:00), with diurnal amplitude variations evident among all the percentiles. This observed radon cycle at the tropospheric MLO site is associated with a system of up/down-slope winds generated by the diurnal cycle of solar heating on the sides of the Mauna Loa volcano. Applicable to the median (50th percentile), the relative difference (factor) between the maxima and minima observed during the day (see Figure 5-13, section C) and night (see Figure 5-13, A) range with a factor of 2.6, 1.7, and 1.7 for CGO, CPO, and MLO, respectively. This factor serves as an indicator of how much larger the respective radon levels is observed during the day vs the night. The key difference between the CGO and CPO's diurnal cycle results compared to MLO are due to the following:

1. MLO radon observations are made above the boundary layer in the lower troposphere.
2. During the evening MLO are exposed to katabatic winds which are the flow of air down the slopes of the volcano. During the afternoon MLO is prone to be exposed to anabatic rising air.

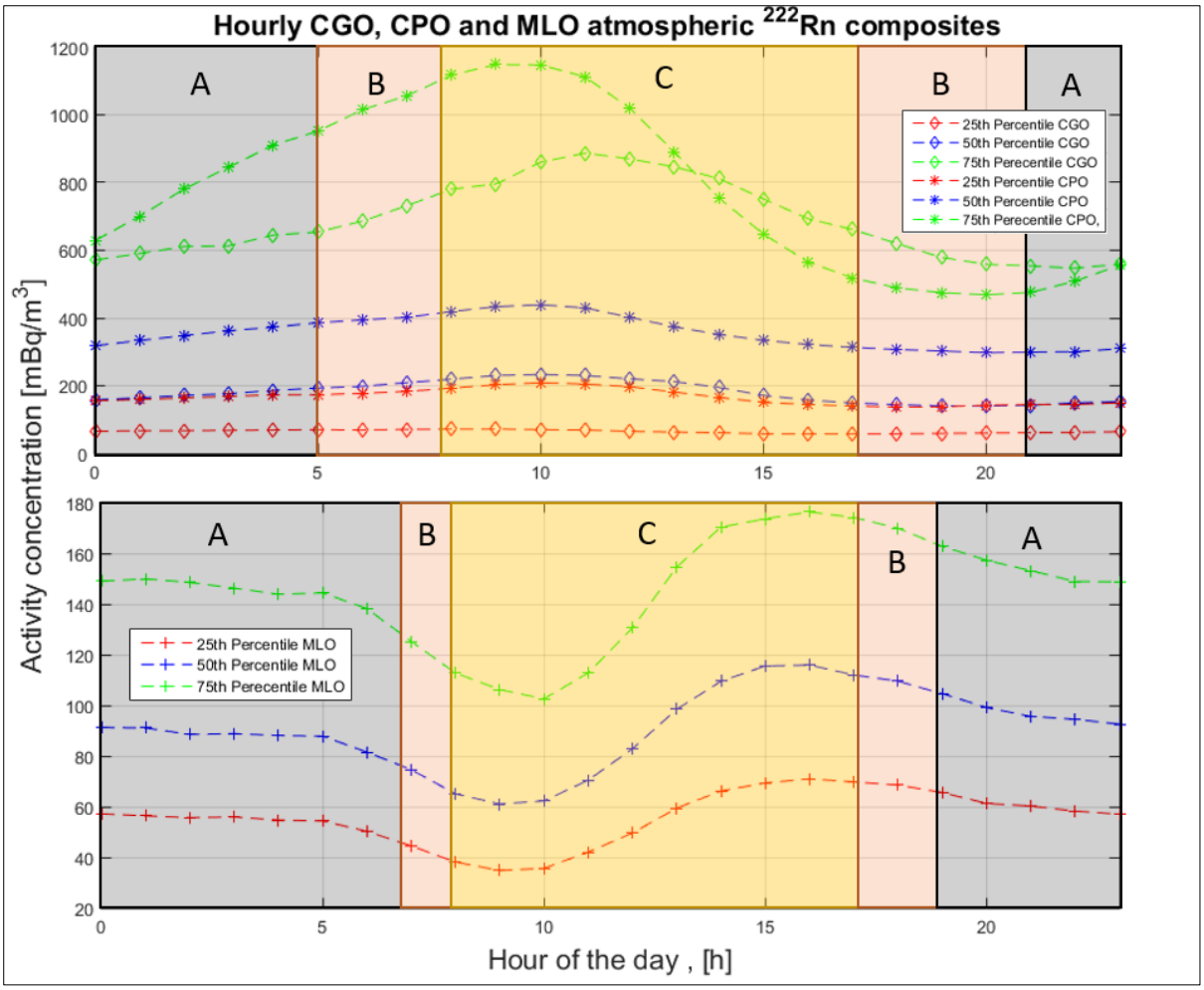

Figure 5-13: CGO, CPO and MLO atmospheric radon diurnal cycle composite analysis making use of the cumulative signals. The nocturnal sections of the day are indicated with a black shade (A), hours which can be either day or night depending on season with an orange shade (B), and the hours representing day are in yellow (C). The composite analysis is performed for the 25th, 50th (median), and 75th percentiles.

The radon time-series will now be studied by filtering the signals into "pure" nocturnal (night) and non-nocturnal (day) radon signals by making use of the results obtained from Table 5-4 and Figure 5-13. The cumulative CGO, CPO and MLO diurnal analysis are presented in Figure 5-14. The cumulative day or night radon signal is generated by selecting only the datapoints associated with hours occurring during night or day (see Table 5-4). The exact time of transition between night and day (sunrise and sunset) shifts continuously throughout the year, with longer days during the summers. A diurnal difference (amplitude) is defined as the difference (residual) between average radon values within the day and night (nocturnal) windows. As seen in Figure 5-13, the CGO and CPO atmospheric radon are higher during the day compared

to the night, especially for CPO (see Figure 5-14). Nevertheless, making use of the 25th CGO diurnal percentile, higher radon is observed during the night vs day (see Figure 5-14). MLO exhibits systematic higher radon exposure during the night compared to the day.

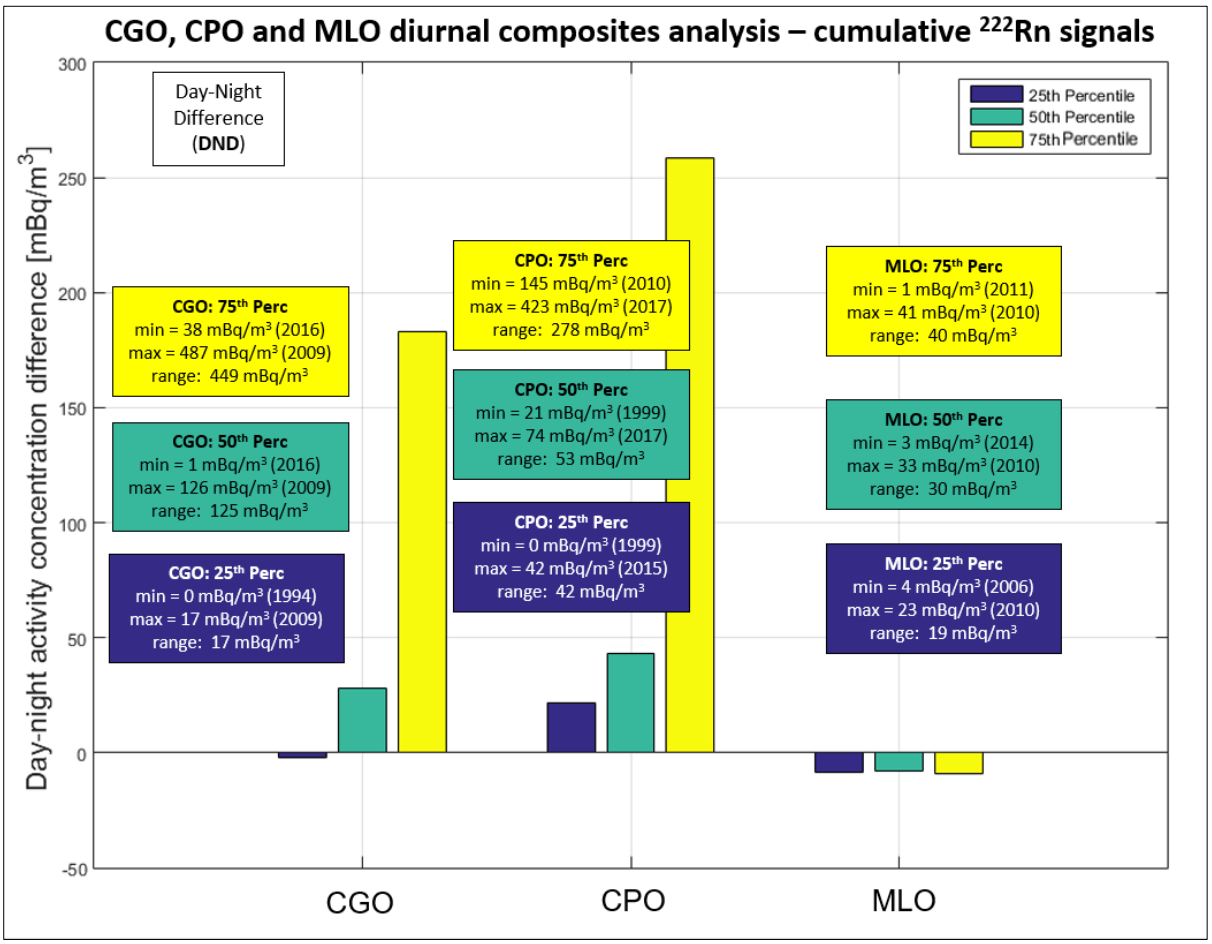

Figure 5-14: CGO, CPO and MLO atmospheric radon composite diurnal differences for the cumulative time-series filtered according to daytime or night-time. The composite analysis is performed for the 25th, 50th (median), and 75th percentiles combined with day-night difference statistics.

In the following section, aspects of the CGO, CPO and MLO diurnal radon signals will be studied on an inter-annual temporal scale (see Figure 5-15 to Figure 5-17). The aim is to identify long-term diurnal radon variations. It is once again evident that the day-time averages of the CGO and CPO radon composites are systematically higher compared to the nocturnal values (see Figure 5-15 and Figure 5-16). Inter-annual diurnal composite variations are apparent of which the most significant are for CGO (2016) and CPO (2017). The inter-annual atmospheric radon diurnal difference is larger for CPO (Figure 5-16, B) compared to CGO (see

Figure 5-15, B). The median is used to represent the bulk data of an associated parameter. The CGO median diurnal signal (see Figure 5-15, B) is fluctuating considerably more compared to CPO (see Figure 5-16, B). During some years the CGO diurnal median becomes almost zero, for example during 2003, 2006 and 2016 (see Figure 5-15).

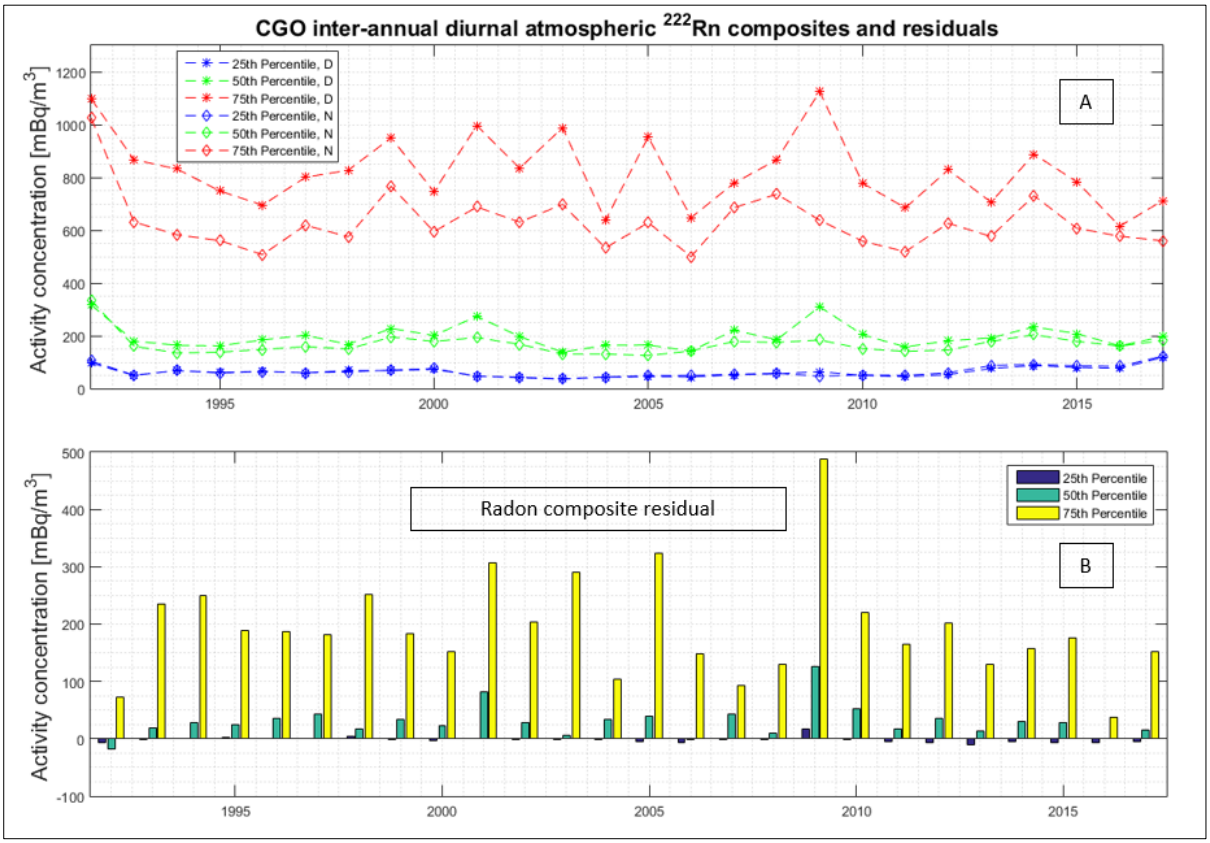

Figure 5-15: C CGO inter-annual atmospheric radon composite diurnal analysis. Average values across the Nocturnal (N) and day-time (D) composite windows are shown for the 25th, 50th (median), and 75th percentiles. (B) The associated day-time versus nocturnal radon composite differences (diurnal residual) making use of the results of (A).

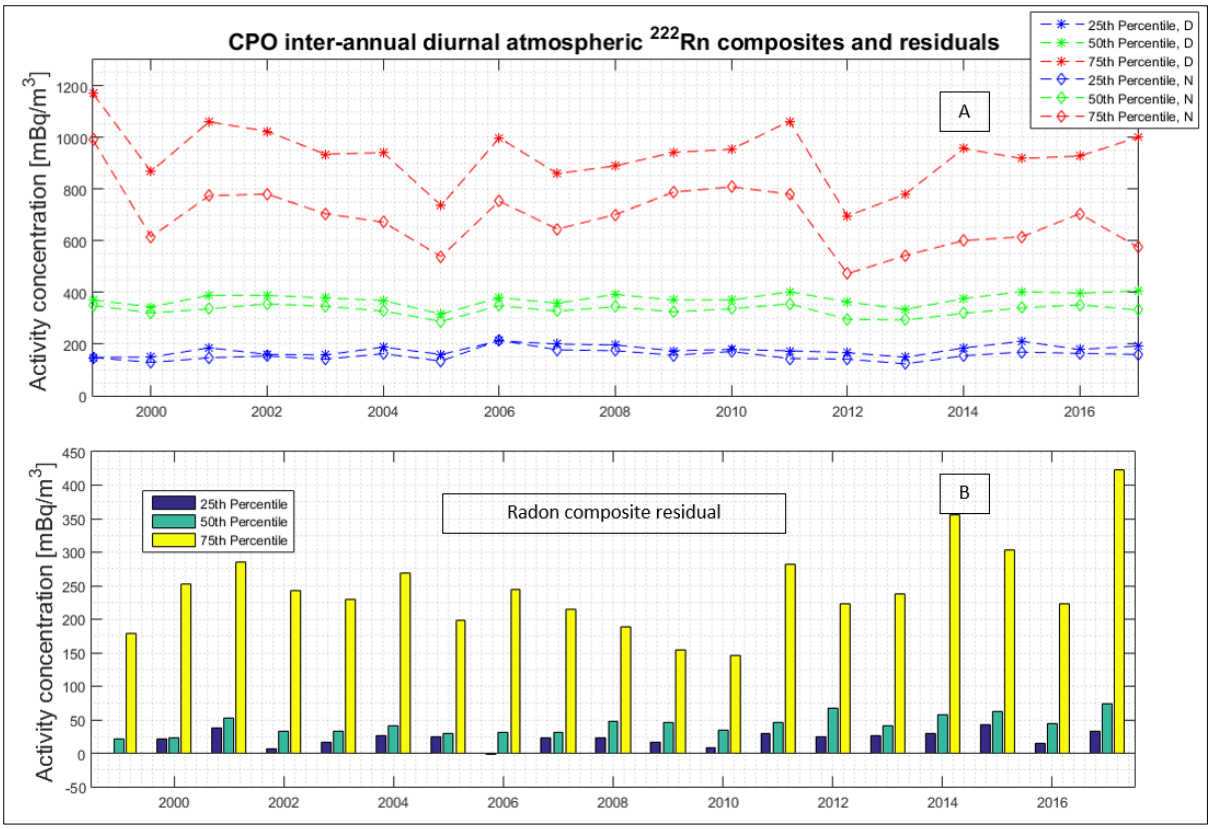

Figure 5-16: CPO inter-annual atmospheric radon composite diurnal analysis. Average values across the Nocturnal (N) and day-time (D) composite windows are shown for the 25th, 50th (median), and 75th percentiles. (B) The associated day-time versus nocturnal radon composite differences (diurnal residual) making use of the results of (A).

The median MLO diurnal radon cycle illustrated steady inter-annual variance apart from the peak during 2010 (see Figure 5-17, A). It will be noted that for the high-altitude MLO the nocturnal atmospheric radon is systematically higher than during the day-time. MLO's lower daytime-average radon values can be attributed to a high incidence of clean tropospheric air events in the period 07:00-12:00 (see Figure 5-13), when there is a lull in mesoscale circulation patterns between the cessation of radon-rich down-slope flows at night and up-slope flows in the afternoon (Chambers et cl. 2013).

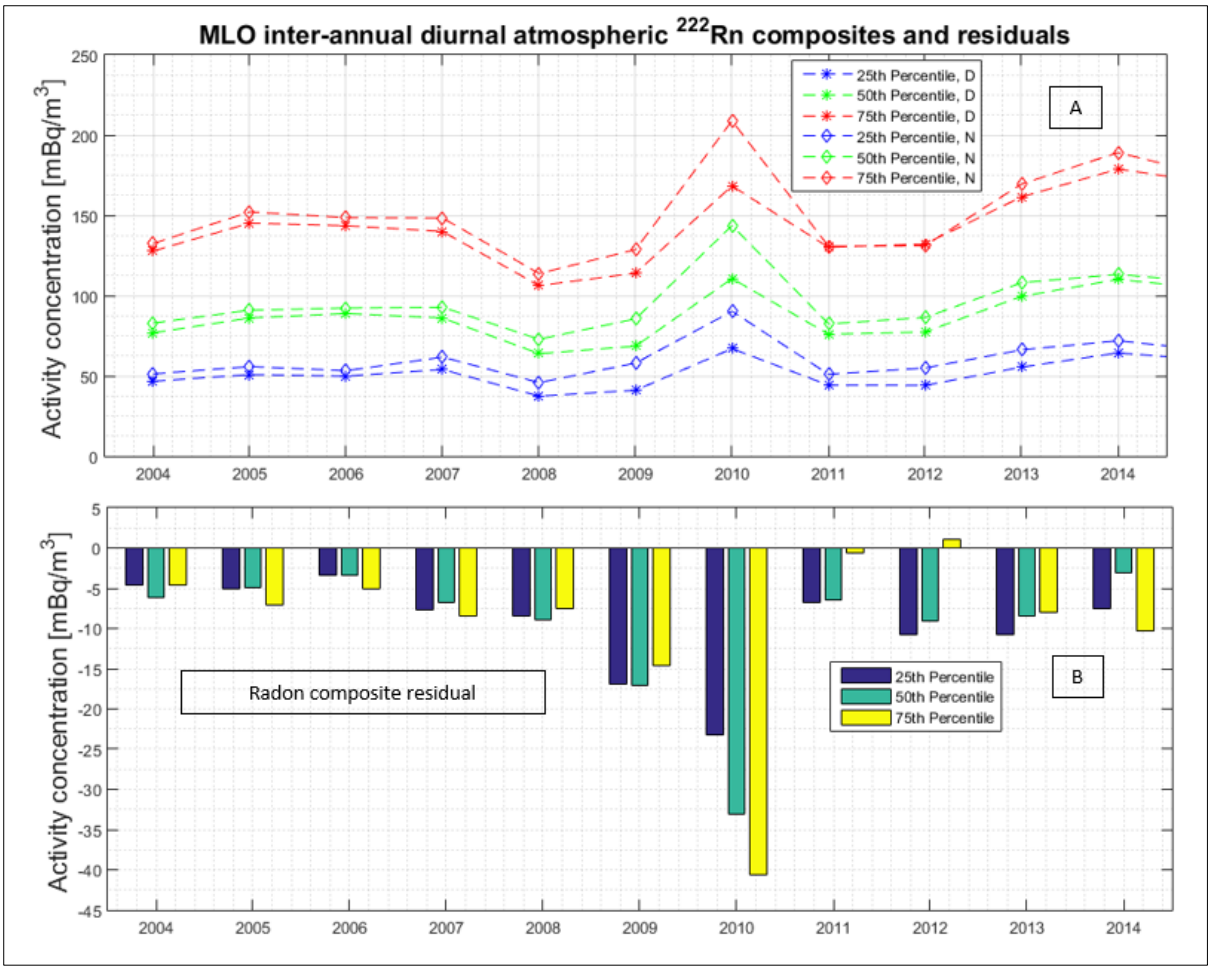

Figure 5-17: MLO inter-annual atmospheric radon composite diurnal analysis. Average values across the Nocturnal (N) and day-time (D) composite windows are shown for the 25th, 50th (median), and 75th percentiles. (B) The associated day-time versus nocturnal radon composite differences (diurnal residual) making use of the results of (A).

In the above, inter-annual variations in the respective day and night average atmospheric radon results were presented. As it is known that radon signals can also be used to illustrate key seasonal differences, in the following section a closer investigation will be made on the diurnal atmospheric results on a seasonal scale. The most prominent seasonal observation is that for both CGO and CPO the median radon diurnal differences (see Figure 5-18, b and d) are systematically higher during austral winter (JJA). Key differences in the diurnal seasonal components between CGO and CPO are a stronger CPO amplitude (~ 100 mBq/m^3) during Autumn and the absent lower 25th percentile difference at CGO. These differences may be attributed to several factors, including variations in atmospheric stability and mesoscale circulations.

Seasonal atmospheric radon diurnal variations are expected primarily due to change in mesoscale circulation changes throughout the year. For instance, summer has longer days compared to winter (see Table 5-4) resulting in larger temperature and pressure difference between the land and sea. Consequently, during the summer it is expected that stronger and longer mesoscale sea breeze occurs compared to winter. Similarly, for land breezes during the winter due to the longer nights.

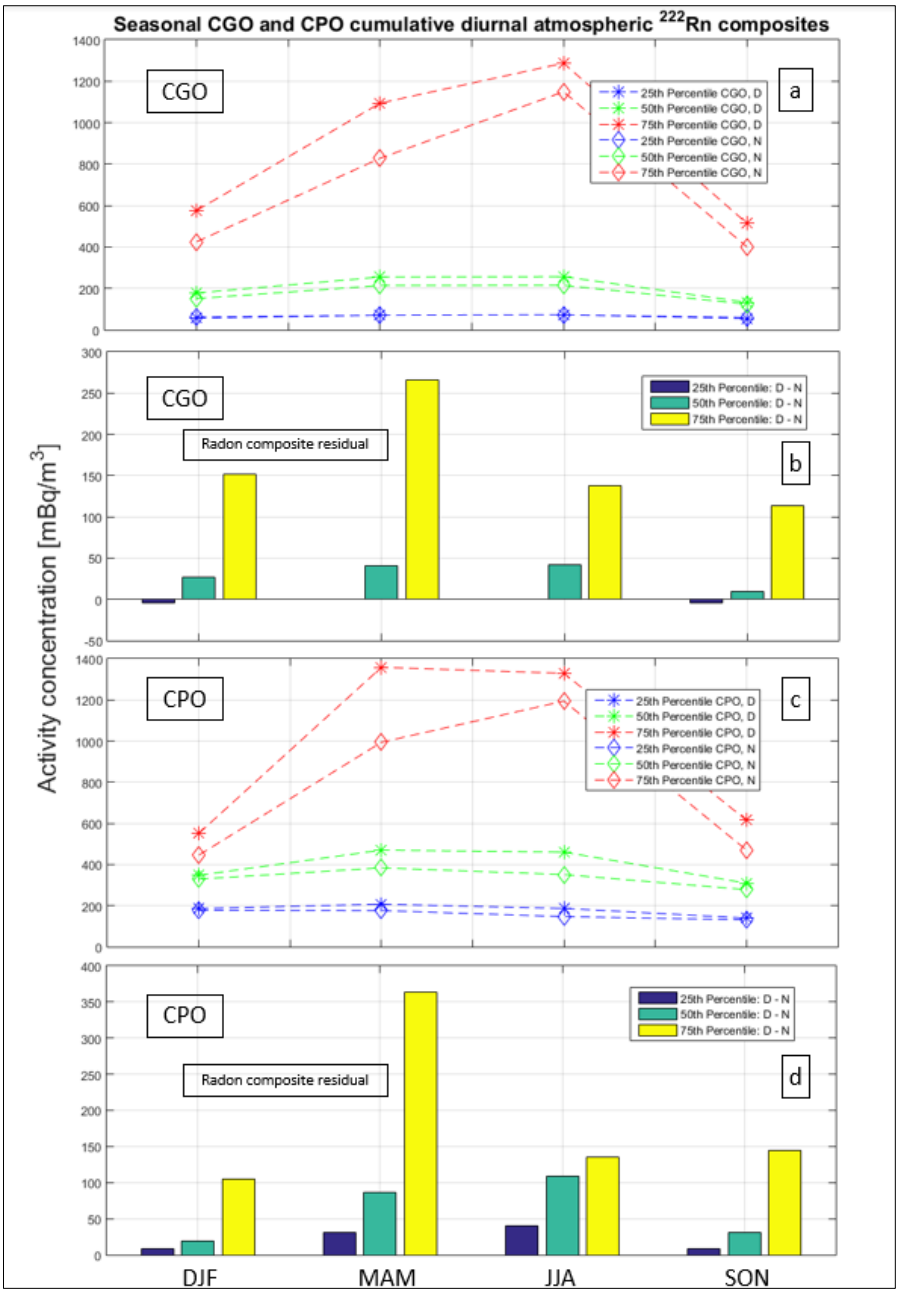

Figure 5-18: Cumulative CGO and CPO seasonal atmospheric radon composite diurnal analysis results (a and c). The total seasonal radon composite day-night differences are illustrated on b and d. Nocturnal (night, N) and daytime (D) composite analysis are performed for the 25th, 50th, and 75th percentiles.

The diurnal radon composite seasonal differences for MLO are in general smaller (see Figure 5-19) compared to either CGO or MLO. The long-term seasonal MLO diurnal differences, in general, is considerably smaller, for instance during winter (DJF), summer (JJA) and autumn (SON) with less than about 12 mBq/m^3.

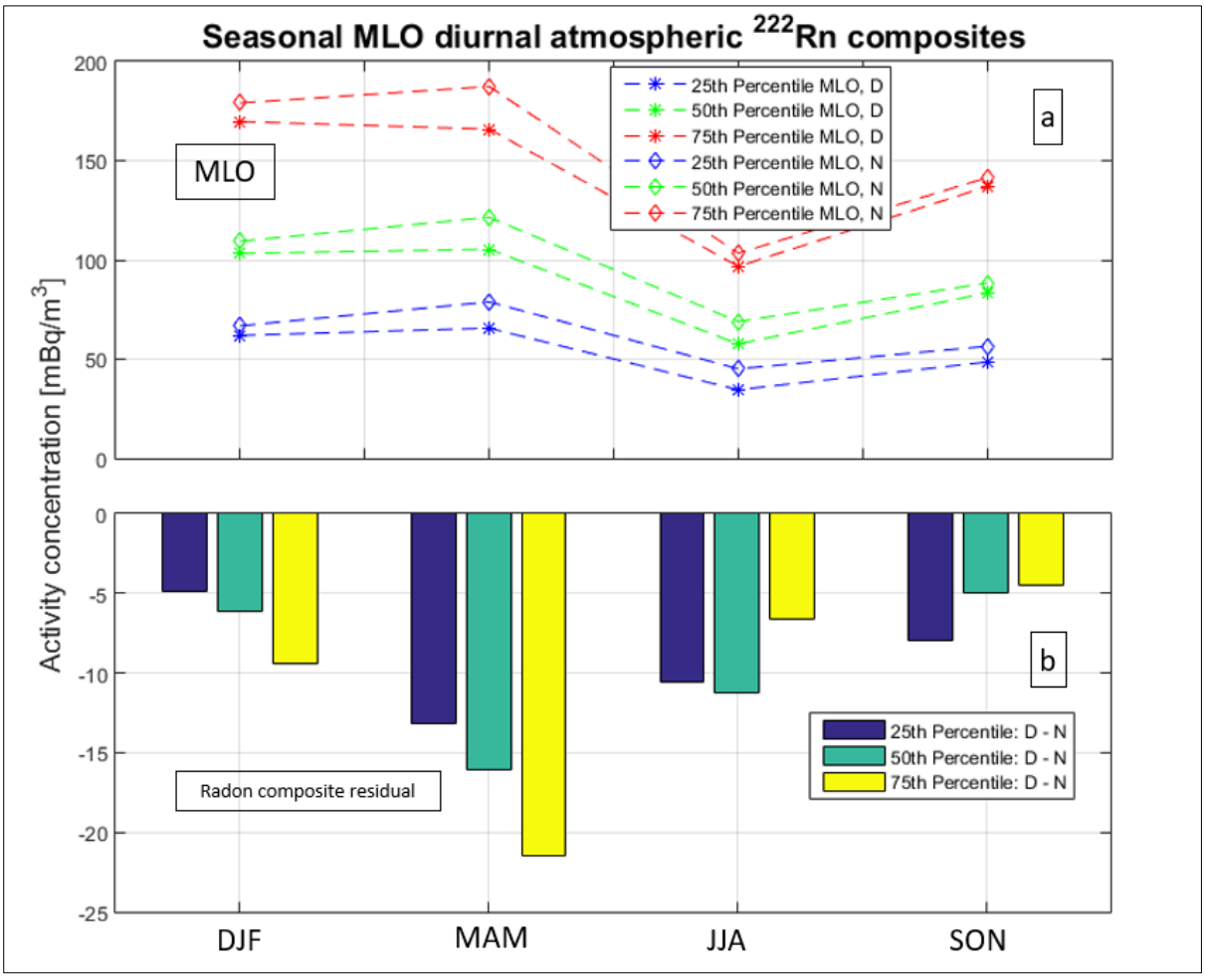

Figure 5-19: Cumulative MLO seasonal atmospheric radon composite diurnal analysis (a). The total seasonal radon composite difference between day and night are illustrated on b Nocturnal conditions (night, N) and daytime (D) composite analysis are performed for the 25th, 50th (median), and 75th percentiles.

The seasonal atmospheric radon diurnal analysis will be extended by performing the analysis on an inter-annual level. The inter-annual seasonal diurnal composite analysis results are presented in Figure 5-20 to Figure 5-22. Anomalies have become evident which was previously not transparent. These include a change in diurnal amplitude from positive to negative and rapid amplitude fluctuations. During the summer (1994, 2016) autumn (2016), winter (2016,

2008) and spring (2002, 2008) the change in amplitude polarity occurred at CGO (see Figure 5-20). Similarly, this has been observed at CPO (see Figure 5-21) and MLO (see Figure 5-22). These inter-annual seasonal diurnal anomalies are directly related to extreme seasonal shifts in the standard mesoscale circulations.

Seasons with a substantially weak to non-existent diurnal signal are identified. For instance, during the summer (2004), autumn (2012), winter (1999), spring (2004) associated with CGO. For CPO the diurnal weak diurnal signals are evident during the summer (2001), autumn (2010), winter (2007) and spring (1999 to 2011). A continuous long weak CPO diurnal signal occurred during the springs of 1999 to 2011 (see Figure 5-21). At MLO the weak diurnal signal is apparent especially during summer (2004) and spring (2000). CGO and CPO's cumulative seasonal diurnal signals are similar (see Figure 5-18). Nevertheless, key differences are transparent when observing the inter-annual seasonal signals (see Figure 5-20 and Figure 5-21). These differences include the anomalies occurring at CPO among all the seasons from 2012 onwards (see Figure 5-21). These anomalies are the strongest during the autumn and spring (see Figure 5-21, b and d).

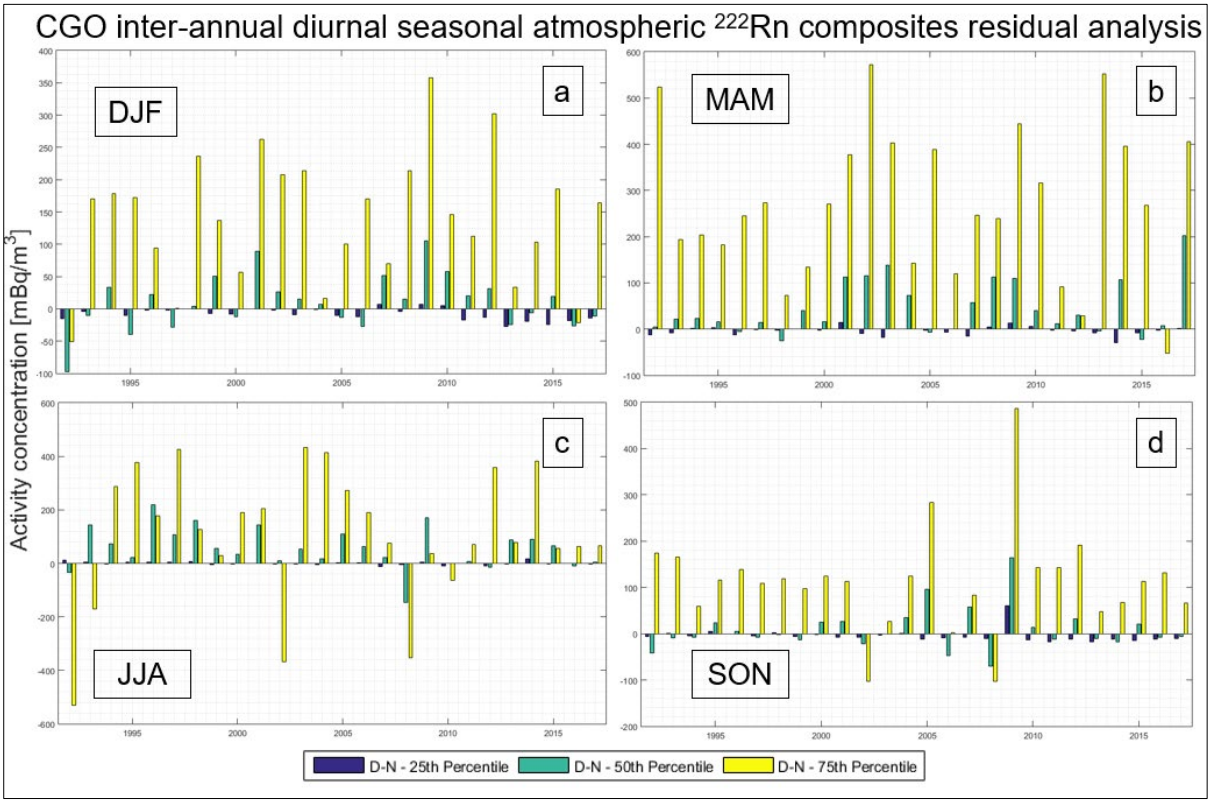

Figure 5-20: (A) CGO inter-annual diurnal radon composite residual analysis from 1992 to 2017 according to summer (DJF, a), autumn (MAM, b), winter (JJA, c) and spring (SON, d).

As discussed, several unique events are associated with CPO's inter-annual seasonal diurnal radon composite residual: including:

(1) From 2012 to 2017 anomalies become evident for all of the seasons. These anomalies include strong diurnal amplitude fluctuations (see Figure 5-21) and, an amplitude polarity change during the summer (see Figure 5-21, d).

(2) From 1999 to 2012 during summer a weak diurnal signal is clear among all percentiles.

(3) A strong diurnal inverse occurred during the winter of 2012 and possibly for 2013 (see Figure 5-21, c).

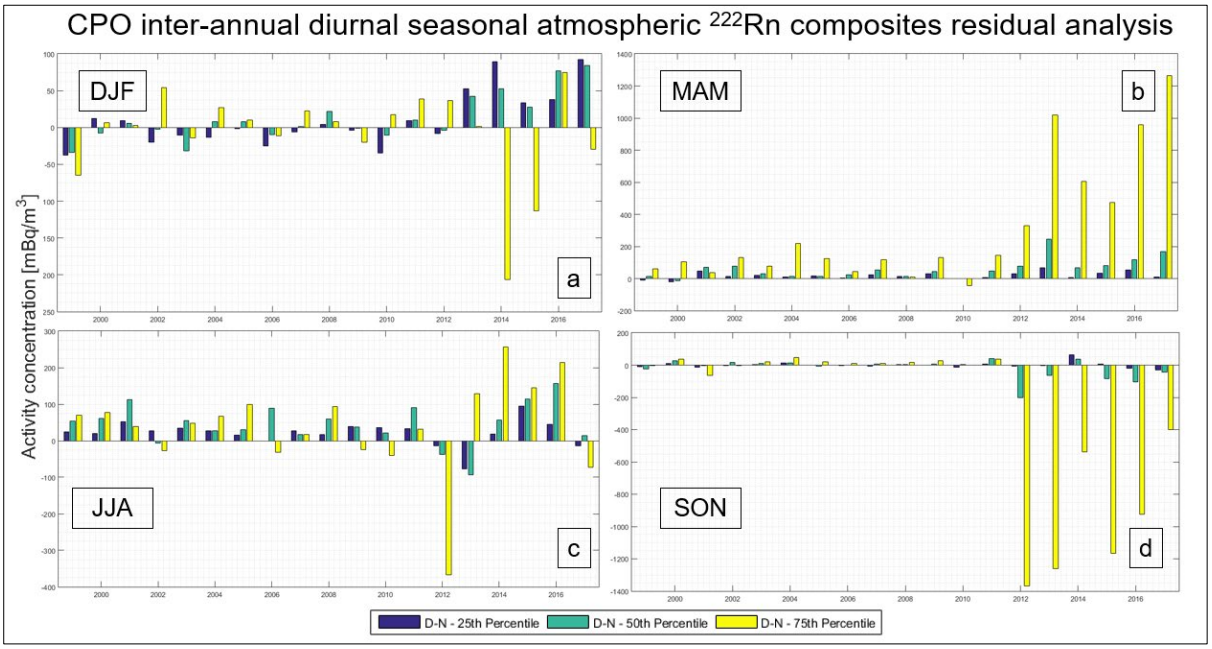

Figure 5-21: (A) CPO inter-annual diurnal radon composite residual analysis from 1999 to 2017 according to summer (DJF, a), autumn (MAM, b), winter (JJA, c) and spring (SON, d).

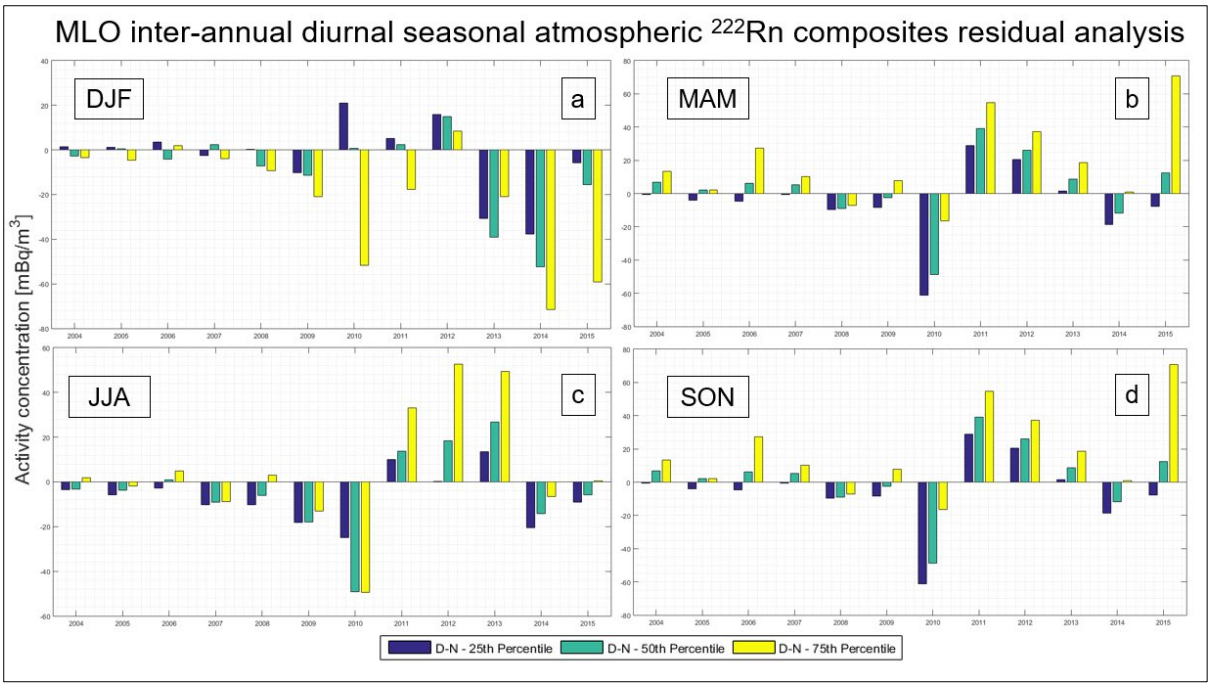

Figure 5-22: (A) MLO inter-annual diurnal radon composite residual analysis from 2004 to 2015 according to summer (DJF, a), autumn (MAM, b), winter (JJA, c) and spring (SON, d).

5.2.5. Meteorological Characteristics

The Southern Hemisphere CGO and CPO radon signals (1999 to 2017) are characterised and investigated in conjunction with the meteorological measurements performed on-site at the respective observatories (see Chapter 4). The CGO radon time-series spans from 1992 onwards, CPO radon measurements commenced in 1999. As a result, for CGO and CPO, the CGO signal is filtered to be from 1999 to 2017, to ensure a temporal overlap occurs with that of CPO.

The CGO and CPO radon signal analysis according to the on-site measured wind direction (WD) are illustrated in Figure 5-23. The elevated CGO radon composites (median > 1100 mBq/m^3) are directly associated with air-masses likely to be originating from continental fetch regions (see Figure 4-5). The lower CGO radon composites (median < 1000 mBq/m^3) are correlating with the WD fetch region associated with the Southern Ocean (see Figure 5-23, upper, O1). An increase observed at CGO of about 500 mBq/m^3 among the 50th and 75th percentiles are associated with the WD fetch sector, 100° < WD < 150°, originating from terrestrial Tasmania (C2).

The largest CGO radon composites increase according to when WD is from 260° to 360° associated with mixed air-masses originating from the Australian mainland (see Figure 5-23, C1). For instance, for the 95th percentile, an increase within this WD sector of about 60 mBq/m^3 per WD degree (clockwise) is observed. Within the marine WD sub-sector, 220° to 250°, the average CGO radon composites levels for the 95th, 75th, 50th, 25th, and 5th percentiles are 510 mBq/m^3, 98 mBq/m^3, 60 mBq/m^3, 37 mBq/m^3 and 11 mBq/m^3, respectively. In general, the 95th radon percentiles will be referred to as an elevated radon composite which most likely is mixed or continental air-masses.

CPO's air-mass fetch regions can be characterised by two distinct groups (see Figure 4-9), the African continent (C3) and marine fetch region (O3) namely the Atlantic and the Indian Ocean (Southern Ocean). Similar to CGO, the highest CPO radon percentiles are observed for WD fetch regions associated with continental origin (339° to 115°) and lowest from the marine regions (115° to 339°). A moderate decrease among the 95th and, 75th CPO radon percentiles are observed within the continental region from 60° to 75°, C3 (see Figure 5-23). This decrease is associated with False Bay to the east of CPO (see Figure 4-7, a). An odd peak on the 50th, 75th and 95th CPO radon percentiles are observed at 150° which is associated with a marine fetch region (Atlantic Ocean). The CPO WD sector prone to contain baseline events is between 190° to 250° (see Figure 5-23, O3) based on the lowest radon levels.

Air-masses move in three-dimensional spatial trajectories with time-dependent non-linear motion. Consequently, WD detected at the observatories is not necessarily a true indicator of the back-trajectory. The long-term results (see Figure 5-23 to Figure 5-25), however, show that the expected higher atmospheric radon levels originate from air-masses associated with continental fetch regions and the lower levels from the marine as expected. For this reason, the CPO and CGO radon time-series will be further studied by computing high-resolution back-trajectories to assign a secondary method to determine the air mass classification (HYSPLIT, see Section 3.4.3).

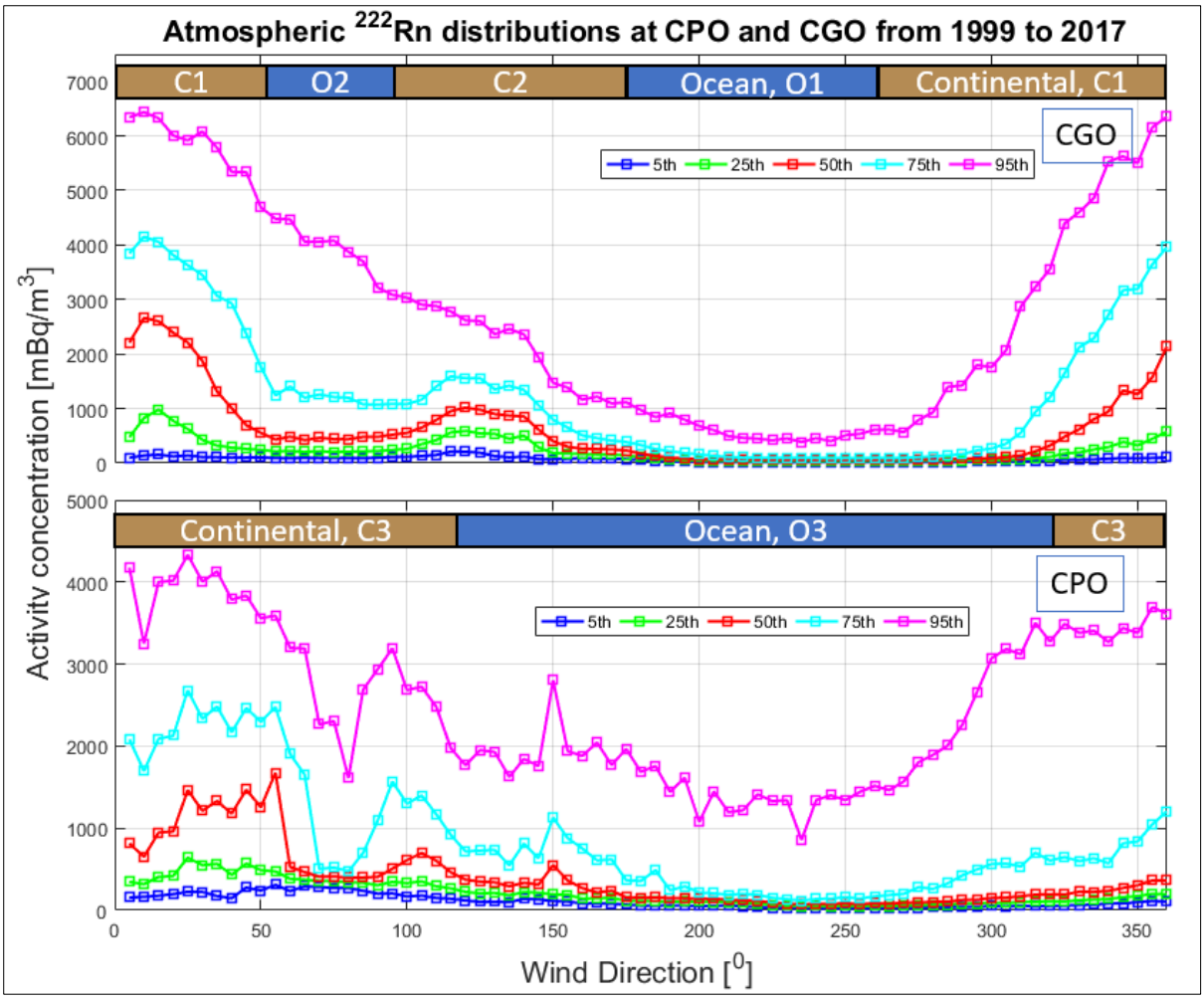

Figure 5-23: WD-dependence of CGO and CPO atmospheric radon distribution characterised by 5th, 25th, 50th (median), 75th and 95th percentiles within continental (C1 = Australian Mainland, C2 = Tasmania, and C3 = Africa Mainland) and marine (O1 = Southern Ocean; O2 = Bass Strait, and O3 = Atlantic and Indian Ocean). See also Figure 4-5.

The cumulative seasonal CGO and CPO atmospheric radon composites variations with WD are illustrated in Figure 5-24 and Figure 5-25, respectively. The seasonal CGO radon composites (see Figure 5-24) have broadly similar characteristics to the whole-year CGO radon composites (see Figure 5-23). However, there are some unique seasonal variations observed (see Figure 5-24). The largest radon increases according to WD (260° to 360°) and decrease (0° to 200°) for all the CGO radon percentiles occurred during autumn (MAM) and winter (JJA) compared to the summer (DJF) and spring (SON). For all the autumn CGO percentiles associated with the WD-sector from 220° to 250°, prominent baseline conditions occur (see Figure 5-24). It can additionally be characterized as the lowest seasonal radon composites WD-sector from 1999 to 2017. Within the specified marine WD-sector, 220° to 250°, during autumn

(MAM) the average CGO radon levels for the 95th, 75th, 50th, 25th, and 5th percentiles are 94 mBq/m^3, 75 mBq/m^3, 56 mBq/m^3, 37 mBq/m^3 and 18 mBq/m^3, respectively. The most prominent radon build-up associated with the WD-sector spanning Tasmania, C2, can be observed during summer (DJF) and autumn (MAM). During winter (JJA) the Tasmanian WD-sector radon build-up is almost non-existent.

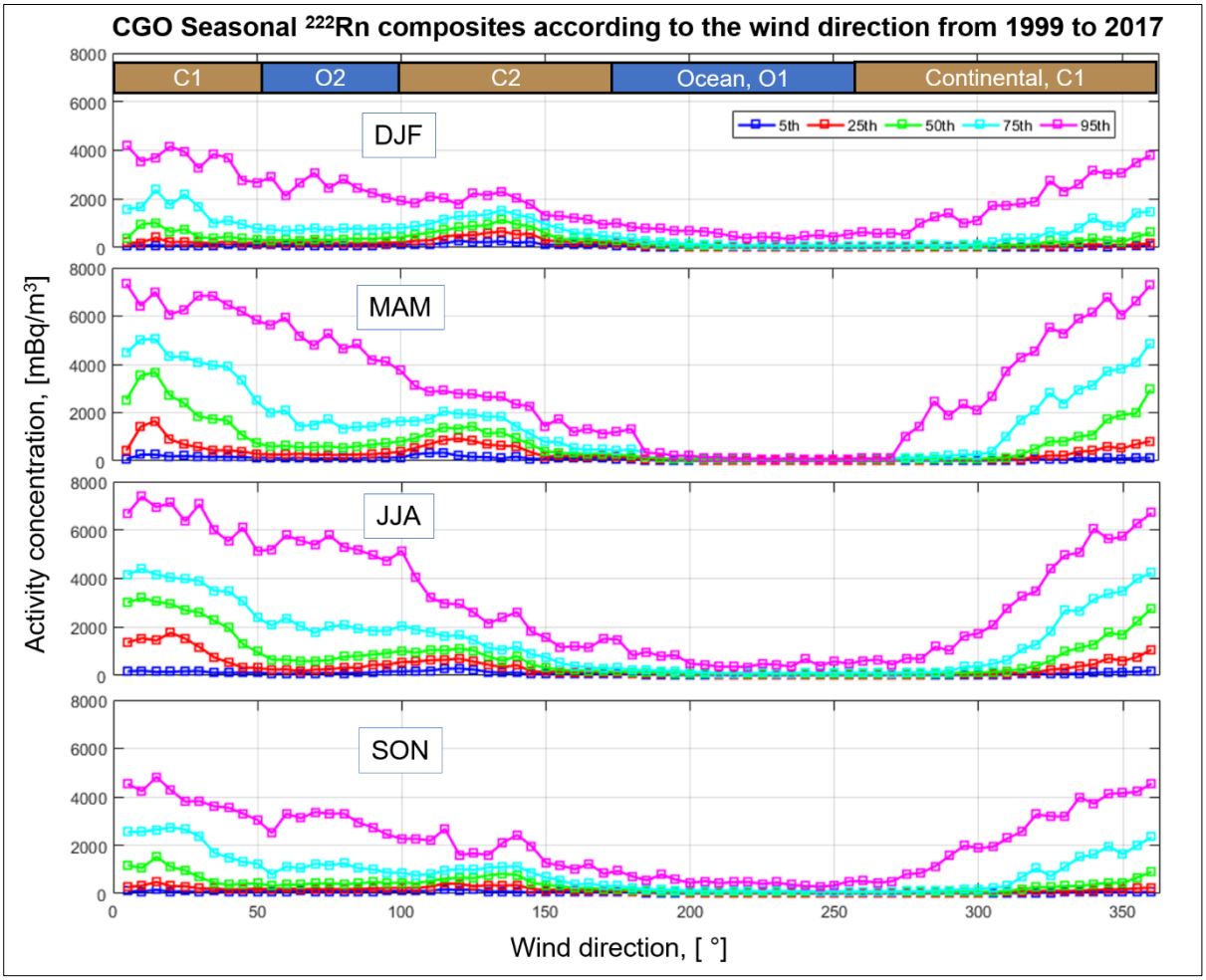

Figure 5-24: CGO seasonal atmospheric radon distribution characterised by 5th, 25th, 50th (median), 75th and 95th percentiles within continental (C1 = Australian Mainland, C2 = Tasmania), and marine (O1 and O2 = Indian Ocean) according to the WD.

CPO radon WD composites vary significantly between seasons (see Figure 5-25). It is noticed that the profile (shape) is unlike the cumulative CPO radon composites WD plot (see Figure 5-23). During the spring (SON) and summer (DJF) at CPO, elevated radon composites from the continental spanning WD-sector (339° to 115°, C3) and lower marine sector (115° to 339°) are similar and relatively small in comparison to autumn (MAM) and winter (JJA). This observation is related to the lowest CPO radon which is observed during the summer and spring

(see Figure 5-11, a) due to a lower incidence of continental air-masses (see Figure 5-26). The lower continental radon composites (C3) occur during spring and summer. This seasonal profile variability was also observed at CGO (see Figure 5-10), but it is not as strong (see Figure 5-24). In contrast to CGO, relatively high levels occur in the marine O3 sector at CPO (see Figure 5-25, O3). This is noted for all of the seasons, however, is particularly evident during autumn (MAM). This could be associated with mixing by diurnal sea breeze or other mesoscale activity. The seasonal CPO radon (see Figure 5-25) variability according to WD is stronger compared to CGO (see Figure 5-24). The CPO seasonal diurnal (see Figure 5-21) variability (apart from 2012 onwards) is less than at CGO (see Figure 5-20).

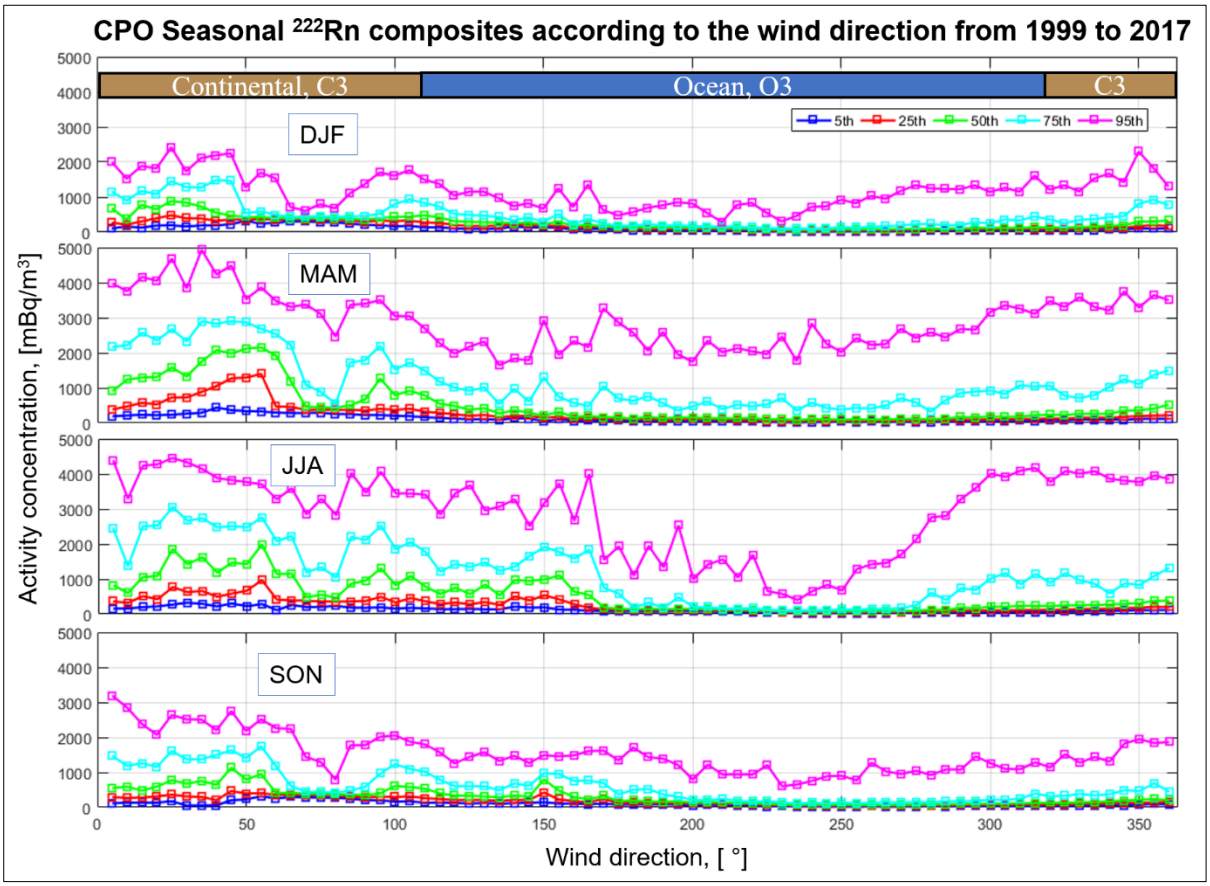

Figure 5-25: CPO seasonal atmospheric radon distribution characterised by 5th, 25th, 50th (median), 75th and 95th percentiles within continental (C3 = African Mainland, C2 = Tasmania), and marine (O3 = Atlantic and Indian Ocean) according to the WD.

Figure 5-26 presents an analysis of the frequency of radon occurrence (events) of air parcels incident at CGO and CPO as a function of wind direction (WD). The number of events is

defined as the number of times a detection is made. The first prominent feature of the CGO occurrence distribution is a strong peak centred around 90° (see Figure 5-26, a), corresponding to easterly flow through the Bass Strait and associated with mid-range radon values (Figure 5-24) due to the proximity of two adjacent land masses (see Figure 4-5). Periods of airflow from this direction occur throughout the year but are most frequently encountered in summer (DJF) and least in winter (JJA). The most prominent feature of the CGO occurrence frequency distribution, however, is a broad region of high occurrences through the entire "baseline" WD range of 160° to 320° (see Figure 5-26, a). Two distinct sub-regions of particularly high occurrences can be observed within this broader region, centred on 200° in summer and 270° in winter. Generally speaking, in summer there are significantly more events in the oceanic sectors and fewer in the continental sectors, whilst in winter the events are more evenly distributed.

Figure 5-26, c presents an analysis of the frequency of occurrence of air parcels incident at CPO as a function of wind direction (WD). Two strong peaks occur centred around 85° and 115°. The first radon occurrence distribution peak (85°) corresponds to air parcels coming across False Bay likely from the Overberg valley. The second peak and also the strongest (115°) correspond to air parcels from the contact line (mixing zone) between the coastline and Indian Ocean air parcels (see Figure 4-9). It should be noted that CPO (see Figure 5-26, c) does not show a broad region across the oceanic sector which is evident for CGO (see Figure 5-26, a). Hence, CPO is not such as optimal baseline measurement location compared to CGO. Nevertheless, for the African continent, it is one of the prime locations. The CPO mean WS according to the WD analysis results are presented in Figure 5.26, d. Within the mixing WD-sector between the continental (C3) and Atlantic Ocean (O3) air-masses, 80° to 110°, a sharp increase in the mean WS is observed (see Figure 5-26, d). The CPO peak of the radon frequency of occurrence (80° to 110°, see Figure 5-26, c) coincides with the mean WS spike (80° to 110°, see Figure 5-26, d) which is observed throughout the year. In general, an elevated radon frequency of occurrence (see Figure 5-26, a and c) does not translate to an elevated associated activity concentration (see Figure 5-23).

Seasonal variability for the CGO and CPO atmospheric radon incidence is observed. A key aspect which was noticed is that most of the prominent radon event peaks for both CGO and CPO (see Figure 5-26) occurs approximately at the transition between the continental and marine mixing zones. The higher frequency radon events occur almost exclusively within the marine WD-sectors (see Figure 5-26).

The seasonal radon events according to the local wind speed (WS) are also analysed (see Figure 5-26, b and d). The in-situ measured WS is an indicator of how fast the air-masses are moving. For CGO an elevation in the mean WS is detected in the marine WD-sector centred around 80° (Bass Strait: see Figure 5-26, b). The broad CGO radon events peak within the marine sector, O1 (Southern Ocean), coincides with general elevation in WS (see Figure 5-26, a and b). A notable decrease in WS is associated with the Tasmanian fetch region.

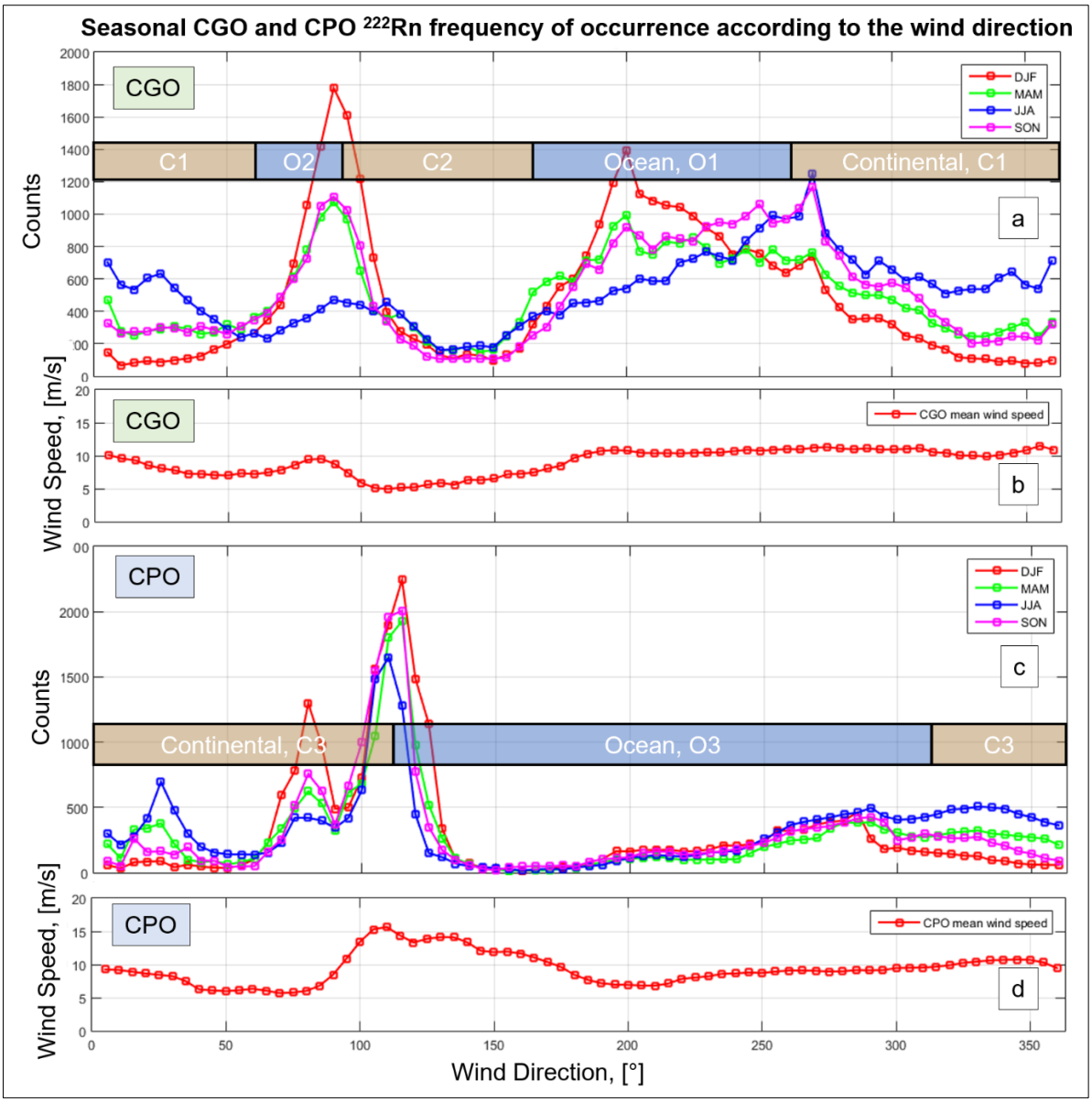

Figure 5-26: (a & c) CGO and CPO seasonal atmospheric frequency of radon occurrence (events) according to the locally observed wind speed from 1999 to 2017. (a) CGO sectors include the continental (C1 = Australian Mainland, C2 = Tasmania), and marine (O1 and O2 = Indian Ocean). (c) CPO sectors continental (C3 = African Mainland, C2 = Tasmania), and marine (O3 = Atlantic and Indian Ocean). (b & d) Associated mean in-situ wind speed according to the wind direction (WD).

The atmospheric radon signals are analysed in conjunction with the on-site measured ambient air temperature and pressure. The ambient air temperature according to the atmospheric CGO and CPO radon analysis are represented in Figure 5-27. The ambient air temperatures at CGO and CPO resemble a Gaussian distribution, albeit slightly skewed. Six regions are unique only to CGO which is not encountered at CPO (see Figure 5-27, a, purple dots), all but one of which are in the high radon range (> 8000 mBq/m^3) indicating air masses that have spent a longer time over land. Figure 5-24 indicates that these are most likely to have been inland continental air masses occurring in autumn or winter, which also explains their mid-range temperatures. On the other hand, the regions unique only to CPO occur in the higher temperature (> 25 °C) and lower radon (< 4000 mBq/m^3) range (see Figure 5-26, c, green). This may indicate the influence of summer coastal mesoscale breezes and/or downslope mountain flows that have spent time over a hot land surface.

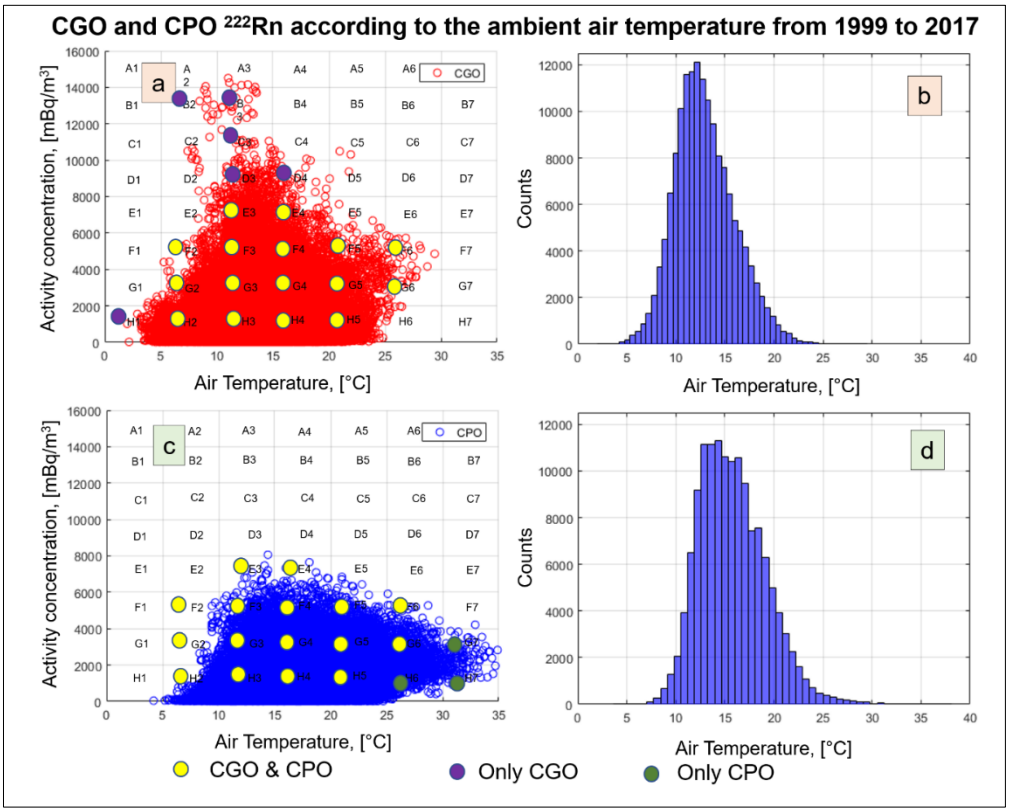

Figure 5-27: (a and c) CGO and CPO atmospheric radon levels as function of the on-site recorded ambient air temperature. Radon-temperature regions which occur at both CGO and CPO (yellow dots), only at CGO (purple dots), and only at CPO (green dots) are indicated. (b and d) CGO and CPO air temperature frequency distributions.

The CGO radon according to the air pressure can be classified as a skewed Gaussian-like distribution centred around 1107 mb (see Figure 5-28, b). This distribution is consistent with a scenario of the passage of the southern edge of synoptic weather systems moving from west to east across southern Australia, bringing continental (high radon) air south to Cape Grim when the atmospheric pressure is intermediate between high and low centres. For CPO a similar distribution is evident, centred respectively around 988 mb (see Figure 5-28, d). An isolated radon cluster is visible for CGO (see Figure 5-28, a) at the higher end of the pressure scale, 1020 mb combined with relatively high radon levels (> 10 000 mBq/m^3).

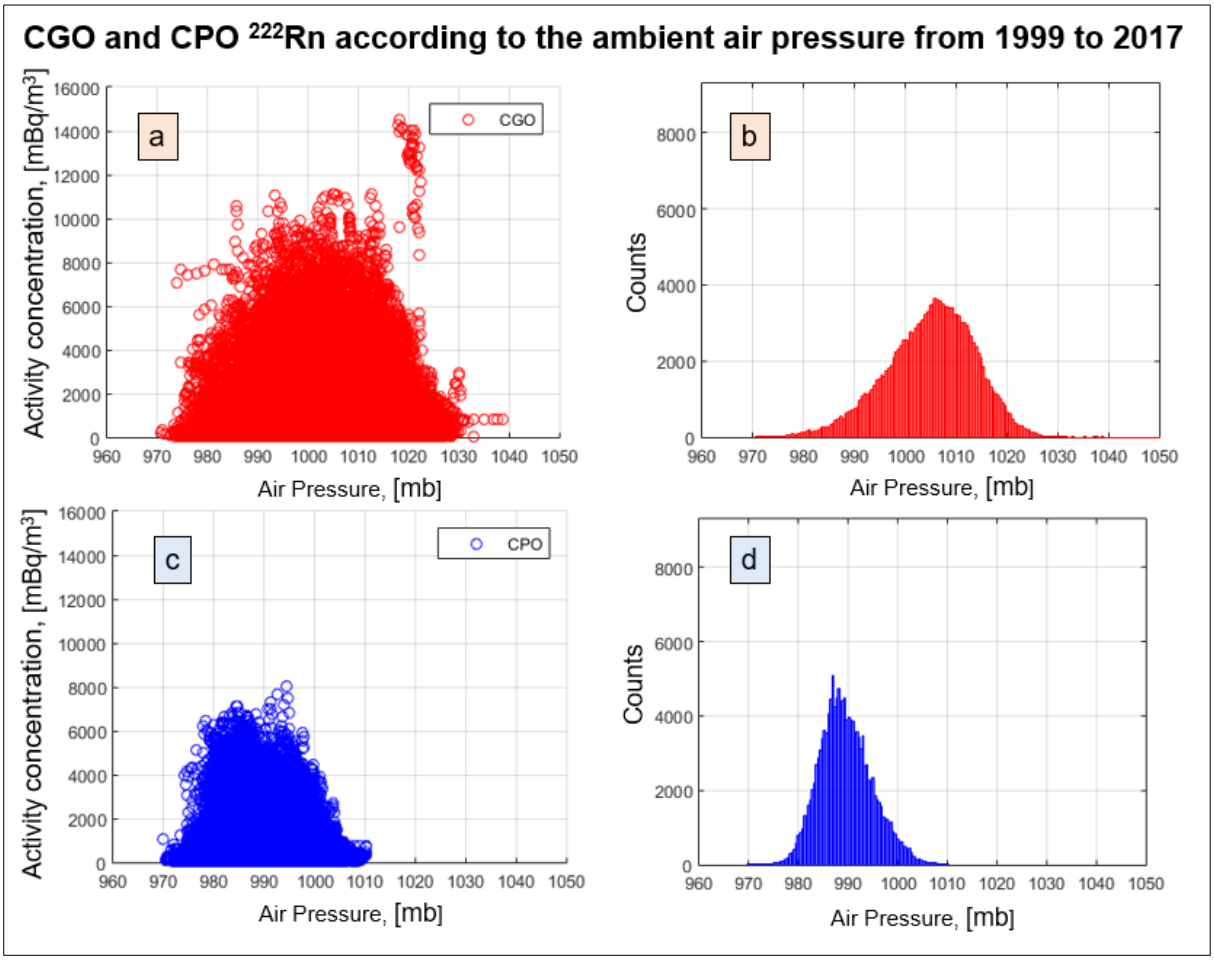

Figure 5-28: (a and c) CGO and CPO atmospheric radon levels as a function of the on-site recorded ambient air pressure. (b and d) CGO and CPO air pressure frequency distributions. Note that different bin sizes are utilized for histogram b (N = 1000) and d (N = 100).

5.3. Long-Term Variation Analysis

5.3.1. Long-Term Variation and Trend Analysis

The inter-annual atmospheric radon signals are further investigated to gain understanding surrounding its long-term nature. Two statistical methods are utilised to determine potential trends. The first method is the linear interpolation trend analysis approach combined with the goodness of fit parameters (R^2). However, for a dynamic time-series such as the CGO and CPO radon signals, it is expected that no single linear interpolation (see Figure 5-1) will be able of providing a good fit ($R^2 > 0.80$). For this reason, a second trend analysis method is used. The second method is the non-parametric Mann-Kendal (MK) test which is optimized for indicating statistical significance of monotonic trends most efficient for large datasets (Sharma et al., 2019). By default, a 95% confidence interval is used (MK-test) in this thesis. The data-rich radon signals are processed in some cases into percentile composites. This has proven to offer many advantages. The higher radon percentiles (75^{th} and above) by default due to the elevated radon levels (> 700 mBq/m^3) can be characterised to be continental air-masses. The lower radon percentiles (25^{th} and below) can be assumed to be predominantly marine (< 200 mBq/m^3) or deep baseline (< 50 mBq/m^3) air-masses (see Table 5-2). The median represents the bulk of the signal.

The inter-annual radon composite distributions for both CGO and CPO can be characterised to be profoundly skewed, especially for the 50^{th} to 75^{th} percentile (see Figure 5-29). However, MLO is more evenly distributed. The CGO, CPO and MLO cumulative inter-annual radon composite distributions combined with trend analysis are presented in Figure 5-30 and Table 5-5. A systematic strong decrease in the CGO inter-annual 95^{th} percentile systematic is noticed (see Figure 5-30, a and b). The CGO 95^{th} radon percentile decreases at an estimated ($R^2 = 0.55$, see Appendix Table 3) mean annual rate of about 58 mBq/m^3 (see Table 5-5) determined by making use of linear trend analysis. The 95^{th} percentile downward trend's statistical significance is confirmed with $p < 0.001$ making use of MK-test. The remaining percentiles (5^{th}, 25^{th}, 50^{th}, and 75^{th}) were relatively unchanged ($p > 0.1$, see Figure 5-30 and Table 5-5).

Similarly, the CPO 95^{th} radon percentile decreased at an estimate ($R^2 = 0.31$, see Appendix Table 3) rate of about 31 mBq/m^3 per year (see Table 5-5) which is about half that of the CGO.

There are also decreases in the 75th percentiles at both CPO and CGO, albeit much more gradual. The CPO 95th percentile downwards trend's statistical significance is lower compared to CGO with p = 0.05 making use of the MK-test. The lower CPO and CGO percentiles (5th, 25th, and 50th) can be considered stable from year to year (see Table 5-5). The CGO and CPO 95th percentile radon decrease seem to indicate a long-term decrease in the number or extent of surface contact of a continental air-masses incident at the two stations (see Figure 5-30, a and b). This will be independently verified making use of back-trajectory analysis (HYSPLIT) in Section 5.4.1. The observation of decreasing radon levels associated with continental air-masses could be associated with the changes in Southern Hemisphere tropospheric circulation trends that have been identified (Banerjee t al., 2020; NC Swart, 2012).

In contrast to CGO and CPO, the inter-annual MLO 95th percentile trend analysis indicated a small increase (see Figure 5-30, c) from 2004 to 2015 of 6 mBq/m^3 (see Table 5-5). The most significant time during which the MLO 95th radon percentile increased is from 2012 to 2014 (see Figure 5-5). A notable MLO atmospheric radon peak among all the percentiles is observed during 2010 (see Figure 5-29 and 5-30, c). In summary, inter-annual atmospheric radon distribution variations are evident for the higher percentiles (75th and 95th) for CGO, CPO, and MLO.

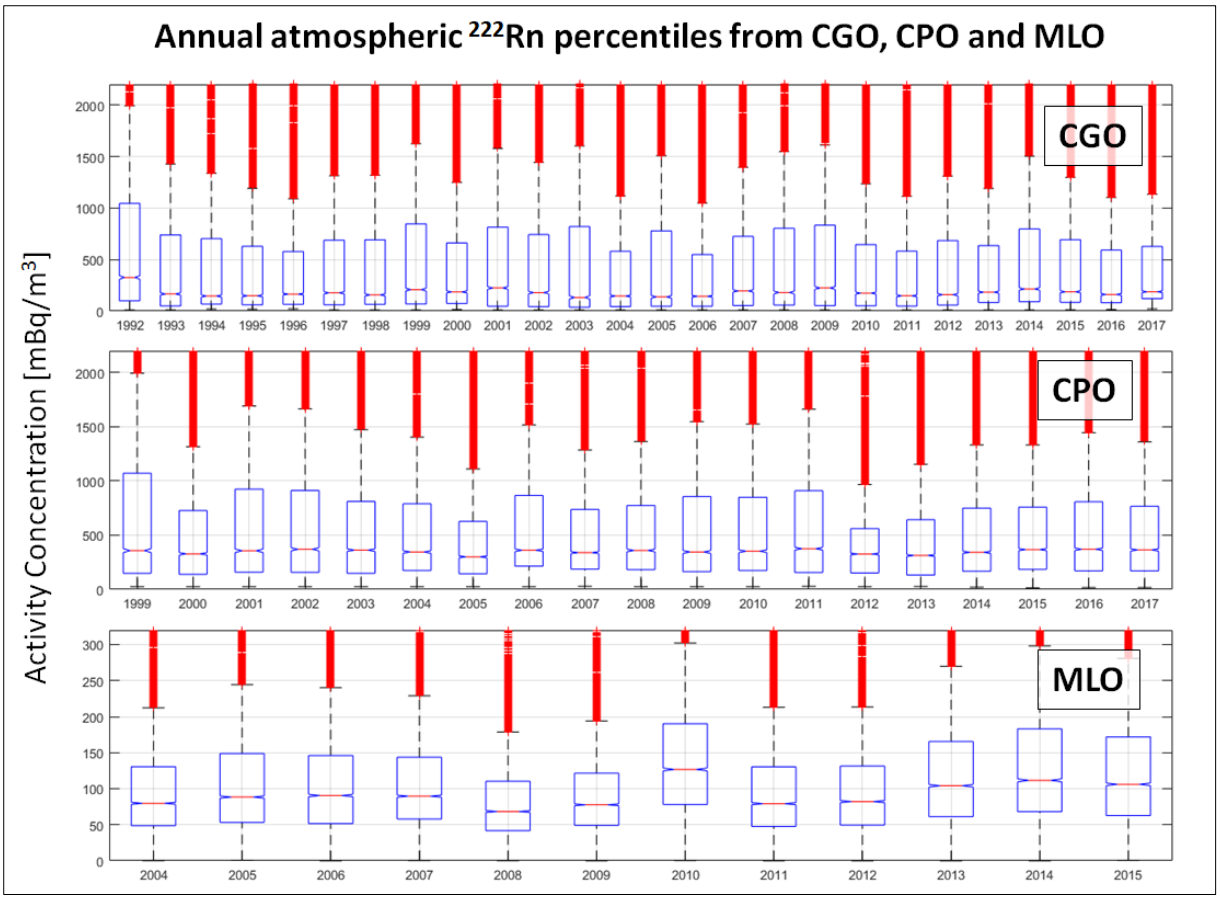

Figure 5-29: CGO, CPO, MLO inter-annual atmospheric radon concentration percentile distributions. The long-term radon distributions are characterised by the whiskers, bars and central horizontal line within the bars which refer to regions of most extreme data points characterised as outliers (red+), 25th/75th, 50th (median) percentiles, respectively.

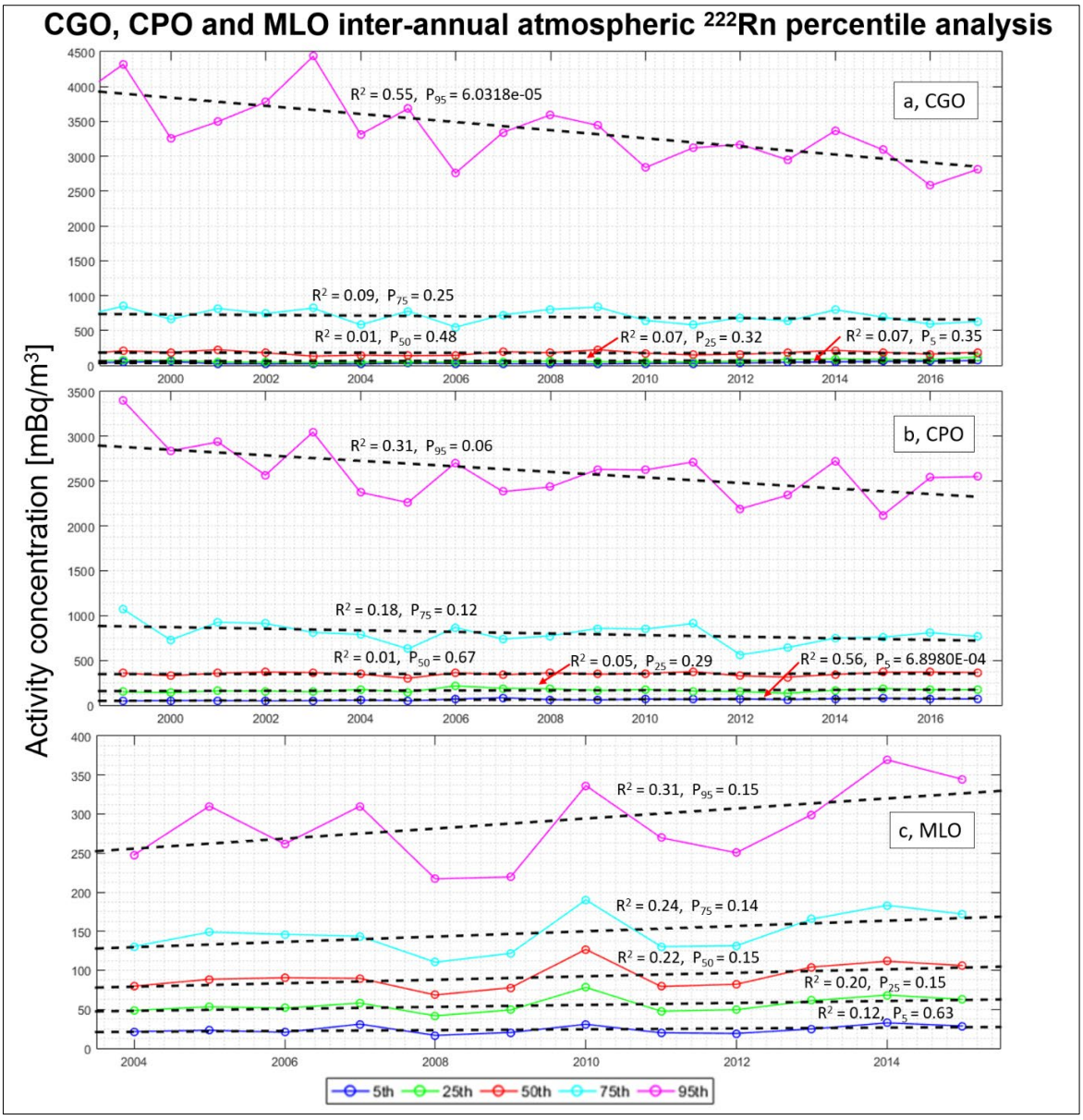

Figure 5-30: CGO, CPO and MLO inter-annual atmospheric radon percentile composites. The associated linear trendline (black line) combined with goodness of fit (R-square) and MK-test (p_i-values where i represents the associated percentile) are presented. The linear trendline coefficients are given in Table 5-5.

Inter-annual linear trendline analysis m (gradient) coefficients, f(x) = m*x + c					
Location	**5th Percentile**	**25th Percentile**	**50th Percentile**	**75th Percentile**	**95th Percentile**
CGO	0.5	0.7	-0.6	-4.4	-58.2
CPO	1.4	0.8	0.4	-8.8	-30.9
MLO	0.5	1.2	2.2	3.4	6.43

Table 5-5: Trend analysis (gradient in mBq/m^3) results of CGO, CPO, and MLO inter-annual radon signal percentile composites distributions.

5.3.2. Analysis of the Wind Direction Sectors

The long-term radon signals analysis is extended by studying the dependence on selected WD-sectors. WD-sectors are selected to be predominantly either marine, baseline, mixing or continental. The selection of the specified WD fetch sectors based on angular distributions projecting either landmasses or oceans relative to the respective observatories (Figure 4-5, Figure 4-9 and Table 5-6), atmospheric radon levels according to the WD. The trend analysis is performed to gauge whether long-term (1999 - 2017) temporal atmospheric radon variations associated with a particular WD-sector can be identified.

The statistical analysis of the CGO and CPO radon composite distributions according to selected WD-sectors are presented in Table 5-6. The mixed WD-sector (M) is defined as an angular distribution spanning space of air-masses from a combined marine (O) and continental (C) origin. Deep baseline (D) air-masses are defined as those air masses originating from a marine WD-sector which are the lowest in radon and air pollution (Chambers et al., 2016). Continental regions generate the most anthropogenic air pollution compared to marine regions (Whittlestone et al., 1992).

The highest CGO mean continental radon is observed as expected from the Australian mainland (C1). However, surprisingly the highest median is associated with the WD-sector C2, Tasmania. The highest standard deviation observed for all the WD-sectors are associated with the Australian continental mainland (1750 mBq/m^3). The mean (964 mBq/m^3) and median (476 mBq/m^3) CGO radon levels are associated with the marine WD-sector O2 (see Table 5-6). It is a strong indicator that air-masses observed at CGO from the WD-sector O2 will be mixed with continental air-masses from both Australia and Tasmania. This is plausible based on the geographical setting (see Figure 4-5). The mixing zone M3 (959 mBq/m^3) and surrounding marine sector O2 (964 mBq/m^3) have similar mean radon levels. The CGO baseline WD-sector DD has a mean of 133 mBq/m^3 and a median of 59 mBq/m^3. The presumed mixing WD-sectors, M4 and M5 can be considered to be in the baseline range based on the low mean (< 70 mBq/m^3) and median (< 180 mBq/m^3) atmospheric radon (see Table 5-6).

By contrast, CPO's continental atmospheric radon is about a factor of 2 higher compared to the marine WD-sector (see Table 5-6). The mean continental atmospheric radon observed at CPO (835 mBq/m^3) is similar to the CGO WD-sector associated with Tasmania, C2 (846 mBq/m^3),

however about 34% lower compared to Australia (1302 mBq/m^3). The CPO baseline WD-sector's mean and median atmospheric radon is about two times higher relative to CGO. CGO is subjected to higher incidence of "pure" (deep baseline) air-masses compared to CPO, which is also reflected the lower radon levels (see Table 5-6).

Station	Air Mass Sector	Mean Atmospheric Radon Levels, [mBq/m^3]	Median Atmospheric Radon Levels, [mBq/m^3]	Standard Deviation Atmospheric Radon Levels, [mBq/m^3]
CGO	Continental C1 (275° - 54°)	1302	416	1750
	Continental C2 (90° - 167°)	846	575	870
	Marine O1 (167° - 275°)	171	68	349
	Marine O2 (54° -90°)	964	476	1255
	Mixed M3 (60° - 110°)	959	543	1158
	Mixed M4 (195° - 205°)	167	67	322
	Mixed M5 (265° - 275°)	174	64	412
	Deep Baseline (120° -150°)	133	59	304
CPO	Continental C3 (339° -115°)	835	433	900
	Marine O3 (115° - 339°)	488	168	798
	Mixed M1 (100° - 150°)	708	422	722
	Mixed M2 (250° - 339°)	548	145	938
	Deep Baseline (180° - 273°)	320	106	585

Table 5-6: CGO and CPO statistical analysis of atmospheric radon levels for specified WD-sectors (1999 to 2017).

The inter-annual CPO radon percentile composites associated with the predominant marine (O3) and continental sector (C3) WD-sectors are illustrated in Figure 5-31, a. The CPO marine sector (O3) shows an increase in the 95th radon percentile of about 29% based on linear trend analysis (see Figure 5-31 and Table 5-6). The increase is of moderately statistically significance

based on the MK-test, $p_{95th} = 0.118$. It should be noted that the 95th marine percentile surpasses 1900 mBq/m^3, indicating a significant residual terrestrial effect even when the WD is in the marine sector. The high radon levels associated with the 95th percentile is an indication of strong mixing (recirculation) with continental air-masses. The 75th and 50th CPO marine sector O3 radon percentiles (< 500 mBq/m3) can be considered to be relatively steady with minor observed fluctuations (see Figure 5-31).

A strong decline is observed associated with CPO's continental C3 fetch region especially among the higher radon percentiles (see Figure 5-31, b). The CPO continental sector (C3) shows a decrease in the 95th and 75th radon percentiles of about 31% and 44%, respectively (see Figure 5-31, b). The 95th and 75th percentile clear decreases are confirmed with respective significantly low p-values, $p_{95th} = 0.004$ and $p_{75th} = 0.002$. For the continental C3 and marine O3 median (50th percentile), a decrease of 25% and 19% was noted, respectively.

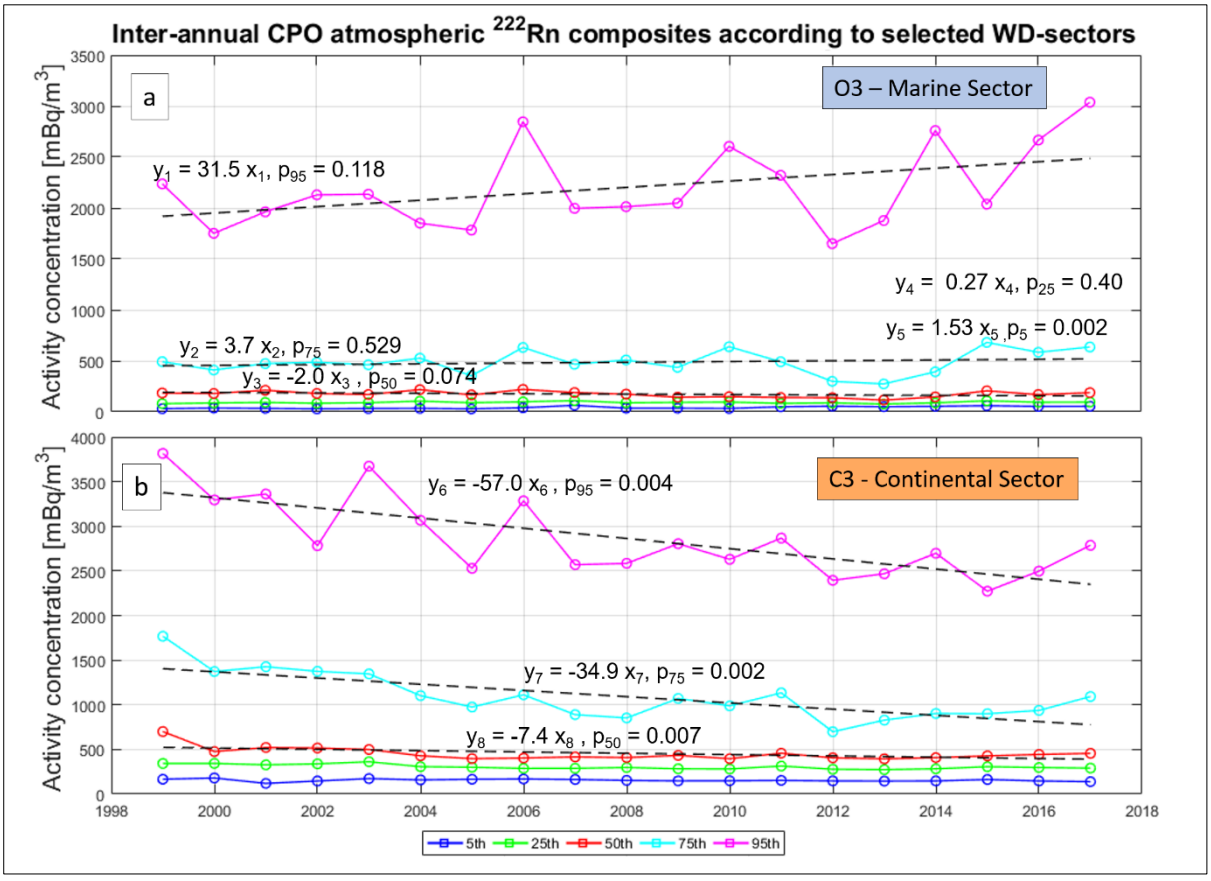

Figure 5-31: CPO atmospheric radon percentile distribution composites and trend analysis expressed according to marine (O3) and continental (C3) WD-sectors from 1999 to 2017. The associated linear trendline (black line) gradient coefficients and MK-test (p-values) are presented.

The CPO deep baseline WD-sector (see Figure 5-32, c) is most accurately represented by the median (50^{th} percentile) which has lower radon levels (< 120 mBq/m^3). The 95^{th} radon percentile from the baseline WD-sector, D, have relatively high radon levels (> 1000 mBq/m^3), again indicating a significant residual terrestrial influence even in deep baseline air at CPO However, the other radon percentiles which are more representative of a baseline environment will be the 75^{th} (< 400 mBq/m^3), and especially the 50^{th} (< 120 mBq/m^3). An estimated CPO baseline WD-sector (D) increase applicable to the 95^{th} ($p = 0.059$), 75^{th} ($p = 0.093$), and 50^{th} ($p = 0.006$) radon percentiles of 43%, 78% and 40%, respectively, are observed in total over the entire 19-year period.

For the mixed WD-sectors, M1 and M2, an estimate 19 years variations for 95^{th}, 75^{th} and 50^{th} are represented by 8%, 30%, 10% and –2%, 50% and 53%, respectively (see Figure 5-32, a and b). The most noteworthy increase within the CPO mixing WD-sector is for M2 (250° - 339°) and the 75^{th} (50%) and 50^{th} (53%) radon percentiles. A systematic increase in the radon levels is observed associated with the marine WD-sector (O3) and decrease associated with the continental WD-sector (C3). This could be attributed to change in mesoscale and hemispherical circulations or recirculation.

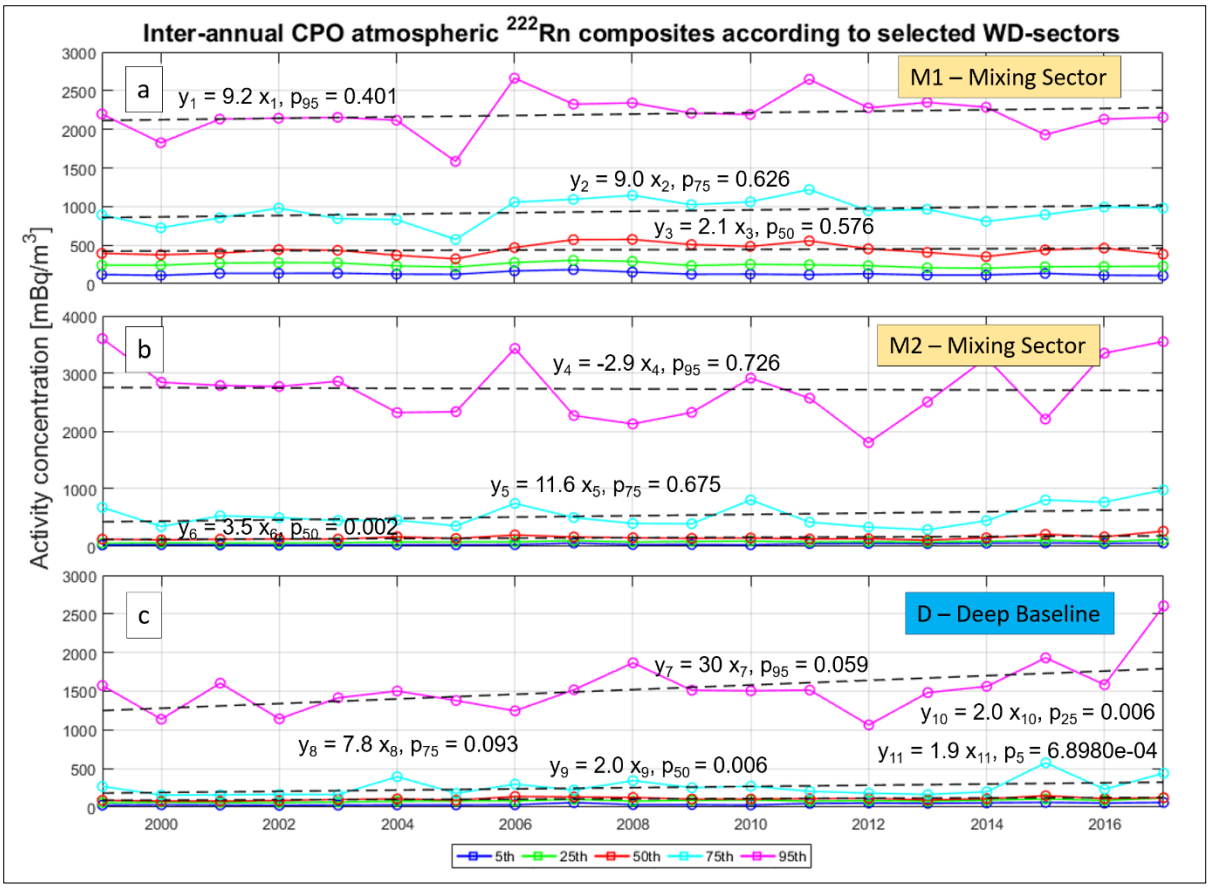

Figure 5-32: CPO atmospheric radon percentile distribution composites and trend analysis expressed according to mixing (M2) and deep baseline (D) WD-sectors. The associated linear trendline (black line) gradient coefficients and MK-test (p-values) are presented.

The CGO radon percentiles according to specified WD-sectors analysis results are presented in Figure 5-33 to Figure 5-35. CGO has more specified WD-sectors (see Table 5-6) compared to CPO based on the geographical setting (see Figure 4-5). The first part of the discussion will be on the CGO atmospheric radon percentiles associated with the continental regions (see Figure 5-33), Australian mainland (C1) and the Tasmanian Island (C2). It should be noted that the closest distance between CGO (Tasmania) to the Australian mainland is about 220 km (marine sector, Bass Strait).

A systematic multi-annual decrease concerning CGO radon percentiles associated with the continental WD-sectors C1 is evident. The estimated respective long-term 95th, 75th and 50th percentiles linear decreases are 28% ($p = 7.83 \times 10^{-4}$), 31% ($p = 0.108$), and 49% ($p = 0.074$). The Australian mainland (C1) WD-sector median decreased by almost a factor of two (see Figure 5-33, a). A decrease associated with the CGO 95th percentile continental sector C2 (Tasmania) of 23% ($p = 0.03$) is noted (see Figure 5-33, b). However, for the continental C2

WD-sector's (Tasmania) 75th and 50th radon percentiles, no prominent trends are evident (p = 0.834).

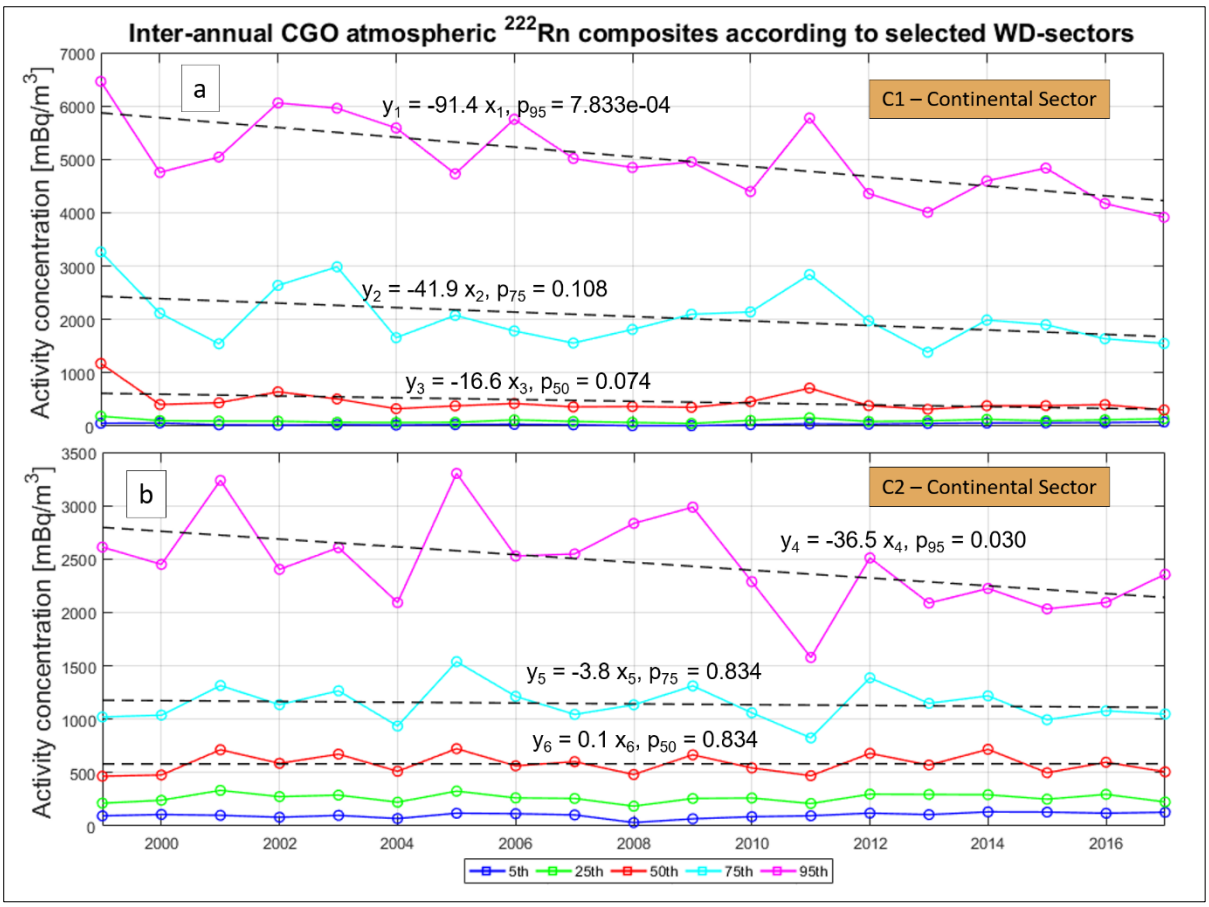

Figure 5-33: CGO atmospheric radon percentile distribution composites and trend analysis expressed according to continental (C1 – Australian mainland and C2 - Tasmania) WD-sectors from 1999 to 2017. The associated linear trendline (black line) gradient coefficients and MK-test (p-values) are presented.

Next, the CGO inter-annual marine sectors (O1 and O2) radon percentile distributions analysis results (see Table 5-6 and Figure 5-34) will be presented and discussed. A minor decrease (14%, p = 0.263) is noted for the 95th radon percentile applicable to the WD-sector O1 (Indian Ocean, Figure 5-34, a). Based on the relatively high radon levels (> 600 mBq/m^3) it will be considered as mixed air-masses. The 75th percentile from the WD-sector O1 illustrate a steady low (< 200 mBq/m^3) inter-annual radon level. An increase associate with the 50th percentile from the WD-sector O1 of about 107% is noteworthy, especially from 2011 onwards (see

Figure 5-34, a). The statistical significance of this upward trend is also strong, p = 0.016. The O1 WD-sector median can be characterised as baseline air-masses (< 80 mBq/m^3).

For the O2 WD-sector, decreases of 19% and 15% are applicable to the 95th and 75th percentile. The 50th percentile indicates a slight increase of 13%. For the CGO marine WD-sectors (O1 and O2) the higher percentiles (> 1000 mBq/m^3, mixed air-masses) demonstrated a long-term decrease, especially for the O2 sector.

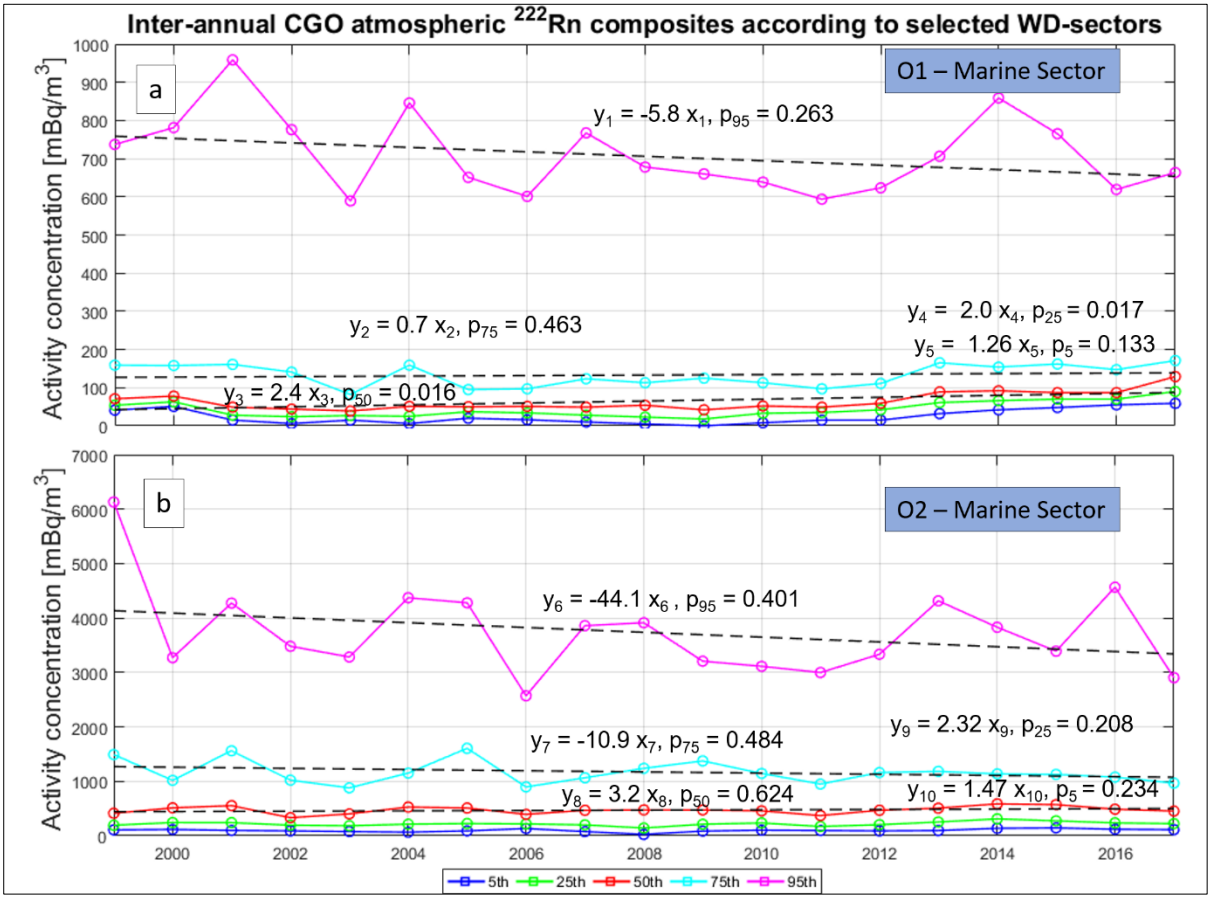

Figure 5-34: CGO atmospheric radon percentile distribution composites and trend analysis expressed according to marine (O1 and O2, Indian Ocean) WD-sectors from 1999 to 2017. The associated linear trendline (black line) coefficients and MK-test (p-values) are presented.

The WD-sector of particular interest is the baseline (< 100 mBq/m^3, D) and deep baseline (< 50 mBq/m^3, DD) WD-sectors. The 95th percentile associated with the baseline WD-sector, DD, is not considered as a true baseline representative based on the relatively high radon level (> 550 mBq/m^3, excluded from Figure 5-35, d). The 75th and 50th CGO radon percentiles

associated with the WD-sector, DD, indicates a long-term increase of about 37% (75 mBq/m^3 to 103 mBq/m^3) and 241% (34 mBq/m^3 to 82 mBq/m^3), respectively (see Figure 5-35, d). The most notable DD fetch-sector radon increases occurred from 2012 onwards (see Figure 5-35, d). It is optimal for coastal atmospheric observatories that the baseline air-masses do not exhibit an increase in radon levels. An increase in radon levels is an indicator of a higher incidence of continental air-masses which is more prone to contain anthropogenic air pollution.

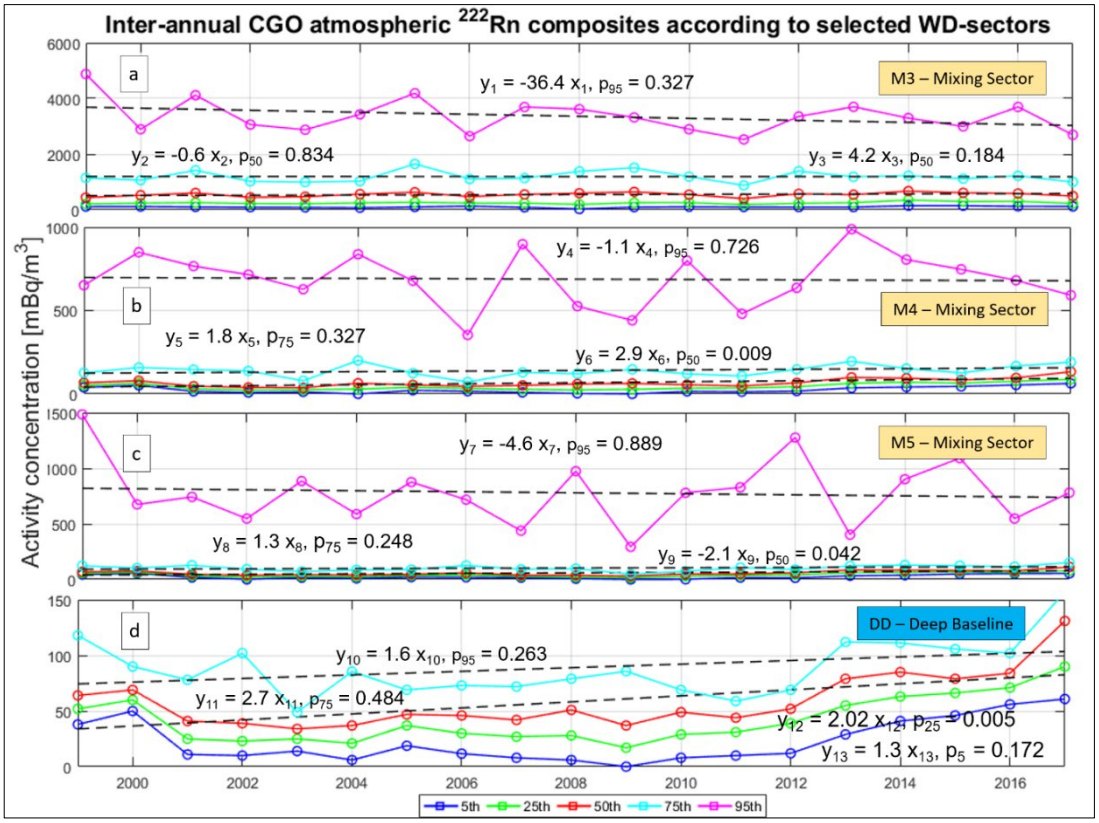

Figure 5-35: CGO atmospheric radon percentile distribution composites and trend analysis expressed according to mixed (M3, M4 and M5) and deep baseline (DD) WD-sectors from 1999 to 2017. The associated linear trendline (black line) gradient coefficients and MK-test (p-values) are presented.

In summary, a decline is evident among the continental WD-sectors for both CPO (see Figure 5-31, b) and CGO (see Figure 5-33) radon composite distributions (see Table 5-6). The continental sector's 95th percentile decreases at CPO (31%) and CGO (28%) are remarkably similar in magnitude. On the other hand, by making use of the marine WD-sectors results, the associated median radon at CPO indicated a 19% decrease (see Figure 5-31, a) while for CGO

(see Figure 5-34) an increase is noted, especially for O1 by 107%. For both CGO (see Figure 5-35, d) and CPO (see Figure 5-32, c) the baseline sectors presented systematic inter-annual increases in the radon composite distributions. These atmospheric radon variations are an indicator of SH circulation changes. These findings will be independently verified making use of back-trajectory analysis.

5.4. Long-term Atmospheric Air-Masses Back-trajectory Modelling

The wind (movement of air-masses) acts as a transport mechanism for atmospheric radon. High-resolution air-masses back-trajectory (HYSPLIT) analysis will serve as an independent approach to potentially verify the previous results and to expand on the understanding of the Southern Hemisphere atmospheric radon signals. Turbulent dispersion is also a key transport mechanism for radon in the atmosphere. Lagrangian dispersion models in which a large number of stochastically-perturbed trajectories (turbulent dispersion) are computed will be utilized in future. However, an extensive number of trajectories is considered here and analysed in a statistical approach. To a certain extent, the statistical consideration of a great number of different meteorological patterns compensates for the absence of turbulence in the model.

The purpose of this section is to study the origins of air-masses observed at CGO and CPO between 1999 to 2017 in more detail. The HYSPLIT computation and cluster (trajectory density) analysis methods applied are described in Section 3.4.3. The back-trajectory analysis is performed on the cumulative signals (see Section 5.3.1 and 5.3.2), inter-annual (see Section 5.3.3 and 5.3.5), and on a monthly (seasonal, see Section 5.3.4 and 5.3.6) temporal scale. The results from this section will provide insights into the temporal and spatial prevalence of marine and continental air-masses and altitude dynamics. These insights will assist in understanding the radon signals better.

5.4.1. Air-Masses Back-Trajectory – Spatial Analysis

In Figure 5-36, CGO and CPO air-mass back-trajectories are computed on an hourly temporal resolution from 1999 to 2017 for 60 hours back in time (T = 60 h). The back-trajectory computation is performed in conjunction with the cumulative individual radon signals of CGO and CPO. This serves as a representation of about two decades of recent fetch back-trajectories.

Generally, CGO and CPO are subjected to continental, marine and mixed air-masses. The air-masses fetch regions and altitude can now be qualitatively and quantitatively determined by making use of high-quality back-trajectory analysis (HYSPLIT). Figure 5-36 is useful to identify the spatial prevalence of trajectories. The qualitative plot is of use for optimizing the analysis algorithms by only applying it to regions in which the back-trajectories occurs. As a result, this saves computational time.

CGO is subjected to continental air-masses originating from regions such as Southern Australia, Tasmania, and New Zealand. For marine air-masses exposure, the Indian Ocean is the main fetch region. CPO is subject to continental air-masses fetched from the entire South Africa, Lesotho, Namibia, and Botswana (T = 60 h). CPO is subjected to the South Atlantic Ocean and Indian Ocean marine air-masses (T = 60 h). Both CGO and CPO even receive a limited number of air-masses originating as distant as Antarctica within a period of 60 hours (see Figure 5-36).

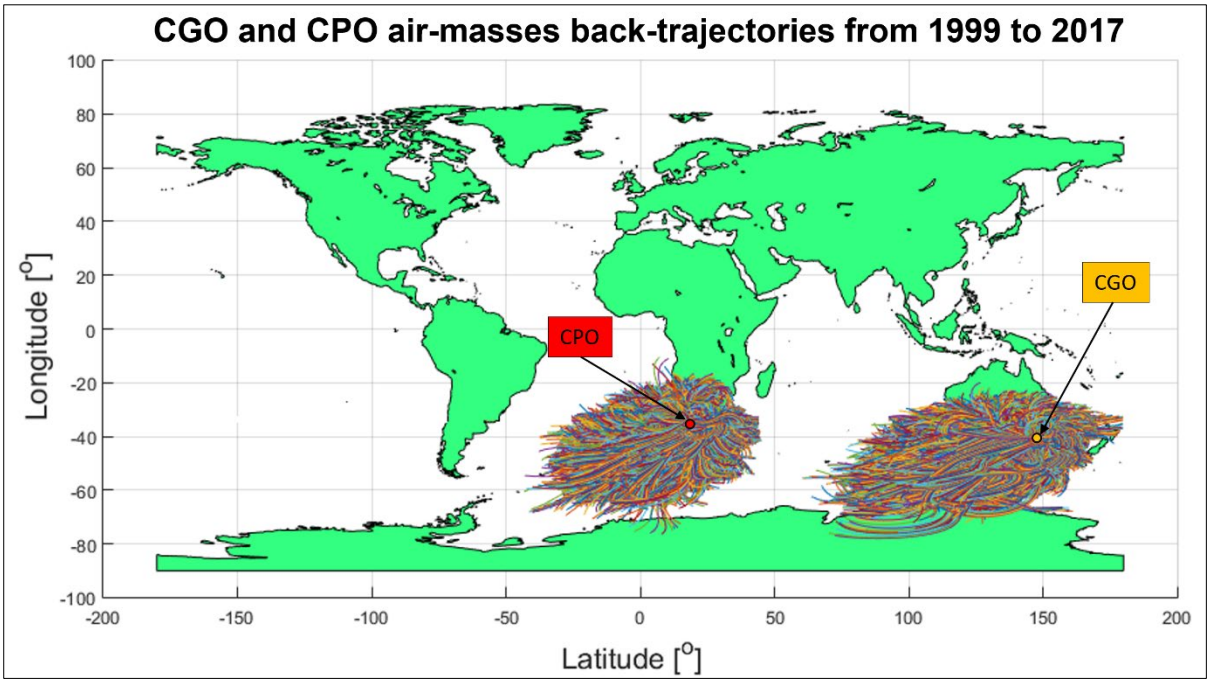

Figure 5-36: Illustration of about two decades of CGO and CPO air-masses back-trajectories computed on an hourly resolution projected up to 60 hours back in time. The various coloured lines represent the various back-trajectories.

5.4.1.1. CGO Air-Masses Back-Trajectory – Spatial Analysis

The first element studied is the cumulative historic back-trajectories at various durations back in time (temporal evolution), T_i = 0 h to T_f = 60 h (see Figure 5-37). It provides a qualitative overview of the expansion of the back-trajectories back in time. Within ten hours before the air-masses arrives at CGO the fetch regions include the southern tip of Australia, Tasmania and some regional marine sectors, 0 km ≤ $longitude_{span}$ ≤ 1507 km and 0 km ≤ $latitude_{span}$ ≤ 2140 km (see Figure 5-37). The air-masses fetch region expansion up to T = 60 h, spans a vast region, 0 km ≤ $longitude_{span}$ ≤ 6429 km and 0 km ≤ $latitude_{span}$ ≤ 12 884 km, including the Southern half of Australia, large sections of the South Indian and Southern Oceans extending down to Antarctica. The fetch region extent in latitude is about a factor of two larger compared to longitude. The westerly flow of air-masses is transparent. The furthest northwards expansion is capped at about -25° latitude, consequently, the CGO continental fetch regions are limited to mostly the southern section of the Australian mainland. An extensive westwards expansion occurs relative to the limited eastward expansion which includes New Zealand. However, the large number (N = 166 440) of back-trajectories in these plots tends to obscure the information on their associated density. A more qualitative analysis approach will be applied from hence forth.

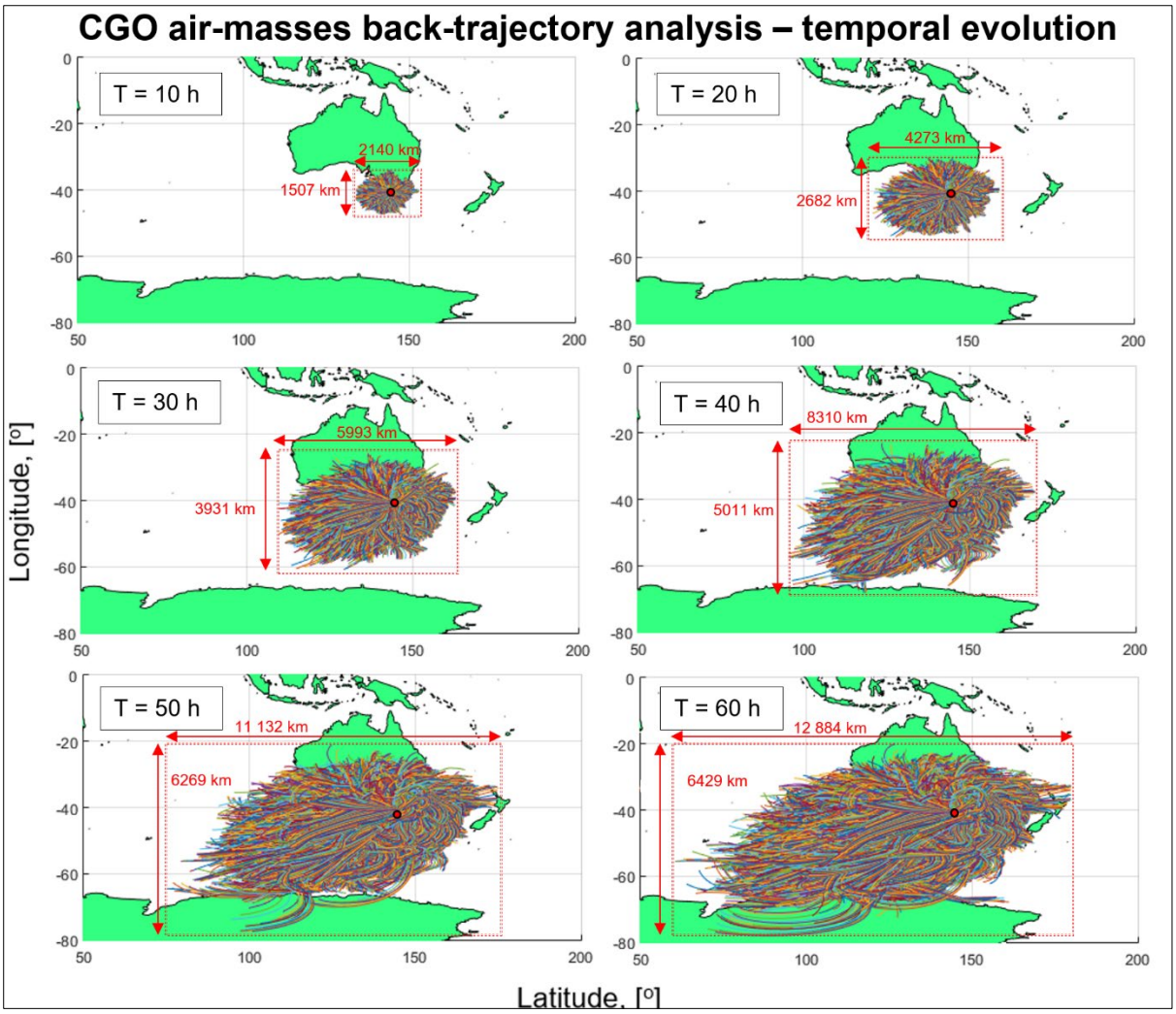

Figure 5-37: CGO atmospheric air-masses back-trajectories computed at various durations back in time (T). The grid domains for back-trajectories are indicated by the dashed red line while the red dot represents the location of the CGO.

5.4.1.2. CGO Air-Masses Back-Trajectory – Density Analysis

As discussed in Section 3.4.3, trajectory density (cluster) analysis is an analytical quantitative method utilised to identify the spatial prevalence trajectories within a specified spatial dimension known as a cluster (grid). A cluster (see Figure 3-24) represent a square spatial area of 123 km^2 or 11.1 km (longitude, 0.1°) x 11.1 km (latitude, 0.1°). By making use of the 19 years of back-trajectory data the trajectory density analysis results for CGO are presented in Figure 5-38. The upper trajectory plot (see Figure 5-38, a) presents the unfiltered version whereas the lower plot (see Figure 5-38, b) presents a filtered version in which the clusters

associated with a count of 250 or more are removed. The purpose of the filtering is to enlighten the lower visibility density structures which otherwise is not transparent.

A systematic higher density of air-masses originates from the marine regions. The continental regions are generated with very low intensity to ensure it does not overshadow the trajectory densities (see Figure 5-38). The highest density region is identified to be within the North-Eastern direction, the Bass-Strait. A slightly elevated continental region is visible across the Bass Strait within the Northern direction (Melbourne). Inter-annual variations are investigated and are evident and are presented in Appendix, Figure 5-42.

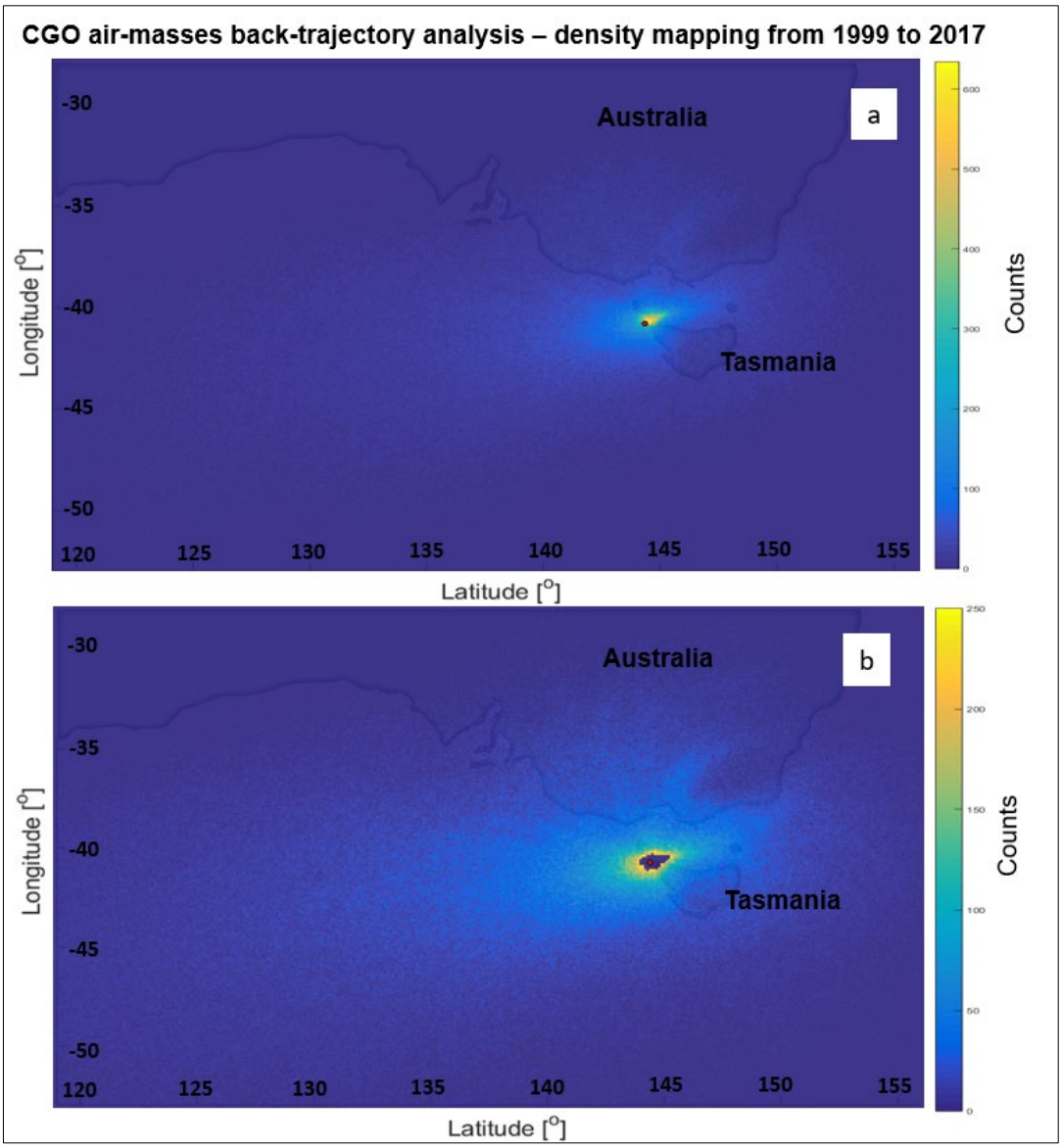

Figure 5-38: (a) CGO cumulative trajectory density (cluster) analysis making use of air-masses back-trajectories up to T = 60 h. The upper land mass represents the southern Australia and the lower land mass Tasmania. (b) Contrast filtered cumulative trajectory density plot with clusters associated with counts greater than 250, removed.

The continental (C) and marine (M), CM identification algorithm is utilised to obtain the following inter-annual analysis results (see Figure 5-39). The air-masses C or M identification methods are discussed in Section 3.4.3. The inter-annual ratio split of continental to marine (CM) air-masses according to various back-trajectories times are presented in Figure 5-39. There is a rapid decline in the C percentage according to time as the trajectory moves away from Cape Grim (see Figure 5-39). A CM identification algorithm test is to check if a 100% C is delivered for 0 h $\leq$ T $\leq$ 1 h. Since CGO and CPO are land-based atmospheric monitoring sites (i.e., within a grid cell classed at land), at T = 0 h the air-masses should be characterised only as continental and as a result, the C contribution should be 100%.

The variation in the continental to marine percentage of air-masses between years is generally small, with a maximum variation of about 11% (Figure 5-39). However, if we exclude the first 4h for the reasons discussed above, Figure 5-39 indicates a small inter-annual decrease in the CM ratio with time over the last 19 years, at least up to T = 40h. The years 1999 and 2000 had the highest CM ratios compared to the other years (see Figure 5-39), and this observation is also noted by making use of the trajectory density analysis (see Figure 5-38). After T = 40 h back in time, air-masses incident at CGO are subjected to a much more consistent continental influence of around 7%.

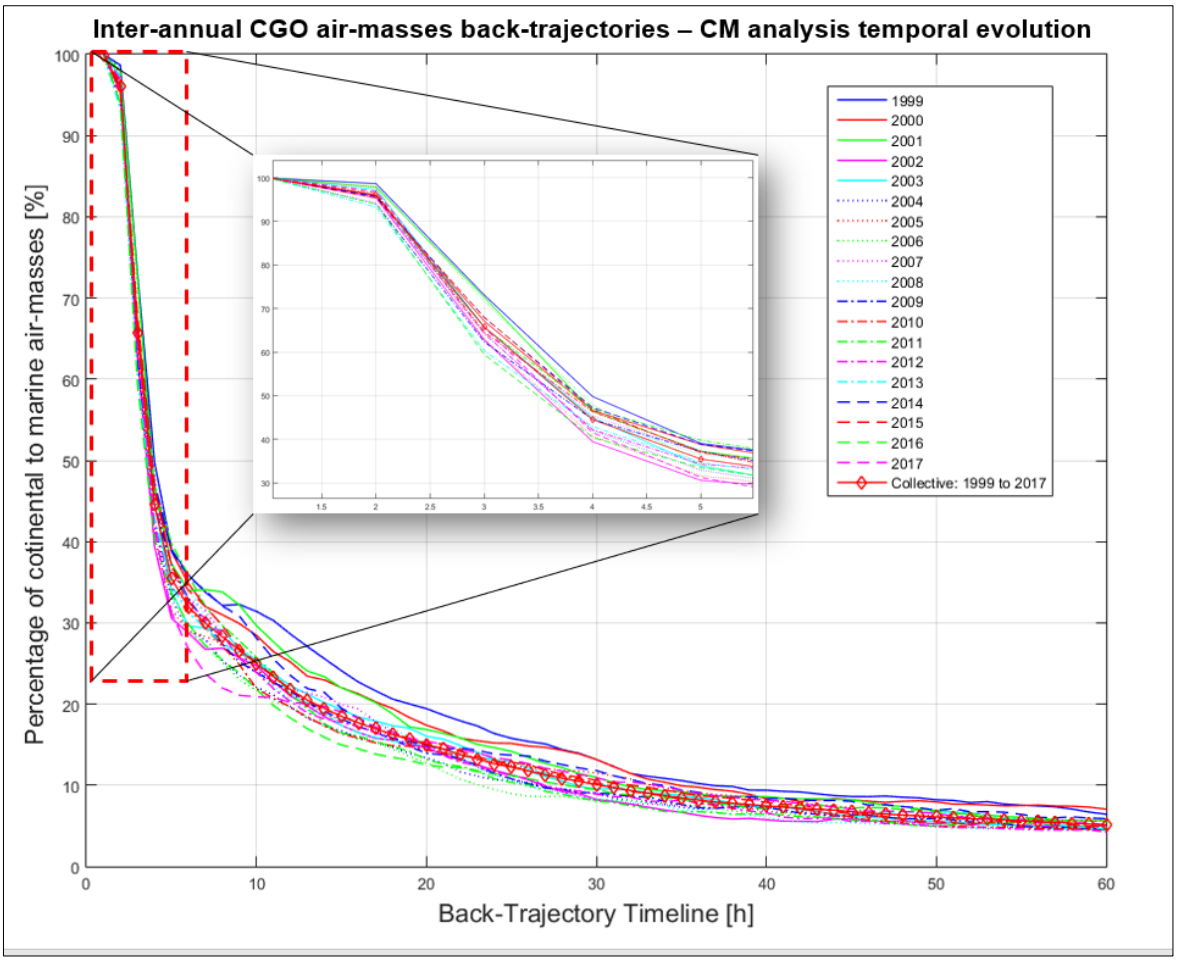

Figure 5-39: Percentage split of inter-annual CGO continental and marine (CM) air-masses from 1999 to 2017 according to various hours back in time up to T = 60 h.

The split (percentage) between continental and marine air-masses analysis is conducted on a monthly temporal scale in Figure 5-40. In general, the monthly CM ratio variations back in time can be considered low. During 0 h ≤ T ≤ 7 h, the highest CGO monthly CM ratios tend to occur in January to April (summer/autumn), which will be predominantly associated with air-masses originating directly from Tasmania. During 7 h ≤ T ≤ 40 h, however, the higher CM ratios tend to switch to the autumn/winter months (April to July), with the largest changes occurring in June and July. This likely indicates a shift to a greater influence of air-masses from the Australian mainland (see also Figure 5-10). The largest range of CM ratios observed occurs at about T = 8 h, and after about T = 40 h the range reduces to about 4% (see Figure 5-40).

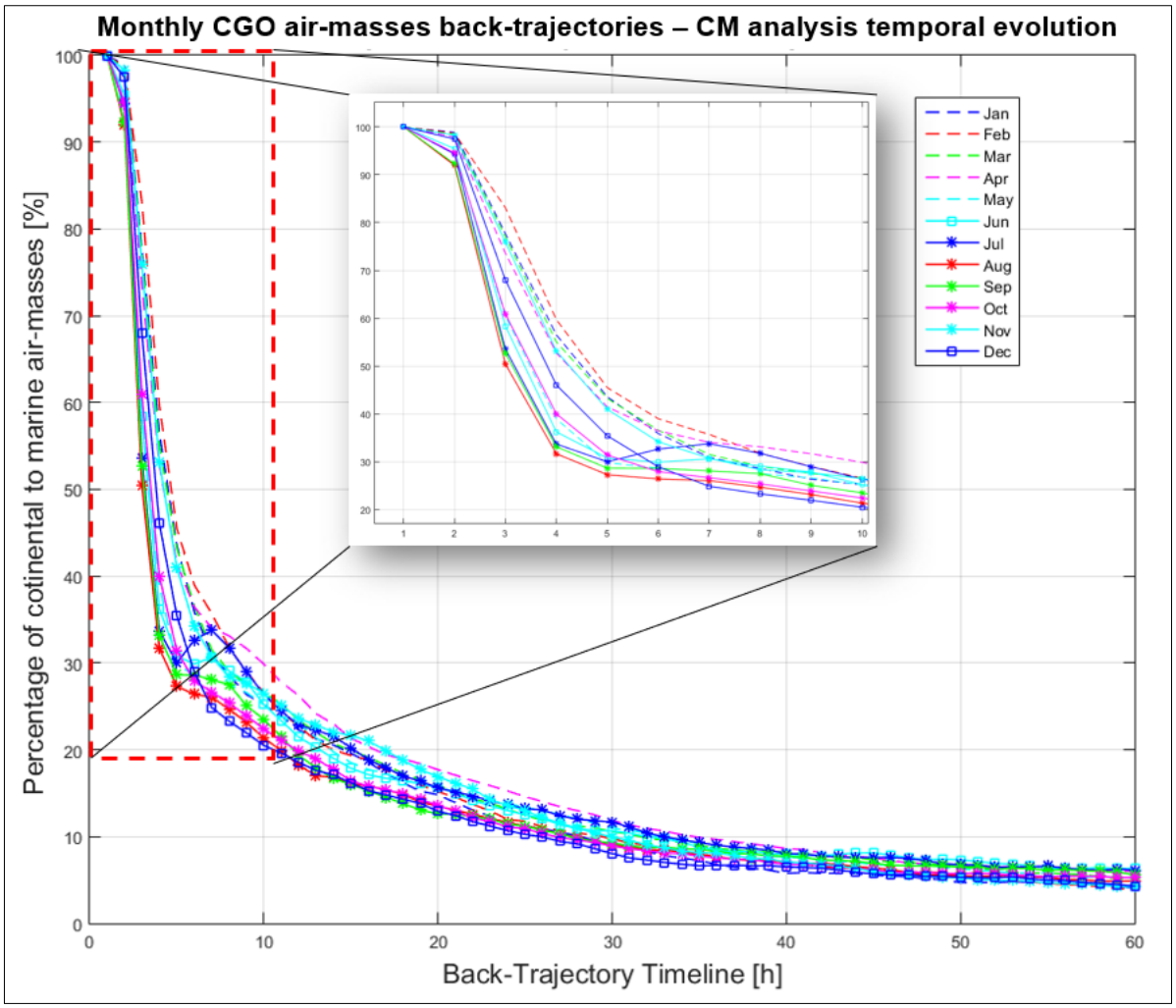

Figure 5-40: Monthly CGO continental to marine (CM) air-masses splits from 1999 to 2017 according to various hours back in time up to T = 60 h.

The results obtained making use of the CM identification algorithm applied to specified regions will be presented and discussed. The aim is to determine the number of inter-annual and seasonal marine and selected continental air-masses observed at CGO. Similar to the results obtained using the first CM identification algorithm (see Figure 5-40), a total mean of about 89% of the air-masses observed are from a marine origin (see Figure 5-41, b). By making use of the linear trend analysis a respective CGO marine and a continental total decline of about 24% and 3% are observed from 1999 to 2017 (see Figure 5-41, A and B). The respective declines are confirmed by making use of the MK-test with p = 0.012 (marine) and p = 0.003 (continental).

Based on the total number of annual air-masses observed for back trajectories up to 60 hours back in time the percentage of continental and marine origins are presented (see Figure 5-41, C and D). The percentage of continental air-masses observed at CGO is decreasing at an annual rate of about 0.13% (see Figure 5-41, B). The decrease could potentially coincide with the decrease observed in radon levels from continental sectors (see Figure 5-33) and especially for 95^{th} radon percentile (see Figure 5-30). The decrease in inter-annual 95^{th} percentile radon levels from marine fetch regions is noted (see Figure 5-34). However, as discussed, the more representative radon percentiles associated with marine sectors will be the lower percentiles such as the 50^{th} and it indicates a low increase in radon levels, especially from sector O1 (see Figure 5-34, a). The variations could be related to the changes observed in Southern Hemisphere tropospheric circulation trends in which changes in the mid-latitude jet stream has occurred (Banerjee et al., 2020; NC Swart, 2012).

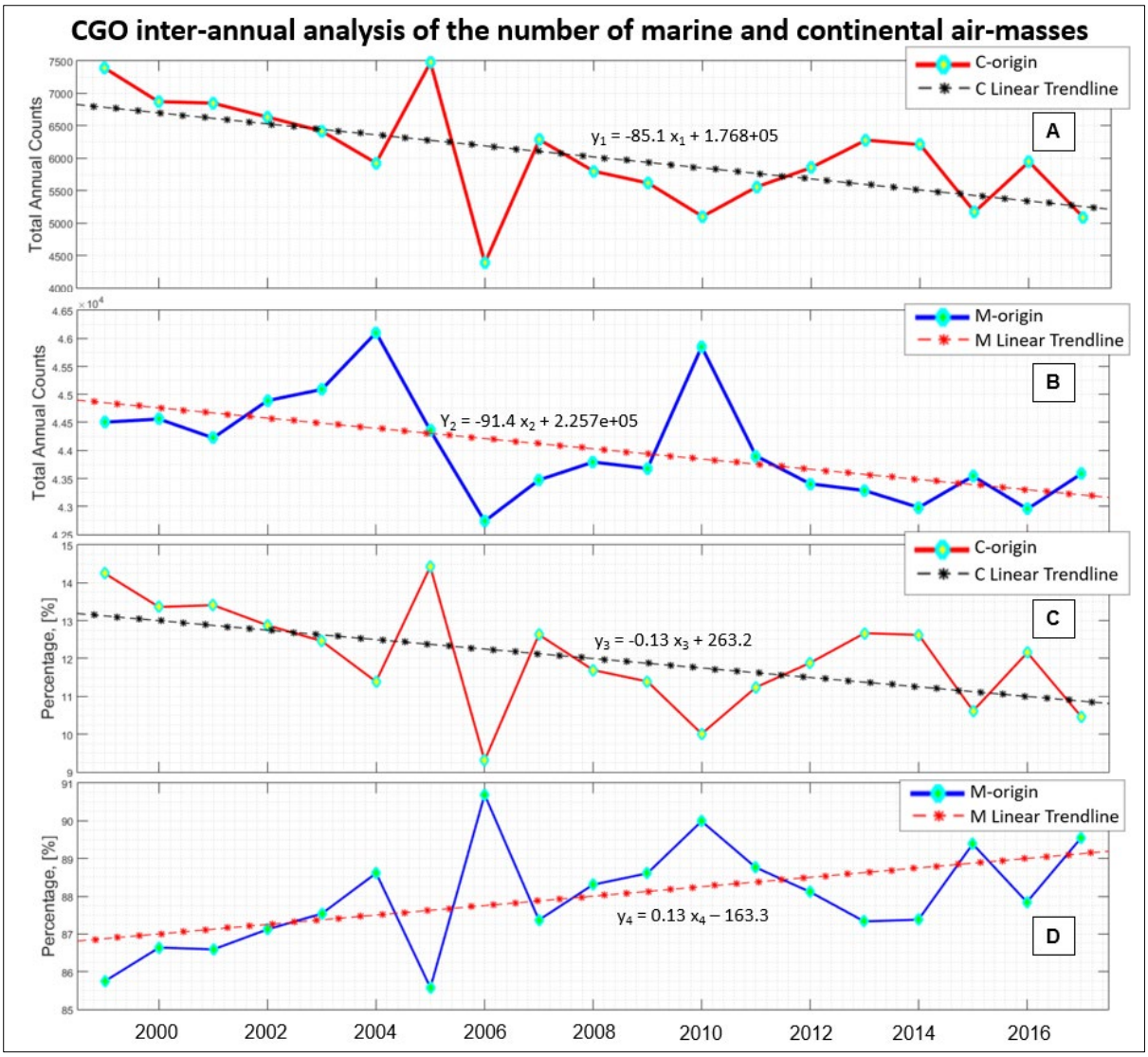

Figure 5-41: (A) CGO inter-annual cumulative number of continental (C) and marine (M) air-masses making use of back-trajectory time up to T= 60 h from 1999 to 2017 and associated linear interpolation trend analysis. (B) Percentage of CGO observed continental and marine air-masses and associated linear interpolation trend analysis. (C) The percentage of continental air-masses and (D) the percentage of marine air-masses based on the total annual number of air-masses.

CGO from 1999 to 2017 (up to T = 60 h) is exposed to continental air-masses coming predominantly from two main regions, the Australian continent and Tasmania (see Figure 5-37). A limited number of back-trajectories from the continental regions such as Antarctica, King Island, Flinders Island and New Zealand (see Figure 5-37) are excluded. The continental air-masses trajectories density analysis results are presented in Figure 5-42. Of the total mean continental air-masses observed at CGO, 75 ± 4% is from the Australian mainland and the remaining 25 ± 4% from Tasmania. A particular steady period with small relative fluctuations

occurred from 2008 to 2014. In 2015, the largest total contribution of Tasmanian continental air-masses is observed at about 33% (see Figure 5-42).

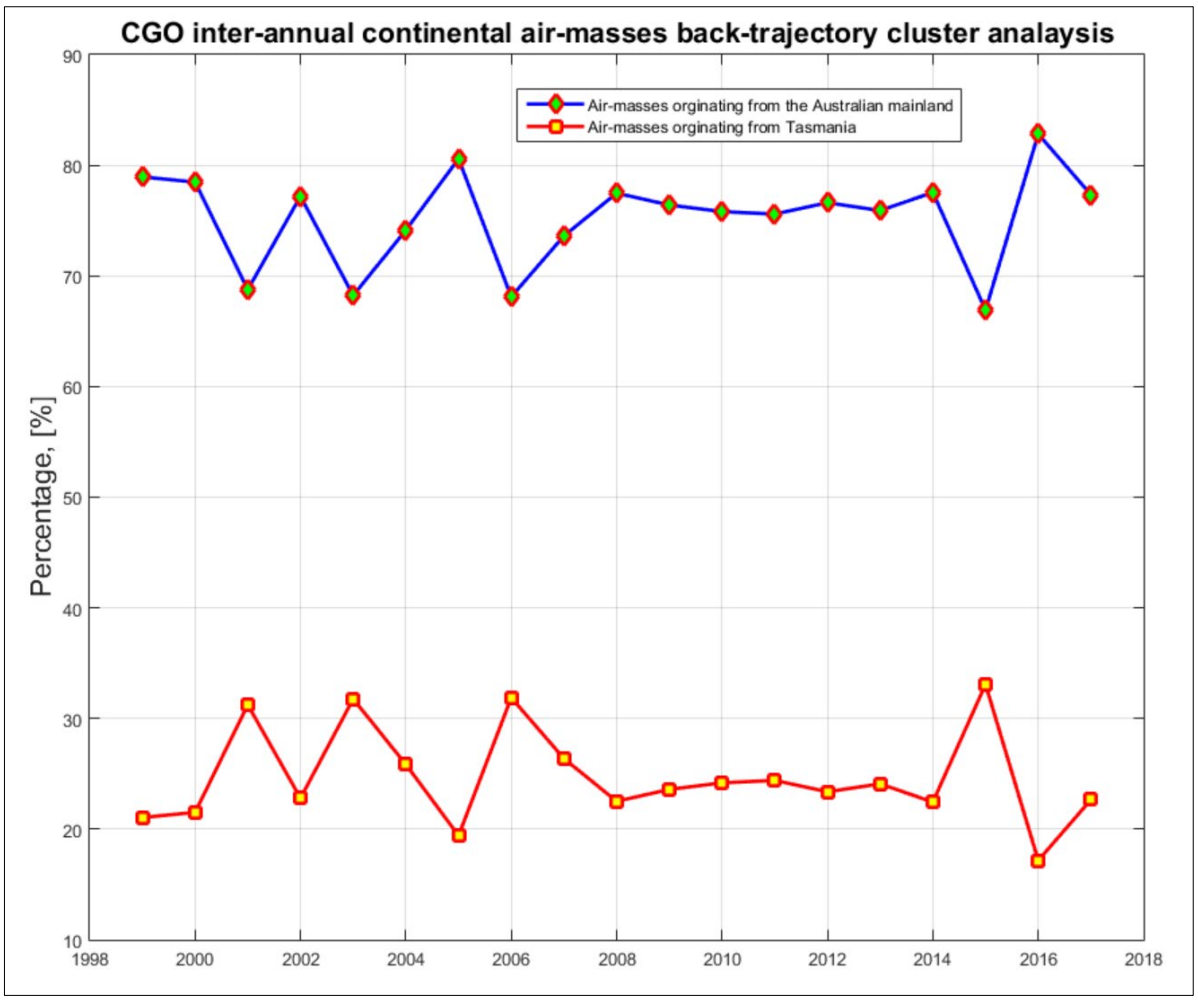

Figure 5-42: Inter-annual percentage of Tasmanian and Australian air-masses observed at CGO making use of density analysis with back-trajectories up to T = 60 h from 1999 to 2017.

The CGO cumulative seasonal incidence percentage of continental and marine air-masses from 1999 to 2017 making use of back-trajectories up to T = 60 h are presented in Figure 5-43. By making use of the trajectory density analysis results it is evident that CGO are exposed to the most marine air-masses during summer (93%) and the least during winter (7%). This coincides with the highest seasonal radon occurring during winter, a higher incidence of continental air-masses and the lowest during summer during which the largest number of marine air-masses is observed (see Figure 5-10, b).

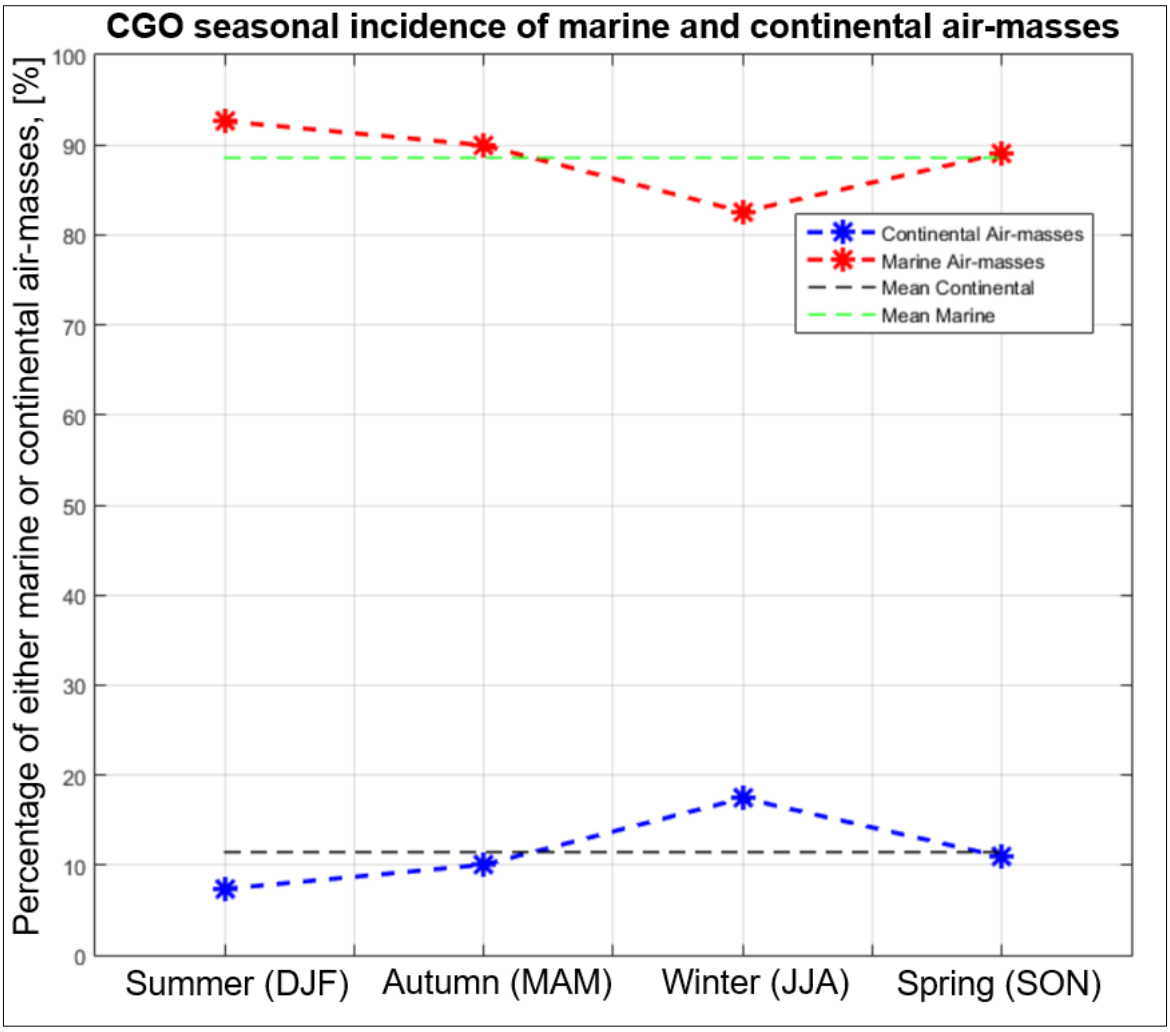

Figure 5-43: Cumulative CGO seasonal incidence percentage of continental and marine air-masses making use of back trajectories up to T = 60 h from 1992 to 2017.

5.4.1.3. CPO Air-Masses Back-Trajectory – Spatial Analysis

The cumulative CPO's back-trajectories at various durations back in time, T_i = 0 h to T_f = 60 h is presented in Figure 5-44. Within ten hours before air-masses are detected at CPO, the fetch region can be characterized by 0 km ≤ longitude_{span} ≤ 1346 km and 0 km ≤ latitude_{span} ≤ 1705 km (see Figure 5-43). The air-masses fetch region expansion up to T = 60 h, spans a vast region, 0 km ≤ longitude_{span} ≤ 7318 km and 0 km ≤ latitude_{span} ≤ 9893 km, including the whole of South Africa, Lesotho, Namibia, and Botswana, a large part of the South Atlantic and Southern Oceans almost down to Antarctica, and even extending a little way east into the Indian Ocean. The air-masses observed at CPO are confined from a longitude of about -19° (see Figure 5-44,

T = 60h). The back-trajectory spatial expansion up to T = 60 h (see Figure 5-44) is smaller relative to CGO (see Figure 5-37). Quantitatively, most of the back-trajectories originate from the South Atlantic Ocean (see Figure 5-44).

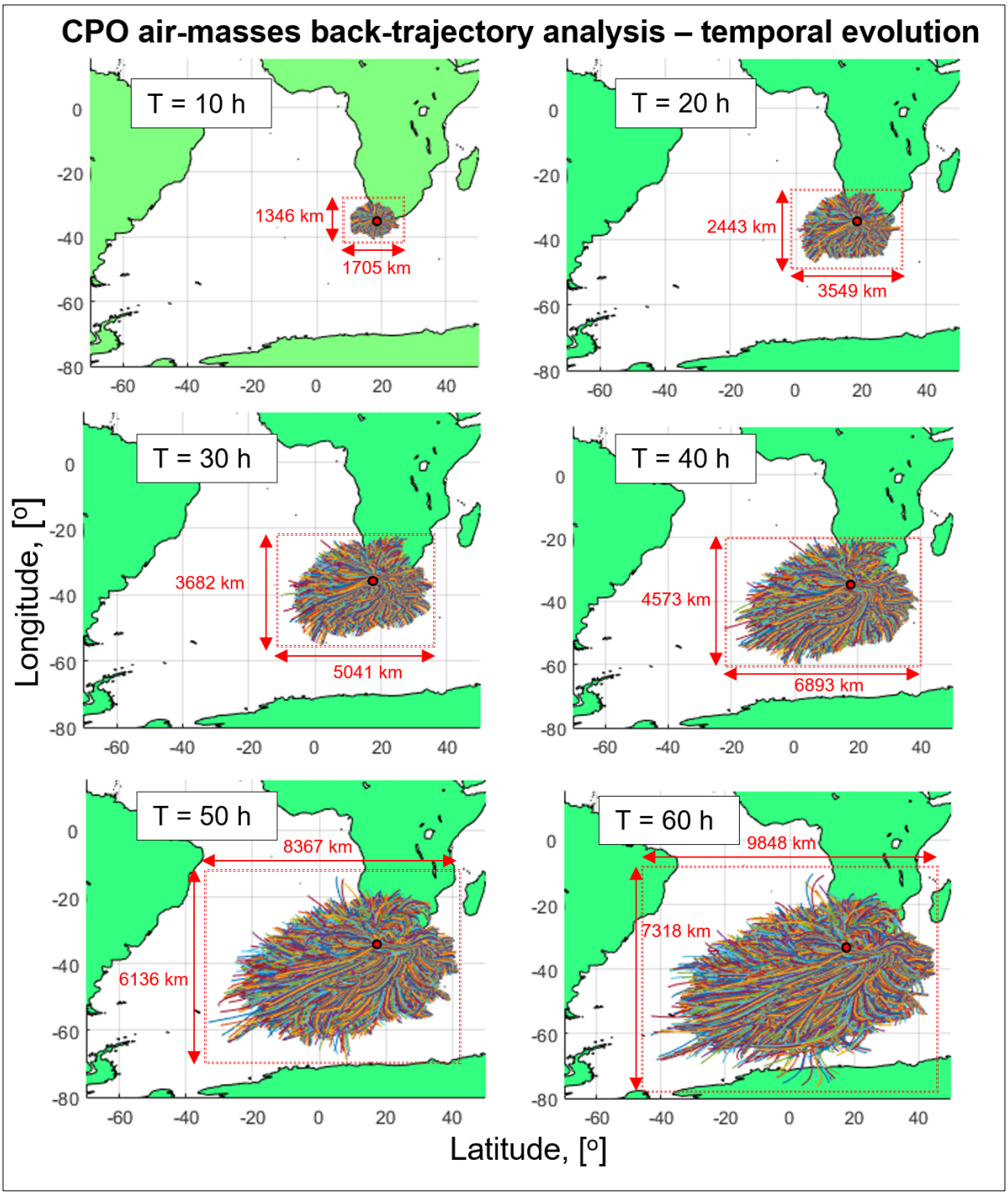

Figure 5-44: CPO atmospheric air-masses back-trajectories computed at various durations (T) back in time. The grid domains for back-trajectory density computations are indicated by the dashed red line and the red dot represents CPO's location.

5.4.1.4. CPO Air-Masses Back-Trajectory – Density Analysis

The above qualitative approach studying the CPO air-mass back-trajectories is once again expanded by performing quantitative trajectory density analysis (see Section 3.4.3). It becomes apparent that most of the higher density regions are strongly localized, similar to CGO (see Figure 5-38). However, the CPO regional (radius of 150 km) density (cluster counts) is about a factor of 2 higher compared to CGO. The largest high prevalence fetch region (> 500 counts) is marine (see Figure 5-45). The slightly elevated continental air-masses fetch regions include two uranium rich areas, Karoo and Namaqua (see Figure 4-10). The mountain ranges (Boland, Cederberg, Langeberg, Qutenique) acts as a barrier for to the central plateau (T = 60 h). A granite rich area, Paarl, is 81 km in the northern direction of CPO. It is well-document that Paarl has some of the highest radon emissions in South Africa due to the radium rich geology (Botha et al., 2017; Lindsay et al., 2008). The Paarl granite mountain is within the high prevalence fetch region (see Figure 5-45) which will contribute to the atmospheric radon observed at CPO under certain wind conditions.

A strong mesoscale recirculation between continental and marine air-masses occurs in the eastern direction from CPO (70° < WD < 120°). A peak in atmospheric radon levels and frequency of radon occurrence are identified between 70° < WD < 120° (see Figure 5-23 and Figure 5-26, c) which coincides with the elevated density region within the easterly direction (see Figure 5-44).

The CPO regional high density (> 1000 counts) clusters decreased from 2008 to 2010 and remerged in 2011 (see Appendix Figure – 43). Inter-annual back-trajectory cluster density variations are evident. The profile of the high-density region during 2015 and 2016 are unique compared to the previous years (see Appendix Figure – 43). During 2015, South Africa experienced a strong El-Niño southern oscillation (ENSO) which resulted in the most extreme national drought in recorded history (Baudoin et al., 2017; Richman and Leslie, 2018). ENSO, is known to generate large-scale changes in sea-level pressures and temperatures, wind and ambient temperatures (Chen et al., 2020; Perry et al., 2020).

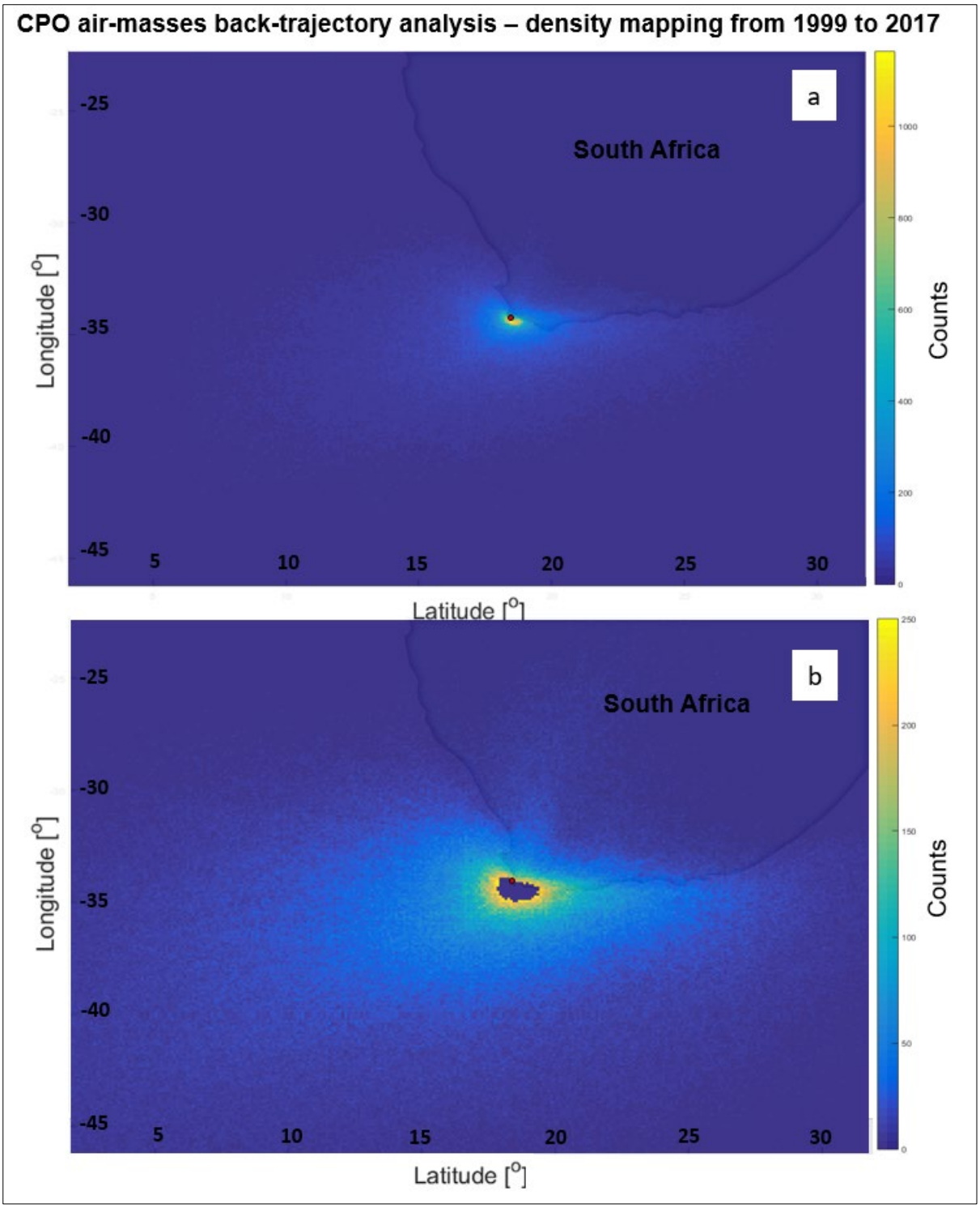

Figure 5-45: (a) CPO cumulative trajectory density (cluster) analysis making use of air-masses back-trajectories up to T = 60 h. The upper land mass represents the Southern tip of South Africa. (b) Contrast filtered cumulative trajectory density plot with clusters associated with counts greater than 250, removed.

The inter-annual continental to the marine number of air-masses ratio analysis results is presented in Figure 5-46. The typical exponential decrease in the CM ratio according to back-trajectory time is once more evident (see Figure 5-46). After about T = 8 h, the inter-annual variation in the C contribution increases up to a maximum of around 15% at about 15 hr and then reduces again to a small part at T = 50 h. The overall inter-annual CPO CM ratios are in general smaller compared to CGO (see Figure 5-39). It will be noted that after T = 60 h the contribution of continental air-masses will be below 5%.

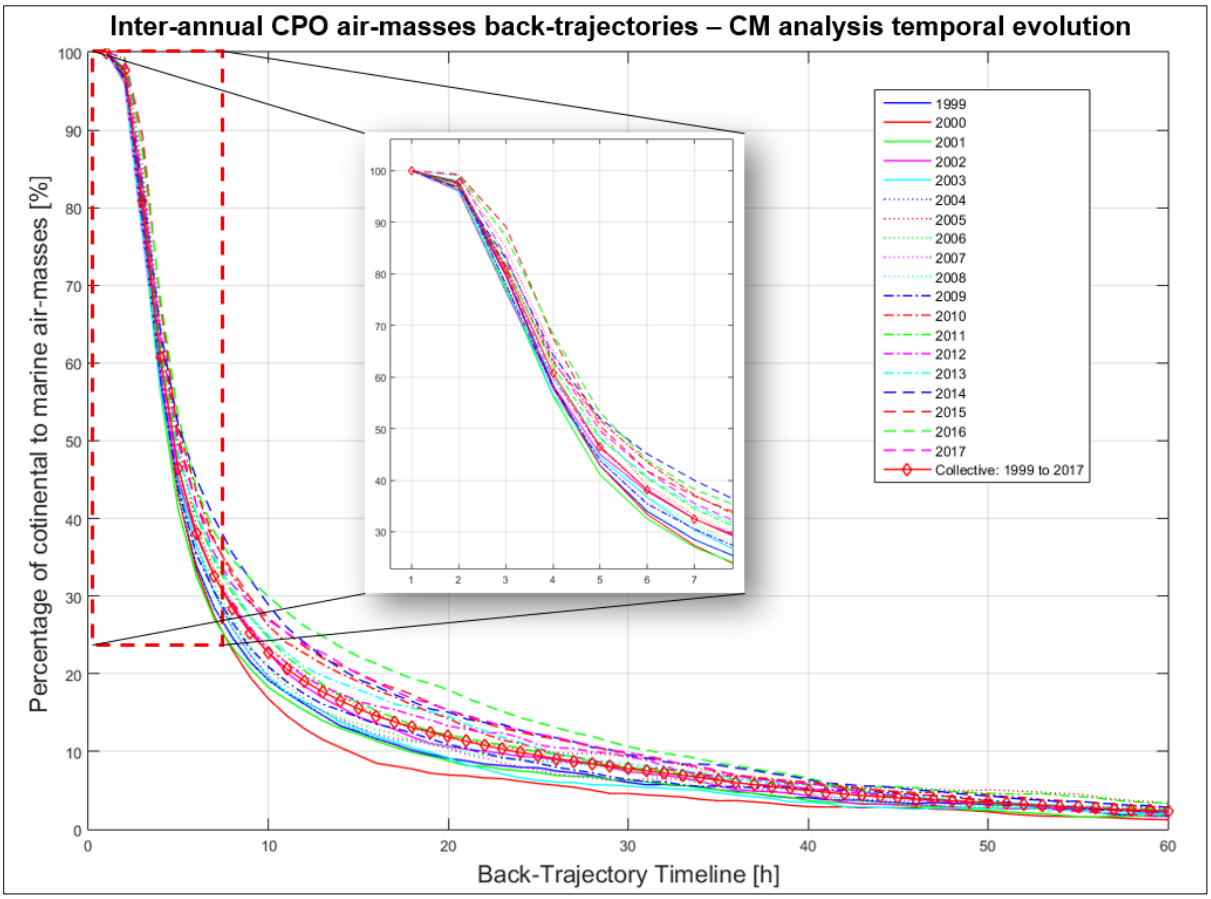

Figure 5-46: Inter-annual CPO continental and marine (CM) air-masses contribution results from 1999 to 2017 computed according to various hours back in time up to T = 60 h.

The CPO ratio of continental to marine air-masses analysis on a monthly temporal scale is presented in Figure 5-47. The highest CPO CM ratio occurs during autumn (MAM) aligning with the season during which atmospheric radon is starting to peak (see Figure 5-11). This seasonal effect is expected based on during the austral autumn and winter the highest radon levels are observed. Higher radon levels are associated with continental air-masses and a higher

CM ratio during this season verifies the statement. CGO's June and July (winter) peaks identified centred at around T = 7 h (see Figure 5-40) are not evident for CPO (see Figure 5-46). The season with the overall lowest CM ratio is during summer (see Figure 5-47). CPO is experiencing some of the lowest radon levels (see Figure 5-11, b) during summer due to a lower incidence of continental air-masses. Contrasting to CGO, CPO's monthly CM ratio is showcasing seasonal behaviourism.

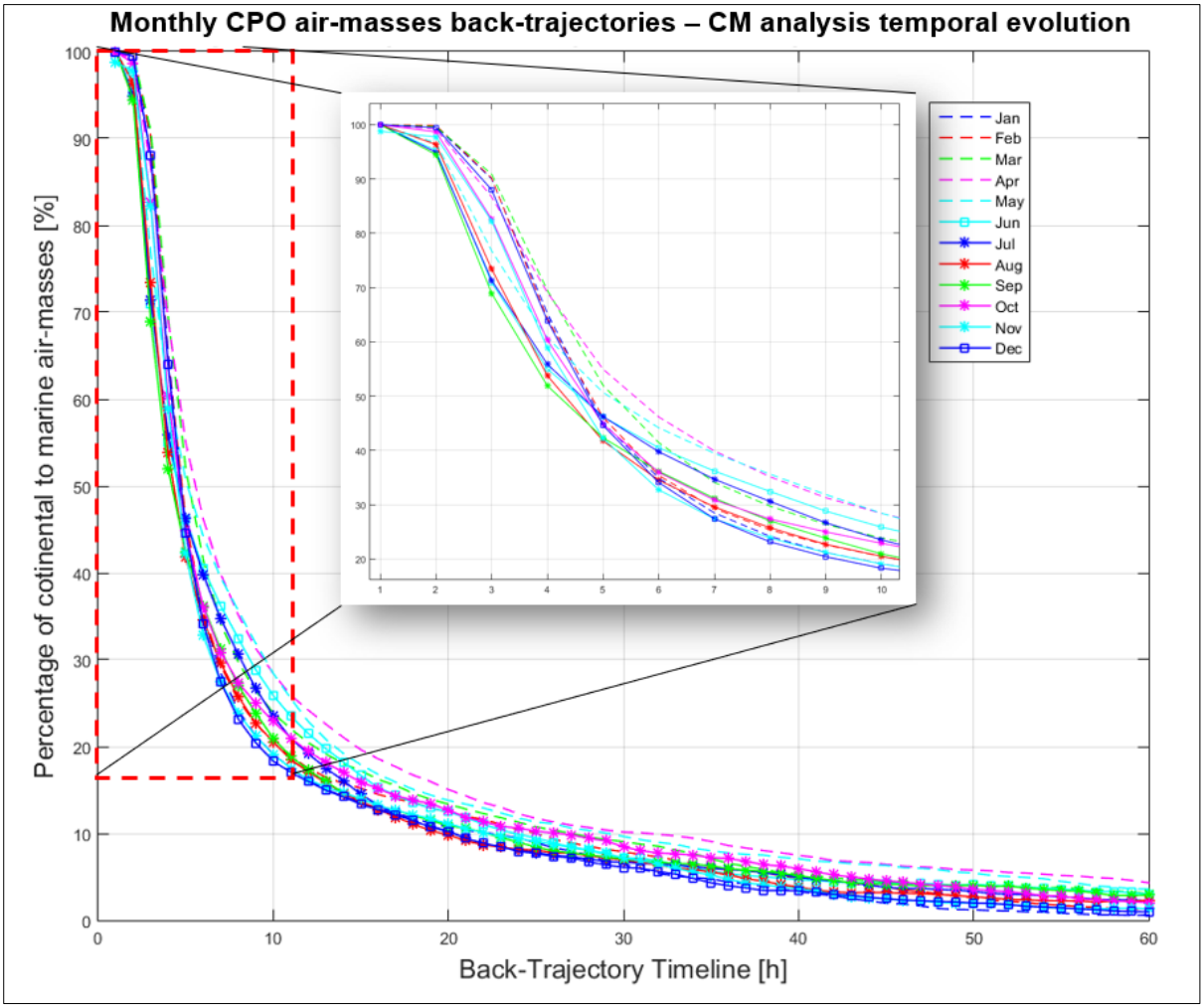

Figure 5-47: Monthly CPO continental to marine (CM) air-masses contributions from 1999 to 2017 according to various hours back in time up to T = 60 h.

The inter-annual trajectory density analysis results are presented in Figure 5-48 (second CM identification algorithm). The total average percentage of marine and continental air-masses incidence at CPO is 73 ± 1% and 27 ± 1% (see Figure 5-48, B), respectively. On the other hand,

for CGO respective average percentage of marine and continental air-masses incidence are 88 ± 2% and 12 ± 2% (see Figure 5-41, B). CPO is subjected to a relatively higher overall incidence of continental air-masses. Making use of linear trend analysis and the MK-test a respective cumulative marine and continental air-masses inter-annual decline of about 6% ($p = 0.624$) and 4% ($p = 0.003$) per annum are confirmed (see Figure 5-48, A). The systematic decrease in atmospheric radon (especially associated with the 95^{th} percentile) from the continental sector C3 (see Figure 5-31, b) coincides with the decrease in air-masses prevalence from continental sectors (see Figure 5-47, A). A decrease in the number of marine air-masses could be linked to an increase in the observed radon levels. It is well defined that marine air-masses are prone to have lower radon levels. The median atmospheric radon decreases ($p = 0.074$) associated with the marine sector O3 (see Figure 5-31, a) coincides with the decrease in marine air-masses (see Figure 48, A). However, this is not the case for the deep baseline air-masses showcasing an evident ($p = 0.006$) increase in atmospheric radon (see Figure 5-32, c).

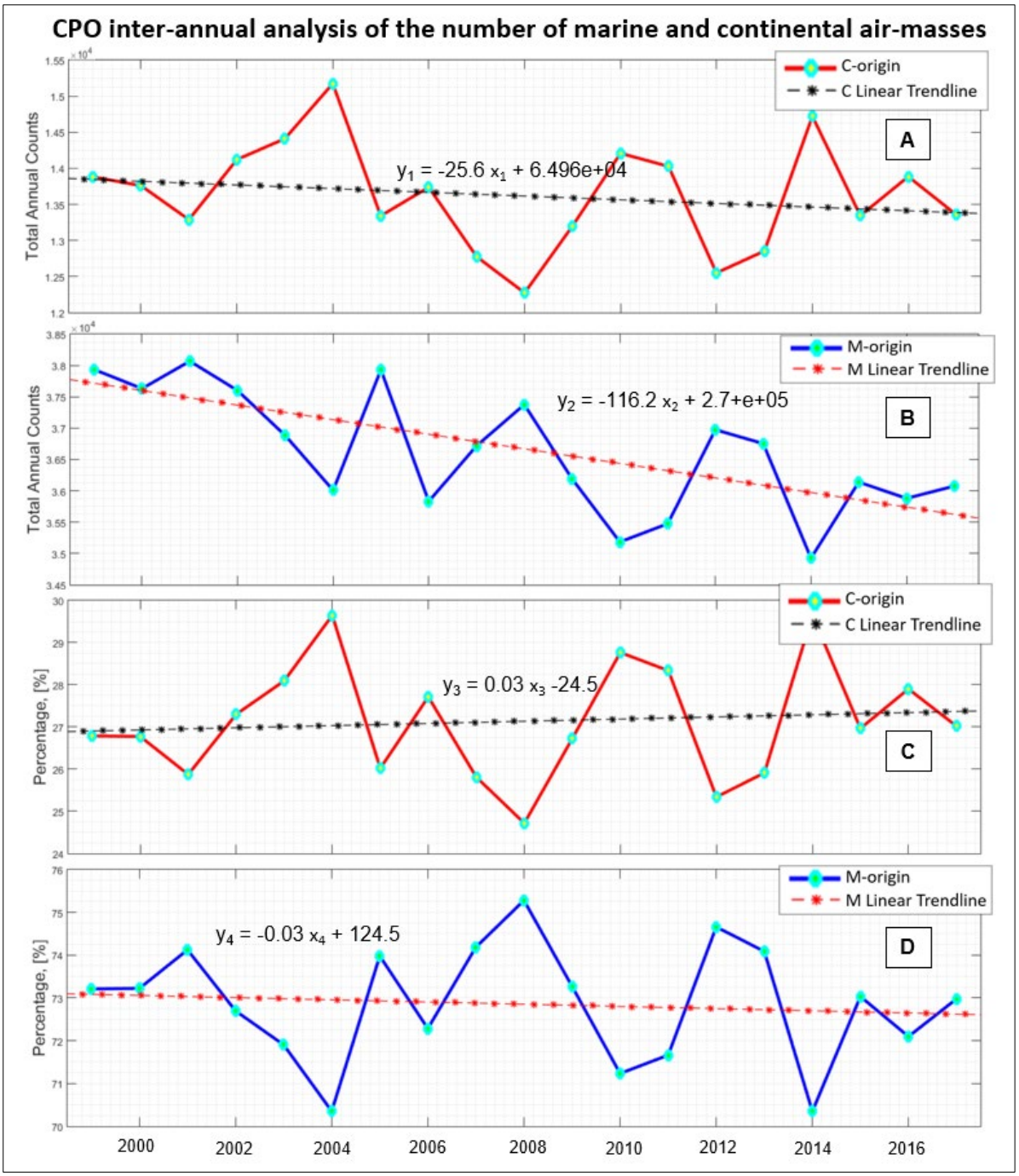

Figure 5-48: (A) Inter-annual cumulative number of continental (C) and marine (M) air-masses making use of back-trajectory time up to T = 60 h from 1999 to 2017 observed at CPO and associated linear interpolation trend analysis. (B) Percentage of CPO observed continental and marine air-masses and associated linear interpolation trend analysis. (C) The percentage of continental air-masses and (D) the percentage of marine air-masses based on the total annual number of air-masses.

CPO's cumulative seasonal incidence of continental and marine air-masses from 1999 to 2017 are presented in Figure 5-49. An increase of about 10% incidence to continental air-masses

occurs during the autumn and winter compared to summer and spring (see Figure 5-49). The seasonal increase in continental air-masses coincides with the seasons as expected when the highest radon levels throughout the year occur (see Figure 5-11, b). A key difference between CPO (see Figure 5-49) and CGO's (see Figure 5-43) seasonal air-masses incidence is that from summer to autumn a continental increase of about 12% applies to CPO. During summer both CGO and CPO are subjected to the largest incidence of marine air-masses.

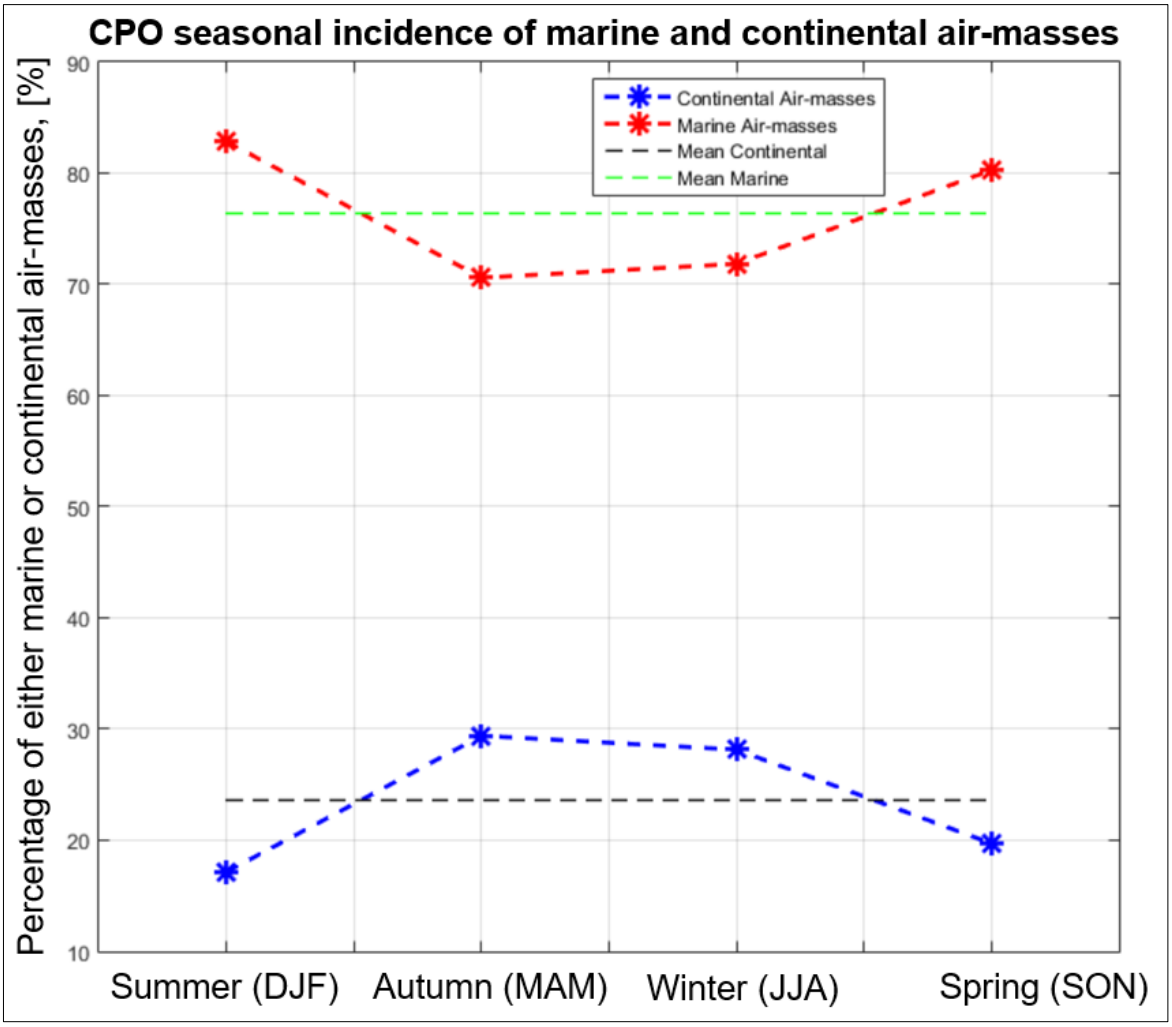

Figure 5-49: Cumulative CPO seasonal incidence percentage of continental and marine air-masses making use of back trajectories up to T = 60 h from 1992 to 2017.

5.4.2. Air-Masses Back-Trajectory – Altitude Analysis

The remaining parameter associated with the air-masses back-trajectory is the altitude above sea level which will be referred to as altitude. The atmospheric radon levels observed depend on the altitude from where it originated (Chambers et al., 2011; CMSA, 2016; Richon et al., 2004). In theory, it is expected that surface air-masses (continental) will exhibit the highest radon levels simply due to the land proximity, which is the physical source of radon (^{226}Ra). In theory, it is expected that a potential decrease in atmospheric radon levels will coincide with an increase in altitude. Furthermore, higher altitude air-masses are expected to exhibit a longer path from source to the observation point resulting in more time to decay and as a result potentially a lower radon level. The historic CGO and CPO air-masses altitude analysis will extend the radon signals characterisation.

5.4.2.1. CGO Air-Masses Back-Trajectory – Altitude Analysis

The CGO altitude temporal evolution histograms are presented in Figure 5-50. The analysis presents an overview of the air-masses altitude at various times in the back-trajectory flight. To be noted, the bin with the highest count is the one with an altitude of 300 m (see Figure 5-50). This is expected since the initial back-trajectory representing the altitude for CGO and CPO are set at 300 m (see Section 3.4.3). The altitude distribution up to T = 10 h is symmetrically centred around 300 m. As the air-masses move further back in time (10 h < T ≤ to 60 h), the largest part of the altitude distribution is a tail of higher altitudes (> 300 m). The higher altitude air-masses illustrates a typical exponential decrease in numbers as the altitude increases (see Figure 5-40). For the lower altitudes range (< 300 m, surface winds) an elevation in the count is noticed in the first bin (50 h ≤ T ≤ 60 h). Most of the air-masses observed at CGO originate from altitudes exceeding that of the observatory. The air-masses observed at CGO, in general, rarely exceed an altitude of 3000 m within the troposphere (see Figure 5-50).

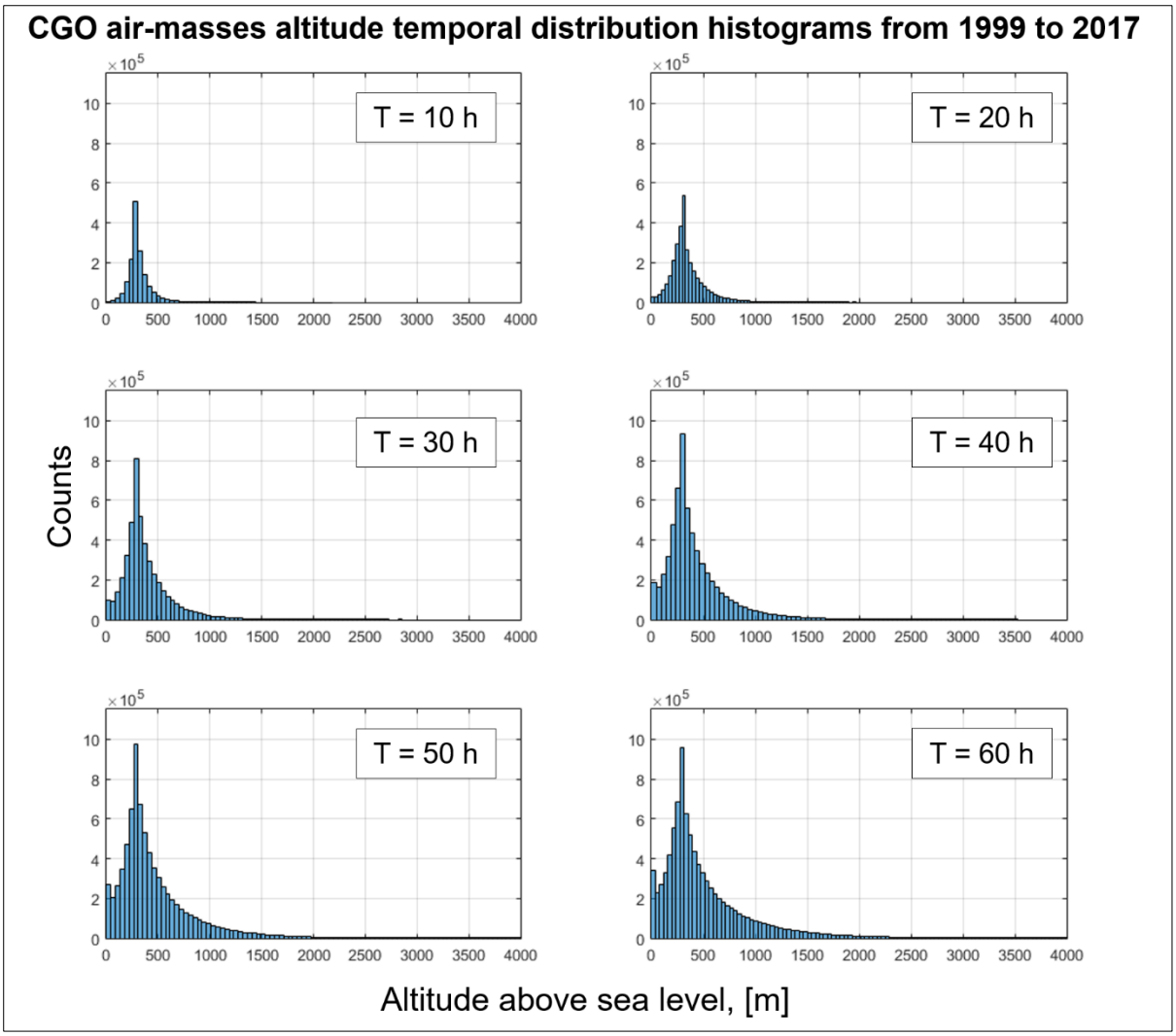

Figure 5-50: CGO air-masses back-trajectory altitude histogram computed for various durations back in time up to T = 60 h.

The CGO inter-annual air-masses back-trajectory altitude density plot for up to 100 h back in time is presented in Figure 5-51. The variations in the air-masses altitude provide insights into atmospheric boundary layer mixing. For any given time after about T = 10 h back in time (y-axis), it is transparent that the inter-annual altitude (x-axis) varies greatly (see Figure 5-51). Some unique regions of interest (ROI) are identified, A1, A2, A3, and A4. The air-masses which CGO are subjected to within about 10 h back in time are mostly below 1000 m (see Figure 5-51, A1). During certain times, the altitude (300 m) remains steady for the entire flight, for example, between 2002 to 2003 (see Figure 5-51, A2, sharp blue lines) indicating minimal vertical mixing.

During mid-2003 and 2014 to 2015, CGO is subjected to very high-altitude air-masses from the upper troposphere (> 7000 m). Especially from 2014 to 2015 (see Figure 5-51, ROI A3) some of the highest air-masses back-trajectories are observed (> 7000 m). This coincides with the strong regional El-Niño southern oscillation of 2015 (Perry et al., 2020). Two or more events are observed during which very high air-masses decrease rapidly in a short time towards CGO (5 h < T < 9 h), mid-2003 and specifically during 2014 (see Figure 5-51, A4). During these two years, the annual radon signal illustrated greater skewed distributions (see Figure 5-29).

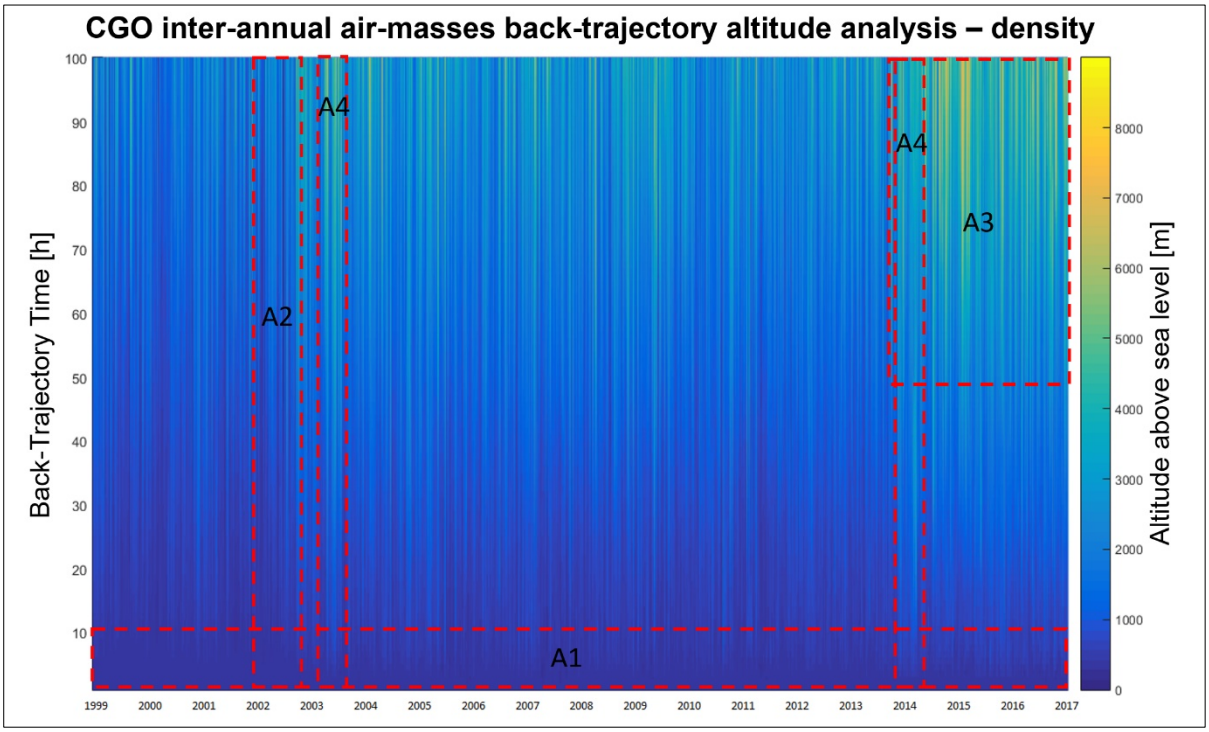

Figure 5-51: CGO inter-annual air-masses altitude densities. Key regions of interest are indicated: (A1) low-altitude air-masses (< 1000 m), (A2) steady continuous low-altitude states for the entire back-trajectory, (A3) high-altitude (< 7000 m), and (A4) rapidly decreasing high-altitude air-masses.

The mean CGO inter-annual altitude according to various back-trajectory times is presented in Figure 5-52. The mean air-mass altitude for an entire back-trajectory, in general, does not exceed 1000 m. After T = 10 h two distinct groups of altitudes become visible (see Figure 5-51 and 5-52). The higher altitudes group include the following seven years, 2007 to 2014. The lower air-masses altitudes group include 1999 to 2004, and 2015 to 2017. During 2016 the

mean altitude back-trajectory up to about T = 16 h is below that of CGO's altitude (see Figure 5-52). Making use of the inter-annual CGO continental to marine (CM) air-masses percentage analysis, and the lowest ratio also occurred in 2016 (see Figure 5-39). The total continental air-masses percentage from Tasmania is at a historic low and the Australian mainland at a high during 2016 (see Figure 5-42). This is an indicator of a larger incidence of surface air-masses coming from Southern Australia during 2016. The associated prominent features in conjunction with the radon signal are as follow; the 95th percentile, continental air-masses, is at a historic low during 2016 (see Figure 5-30, a), and the radon diurnal difference during 2016 is at its lowest (see Figure 5-15, B).

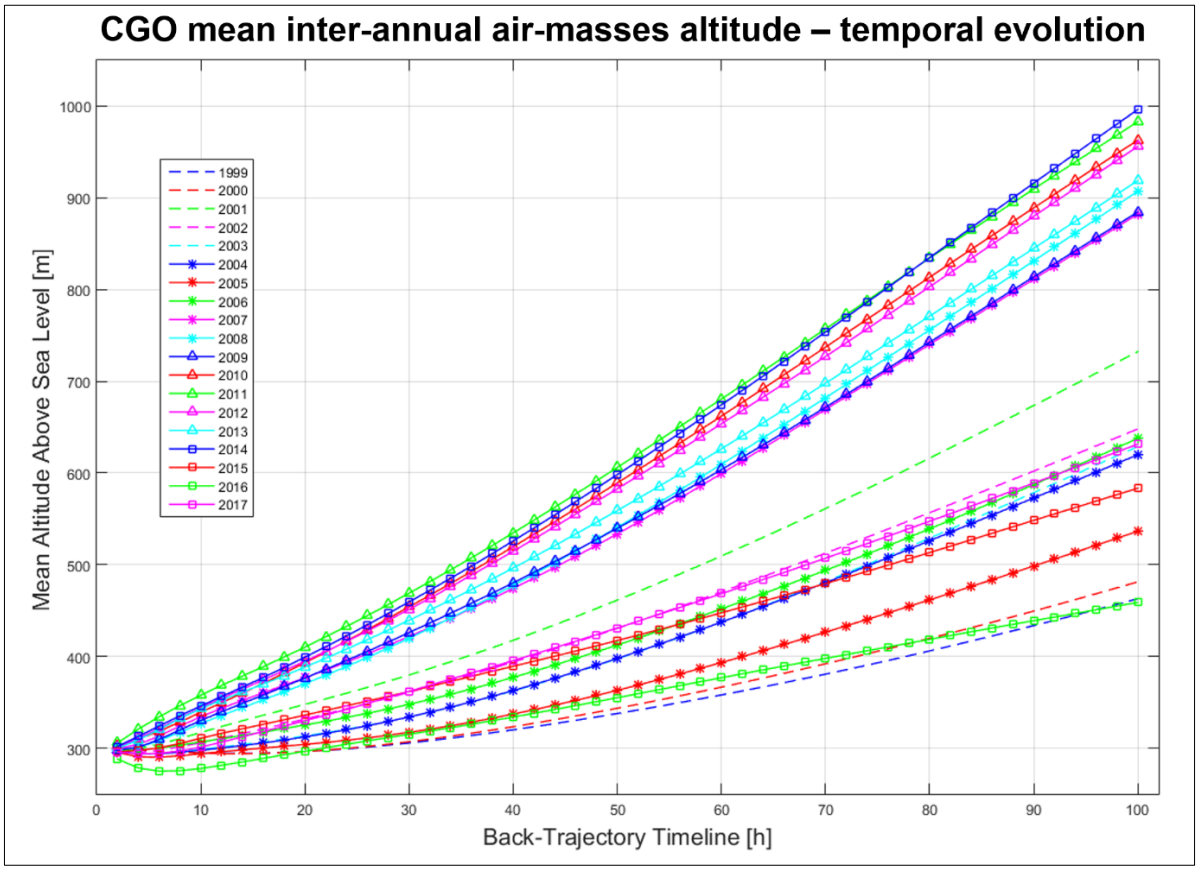

Figure 5-52: Inter-annual CGO air-masses back-trajectories mean altitude above sea level temporal evolution from 1999 to 2017.

The CGO inter-annual altitude composite results are presented in Figure 5-53. From 2006 up to the beginning of 2014 the 25th, 50th, 75th and 95th altitude percentiles exhibit a long period of larger contributions from higher altitude. The most substantial altitude increase occurred

from 2005 to the beginning of 2007 (see Figure 5-53). An increase is noted in CGO radon levels from 2006 to the end of 2008 (see Figure 5-30). The 75th radon diurnal percentile decreased prominently (see Figure 5-15). At around the 2015 El-Niño southern oscillation (Perry et al., 2020), a substantial drop in the altitude of the air-masses occurred (see Figure 5-51).

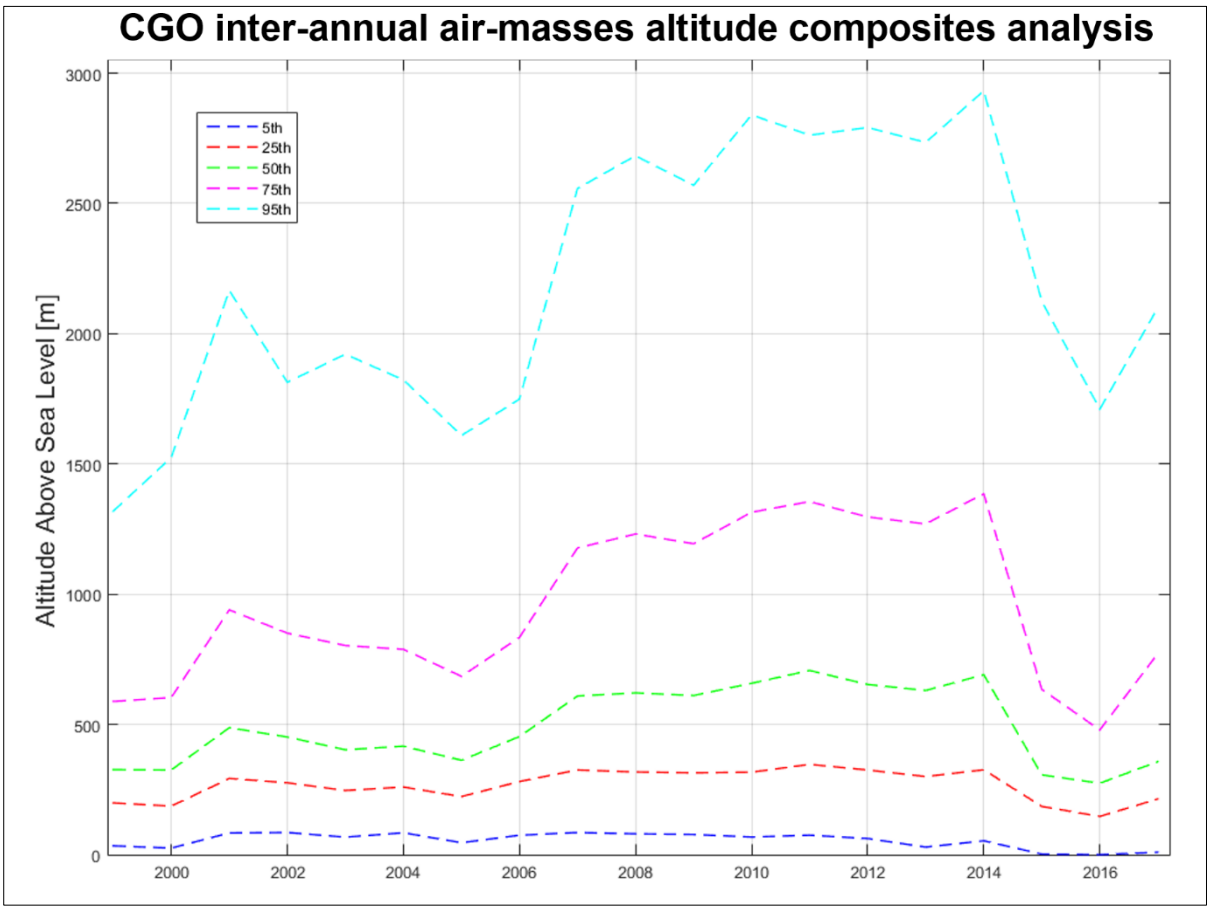

Figure 5-53: Inter-annual CGO air-masses back-trajectories altitude above sea level percentile composite distributions analysis (0 h ≤ T ≤ 60 h) characterised by 5th, 25th, 50th (median), 75th and 95th percentiles from 1999 to 2017.

The monthly (seasonal) CGO air-masses altitude composites distributions results are presented in Figure 5-54. The 95th percentile high-altitude air-masses (> 2100 m) show seasonal variations which can be characterised with a low during the summer, highest increase during winter, and sharpest decrease during spring. The 75th altitude percentile (> 900 m) displays a prominent peak around March (see Figure 5-54). By making use of the median, it will be seen

that the lowest altitude occurs during the winter which is the season in which some of the highest radon levels are observed, see Figure 5-10.

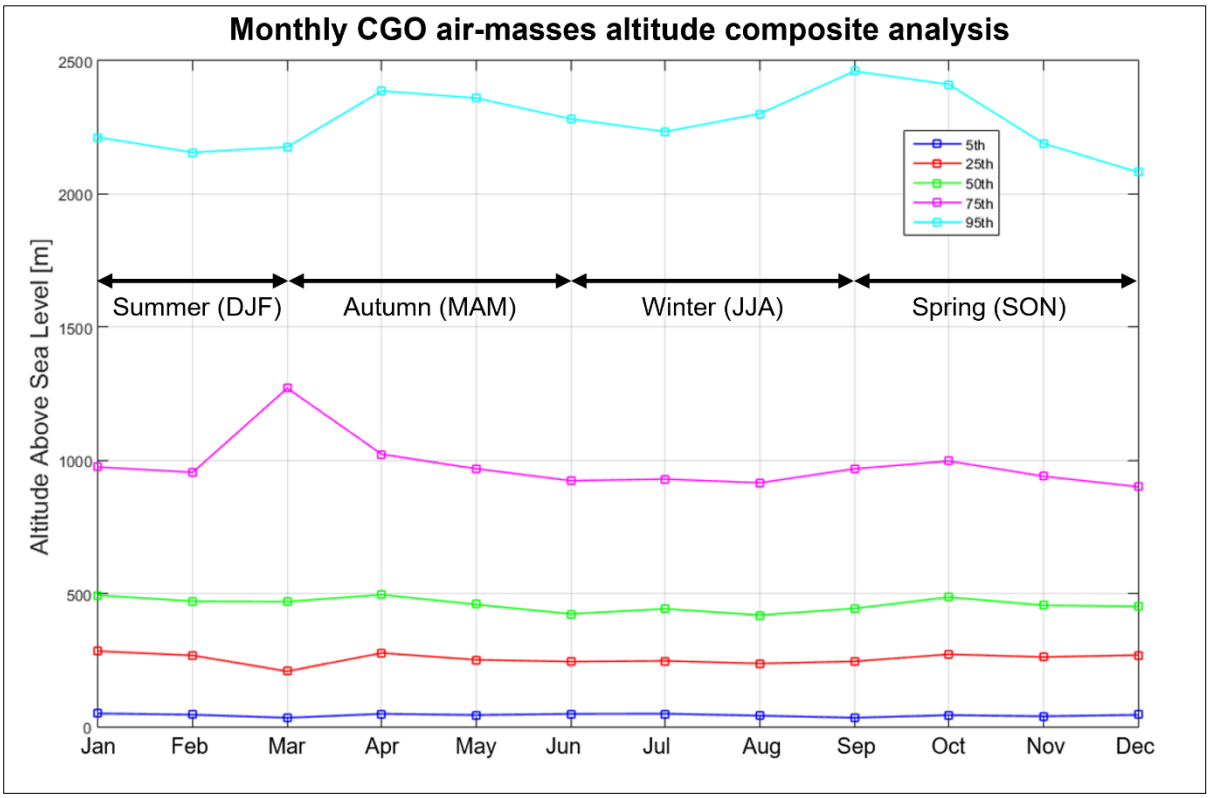

Figure 5-54: Monthly CGO air-masses back-trajectories altitude above sea level percentile composite distributions analysis (0 h ≤ T ≤ 60 h) characterised by 5th, 25th, 50th (median), 75th and 95th percentiles computed up to 60 h back in time from 1999 to 2017.

5.4.2.2. CPO Air-Masses Back-Trajectory – Altitude Analysis

The CGO air-masses altitude back-trajectory characterization is performed within Section 5.4.2.1 and will now be compared to that of CPO in this section. The CPO altitude temporal evolution histogram is presented in Figure 5-55. CPO, in general, is exposed to air-masses from higher altitudes. CPO exhibits a longer altitude "tail" (see Figure 5-55) compared to CGO (see Figure 5-50). A similar comparison is noticed in section 5.2.1 where the CPO radon histogram is wider (longer tail) compared to CGO (see Figure 5-2). CPO (see Figure 5-55) is subjected to a factor of about two times more surface winds than CGO (see Figure 5-50).

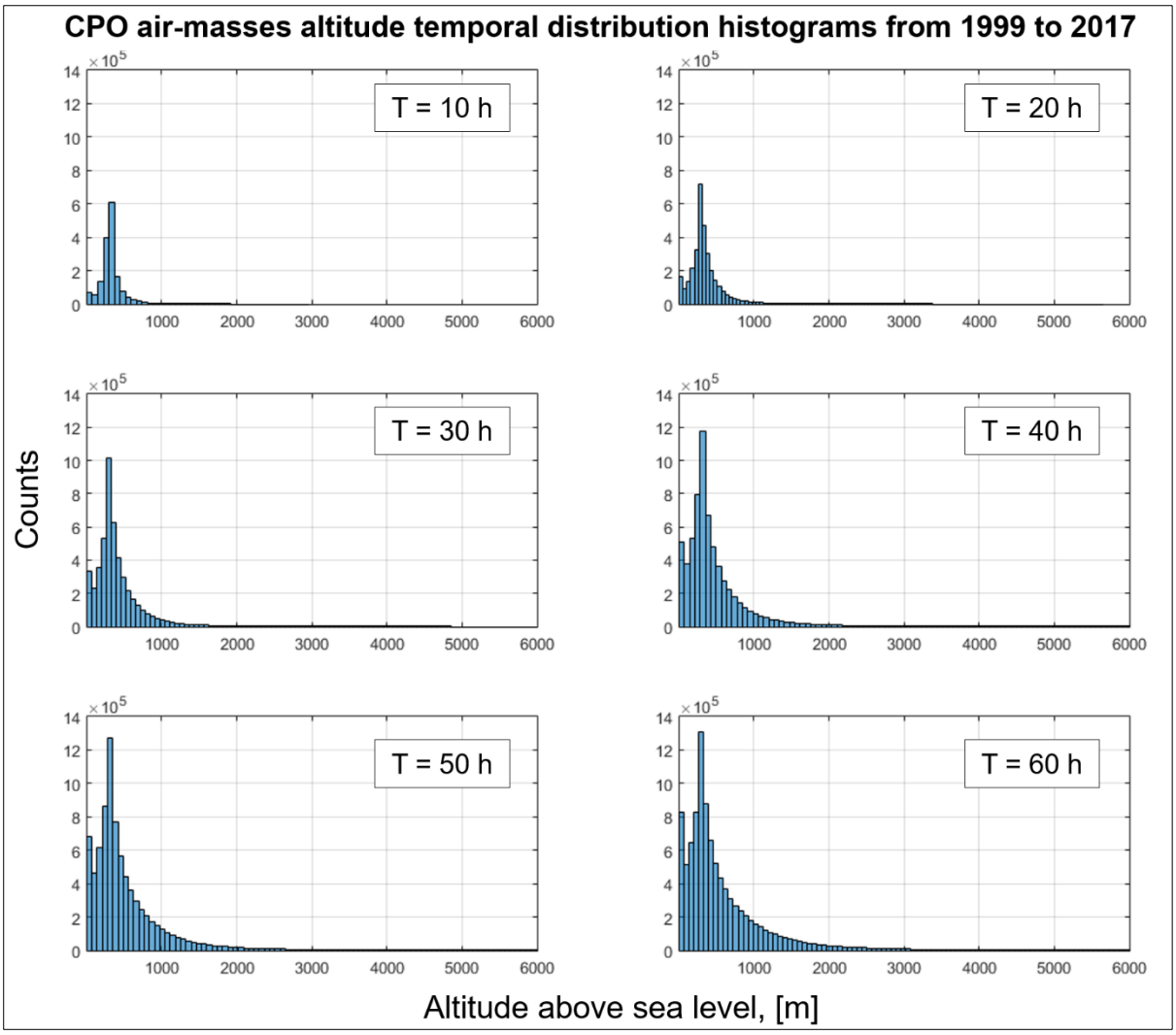

Figure 5-55: CPO air-masses back-trajectory altitude above sea level histogram computed for various duration back in time up to T = 60 h.

The CPO inter-annual air-masses back-trajectory altitude density plot projected back in time for up to 100 h is presented in Figure 5-56. The CPO back-trajectory altitude density profile (see Figure 5-56) is similar to CGO's (see Figure 5-51) in many regards. Most prominent is the coinciding high-altitude (> 7000 m) air-masses encountered around 2015 with the strong El-Niño southern oscillation. Up to about T = 10 h, the air-masses are coming from an altitude of mostly below 1000 m (see Figure 5-56). A key difference noted is that CPO is subjected to air-masses with an altitude as high as 11 000 m (upper troposphere).

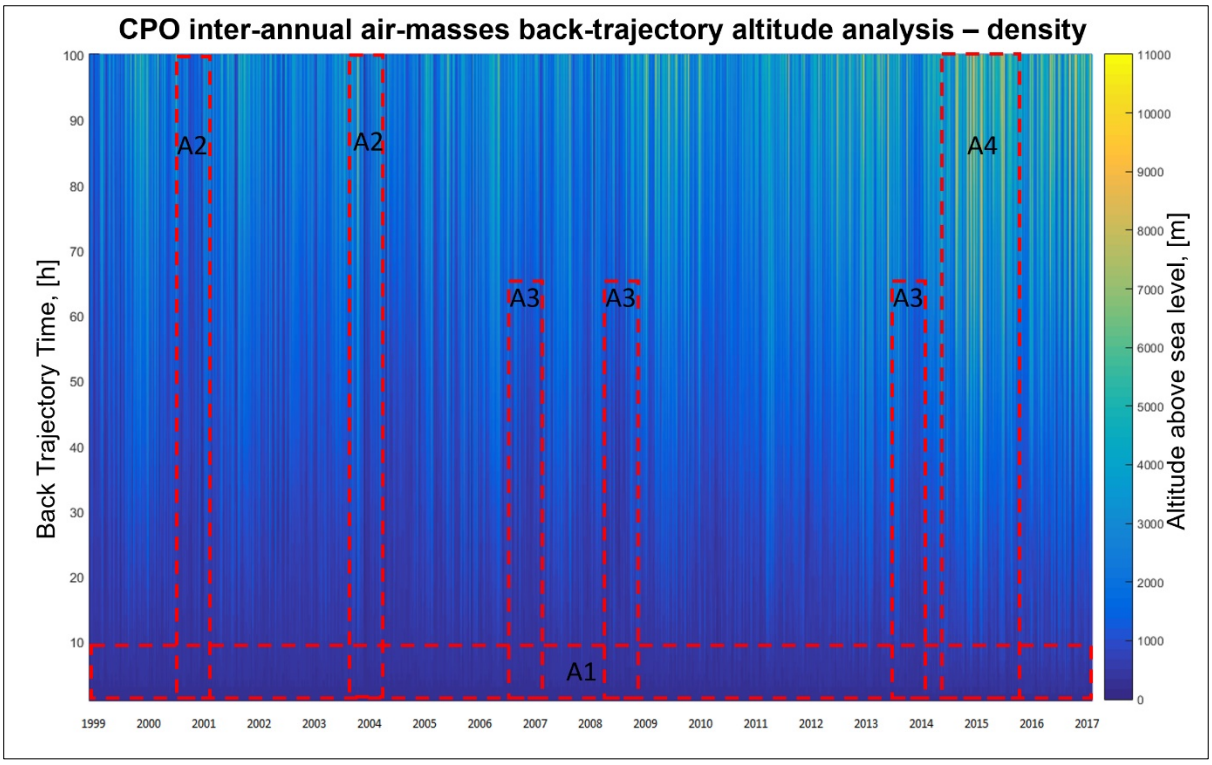

Figure 5-56: CPO inter-annual air-masses altitude densities results. Key regions of interest are indicated: (A1) low-altitude air-masses (< 1000 m), (A2) steady continuous low-altitude states for the entire back-trajectory, (A3) regions of long low-altitude pockets, (A4) high-altitude (< 8000 m) air-masses.

Similar to CGO's mean inter-annual altitude (see Figure 5-52), at CPO two distinct air-masses altitude groups can be identified (see Figure 5-57). A higher and lower altitude group. Nonetheless, there are differences between the results from CGO and CPO. The groups become distinguishable considerably quicker back in time (see Figure 5-55, T = 2 h) relative to CGO (see Figure 5-52, T = 10h). The lower CPO altitude group is also considerably larger with respect to individual years of data. The high-altitude air-masses CPO group occurs for the following years, 2010 to 2014. An anomaly which is observed is the air-masses inbound to CPO from 2015 to 2016 is lower than the observatory itself. In other words, predominantly marine surface winds (see Figure 5-57). Furthermore, the air-masses remain below an altitude of 500 m for the remainder of the back-trajectory (see Figure 5-57) during these two years. The question now arises whether this phenomenon is connected to the strong El-Niño southern oscillation of 2015. No variations can be identified in the radon signals in 2015 apart from the 95th percentile (continental air-masses) which are then at its lowest (see Figure 5-31, b).

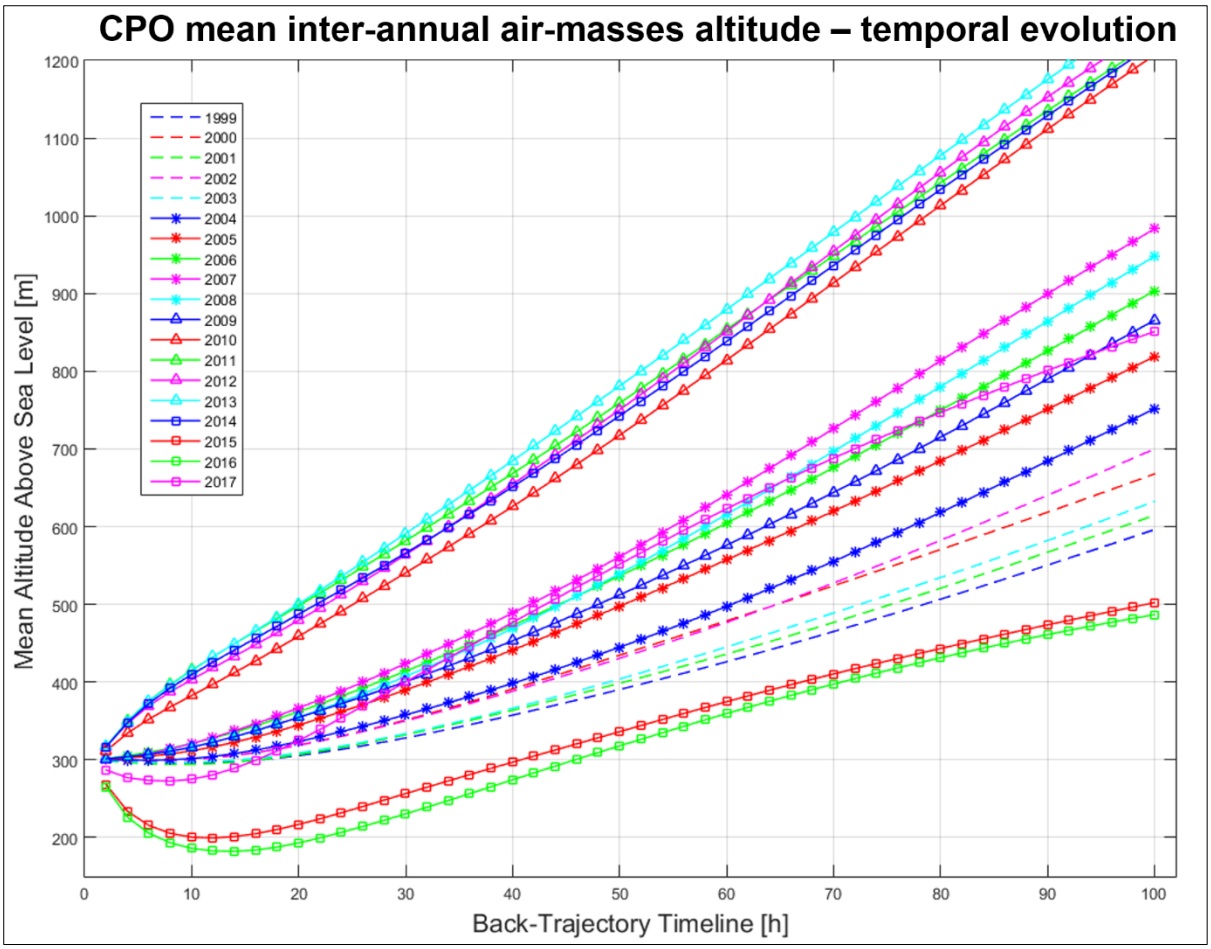

Figure 5-57: Inter-annual CPO air-masses back-trajectories mean altitude temporal evolution from 1999 to 2017.

For both CGO (see Figure 5-53) and CPO (see Figure 5-58), the inter-annual altitude composite analysis shows similar results. However, it will be noted that CPO's strong increase in air-masses altitude occurs three years (see Figure, 5-56, 2009) after that of CGO (see Figure 5-53, 2006). CPO exposure to record low-altitude air-masses are again evident during 2015 and 2016 (see Figure 5-58). CPO's inter-annual air-masses altitude composite profile (see Figure 5-58) is similar in many regards to CGO, the highest occurs from 2010 to 2014 and record lows from 2015 to 2016 (see Figure 5-53).

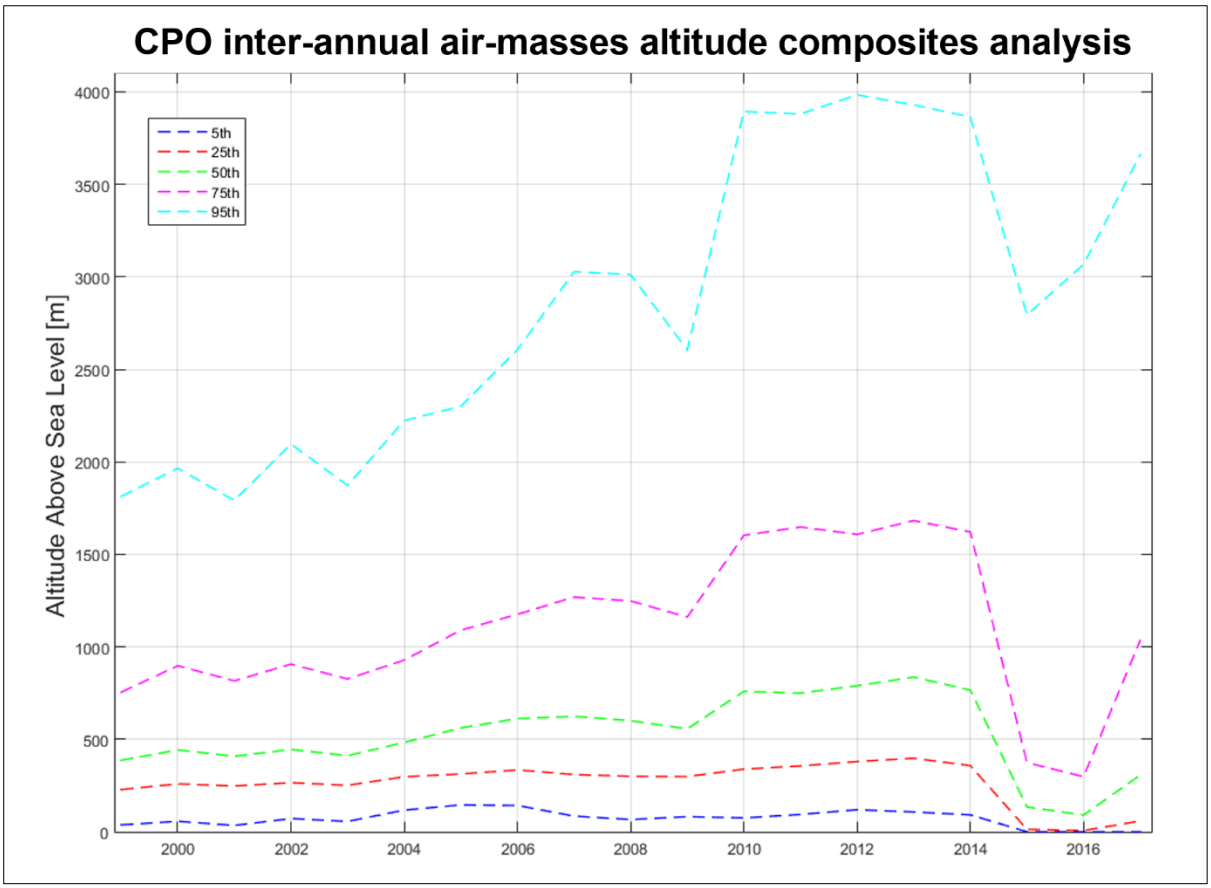

Figure 5-58: Inter-annual CPO air-masses back-trajectories altitude percentile composite distribution analysis (0 h ≤ T ≤ 60 h) for 5th, 25th, 50th (median), 75th and 95th percentiles from 1999 to 2017.

The monthly (seasonal) CPO air-masses back-trajectory altitude analysis is presented in Figure 5-59. The higher altitude air-masses, 95th percentile, illustrates seasonal dependence with a maximum during the end of winter and minimum during spring and summer. No prominent altitude seasonal dependence is evident when making use of the median (see Figure 5-59). It is noted that monthly median altitude for both CPO (see Figure 5-59) and CGO (see Figure 5-54) occurs at an altitude of about 500 m. A unique feature is identified exclusively during March in which both CPO and CGO's 75th percentile is peaking and for the 25th percentile, a slight decline occurs.

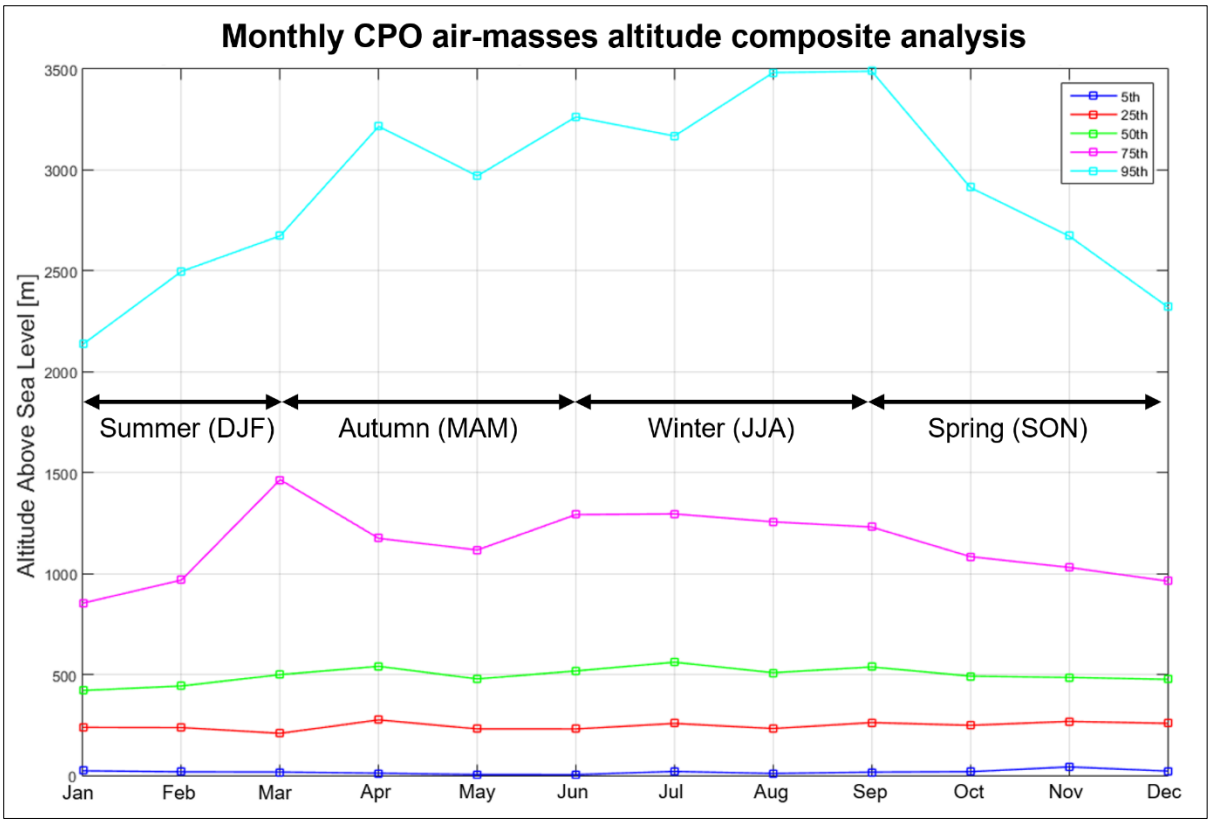

Figure 5-59: Monthly CPO air-masses back-trajectories altitude percentile composite distributions (0 h ≤ T ≤ 60 h) characterised by 5th, 25th, 50th (median), 75th and 95th percentiles from 1999 to 2017.

CHAPTER 6 General Conclusion

6.1 Discussion and Conclusion

The primary focus of the characterisation study presented in this thesis is the analysis, discussion and interpretation of the Cape Point (CPO) and Cape Grim (CGO) atmospheric radon signals. These Southern Hemisphere coastal observatories were selected for this study based on a similar geographical / climatological position (S 34° - 40°), with the Southern Ocean directly to the south and large semi-arid land masses to the north. The downward limb of the Hadley cell brings surface air slowly southwards at these latitudes, into the predominantly westerly flow with its embedded synoptic frontal systems. There is some evidence from previous studies (e.g., Banerjee et al., 2020; Kuttippurath et al., 2018) that the chosen region may be experiencing changes in large-scale atmospheric circulation patterns connected with climate.

The hemispheric changes in climate can be put in context based on the following. In 1987 the international Montreal Protocol was instated banning the production of ozone-depleting substances as a response to the anthropogenic hole in the ozone layer above Antarctica (Epstein et al., 2014). As a result of the instated protocol, the hole in the ozone layer is continuing to recover (Kuttippurath and Nair, 2017). The Antarctic ozone hole contributed to changes in Southern Hemispheric circulations(Banerjee et al., 2020; DWJ Thompson, 2002; NC Swart, 2012). A recent impact study referred to in this thesis (Banerjee et al., 2020) showcased that before 2000 the Southern Hemisphere mid-latitude jet stream had been gradually shifting towards the South Pole, and the Hadley cell, associated with tropical rain-belts, hurricanes, trade winds and subtropical deserts, had been getting wider. Banerjee et al. (2020) showed that the widely reported Southern Hemisphere circulation trend paused, or slightly reversed around the year 2000. These variations correspond to significant changes in the Southern Hemispheric climate (Kuttippurath et al., 2018).

The atmospheric radon observations used in this study would not have been achievable without the advanced ultra-sensitive ANSTO research detectors. The unique dual-flow-loop two filter radon detector design (see Section 3.2) with autonomous calibration is capable of achieving an LLD of about 33 ± 10 mBq/m^3 (see Table 3-1). Extensive post-measurement data analysis, quality control, quality assurance and processing are performed to ensure that high-quality radon signals are sustained.

In Chapter 5, the main analysis results are presented. The cumulative radon time-series (signals) and distributions analysis results are first presented in Section 5.2.1; distributions, periodicities and trends in the radon signals are then examined using a combination of spectral, compositing and other analysis tools. The CGO and CPO radon time-series can be characterised by seasonal cycles of maxima during the austral winters (greater occurrence of frontal passages) and minima during the summers (see Figure 5-1, 5-10 and 5-11). The winter maxima correspond to a higher incidence of continental air-masses compared to the summer minima corresponding to more marine air-masses. The radon distributions are strongly skewed (Figure 5-3), exhibiting a large number of events falling into a compact range of low values (corresponding to marine air-masses), and a smaller number of events with high radon values spread over a wide range (corresponding to continental air-masses). The CPO (see Figure 5-2, A2) radon distribution is wider (thicker "tail") compared to that of CGO (see Figure 5-2, A4). This occurs due to CPO being subjected to a larger number of continental and mixed air-masses, which is independently verified by making use of the high-quality back-trajectory calculations combined with cluster analysis (see Section 5-3, Figure 5-41, C, and Figure 5-48, C). The respective total average percentage of marine and continental air-masses incident at CPO is 73 ± 1% and 27 ± 1% (see Figure 5-48, B), whereas for CGO it is 88 ± 2% and 12 ± 2% (see Figure 5-41, B), based on hourly data. The cumulative average radon levels at CGO (1992 to 2017) and CPO (1999 to 2017) are about the same, 708 mBq/m^3 and 674 mBq/m^3, respectively (see Table 5-1). Nevertheless, CGO exhibits a smaller median of 177 mBq/m^3 which is about two times smaller compared to CPO, and a maximum of 16196 mBq/m^3, which is about two times larger than CPO (see Table 5-1). The high altitude volcanic MLO is subjected to the lowest overall atmospheric radon levels.

The power spectral FFT analysis has proven to be a valuable analytical tool. The spectral analysis provided insightful information on the temporal periodic features embedded in the atmospheric radon signals. A large amplitude annual (seasonal) periodicity is evident for CGO (see Figure 5-4), CPO (see Figure 5-6) and MLO (see Figure 5-8) in the power spectra. Prominent annual radon periodicities are expected due to the re-occurring summer minima and winter maxima (see Figure 5-2, 5-10 and 5-11). Marked periodicities were also apparent on shorter timescales (< 3 days) in the spectra, corresponding to diurnal variability in the data record. A family of diurnal and sub-diurnal peaks are identified for CPO (see Figure 5-7) at frequencies of 1.03 ± 0.04 day^{-1} and 2.07 ± 0.15 day^{-1}. The MLO radon diurnal and semi-diurnal signals (see Figure 5-9) are stronger compared to CPO (see Figure 5-7), again at

frequencies of 1.01 ± 0.01 day^{-1} and 2.01 ± 0.07 day^{-1}. However, for CGO the diurnal radon periodicities are non-existent (see Figure 5-5). The annual peak reflects main seasonal changes in the patterns of offshore versus onshore flow associated with regional/hemispheric circulation patterns, whereas the diurnal and semi-diurnal peaks together reflect the impact on the stations of local patterns of nocturnal radon build-up over land, and the interplay between mesoscale sea/land breezes. The spectral analysis, particularly the results obtained from the power spectral FFT analysis, provided the catalyst to conduct a more in-depth proceeding diurnal radon analysis (see Section 5.2.4).

The primary aim of the diurnal analysis is to study the radon signal according to its respective day and night variations over long durations. The diurnal CGO and CPO radon cycles are mutually characterised by a shallow minimum during the early evening (18:00 – 20:00) when the lower atmosphere is most deeply mixed, and a strong maximum during late morning (10:00 to 11:00) when the lower atmosphere is likely at its shallowest (see Figure 5-13). It is expected that the boundary layer will be at its shallowest in the early morning, not in the late morning (convective boundary layer starts to grow after sunrise) as observed. The delayed timing is due to the complex local mesoscale effects. For both Southern Hemisphere observatories, the radon levels are in general higher during daylight hours compared to the night, mainly because the large radon diurnal maximum occurs in the late morning (daylight) as mentioned above. In contrast, the opposite is true at MLO (see Figure 5-13 and Figure 5-14), which exhibits a strong minimum during the late morning (tropospheric air descending from above) and a weak maximum during the late afternoon (anabatic flow up the sides of the volcano, driven by solar heating). Seasonal exceptions did occur (see Figure 5-20, to 5-22), especially at CPO when observing inter-annual variations in the seasonal diurnal analysis results from 2012 to 2017 (see Figure 5-21). These anomalies apply to all the seasons, however, particularly during spring (see Figure 5-21, d). A strong emphasis is to be placed on the time between 2015 and 2017 at CPO. This was the years leading up to Cape Town getting within days (2017) to become the first metropolitan city in the world running out of freshwater due to an intense regional drought. This natural disaster is also known as “day-zero” (Booysen et al., 2019; Richman & Leslie, 2018). South Africa experienced a record national drought in 2015 (Baudoin et al., 2017). This coincides with the strong El Niño of 2015 which affected the Southern Hemispheric circulations (Perry et al., 2020; Thomson et al., 2003). Several CPO inter-annual seasonal diurnal radon anomalies are observed in 2015 to 2017 (see Figure 5-21) which could be connected to above-mentioned meteorological events. Inter-annual diurnal radon composite

variations are evident, especially when observing the 75th percentile (see Figure 5-15, 5-16, and 5-17). The CGO median diurnal amplitude vanished during 2016 (see Figure 5-15, B) overlapping with the year during which it was exposed to the lowest observed altitude air-masses (see Figure 5-53). Seasonal variability in CGO, CPO, and MLO diurnal radon differences are largest during autumn and winter (see Figure 5-18, b and d, and Figure 5-19, b), probably due to changes in the occurrence and strength of mesoscale circulations. CPO winter and summer diurnal radon variations significantly increased from 2012 onwards (see Figure 5-21, b and d), reflecting increases in the strength of mesoscale circulations and seasonal atmospheric stability variations. CPO exhibits a larger diurnal percentile composite distribution range compared to CGO (see Figure 5-14). This observation is verified with the spectral analysis results of a strong CPO PSD inter-annual diurnal peak (see Figure 5-7, lower) compared to the almost non-existent peak of CGO (see Figure 5-5, lower). Nonetheless, assuming that a large diurnal radon difference (amplitude) is correlated with a strong PSD diurnal peak is not necessarily applicable. For instance, MLO is exhibiting the strongest PSD inter-annual diurnal radon amplitudes (see Figure 5-9), nonetheless, exhibits the smallest diurnal difference based on the day vs night radon level differences (Figure 5-14).

The two meteorological parameters which provided the most promising results to characterise the radon signals are the wind direction (WD) and wind speed (WS). The frequency of occurrence (events) observed is strongly dependent on the WD (see Figure 5-26). At CGO, the wind directions most commonly encountered are from the broad oceanic "baseline" sector (160° to 320°), as well as a smaller band corresponding to easterly flow through Bass Strait. At CPO, two prominent WD occurrence peaks are found, corresponding to flow through False Bay (85°) and from the Indian Ocean (115°). After this, there is a low occurrence of wind directions from the SE and S, and then a slow increase in occurrence from S to NW. As expected, elevated CGO and CPO radon levels (see Figure 5-23, > 2000 mBq/m^3) are directly associated with WDs originating from continental fetch regions (see Figure 4-5), whilst low radon levels are evident from the oceanic sectors. Seasonal variations are also evident in the distribution of radon with WD. At both CGO and CPO, higher radon values occur in continental sectors in the austral autumn and winter (see Figure 5-24 and 5-25). CGO is subjected to the deepest and most consistent baseline air-masses (< 50 mBq/m^3) in the wind fetch sector from 210° to 270° (Southern Ocean / Indian Ocean; see Figure 4-5) during autumn (see Figure 5-24).

One of the main aims is to identify any long-term atmospheric radon variation trends. The Southern Hemisphere radon signals overlap with the time of the extensive changes in the hemispheric circulations (Banerjee et al., 2020; Chen et al., 2020; Thompson et al., 2002; Jayanarayanan et al., 2017). The discussion focusses firstly on the radon signal associated with continental air-masses and then proceed to marine air-masses. It is systematically demonstrated that a declining trend in the CGO and CPO radon levels associated with continental air-masses occurred over the period of the observations. The downward trend is most apparent for the higher radon percentiles (continental air-masses). By making use of the CGO and CPO inter-annual radon trend and statistical significance analysis (see Figure 5-30, a and b), the downward trend is conclusive (1999 to 2017). Making use of the associated CGO 95th radon percentile an estimated annual decrease of 59 mBq/m^3 per year with a strong statistical significance of $p = 6 \times 10^{-5}$ occurred (see Figure 5-30). The radon level decline in continental air-masses is independently verified by making use of air-mass back-trajectories (HYSPLIT) by performing trajectory density trend and statistical significance analysis. CGO (see Figure 5-39) and CPO (see Figure 5-46) CM ratio between 1999 and 2017 exhibited a low inter-annual variation, especially for back-trajectories times beyond T = 40 h. The CM air-masses ratio decreases exponentially according to the back-trajectory time illustrating that both CGO and CPO are exposed predominantly to air-masses originating from a marine origin. It should be noted that the radon signals and the back-trajectories are two independent systems. The respective inter-annual CGO (see Figure 5-41, A) and CPO (see Figure 5-48, A) observed number of continental air-masses are similarly illustrating a decrease. The CGO (see Figure 5-33) and CPO (see Figure 5-31, a) inter-annual radon percentile composite distributions spanning continental fetch sectors are similarly showing a systematic downward trend. The focus now will be placed onto the long-term radon variations associated with marine air-masses. Making use of the respective CGO and CPO collective analytical results obtained from the inter-annual radon composites (see Figure 5-30, a) combined with the inter-annual radon according to specified WD-sectors (see Figure 5-31, a, Figure 5-32, c, Figure 5-34, and Figure 5-35, d), a small increase in atmospheric radon associated with marine air-masses is plausible. Making use of the results obtained from the back-trajectory density (cluster) analysis an overall decline in the number of marine air-masses at CGO (Figure 5-41, B) and CPO (Figure 5-47, B) is observed. It is expected that a decrease in the incidence of marine air-masses will result in a slight increase in atmospheric radon being observed. The median represents the bulk of the radon signal considered to be a mixture of continental and marine air-masses. By making use

of CGO and CPO inter-annual radon median analysis results (see Figure 5-30 and Table 5-5), no statistically significant variations from 1999 to 2017 are observed.

Computation and analysis of air-mass back-trajectory have proven to be a valuable tool to expand on the radon signals characterisation, even though it has been mainly limited to 60 hours back in time. The atmosphere is the primary transport system of outdoor radon which emphasizes the importance of tracking air-masses. Each data point of a specific back-trajectory in time is classified as either C (higher radon levels expected) or M (lower radon levels expected) on an hourly resolution from 1999 to 2017. The CGO (see Figure 5-39) and CPO (see Figure 5-46) inter-annual percentage of continental to marine air-masses (CM) decreases exponentially as the trajectories move back in time. The predominant number of air-masses observed at CGO (see Figure 5-41) and CPO (see Figure 5-48) are from a marine origin. This observation is confirmed with a total inter-annual average of 75 ± 4% of the recent continental air-masses originating from the Southern Australian mainland (see Figure 5-37) and the remaining 25 ± 4% from Tasmania (see Figure 5-42). The total average percentage of marine and continental air-masses incidence at CPO are 73 ± 1% and 27 ± 1% (see Figure 5-48, B), respectively. On the other hand, for CGO respective average percentage of marine and continental air-masses incidence are 88 ± 2% and 12 ± 2% (see Figure 5-41, B). CGO is exposed to a higher incidence of marine air-masses compared to CPO and verifies the observation of associated superior deep baseline conditions (< 60 mBq/m^3, see Table 5-6). This is beneficial since both CPO and CGO are intended to serve as baseline monitoring observatories and the sustainable incidence of marine air-masses is important.

It is systematically shown the austral seasons with the highest radon levels (CGO and CPO) occur during autumn and winter. It is therefore expected to observe an increase in the number of continental air-masses also during autumn and winter. Making use of the CGO and CPO back-trajectories (up to T = 60 h), an increase during winter of about 10% in continental air-masses is observed (see Figure 5-43 and Figure 5-49). It was noticed that both CGO and CPO are exposed higher altitude air-masses up to 2015 during which the strong El-Niño southern oscillation took place (Perry et al., 2020). For CGO (2007 to 2014) the incidence of higher altitude air-masses occurred a few years before CPO (2010 to 2014, see Figure 5-58). This led to an investigation to check if radon signal variations occurred during the above-mentioned years possibly due to exposure to higher altitude air-masses. However, no significant inter-annual radon signal variations are observed during the years of exposure to higher altitude air-masses (see Figure 5-29).

In this thesis the Southern Hemisphere atmospheric radon signals of which CGO is the longest and most comprehensive in existence, have been extensively characterised. In summary, the main findings in this thesis can be presented as follow:

a) A strong and consistent periodicity structures in the atmospheric radon signals are evident characterised by maxima during the austral autumn and winter and minima during the spring and summer. This is confirmed by making use of power spectral FFT analysis showing a large amplitude annual (seasonal) periodicity in the power spectra.

b) Elevated CGO and CPO radon levels (> 2000 mBq/m^3) are directly associated with WDs originating from continental fetch regions, whilst low radon levels are evident from the oceanic sectors.

c) For shorter timescales (< 3 days) a family of diurnal and sub-diurnal signals occurs at CPO, however, not CPO.

d) The diurnal CGO and CPO radon cycles both show a shallow minimum during the early evening (18:00 – 20:00) when the lower atmosphere is most deeply mixed, and a strong maximum during the late morning (10:00 to 11:00) when the lower atmosphere is likely at its shallowest.

e) Anomalies are identified in the CPO inter-annual summer radon diurnal analysis from 2000 to 2017 (see Figure 5-20, d). These anomalies include a switch of the highest radon levels observed during the day-time to the night-time (especially in 2002, 2006 and 2008)

f) A slow but systematic decline in CGO and CPO radon levels is evident (1999 to 2017), associated with fewer continental and more marine air-masses impacting the coastal stations which may indicate changes in the SH circulations patterns over time.

Atmospheric radon signals can be applied to study a wide range of impact topics such as air-borne pollution, transport pathways, regional and hemispheric circulations variations and more (Chambers et al., 2016; Podstawczyńska and Chambers, 2018; Williams et al., 2016; Zhu et al., 2012). By improving the fundamental understanding of these natural atmospheric radon signals it can offer valuable insights into meteorological and other research fields such as pollution studies. This study also demonstrates that radon can be successfully used as an

independent tool to verify occurrences of changes in larger scale (mesoscale) atmospheric circulation patterns and is a useful indicator of early onset of climate change related changes.

6.2 Future Work

Possible future work starting from the results obtained in this study include the following:

(1) Expand the Southern Hemisphere atmospheric radon signal characterisation by including similar existing signals like for instance those originating from Antarctica.

(2) Expand the Southern Hemisphere atmospheric land-based coastal radon monitoring locations to South America (tip of Argentina) and Marion Island.

(3) Introduce inland continuous atmospheric radon observatories in South Africa.

(4) Implement machine and deep learning data-analysis tools to restore missing data in the radon signals, trends, forecasting, and pattern analysis (supervised learning).

(5) Expand the current 2D-spatial (coordinates) air-masses back-trajectory density analysis algorithm into a 3D cluster analysis approach (coordinates and altitude).

(6) Develop a map of radon flux at the South African land surface.

(7) Develop links to other observations in meteorology and other gases (CO, CO_2, CH_4, O_3, N_2O, halocarbons and GEM) including polluting substances.

REFERENCES

Ali, M.Y.M., Hanafiah, M.M., Khan, M.F., 2018. Potential factors that impact the radon level and the prediction of ambient dose equivalent rates of indoor microenvironments. Sci. Total Environ. 626, 1–10. https://doi.org/https://doi.org/10.1016/j.scitotenv.2018.01.080

Allègre, C.J., Manhès, G., Göpel, C., 1995. The age of the Earth. Geochim. Cosmochim. Acta 59, 1445–1456. https://doi.org/10.1016/0016-7037(95)00054-4

ANSTO, 2016. Making the world's best radon detectors even better [WWW Document]. Phys.Org. URL https://phys.org/news/2016-09-world-radon-detectors.html (accessed 8.19.20).

Banerjee, A., Fyfe, J.C., Polvani, L.M., Waugh, D., Chang, K.L., 2020. A pause in Southern Hemisphere circulation trends due to the Montreal Protocol. Nature 579, 544–548. https://doi.org/10.1038/s41586-020-2120-4

Barman, C., Ghose, D., Sinha, B., Deb, A., 2016. Detection of earthquake induced radon precursors by Hilbert Huang Transform. J. Appl. Geophys. 133, 123–131. https://doi.org/https://doi.org/10.1016/j.jappgeo.2016.08.004

Baudoin, M.A., Vogel, C., Nortje, K., Naik, M., 2017. Living with drought in South Africa: lessons learnt from the recent El Niño drought period. Int. J. Disaster Risk Reduct. 23, 128–137. https://doi.org/10.1016/j.ijdrr.2017.05.005

Bigu, J., 1986. A method for measuring thoron and radon gas concentrations using solid-state alpha-particle detectors. Int. J. Radiat. Appl. Instrumentation. Part A. Appl. Radiat. Isot. 37, 567–573. https://doi.org/10.1016/0883-2889(86)90074-2

Botha, R., Labuschagne, C., Williams, A.G., Bosman, G., Brunke, E.-G., Rossouw, A., Lindsay, R., 2018. Characterising fifteen years of continuous atmospheric radon activity observations at Cape Point (South Africa). Atmos. Environ. 176, 30–39. https://doi.org/10.1016/J.ATMOSENV.2017.12.010

Botha, R., Lindsay, R., Newman, R.T., Maleka, P.P., Chimba, G., 2019. Radon in groundwater baseline study prior to unconventional shale gas development and hydraulic fracturing in the Karoo Basin (South Africa). Appl. Radiat. Isot. https://doi.org/10.1016/J.APRADISO.2019.02.006

Botha, R., Newman, R.T., Lindsay, R., Maleka, P.P., 2017. Radon and Thoron In-air

Occupational Exposure Study within Selected Wine Cellars of the Western Cape (South Africa) and Associated Annual Effective Doses. Health Phys. 112, 98–107. https://doi.org/10.1097/HP.0000000000000574

Botha, R., Newman, R.T., Maleka, P.P., 2016. Radon Levels Measured at a Touristic Thermal Spa Resort in Montagu (South Africa) and Associated Effective Doses. Health Phys. 111, 281–289. https://doi.org/10.1097/HP.0000000000000527

Bouchaou, L., Warner, N.R., Tagma, T., Hssaisoune, M., Vengosh, A., 2017. The origin of geothermal waters in Morocco: Multiple isotope tracers for delineating sources of water-rock interactions. Appl. Geochemistry 84, 244–253. https://doi.org/https://doi.org/10.1016/j.apgeochem.2017.07.004

Brunke, E.-G., Labuschagne, C., Ebinghaus, R., Kock, H.H., Slemr, F., 2010. Gaseous elemental mercury depletion events observed at Cape Point during 2007–2008. Atmos. Chem. Phys. 10, 1121–1131. https://doi.org/10.5194/acp-10-1121-2010

Brunke, E.-G., Labuschagne, C., Parker, B., Scheel, H.E., Whittlestone, S., 2004. Baseline air mass selection at Cape Point, South Africa: application of 222Rn and other filter criteria to CO2. Atmos. Environ. 38, 5693–5702. https://doi.org/https://doi.org/10.1016/j.atmosenv.2004.04.024

Brunke, E.-G., Labuschagne, C., Parker, B., van der Spuy, D., Whittlestone, S., 2002. Cape Point GAW Station 222Rn detector: factors affecting sensitivity and accuracy. Atmos. Environ. 36, 2257–2262. https://doi.org/10.1016/S1352-2310(02)00196-6

Butterweck, G., Porstendörfer, J., Reineking, A., Kesten, J., 1992. Unattached Fraction and the Aerosol Size Distribution of the Radon Progeny in a Natural Cave and Mine Atmospheres. Radiat. Prot. Dosimetry 45, 167–170. https://doi.org/10.1093/oxfordjournals.rpd.a081517

Cameron, R.H., Schüssler, M., 2012. Are the strengths of solar cycles determined by converging flows towards the activity belts? Astron. Astrophys. 548, A57. https://doi.org/10.1051/0004-6361/201219914

Chaboyer, B., 1998. The age of the universe. Phys. Rep. 307, 23–30. https://doi.org/10.1016/S0370-1573(98)00054-4

Chambers, D.B., Zielinski, J.M., 2011. Residential Radon Levels Around the World, in: Encyclopedia of Environmental Health. Elsevier, pp. 508–519.

https://doi.org/10.1016/b978-0-444-63951-6.00097-8

Chambers, S., Guérette, E.-A., Monk, K., Griffiths, A., Zhang, Y., Duc, H., Cope, M., Emmerson, K., Chang, L., Silver, J., Utembe, S., Crawford, J., Williams, A., Keywood, M., 2019. Skill-Testing Chemical Transport Models across Contrasting Atmospheric Mixing States Using Radon-222. Atmosphere (Basel). 10, 25. https://doi.org/10.3390/atmos10010025

Chambers, S., Williams, A.G., Zahorowski, W., Griffiths, A., Crawford, J., 2011. Separating remote fetch and local mixing influences on vertical radon measurements in the lower atmosphere. Tellus B Chem. Phys. Meteorol. 63, 843–859. https://doi.org/10.1111/j.1600-0889.2011.00565.x

Chambers, S.D., Choi, T., Park, S.-J., Williams, A.G., Hong, S.-B., Tositti, L., Griffiths, A.D., Crawford, J., Pereira, E., 2017. Investigating Local and Remote Terrestrial Influence on Air Masses at Contrasting Antarctic Sites Using Radon-222 and Back Trajectories. J. Geophys. Res. Atmos. 122, 13,525-13,544. https://doi.org/10.1002/2017JD026833

Chambers, S.D., Hong, S.B., Williams, A.G., Crawford, J., Griffiths, A.D., Park, S.J., 2014. Characterising terrestrial influences on Antarctic air masses using Radon-222 measurements at King George Island. Atmos. Chem. Phys. 14. https://doi.org/10.5194/acp-14-9903-2014

Chambers, S.D., Podstawczyńska, A., Pawlak, W., Fortuniak, K., Williams, A.G., Griffiths, A.D., 2019. Characterizing the State of the Urban Surface Layer Using Radon-222. J. Geophys. Res. Atmos. 124, 770–788. https://doi.org/10.1029/2018JD029507

Chambers, Scott D, Podstawczyńska, A., Williams, A.G., Pawlak, Włodzimierz, 2016. Characterising the influence of atmospheric mixing state on Urban Heat Island Intensity using Radon-222. Atmos. Environ. 147, 355–368. https://doi.org/https://doi.org/10.1016/j.atmosenv.2016.10.026

Chambers, S.D., Preunkert, S., Weller, R., Hong, S.-B., Humphries, R.S., Tositti, L., Angot, H., Legrand, M., Williams, A.G., Griffiths, A.D., Crawford, J., Simmons, J., Choi, T.J., Krummel, P.B., Molloy, S., Loh, Z., Galbally, I., Wilson, S., Magand, O., Sprovieri, F., Pirrone, N., Dommergue, A., 2018. Characterizing Atmospheric Transport Pathways to Antarctica and the Remote Southern Ocean Using Radon-222. Front. Earth Sci. 6, 190. https://doi.org/10.3389/feart.2018.00190

Chambers, S.D., Wang, F., Williams, A.G., Xiaodong, D., Zhang, H., Lonati, G., Crawford, J., Griffiths, A.D., Ianniello, A., Allegrini, I., 2015. Quantifying the influences of atmospheric stability on air pollution in Lanzhou, China, using a radon-based stability monitor. Atmos. Environ. 107, 233–243. https://doi.org/https://doi.org/10.1016/j.atmosenv.2015.02.016

Chambers, Scott D., Williams, A.G., Conen, F., Griffiths, A.D., Reimann, S., Steinbacher, M., Krummel, P.B., Steele, L.P., van der Schoot, M. V., Galbally, I.E., Molloy, S.B., Barnes, J.E., 2016. Towards a Universal "Baseline" Characterisation of Air Masses for High- and Low-Altitude Observing Stations Using Radon-222. Aerosol Air Qual. Res. 16, 885–899. https://doi.org/10.4209/aaqr.2015.06.0391

Chambers, S.D., Zahorowski, W., Williams, A.G., Crawford, J., Griffiths, A.D., 2013. Identifying tropospheric baseline air masses at Mauna Loa Observatory between 2004 and 2010 using Radon-222 and back trajectories. J. Geophys. Res. Atmos. 118, 992–1004. https://doi.org/10.1029/2012JD018212

Chen, S., Wu, R., Chen, W., Yu, B., 2020. Recent weakening of the linkage between the spring Arctic Oscillation and the following winter El Niño-Southern Oscillation. Clim. Dyn. 54, 53–67. https://doi.org/10.1007/s00382-019-04988-7

CMSA, 2016. Chamber of Mines of South Africa, Mine SA 2016, Facts and Figures. Johannesburg.

Crawford, J., Chambers, S., Cohen, D., Williams, A., Griffiths, A., Stelcer, E., 2016. Assessing the impact of atmospheric stability on locally and remotely sourced aerosols at Richmond, Australia, using Radon-222. Atmos. Environ. 127. https://doi.org/10.1016/j.atmosenv.2015.12.034

Crawford, J., Chambers, S., Kang, C.-H., Griffiths, A., Kim, W.-H., 2015. Analysis of a decade of Asian outflow of PM10 and TSP to Gosan, Korea; also incorporating Radon–222. Atmos. Pollut. Res. 6, 529–539. https://doi.org/10.5094/APR.2015.059

Crawford, J., Cohen, D.D., Stelcer, E., Atanacio, A.J., 2017. Long term fine aerosols at the Cape Grim global baseline station: 1998 to 2016. Atmos. Environ. 166, 34–46. https://doi.org/https://doi.org/10.1016/j.atmosenv.2017.07.012

Csondor, K., Erőss, A., Horváth, Á., Szieberth, D., 2017. Radon as a natural tracer for underwater cave exploration. J. Environ. Radioact. 173, 51–57. https://doi.org/https://doi.org/10.1016/j.jenvrad.2016.10.020

Dance, D.R., Christofides, S., Maidment, A.D.A., Mclean, I.D., Ng, K.H., 2014. Diagnostic Radiology Physics: A Handbook for Teachers and Students. IAEA, Vienna.

De Felice, P., Myteberi, X., 1996. The 222Rn Reference Measurement System developed at ENEA. Nucl. Instruments Methods Phys. Res. Sect. A Accel. Spectrometers, Detect. Assoc. Equip. 369, 445–451. https://doi.org/10.1016/S0168-9002(96)80028-3

Deb, A., Gazi, M., Ghosh, J., Chowdhury, S., Barman, C., 2018. Monitoring of soil radon by SSNTD in Eastern India in search of possible earthquake precursor. J. Environ. Radioact. 184–185, 63–70. https://doi.org/https://doi.org/10.1016/j.jenvrad.2018.01.009

DWJ Thompson, S.S., 2002. Interpretation of recent Southern Hemisphere climate change. Science (80-.). 296, 895–899.

Environmental Measurements Laboratory, 1997. Radionuclide Data, HASL-300. New York.

Epstein, G., Pérez, I., Schoon, M., Meek, C.L., 2014. Governing the invisible commons: Ozone regulation and the Montreal Protocol. Int. J. Commons 8, 337–360. https://doi.org/10.18352/ijc.407

Florea, N., Duliu, O.G., 2012. Eighteen years of continuous observation of Radon and Thoron progenies atmospheric activity. J. Environ. Radioact. 104, 14–23. https://doi.org/10.1016/J.JENVRAD.2011.10.002

Gäggeler, H.W., Jost, D.T., Baltensperger, U., Schwikowski, M., Seibert, P., 1995. Radon and thoron decay product and 210Pb measurements at Jungfraujoch, Switzerland. Atmos. Environ. 29, 607–616. https://doi.org/10.1016/1352-2310(94)00195-Q

Garver, E., Baskaran, M., 2004. Effects of heating on the emanation rates of radon-222 from a suite of natural minerals. Appl. Radiat. Isot. 61, 1477–1485. https://doi.org/https://doi.org/10.1016/j.apradiso.2004.03.107

Gaskin, J., Coyle, D., Whyte, J., Krewksi, D., 2018. Global estimate of lung cancer mortality attributable to residential radon. Environ. Health Perspect. 126. https://doi.org/10.1289/EHP2503

Goto, M., Moriizumi, J., Yamazawa, H., Iida, T., Zhuo, W., Paschoa, A.S., Steinhäusler, F., 2008. Estimation of global radon exhalation rate distribution, in: AIP Conference Proceedings. AIP, pp. 169–172. https://doi.org/10.1063/1.2991199

Griffiths, A.D., Chambers, S.D., Williams, A.G., Werczynski, S., 2016. Increasing the accuracy and temporal resolution of two-filter radon-222 measurements by correcting

for the instrument response. Atmos. Meas. Tech. 9, 2689–2707. https://doi.org/10.5194/amt-9-2689-2016

Griffiths, A.D., Parkes, S.D., Chambers, S.D., McCabe, M.F., Williams, A.G., 2013. Improved mixing height monitoring through a combination of lidar and radon measurements. Atmos. Meas. Tech. 6, 207–218. https://doi.org/10.5194/amt-6-207-2013

Griffiths, A.D., Zahorowski, W., Element, A., Werczynski, S., 2010. A map of radon flux at the Australian land surface. Atmos. Chem. Phys. 10, 8969–8982. https://doi.org/10.5194/acp-10-8969-2010

Griffiths, Chambers, S.D., Williams, A.G., Werczynski, S., 2016. Increasing the accuracy and temporal resolution of two-filter radon-222 measurements by correcting for the instrument response. Atmos. Meas. Tech. 9, 2689–2707. https://doi.org/10.5194/amt-9-2689-2016

Grossi, C., Vargas, A., Camacho, A., López-Coto, I., Bolívar, J.P., Xia, Y., Conen, F., 2011. Inter-comparison of different direct and indirect methods to determine radon flux from soil. Radiat. Meas. 46, 112–118. https://doi.org/10.1016/j.radmeas.2010.07.021

GUPTA, M.L., DOUGLASS, A.R., KAWA, S.R., PAWSON, S., 2004. Use of radon for evaluation of atmospheric transport models: sensitivity to emissions. Tellus B 56, 404–412. https://doi.org/10.1111/j.1600-0889.2004.00124.x

Hathaway, D.H., 2015a. The Solar Cycle. Living Rev. Sol. Phys. 12, 4. https://doi.org/10.1007/lrsp-2015-4

Hathaway, D.H., 2015b. Living reviews in solar physics. Max-Planck-Institut für Sonnensystemforschung.

Hu, Q.-H., Weng, J.-Q., Wang, J.-S., 2010. Sources of anthropogenic radionuclides in the environment: a review. J. Environ. Radioact. 101, 426–437. https://doi.org/10.1016/J.JENVRAD.2008.08.004

ICRP, 2014. Radiological Protection against Radon Exposure, ICRP, Publ. ed. ICRP.

Jamil, K., Fazal-ur-Rehman, Ali, S., Khan, H.A., 1997. Determination of equilibrium factor between radon and its progeny using surface barrier detector for various shapes of passive radon dosimeters. Nucl. Instruments Methods Phys. Res. Sect. A Accel. Spectrometers, Detect. Assoc. Equip. 388, 267–272. https://doi.org/https://doi.org/10.1016/S0168-9002(97)00307-0

Janik, M., Bossew, P., Kurihara, O., 2018. Machine learning methods as a tool to analyse incomplete or irregularly sampled radon time series data. Sci. Total Environ. 630, 1155–1167. https://doi.org/https://doi.org/10.1016/j.scitotenv.2018.02.233

Kelly, F.J., Fussell, J.C., 2015. Air pollution and public health: emerging hazards and improved understanding of risk. Environ. Geochem. Health 37, 631–49. https://doi.org/10.1007/s10653-015-9720-1

Kenan, A.O., Chirenje, E., 2016. Uranium in South Africa: Exploration and Supply Capacity. Nat. Resour. Conserv. 4, 25–33. https://doi.org/10.13189/nrc.2016.040201

Kikaj, D., Chambers, S.D., Kobal, M., Crawford, J., Vaupotič, J., 2020. Characterizing atmospheric controls on winter urban pollution in a topographic basin setting using Radon-222. Atmos. Res. 237, 104838. https://doi.org/https://doi.org/10.1016/j.atmosres.2019.104838

Kikaj, D., Chambers, S.D., Vaupotič, J., 2019. Radon-based atmospheric stability classification in contrasting sub-Alpine and sub-Mediterranean environments. J. Environ. Radioact. 203, 125–134. https://doi.org/https://doi.org/10.1016/j.jenvrad.2019.03.010

Kim, N.K., Kim, Y.P., Kang, C.-H., 2011. Long-term trend of aerosol composition and direct radiative forcing due to aerosols over Gosan: TSP, PM10, and PM2.5 data between 1992 and 2008. Atmos. Environ. 45, 6107–6115. https://doi.org/10.1016/j.atmosenv.2011.08.051

Knoll, G.F., 2010. Radiation detection and measurement. John Wiley.

Krauss, L.M., 2000. The age of globular clusters. Phys. Rep. 333–334, 33–45. https://doi.org/10.1016/S0370-1573(00)00014-4

Kulali, F., Akkurt, I., Özgür, N., 2017. The effect of meteorological parameters on radon concentration in soil gas. Acta Phys. Pol. A 132, 999–1001. https://doi.org/10.12693/APhysPolA.132.999

Kuo, T., Chen, W., Ho, C., 2018. Anomalous decrease in groundwater radon before 2016 Mw 6.4 Meinong earthquake and its application in Taiwan. Appl. Radiat. Isot. 136, 68–72. https://doi.org/https://doi.org/10.1016/j.apradiso.2018.02.015

Kuttippurath, J., Nair, P.J., 2017. The signs of Antarctic ozone hole recovery. Sci. Rep. 7, 585. https://doi.org/10.1038/s41598-017-00722-7

L'Annunziata, M.F., 2003. Handbook of Radioactivity Analysis. Elsevier.

Labuschagne, C., Kuyper, B., Brunke, E.-G., Mokolo, T., van der Spuy, D., Martin, L., Mbambalala, E., Parker, B., Khan, M.A.H., Davies-Coleman, M.T., Shallcross, D.E., Joubert, W., 2018. A review of four decades of atmospheric trace gas measurements at Cape Point, South Africa. Trans. R. Soc. South Africa 73, 113–132. https://doi.org/10.1080/0035919X.2018.1477854

Lee, M.S., Lee, J.M., 2013. Realization of radioactive equilibrium in the KRISS radon chamber. Appl. Radiat. Isot. 81, 226–229. https://doi.org/10.1016/j.apradiso.2013.07.007

Lesouëf, D., Gheusi, F., Delmas, R., Escobar, J., 2011. Numerical simulations of local circulations and pollution transport over Reunion Island. Ann. Geophys. 29, 53–69. https://doi.org/10.5194/angeo-29-53-2011

Levin, I., Schmithüsen, D., Vermeulen, A., 2017. Assessment of ²²²radon progeny loss in long tubing based on static filter measurements in the laboratory and in the field. Atmos. Meas. Tech. 10, 1313–1321. https://doi.org/10.5194/amt-10-1313-2017

Li, C., Zhang, H., Su, H., Zhou, H., Wang, Y., 2017. Spatial distribution correlation of soil-gas radon (222Rn) and mercury with leveling deformation in northern margin fault zone of West Qinling, China. J. Environ. Radioact. 178, 315–324. https://doi.org/10.1016/j.jenvrad.2017.09.011

Liang, J., Yang, Z., Wang, L., Li, Z., Zhang, M., Liu, H., Yuan, D., 2018. Development of the absolute standardization apparatus for radon-222 activity. Appl. Radiat. Isot. 134, 358–362. https://doi.org/10.1016/j.apradiso.2017.07.055

Lin, C.-F., Wang, J.-J., Lin, S.-J., Lin, C.-K., 2013. Performance comparison of electronic radon monitors. Appl. Radiat. Isot. 81, 238–241. https://doi.org/10.1016/j.apradiso.2013.03.024

Lindsay, R., Newman, R.T., Speelman, W.J., 2008. A study of airborne radon levels in Paarl houses (South Africa) and associated source terms, using electret ion chambers and gamma-ray spectrometry. Appl. Radiat. Isot. 66, 1611–1614. https://doi.org/https://doi.org/10.1016/j.apradiso.2008.01.022

Magalhães, M.H., Amaral, E.C.S., Sachett, I., Rochedo, E.R.R., 2003. Radon-222 in Brazil:

An outline of indoor and outdoor measurements. J. Environ. Radioact. 67, 131–143. https://doi.org/10.1016/S0265-931X(02)00175-3

McLaughlin, J.P., Simopoulos, S.E., Steinhäusler, F. (Friedrich), 2005. The natural radiation environment VII : Seventh International Symposium on the Natural Radiation Environment (NRE-VII), Rhodes, Greece, 20-24 May 2002. Elsevier.

Moffat, J.W., 1995. How old is the universe? Phys. Lett. B 357, 526–531. https://doi.org/10.1016/0370-2693(95)00955-K

NC Swart, J.F., 2012. Observed and simulated changes in the Southern Hemisphere surface westerly wind-stress. Geophys. Res. Lett. 39, L16711.

Nemangwele, F., 2005. Radon in the Cango Caves. University of the Western Cape .

Nevinsky, I., Tsvetkova, T., Dogru, M., Aksoy, E., Inceoz, M., Baykara, O., Kulahci, F., Melikadze, G., Akkurt, I., Kulali, F., Vogiannis, E., Pitikakis, E., Katsanou, K., Lambrakis, N., 2018. Results of the simultaneous measurements of radon around the Black Sea for seismological applications. J. Environ. Radioact. 192, 48–66. https://doi.org/https://doi.org/10.1016/j.jenvrad.2018.05.019

Ngan, F., Stein, A.F., 2017. A Long-Term WRF Meteorological Archive for Dispersion Simulations: Application to Controlled Tracer Experiments. J. Appl. Meteorol. Climatol. 56, 2203–2220. https://doi.org/10.1175/JAMC-D-16-0345.1

NNDC, 2018. Chart of Nuclides, Brookhaven National Laboratory, National Nuclear Data Centre [WWW Document]. URL https://www.nndc.bnl.gov/chart/moveCenter.jsp?move=left (accessed 6.29.18).

NNR, 2013. COUNTRY PRESENTATION: SOUTH AFRICA RADON IN EXISTING EXPOSURE SCENARIOS.

Nonka, G.R., Dali, T.P.A., Koua, A.A., Gogon, H.L.D., Monnehan, G.A., Djagouri, K., 2017. Dosimetric impact of indoor radon gas on the population from the commune of Yopougon, Abidjan, Côte d'Ivoire. J. Radiat. Res. Appl. Sci. 10, 295–300. https://doi.org/https://doi.org/10.1016/j.jrras.2017.07.001

Ohara, T., Akimoto, H., Kurokawa, J., Horii, N., Yamaji, K., Yan, X., Hayasaka, T., 2007. An Asian emission inventory of anthropogenic emission sources for the period 1980–2020. Atmos. Chem. Phys. 7, 4419–4444. https://doi.org/10.5194/acp-7-4419-2007

Ongori, J.N., Lindsay, R., Newman, R.T., Maleka, P.P., 2015. Determining the radon exhalation rate from a gold mine tailings dump by measuring the gamma radiation. J. Environ. Radioact. 140, 16–24. https://doi.org/https://doi.org/10.1016/j.jenvrad.2014.10.012

Partington, J.R., 1957. Discovery of Radon. Nature 179, 912–912. https://doi.org/10.1038/179912a0

Paul, H., Sánchez-Parcerisa, D., 2013. A critical overview of recent stopping power programs for positive ions in solid elements. Nucl. Instruments Methods Phys. Res. Sect. B Beam Interact. with Mater. Atoms 312, 110–117. https://doi.org/10.1016/J.NIMB.2013.07.012

Pereira, E.O., 1990. Radon-222 time series measurements in the Antarctic peninsula (1986—1987). Tellus B Chem. Phys. Meteorol. 42, 39–45. https://doi.org/10.3402/tellusb.v42i1.15190

Perry, S.J., McGregor, S., Sen Gupta, A., England, M.H., Maher, N., 2020. Projected late 21st century changes to the regional impacts of the El Niño-Southern Oscillation. Clim. Dyn. 54, 395–412. https://doi.org/10.1007/s00382-019-05006-6

Picolo, J.L., 1996. Absolute measurement of radon 222 activity. Nucl. Instruments Methods Phys. Res. Sect. A Accel. Spectrometers, Detect. Assoc. Equip. 369, 452–457. https://doi.org/10.1016/S0168-9002(96)80029-5

Podstawczyńska, A., Chambers, S.D., 2018. Radon-based technique for the analysis of atmospheric stability - A case study from Central Poland. Nukleonika 63, 47–54. https://doi.org/10.2478/nuka-2018-0006

Qureshi, A.., Kakar, D.., Akram, M., Khattak, N.., Tufail, M., Mehmood, K., Jamil, K., Khan, H.., 2000. Radon concentrations in coal mines of Baluchistan, Pakistan. J. Environ. Radioact. 48, 203–209. https://doi.org/10.1016/S0265-931X(99)00065-X

Radvanyi, P., Villain, J., 2017. The discovery of radioactivity. Comptes Rendus Phys. 18, 544–550. https://doi.org/10.1016/J.CRHY.2017.10.008

Ravindra, K., Singh, T., Mor, Sahil, Singh, V., Mandal, T.K., Bhatti, M.S., Gahlawat, S.K., Dhankhar, R., Mor, Suman, Beig, G., 2019. Real-time monitoring of air pollutants in seven cities of North India during crop residue burning and their relationship with meteorology and transboundary movement of air. Sci. Total Environ. 690, 717–729. https://doi.org/10.1016/j.scitotenv.2019.06.216

Rhodes, J.M., Lockwood, J.P. (Eds.), 1995. Mauna Loa Revealed: Structure, Composition, History, and Hazards, Geophysical Monograph Series. American Geophysical Union, Washington, D. C. https://doi.org/10.1029/GM092

Richman, M.B., Leslie, L.M., 2018. The 2015-2017 Cape Town Drought: Attribution and Prediction Using Machine Learning. Procedia Comput. Sci. 140, 248–257. https://doi.org/10.1016/j.procs.2018.10.323

Richon, P., Perrier, F., Sabroux, J.-C., Trique, M., Ferry, C., Voisin, V., Pili, E., 2004. Spatial and time variations of radon-222 concentration in the atmosphere of a dead-end horizontal tunnel. J. Environ. Radioact. 78, 179–198. https://doi.org/https://doi.org/10.1016/j.jenvrad.2004.05.001

Rolph, G., Stein, A., Stunder, B., 2017. Real-time Environmental Applications and Display sYstem: READY. Environ. Model. Softw. 95, 210–228. https://doi.org/10.1016/J.ENVSOFT.2017.06.025

Rolph, G.D., Ngan, F., Draxler, R.R., 2014. Modeling the fallout from stabilized nuclear clouds using the HYSPLIT atmospheric dispersion model. J. Environ. Radioact. 136, 41–55. https://doi.org/10.1016/j.jenvrad.2014.05.006

Santos, I.R., Eyre, B.D., 2011. Radon tracing of groundwater discharge into an Australian estuary surrounded by coastal acid sulphate soils. J. Hydrol. 396, 246–257. https://doi.org/10.1016/J.JHYDROL.2010.11.013

Sesana, L., Caprioli, E., Marcazzan, G.M., 2003. Long period study of outdoor radon concentration in Milan and correlation between its temporal variations and dispersion properties of atmosphere. J. Environ. Radioact. 65, 147–160. https://doi.org/10.1016/S0265-931X(02)00093-0

Sharma, D., Kumar, B., Chand, S., 2019. A Trend Analysis of Machine Learning Research with Topic Models and Mann-Kendall Test. Int. J. Intell. Syst. Appl. 11, 70–82. https://doi.org/10.5815/ijisa.2019.02.08

Sheppard, S.C., Sheppard, M.I., Ilin, M., Tait, J., Sanipelli, B., 2008. Primordial radionuclides in Canadian background sites: secular equilibrium and isotopic differences. J. Environ. Radioact. 99, 933–946. https://doi.org/10.1016/J.JENVRAD.2007.11.018

Slemr, F., Brunke, E.-G., Whittlestone, S., Zahorowski, W., Ebinghaus, R., Kock, H.H.,

Labuschagne, C., 2013. ^{222}Rn calibrated mercury fluxes from terrestrial surfaces of southern Africa derived from observations at Cape Point, South Africa. E3S Web Conf. 1, 17005. https://doi.org/10.1051/e3sconf/20130117005

SOGA, 2018. State of Global Air. Boston.

Song, G., Wang, X., Chen, D., Chen, Y., 2011. Contribution of 222Rn-bearing water to indoor radon and indoor air quality assessment in hot spring hotels of Guangdong, China. J. Environ. Radioact. 102, 400–406. https://doi.org/10.1016/j.jenvrad.2011.02.010

Stein, A.F., Draxler, R.R., Rolph, G.D., Stunder, B.J.B., Cohen, M.D., Ngan, F., Stein, A.F., Draxler, R.R., Rolph, G.D., Stunder, B.J.B., Cohen, M.D., Ngan, F., 2015. NOAA's HYSPLIT Atmospheric Transport and Dispersion Modeling System. Bull. Am. Meteorol. Soc. 96, 2059–2077. https://doi.org/10.1175/BAMS-D-14-00110.1

Stozhkov, Y.I., Svirzhevsky, N.S., Bazilevskaya, G.A., Kvashnin, A.N., Makhmutov, V.S., Svirzhevskaya, A.K., 2009. Long-term (50 years) measurements of cosmic ray fluxes in the atmosphere. Adv. Sp. Res. 44, 1124–1137. https://doi.org/10.1016/j.asr.2008.10.038

Sundal, A.V., Valen, V., Soldal, O., Strand, T., 2008. The influence of meteorological parameters on soil radon levels in permeable glacial sediments. Sci. Total Environ. 389, 418–428. https://doi.org/10.1016/j.scitotenv.2007.09.001

Swana, K., 2016. Application of hydrochemistry and residence time constraints to distinguish groundwater systems in the Karoo Basin prior to shale-gas exploration.

Szabó, K.Z., Jordan, G., Horváth, Á., Szabó, C., 2014. Mapping the geogenic radon potential: methodology and spatial analysis for central Hungary. J. Environ. Radioact. 129, 107–120. https://doi.org/10.1016/j.jenvrad.2013.12.009

Tchorz-Trzeciakiewicz, D.E., Solecki, A.T., Elío, J., Crowley, Q., Scanlon, R., Hodgson, J., Long, S., Al-Khateeb, H.M., Nuseirat, M., Aljarrah, K.M., Al-Akhras, M.-A.H., Bani-Salameh, H., Wasikiewicz, J.M., Watson, R.J., Smethurst, M.A., Ganerød, G. V, Finne, I., Rudjord, A.L., Al-Khateeb, H.M., Aljarrah, K.M., Alzoubi, F.Y., Alqadi, M.K., Ahmad, A.A., Ferreira, A., Daraktchieva, Z., Beamish, D., Kirkwood, C., Lister, T.R., Cave, M., Wragg, J., Lee, K., Ozdemir, F.B., Selcuk, A.B., Ozkorucuklu, S., Alpat, A.B., Ozdemir, T., Özek, N., Scheib, C., Appleton, J.D., Miles, J.C.H., Hodgkinson, E., Mollo, S., Tuccimei, P., Soligo, M., Galli, G., Scarlato, P., Smethurst, M.A., Watson, R.J., Baranwal, V.C., Rudjord, A.L., Finne, I., Topin, S., Richon, P., Thomas, V., Gréau,

C., Pujos, J., Moulin, J., Hovesepian, A., Deliere, L., 2017. The correlation between indoor and in soil radon concentrations in a desert climate. J. Environ. Radioact. 130, 142–147. https://doi.org/https://doi.org/10.1016/B978-0-12-812056-9.00018-X

Topin, S., Richon, P., Thomas, V., Gréau, C., Pujos, J., Moulin, J., Hovesepian, A., Deliere, L., 2017. Development of a highly sensitive radon-222 amplifier (HiSRA) for low-level atmospheric measurements. J. Environ. Radioact. 171, 124–131. https://doi.org/https://doi.org/10.1016/j.jenvrad.2017.02.008

Trassierra, C.V., Stabile, L., Cardellini, F., Morawska, L., Buonanno, G., 2016. Effect of indoor-generated airborne particles on radon progeny dynamics. J. Hazard. Mater. 314, 155–163. https://doi.org/https://doi.org/10.1016/j.jhazmat.2016.04.051

UNSCEAR, 2008. Sources and effects of ionizing radiaton, Annex B. New York.

Utkin, V.I., Yurkov, A.K., 2010. Radon as a tracer of tectonic movements. Russ. Geol. Geophys. 51, 220–227. https://doi.org/https://doi.org/10.1016/j.rgg.2009.12.022

Valković, V., 2000. Radioactivity in the environment. Elsevier Science B.V.

Vargas, A., Arnold, D., Adame, J.A., Grossi, C., Hernández-Ceballos, M.A., Bolivar, J.P., 2015. Analysis of the vertical radon structure at the Spanish “El Arenosillo” tower station. J. Environ. Radioact. 139, 1–17. https://doi.org/10.1016/j.jenvrad.2014.09.018

Vaupotič, J., 2008. Comparison of various methods of estimating radon dose at underground workplaces in wineries. Radiat. Environ. Biophys. 47, 527–534. https://doi.org/10.1007/s00411-008-0174-z

Victor, N.J., Siingh, D., Singh, R.P., Singh, R., Kamra, A.K., 2019. Diurnal and seasonal variations of radon (222Rn) and their dependence on soil moisture and vertical stability of the lower atmosphere at Pune, India. J. Atmos. Solar-Terrestrial Phys. 195, 105118. https://doi.org/https://doi.org/10.1016/j.jastp.2019.105118

Vinson, D.S., Lundy, J.R., Dwyer, G.S., Vengosh, A., 2018. Radium isotope response to aquifer storage and recovery in a sandstone aquifer. Appl. Geochemistry 91, 54–63. https://doi.org/https://doi.org/10.1016/j.apgeochem.2018.01.006

Vogiannis, E., Niaounakis, M., Halvadakis, C.P., 2004. Contribution of 222Rn-bearing water to the occupational exposure in thermal baths. Environ. Int. 30, 621–629. https://doi.org/https://doi.org/10.1016/j.envint.2003.11.004

Whittlestone, S., Robinson, E., Ryan, S., 1992. Radon at the Mauna Loa observatory:

Transport from distant continents. Atmos. Environ. Part A. Gen. Top. 26, 251–260. https://doi.org/https://doi.org/10.1016/0960-1686(92)90307-7

Whittlestone, S., Zahorowski, W., 1998. Baseline radon detectors for shipboard use: Development and deployment in the First Aerosol Characterization Experiment (ACE 1). J. Geophys. Res. Atmos. 103, 16743–16751. https://doi.org/10.1029/98JD00687

WHO, 2011. Guidelines for Drinking-water Quality FOURTH EDITION WHO Library Cataloguing-in-Publication Data Guidelines for drinking-water quality-4 th ed.

WHO, 2009. WHO Handbook on indoor radon: A public Health Perpective. WHO Press, Geneva.

Wieser, M.E., 2006. Atomic weights of the elements 2005 (IUPAC Technical Report). Pure Appl. Chem. 78, 2051–2066. https://doi.org/10.1351/pac200678112051

Williams, A.G., Chambers, S., Griffiths, A., 2013. Bulk Mixing and Decoupling of the Nocturnal Stable Boundary Layer Characterized Using a Ubiquitous Natural Tracer. Boundary-Layer Meteorol. 149, 381–402. https://doi.org/10.1007/s10546-013-9849-3

Williams, A.G., Chambers, S., Zahorowski, W., Crawford, J., Matsumoto, K., Uematsu, M., 2009. Estimating the Asian radon flux density and its latitudinal gradient in winter using ground-based radon observations at Sado Island. Tellus B Chem. Phys. Meteorol. 61, 732–746. https://doi.org/10.1111/j.1600-0889.2009.00438.x

Williams, A.G., Chambers, S.D., Conen, F., Reimann, S., Hill, M., Griffiths, A.D., Crawford, J., 2016. Radon as a tracer of atmospheric influences on traffic-related air pollution in a small inland city. Tellus B Chem. Phys. Meteorol. 68, 30967. https://doi.org/10.3402/tellusb.v68.30967

Williams, A.G., Zahorowski, W., Chambers, S., Griffiths, A., Hacker, J.M., Element, A., Werczynski, S., Williams, A.G., Zahorowski, W., Chambers, S., Griffiths, A., Hacker, J.M., Element, A., Werczynski, S., 2011. The Vertical Distribution of Radon in Clear and Cloudy Daytime Terrestrial Boundary Layers. J. Atmos. Sci. 68, 155–174. https://doi.org/10.1175/2010JAS3576.1

Xia, Y., Sartorius, H., Schlosser, C., Stöhlker, U., Conen, F., Zahorowski, W., 2010. Comparison of one- and two-filter detectors for atmospheric ²²²Rn measurements under various meteorological conditions. Atmos. Meas. Tech. 3, 723–731. https://doi.org/10.5194/amt-3-723-2010

Yang, J., Busen, H., Scherb, H., Hürkamp, K., Guo, Q., Tschiersch, J., 2019. Modeling of radon exhalation from soil influenced by environmental parameters. Sci. Total Environ. 656, 1304–1311. https://doi.org/10.1016/j.scitotenv.2018.11.464

Yu, K.N., Leung, S.Y.Y., Nikezic, D., Leung, J.K.C., 2008. Equilibrium factor determination using SSNTDs. Radiat. Meas. 43, S357–S363. https://doi.org/https://doi.org/10.1016/j.radmeas.2008.03.024

Yuan, Y.J., Yang, J.C., Xia, J.W., Yuan, P., Qiao, W.M., Gao, D.Q., Xiao, G.Q., Zhao, H.W., Xu, H.S., Song, M.T., Yang, X.D., Cai, X.H., Ma, L.Z., Yang, X.T., Man, K.T., He, Y., Zhou, Z.Z., Zhang, J.H., Xu, Z., Liu, Y., Mao, R.S., Zhang, W., Xie, D.Z., Sun, L.T., Yang, Y.Q., Yin, D.Y., Li, P., Li, J., Shi, J., Chai, W.P., Wei, B.W., Zhan, W.L., 2013. Status of the HIRFL–CSR complex. Nucl. Instruments Methods Phys. Res. Sect. B Beam Interact. with Mater. Atoms 317, 214–217. https://doi.org/10.1016/J.NIMB.2013.07.040

Zahorowski, W., Chambers, S.D., Henderson-Sellers, A., 2004. Ground based radon-222 observations and their application to atmospheric studies. J. Environ. Radioact. 76, 3–33. https://doi.org/10.1016/J.JENVRAD.2004.03.033

Zhang, Liang, Zhang, Liguo, Guo, Q., 2009. A long-term investigation of the atmospheric radon concentration in Beijing, China. J. Radiol. Prot. 29, 263–268. https://doi.org/10.1088/0952-4746/29/2/012

Zhang, Y., Li, H., Wang, X., Wang, C., Xiao, K., Qu, W., 2018. Submarine groundwater discharge and chemical behavior of tracers in Laizhou Bay, China. J. Environ. Radioact. 189, 182–190. https://doi.org/https://doi.org/10.1016/j.jenvrad.2018.04.002

Zhu, C., Yoshikawa-Inoue, H., Matsueda, H., Sawa, Y., Niwa, Y., Wada, A., Tanimoto, H., 2012. Influence of Asian outflow on Rishiri Island, northernmost Japan: Application of radon as a tracer for characterizing fetch regions and evaluating a global 3D model. Atmos. Environ. 50, 174–181. https://doi.org/https://doi.org/10.1016/j.atmosenv.2011.12.043

Zhuo, W., Iida, T., Furukawa, M., 2006. Modeling radon flux density from the earth's surface. J. Nucl. Sci. Technol. 43, 479–482. https://doi.org/10.1080/18811248.2006.9711127

Appendix

Code 1: Matlab script to simulate the decay progeny of radon making use of the Bateman equation (see Equation 2-10 and 2.11)

```
% Bates Equation for the decay progeny of three decays from Rn-222
% 14-02-2018

clear all
close all
clc


%%%%%%%%%%%%%%%%
% [A] Input
%%%%%%%%%%%%%%%%

t = linspace(0,24*50,100000); % Decay Time, (hours), Simulated for 50 days
N_Rn_0 = 10000;       % Initial amount of radon atoms at t = 0

X1_HL = 3.8235*24;    %Half-life (HL) in hours, Rn-222
X2_HL = 3.10/60;      % Po-218, HL
X3_HL = 26.8/60;      % Pb-214, HL
X4_HL = 19.8/60;      % Bi-215, HL

G1 = log(2)/X1_HL;
G2 = log(2)/X2_HL;
G3 = log(2)/X3_HL;
G4 = log(2)/X4_HL;

%%%%%%%%%%%%%%%%
% [B] Comp (Bates Equations)
%%%%%%%%%%%%%%%%

N1 = N_Rn_0 * exp(-G1.*t);
N2 = N_Rn_0 *(G1/(G2-G1))*(exp(-G1.*t)-exp(-G2.*t));
N3= N_Rn_0 * G1*G2 * ( ((exp(-G1.*t))/((G2-G1)*(G3-G1))) + ((exp(-
G2.*t))/((G1-G2)*(G3-G2))) + ((exp(-G3.*t))/((G1-G3)*(G2-G3))) );
N4 = N_Rn_0 * G1*G2*G3 * ( ((exp(-G1.*t))/((G2-G1)*(G3-G1)*(G4-G1))) +
((exp(-G2.*t))/((G1-G2)*(G3-G2)*(G4-G2))) + ((exp(-G3.*t))/((G1-G3)*(G2-
G3)*(G4-G3))) + ((exp(-G4.*t))/((G1-G4)*(G2-G4)*(G3-G4))) );
N_P = N1+N2+N3;
Ratio_1 = N1./N_P

%%%%%%%%%%%%%%%%
% [C] Plot
%%%%%%%%%%%%%%%%

figure1 = figure('Color',[1 1 1]);
subplot(2,1,1)
plot(t, N1,'--r','LineWidth',2);
hold on
ylabel('Amount of atoms','FontSize',16);
xlabel('Decay Time [hours]','FontSize',16);
grid on
legend('Rn-222');
```

```
subplot(2,1,2)
plot(t, N2,'--b','LineWidth',2);
hold on
plot(t, N3,'--g','LineWidth',2);
hold on
plot(t, N4,'--m','LineWidth',2);
ylabel('Amount of atoms','FontSize',16);
xlabel('Decay Time [hours]','FontSize',16);
grid on
ylim([0 50]);
legend('Po-218','Pb-214','Bi-214');
```

Code 2: Matlab script to simulate the percentual thoron as a function of time in an enclosed isolated area (see Equation 2-10 and 2.11).

```
clear all
close all
clc

tt = linspace(0,60,1000);
lam = log(2)/(55.6/60);
N_0 = 100;
tn = N_0.*exp(-lam.*tt);

figure1 = figure('Color',[1 1 1]);
plot(tt, tn,'-b','LineWidth',1);
grid minor
ylabel('Percentual Remaining Thoron Activity Concentration','FontSize',16);
xlabel('Time [min]','FontSize',16);  % T=0 time of first sampling
title('^{220}Rn decay as a function of time','FontSize',16);
xlim([0 10]);
```

Code 3: Matlab script to calculate the build-up of radon making use of radium source (see Equation 2-1, 2-8 and 2-9).

```
% Bates Equation to calculate the build-up of Rn-222 from Ra-226
% 28-08-2018

clear all; close all; clc;

%%%%%%%%%%%%%%%%
% [A] Input
%%%%%%%%%%%%%%%%

t = linspace(0,40,10000); % Decay Time, (days)
X1_HL = 1600*365;     % Half-life (HL) in days, Ra-226
X2_HL = 3.8235;       % Rn-222, HL
G1 = log(2)/X1_HL;
G2 = log(2)/X2_HL;
N_Rn_0 = 19850/G1;    % Number of radium atoms at t = 0, A = lambda * N

%%%%%%%%%%%%%%%%
% [B] Comp (Bates Equations)
%%%%%%%%%%%%%%%%

N1 = N_Rn_0 * exp(-G1.*t);    % Number of Ra-226 atoms as a function of time
N2 = N_Rn_0 *(G1/(G2-G1))*(exp(-G1.*t)-exp(-G2.*t)); % Number of Ra-222
atoms as a function of time
```

```
A_rn = G2.*N2;     % Calculate the radon activity,  A = lambda * N

%%%%%%%%%%%%%%%%
% [C] Plot
%%%%%%%%%%%%%%%%

figure1 = figure('Color',[1 1 1]);
plot(t, A_rn,'--b','LineWidth',2);
grid on
ylabel('Radon Activity [Bq]','FontSize',16);
xlabel('Time [days]','FontSize',16);
title('^{222}Rn build-up profile from a ^{226}Ra source (A = 19.85
kBq)','FontSize',16);
```

Appendix Table 1: Passive ambient radon measurements at CPO radon lab 2018.

Location	E-PERM Detector	Electret Initial Voltage, I, [V]	Electret Final Voltage, F, [V]	Gamma Background, BG, [nSv/hr]	Gamma Background, BG, [µR/hr]	Duration, D, [days]	Radon Measurement Levels, RnC, [Bq/m^3]	Radon Measurement Uncertainty, [Bq/m^3]
1	882	290	223	79	7.9	19.9	40.9	8.2
	795	342	281	79	7.9	19.9	33.8	7.9
	866	413	351	79	7.9	19.9	33.6	7.9
2	836	281	222	50	5.0	19.9	42.3	8.3
	753	254	195	50	5.0	19.9	42.8	8.3
	850	222	166	50	5.0	19.9	40.2	8.2
3	896	253	193	79	7.9	19.9	34.5	7.9
	679	207	150	79	7.9	19.9	32.2	7.8
	925	336	271	79	7.9	19.9	38.0	8.1
QC	0	-1	-1	-	-	19.9	-	-
	4451	234	231	-	-	19.9	-	-
	4579	224	224	-	-	19.9	-	-

Appendix Figure Set 1: Decay charts of radon progeny, 1 to 8.

^{218}Po (α-decay, $t_{1/2}$ = 3.10 min)

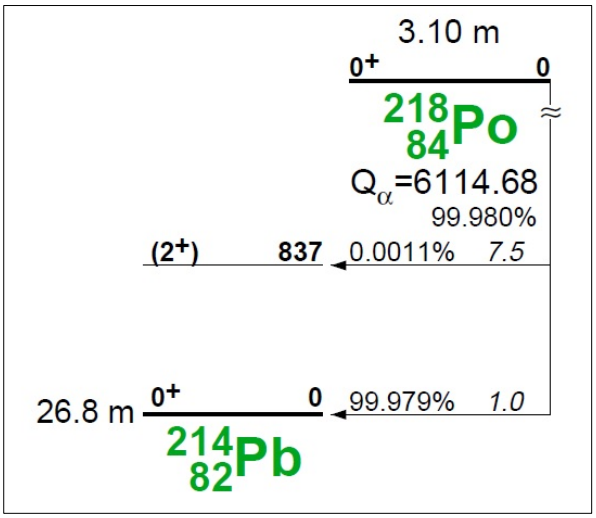

Appendix Figure - 1: Alpha-decay scheme of ^{218}Po (NNDC, 2018)

^{214}Pb (β-decay, $t_{1/2}$ = 26.8 min)

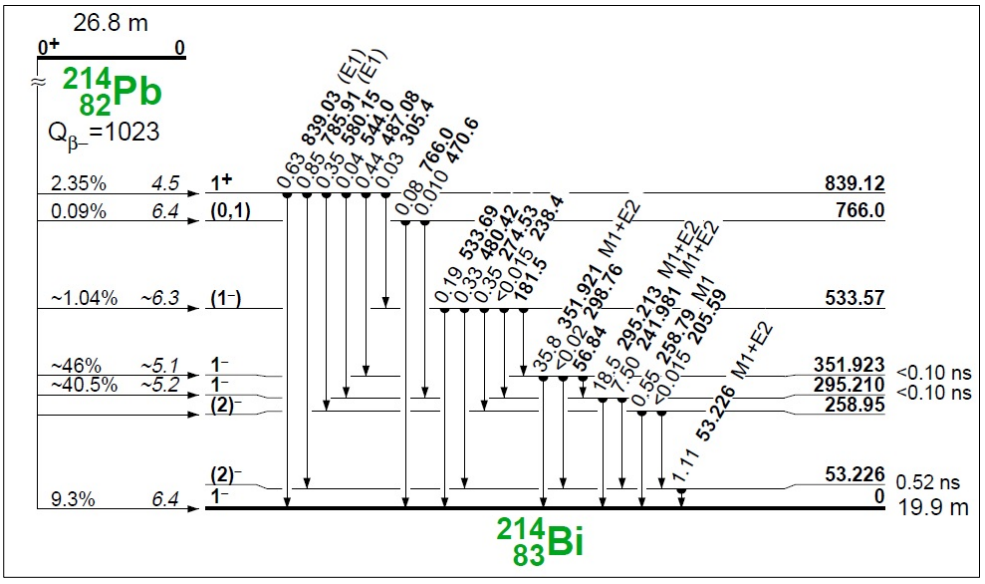

Appendix Figure - 2: Beta-decay scheme of ^{214}Pb (NNDC, 2018)

^{214}Bi (β-decay with BR = 99.979 % and α-decay with BR = 0.021 %, $t_{1/2}$ = 19.9 min)

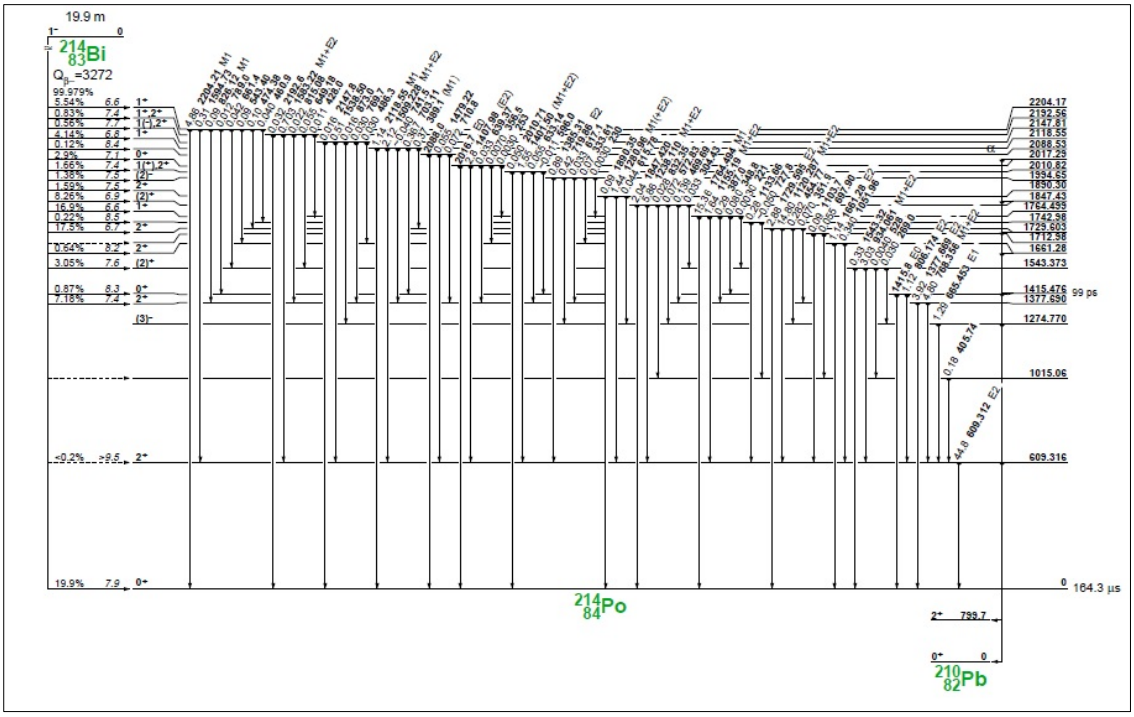

Appendix Figure - 3: Beta-decay scheme of ^{214}Bi (NNDC, 2018)

^{214}Po (α-decay, $t_{1/2}$ = 164.3 µs)

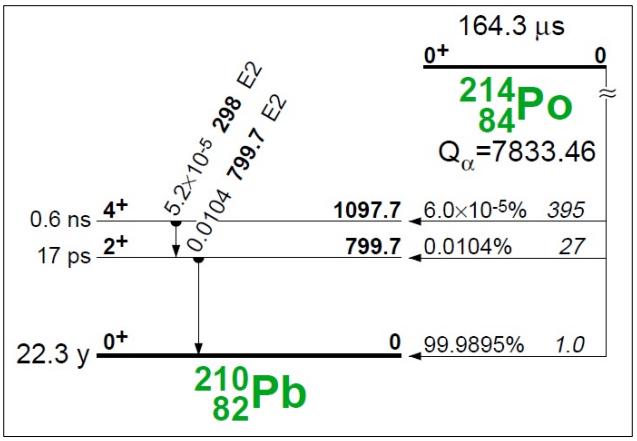

Appendix Figure - 4: Alpha-decay scheme of ^{214}Po (NNDC, 2018)

^{210}Pb (B-decay with BR = 100 % and α-decay with BR = 1.9 x 10^{-6} %, $t_{1/2}$ = 22.3 years)

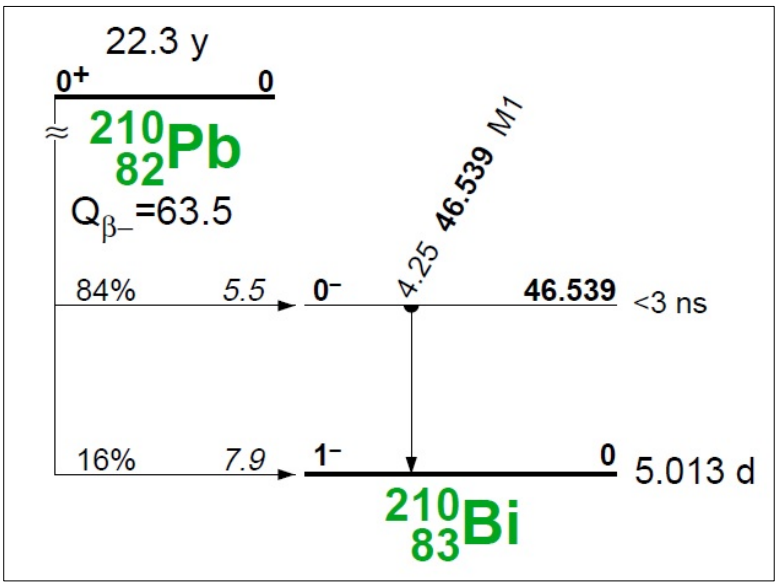

Appendix Figure - 5: Beta-decay scheme of ^{214}Pb (NNDC, 2018)

^{210}Bi (B-decay with BR = 100 % and α-decay with BR = 1.2 x 10^{-4} %, $t_{1/2}$ = 5.013 days)

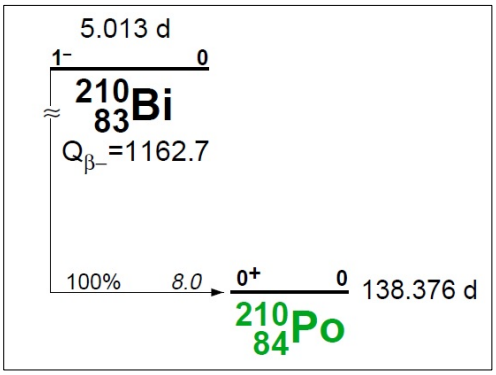

Appendix Figure - 6: Beta-decay scheme of ^{210}Bi (NNDC, 2018)

^{210}Po (α-decay, $t_{1/2}$ = 138.376 days)

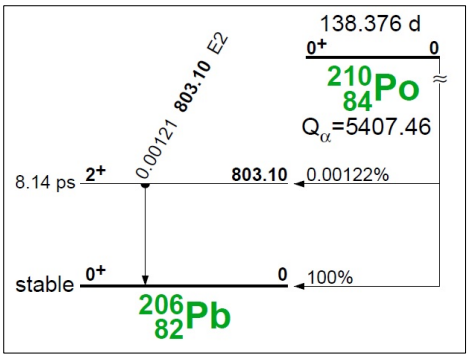

Appendix Figure - 7: Alpha-decay scheme of ^{210}Po (NNDC, 2018)

^{206}Pb (Stable Isotope)

Appendix Table 2: Inter-annual monthly number of data points from CPO, CGO and MLO utilised for percentile analysis.

Inter-annual monthly number of data points (N)													
	Year	**Jan**	**Feb**	**Mar**	**Apr**	**May**	**Jun**	**Jul**	**Aug**	**Sep**	**Oct**	**Nov**	**Dec**
CPO	**1999**	0	0	634	647	687	636	671	655	582	682	625	655
	2000	536	548	518	560	359	544	718	650	675	702	235	697
	2001	595	109	517	610	564	666	470	556	543	578	385	380
	2002	357	456	677	663	638	457	526	600	561	571	600	713
	2003	615	637	445	382	737	586	705	621	625	703	511	713
	2004	673	447	489	355	563	674	634	613	696	556	665	625
	2005	586	561	732	673	713	562	706	699	675	602	469	671
	2006	549	653	589	654	725	593	744	552	700	585	686	701
	2007	615	603	703	573	719	666	578	723	698	588	647	558

	2008	695	548	413	217	702	641	543	646	458	692	385	7
	2009	654	559	294	573	683	654	587	521	484	513	710	565
	2010	536	477	689	644	535	619	697	704	431	434	535	514
	2011	481	672	731	691	732	720	744	630	717	744	719	743
	2012	729	683	626	705	600	705	637	686	706	625	707	731
	2013	744	672	744	666	744	692	708	716	699	744	635	688
	2014	603	655	721	602	727	706	618	721	701	625	701	724
	2015	621	658	730	562	716	664	626	729	703	627	700	726
	2016	621	684	732	596	678	704	625	732	706	621	701	674
	2017	733	672	733	585	733	708	628	686	709	72	430	706
CGO	**1992**	473	583	720	656	691	670	667	689	579	659	634	698
	1993	710	576	689	613	702	677	616	729	689	699	698	733
	1994	728	592	690	706	727	616	724	730	694	667	665	709
	1995	662	627	732	710	723	692	647	730	707	734	637	733
	1996	634	625	684	695	713	703	728	719	705	732	670	685
	1997	728	659	691	706	721	706	731	728	707	727	707	711
	1998	695	657	731	706	340	706	730	713	705	651	707	728
	1999	730	672	744	720	741	712	740	744	714	744	711	744
	2000	744	696	743	720	744	719	744	744	720	743	718	743
	2001	737	671	744	719	744	718	744	741	719	730	692	678
	2002	687	646	731	703	744	493	704	721	576	640	636	698

	2003	690	618	728	0	592	720	744	716	700	682	707	729
	2004	686	410	591	642	701	707	721	741	703	697	700	721
	2005	732	671	744	720	744	720	742	744	717	733	632	679
	2006	737	651	743	720	742	718	744	743	718	710	700	699
	2007	723	671	737	717	738	718	739	720	711	694	700	623
	2008	672	475	707	711	703	720	732	700	660	705	696	519
	2009	502	671	587	672	611	644	705	702	603	605	640	692
	2010	669	654	692	700	717	632	704	728	714	703	670	503
	2011	687	647	726	719	743	719	726	744	712	723	692	712
	2012	710	680	723	713	744	680	744	648	370	718	678	703
	2013	732	431	596	709	519	634	733	733	716	740	715	726
	2014	728	631	744	720	744	720	744	734	720	744	716	729
	2015	744	672	744	720	744	720	744	744	718	744	715	741
	2016	744	687	744	720	744	720	744	744	719	743	720	744
	2017	743	672	744	720	711	717	744	744	626	735	711	686
MLO	**2004**	602	594	720	675	719	703	719	706	707	725	704	719
	2005	668	660	730	708	701	705	730	725	656	732	708	719
	2006	671	658	732	707	675	681	726	665	684	589	704	719
	2007	667	658	732	618	732	707	732	732	672	731	707	643
	2008	671	663	639	704	674	703	672	600	665	729	687	719
	2009	679	612	697	701	726	675	726	728	662	711	703	618

	2010	442	654	693	708	613	643	723	727	611	687	708	456
	2011	727	661	604	615	728	686	677	718	616	702	703	733
	2012	700	626	691	595	726	702	619	711	622	675	709	718
	2013	675	660	733	679	733	695	680	696	700	597	707	717
	2014	705	652	722	620	660	684	695	360	680	612	528	607
	2015	731	656	733	683	728	708	707	731	708	702	710	730

Appendix Table 3: Inter-annual atmospheric radon distributions linear trend analysis goodness of fit result (R-square).

Inter-annual linear trendline analysis, goodness of fit results					
Location	**5th Percentile, R-square**	**25th Percentile, R-square**	**50th Percentile, R-square**	**75th Percentile, R-square**	**95th Percentile, R-square**
CGO	0.0071	0.0068	0.0134	0.0903	0.5481
CPO	0.5608	0.0566	0.0092	0.1792	0.3084
MLO	0.1298	0.1973	0.2272	0.2373	0.2185

Appendix Table 4: Inter-monthly atmospheric radon distributions linear trend analysis and goodness of fit result (R-square).

Inter-Annual Linear trendline analysis p1 coefficients, f(x) = p1*x + p2											
Month	**Site**	**5th PCTL**	**R^2, 5th PCTL**	**25th PCTL**	**R^2, 25th PCTL**	**50th PCTL**	**R^2, 50th PCTL**	**75th PCTL**	**R^2, 75th PCTL**	**95th PCTL**	**R^2, 95th PCTL**
January	CGO	0.26	0.02	-0.02	0.01	-4.22	0.06	-7.77	0.08	-7.9	0.01
	CPO	2.91	0.16	5.8	0.20	8.1	0.26	8.72	0.15	18.96	0.12
	MLO	1.41	0.17	1.92	0.12	2.3	0.11	2.91	0.10	8.82	0.25
February	CGO	0.79	0.11	1.04	0.02	-2.31	0.02	-6.909	0.04	-37.61	0.09
	CPO	1.11	0.04	1.45	0.02	4.56	0.06	7.8	0.03	33.47	0.17
	MLO	-0.42	0.01	-1.37	0.03	-2.46	0.05	0.28	0.00	7.07	0.05
March	CGO	0.75	0.08	1.59	0.11	4.06	0.06	1.85	0.00	-18.00	0.04
	CPO	1.82	0.09	2.35	0.03	5.69	0.08	11.85	0.04	21.41	0.04
	MLO	4.23	0.30	5.6	0.23	7.01	0.20	8.89	0.15	9.62	0.07
April	CGO	1.39	0.18	1.99	0.08	4.18	0.03	17.31	0.05	-79.86	0.13
	CPO	0.72	0.02	-1.35	0.01	3.2	0.01	0.03	0.00	0.84	0.00
	MLO	1.48	0.06	2.067	0.07	3.69	0.13	3.92	0.10	4.15	0.07
May	CGO	0.13	0.00	-1.33	0.02	-6.75	0.03	-4.97	0.00	-89.28	0.19

	CPO	2.08	0.20	6.41	0.18	15.74	0.12	18.06	0.05	-23.91	0.04
	MLO	2.11	0.26	2.39	0.32	2.79	0.29	4.49	0.41	7.04	0.45
June	CGO	0.67	0.08	0.00	0.00	-5.69	0.02	-33.76	0.09	-104.1	0.18
	CPO	1.15	0.06	-0.79	0.00	-12.41	0.06	-54.83	0.21	-43.64	0.10
	MLO	0.24	0.00	1.18	0.15	1.74	0.18	2.27	0.15	1.80	0.04
July	CGO	0.45	0.03	-0.95	0.03	-6.80	0.06	-10.58	0.02	-104.8	0.39
	CPO	2.39	0.35	-2.56	0.05	-17.16	0.14	-45.73	0.15	-27.54	0.07
	MLO	0.34	0.07	0.57	0.08	0.51	0.02	0.43	0.00	-0.29	0.00
August	CGO	0.65	0.05	0.47	0.00	-2.11	0.01	-12.65	0.05	-79.31	0.31
	CPO	1.81	0.35	3.58	0.23	6.21	0.05	-10.37	0.01	-9.53	0.00
	MLO	0.52	0.02	1.137	0.03	1.62	0.04	2.76	0.09	2.65	0.06
September	CGO	0.67	0.06	0.63	0.03	-1.42	0.02	-2.71	0.01	-16.3	0.02
	CPO	0.65	0.05	0.20	0.00	1.19	0.01	-2.32	0.00	-5.83	0.00
	MLO	0.83	0.03	1.63	0.07	2.19	0.08	2.91	0.09	4.78	0.17
October	CGO	0.46	0.03	0.48	0.02	-0.07	0.00	-1.71	0.00	-37.85	0.11
	CPO	2.88	0.24	1.41	0.04	3.59	0.05	1.45	0.00	10.83	0.02

	MLO	-0.59	0.01	0.52	0.01	2.90	0.10	5.83	0.20	12.58	0.27
November	CGO	0.77	0.09	0.82	0.04	0.85	0.01	2.31	0.01	-15.21	0.04
	CPO	-0.61	0.01	-2.13	0.04	-0.93	0.01	-4.08	0.05	-11.21	0.09
	MLO	0.89	0.04	1.69	0.08	1.72	0.05	1.19	0.02	4.8	0.07
December	CGO	0.35	0.01	0.27	0.00	-1.78	0.02	-0.751	0.00	-41.2	0.10
	CPO	1.37	0.01	0.52	0.00	0.69	0.00	-3.73	0.03	5.64	0.00
	MLO	0.43	0.02	0.57	0.02	1.36	0.05	2.82	0.06	6.54	0.06

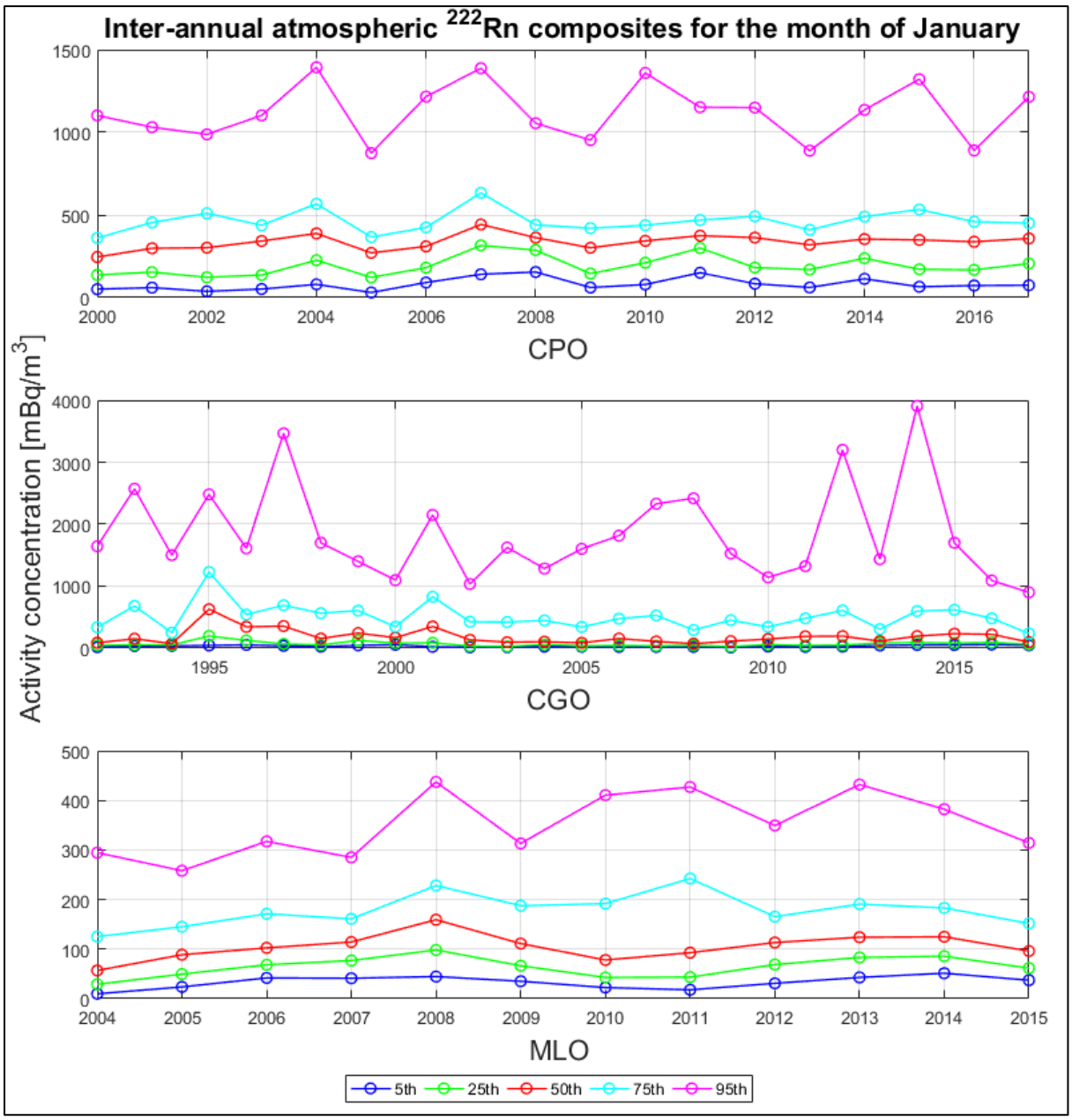

Appendix Figure - 8: Long-term inter-annual atmospheric radon concentration percentile distributions for January associated with CPO, CGO and MLO.

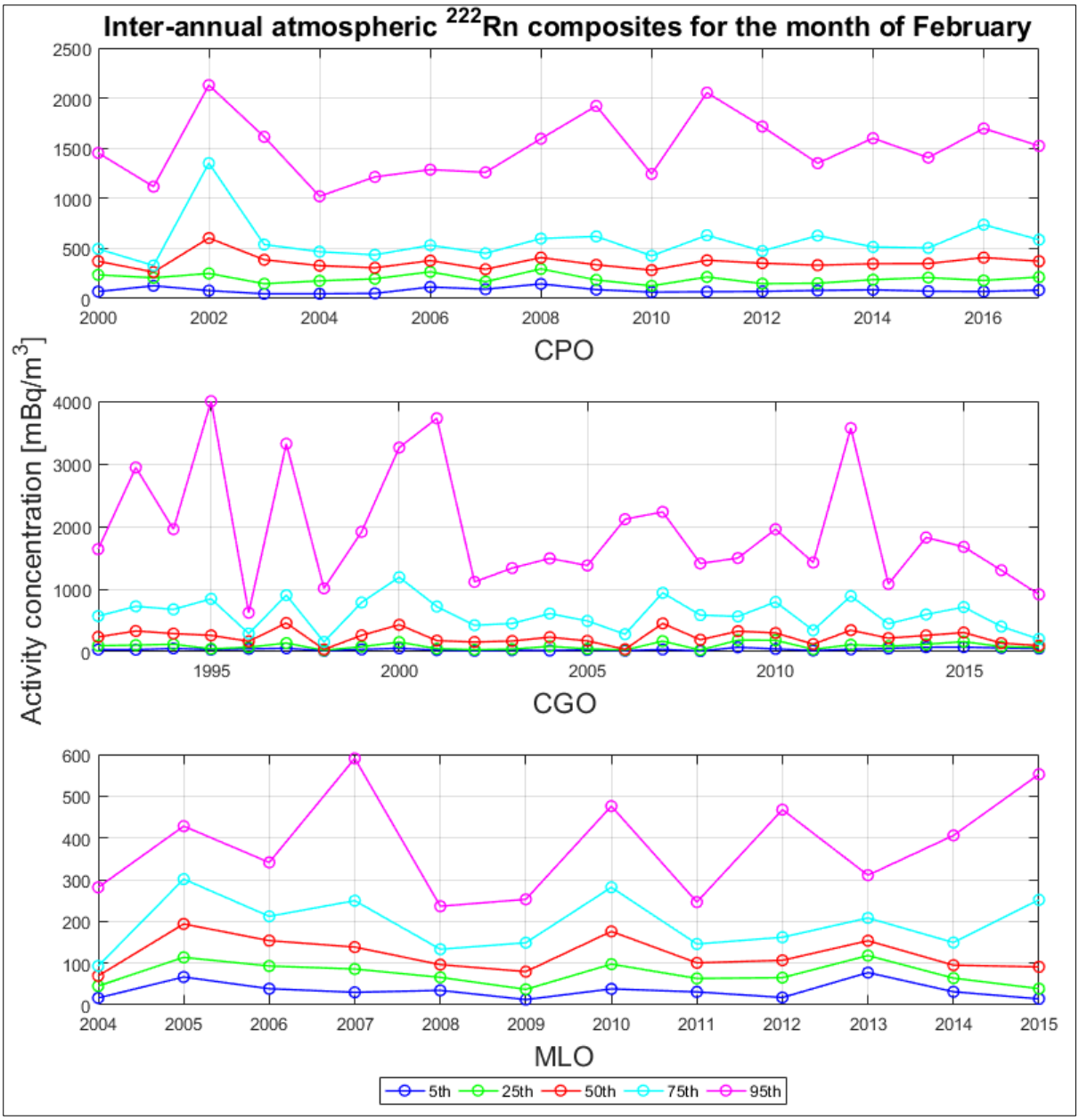

Appendix Figure - 9: Long-term inter-annual atmospheric radon concentration percentile distributions for February associated with CPO, CGO and MLO.

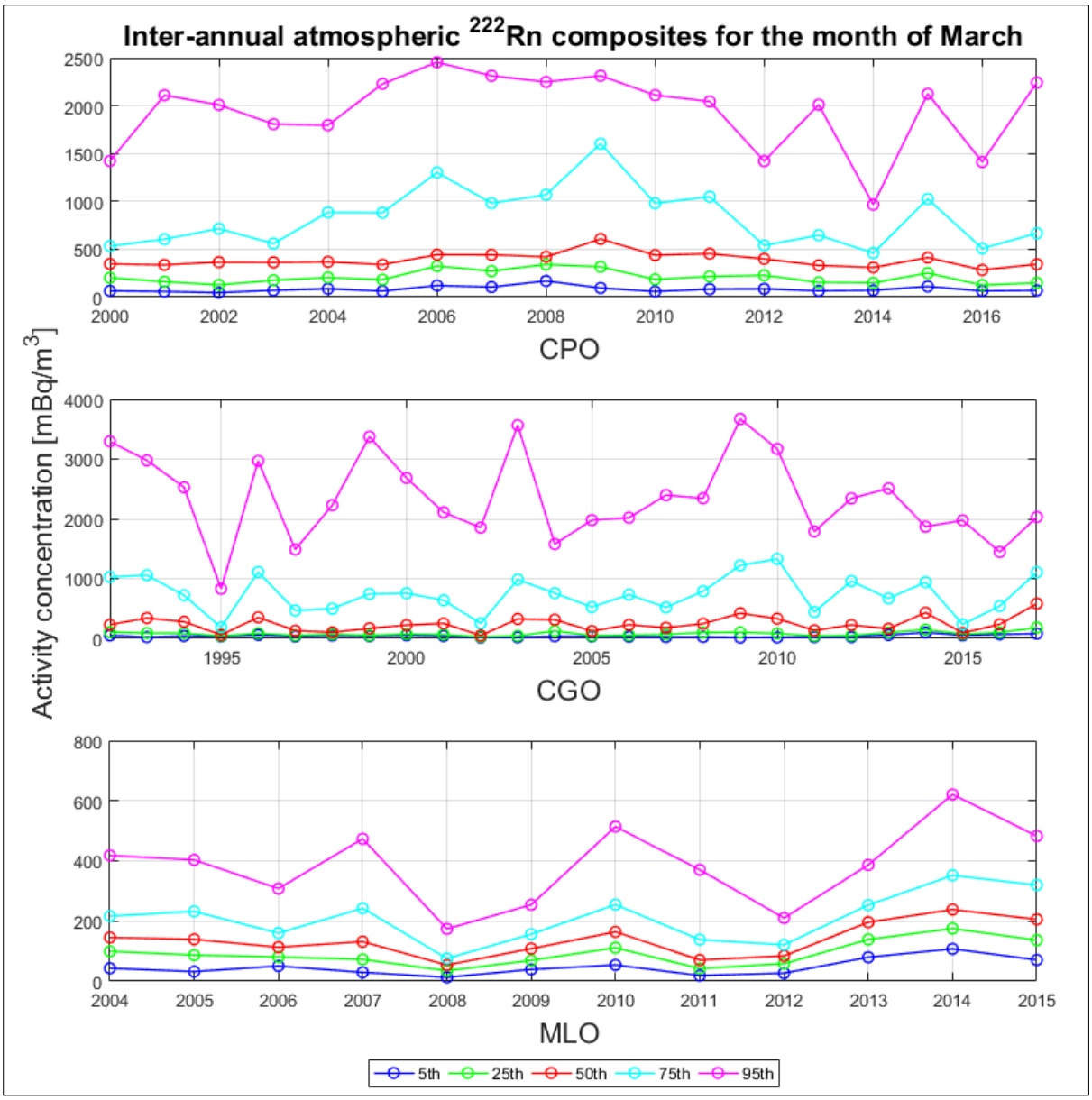

Appendix Figure - 10: Long-term inter-annual atmospheric radon concentration percentile distributions for March associated with CPO, CGO and MLO.

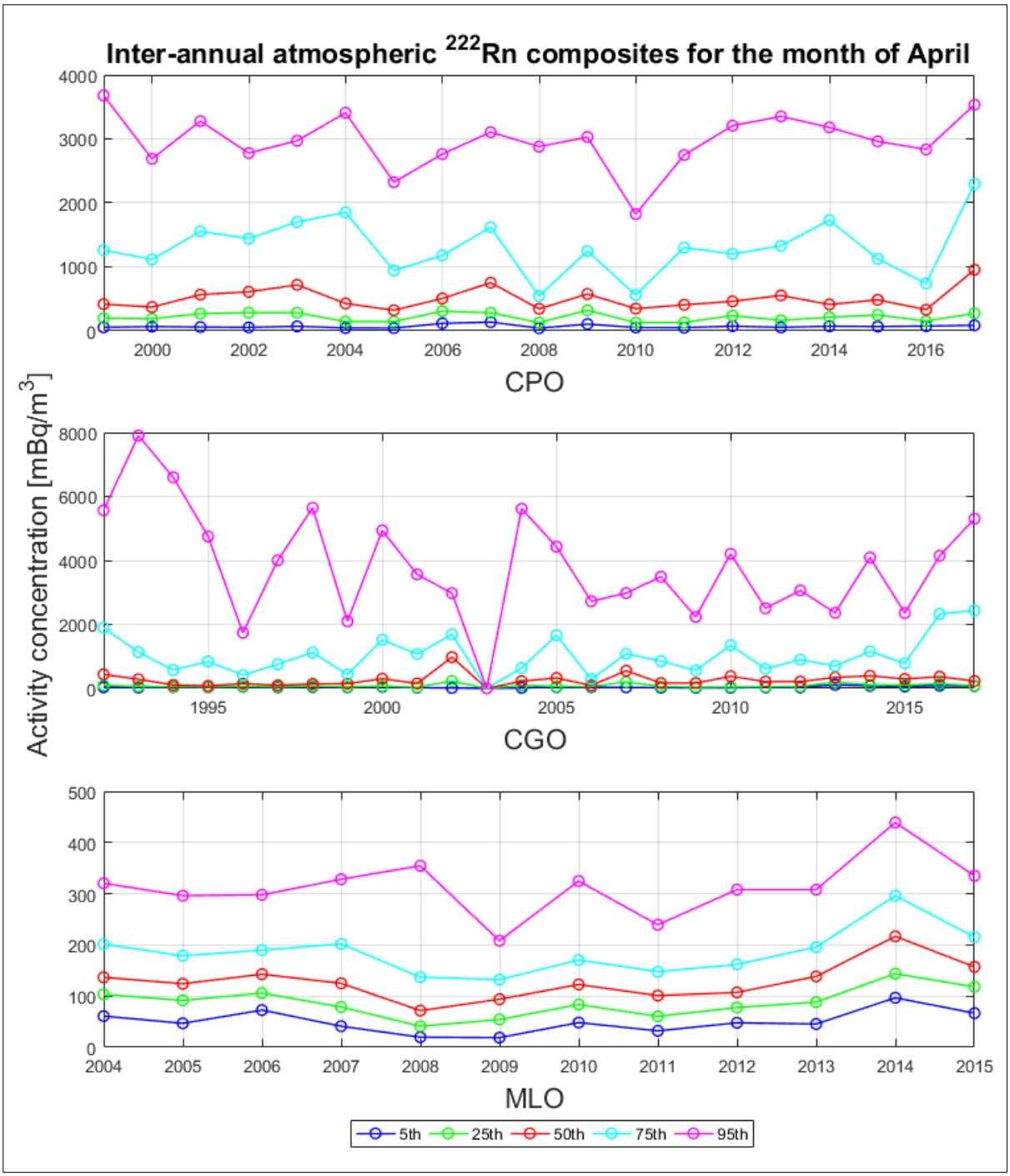

Appendix Figure - 11: Long-term inter-annual atmospheric radon concentration percentile distributions for April associated with CPO, CGO and MLO.

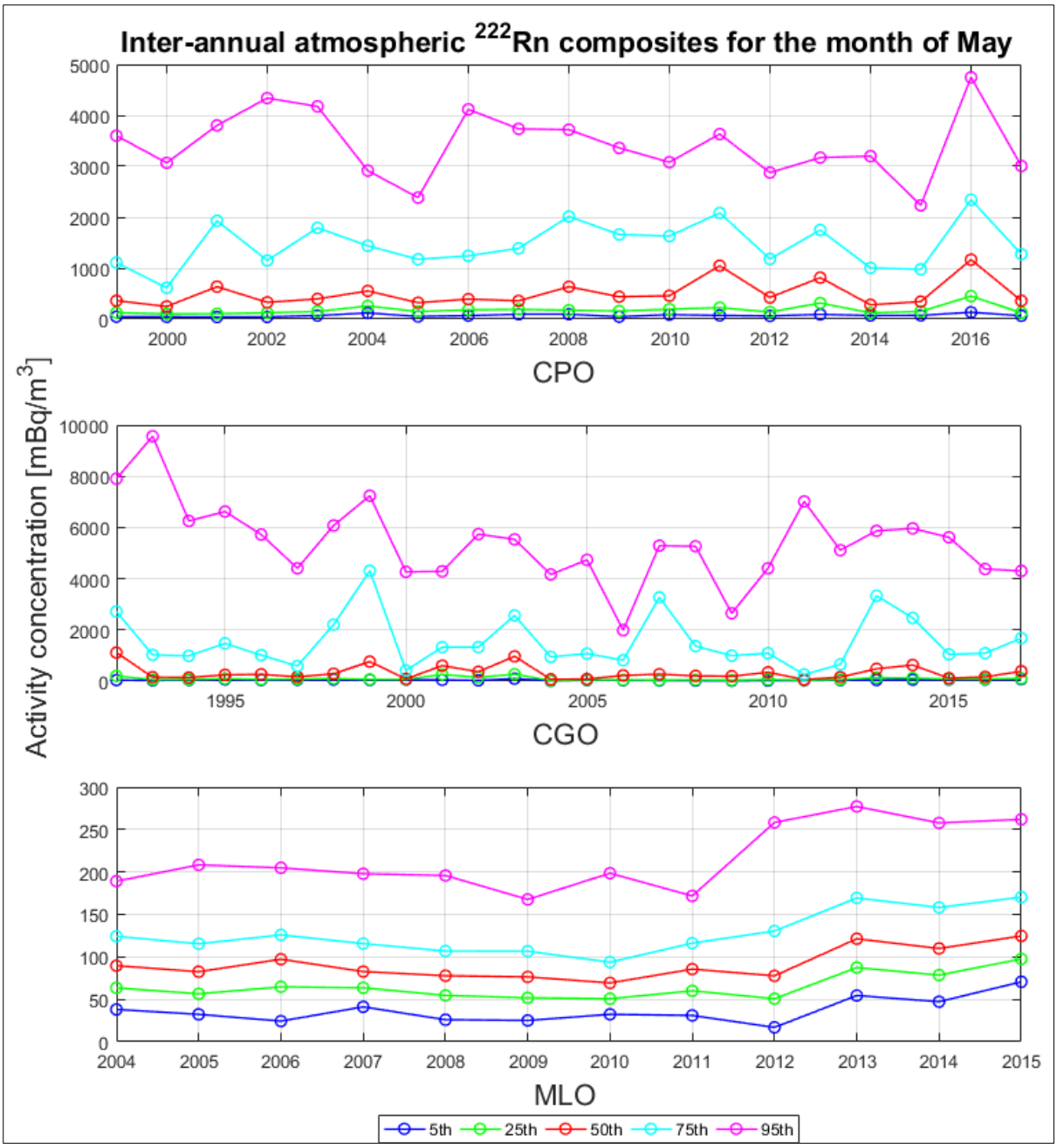

Appendix Figure - 12: Long-term inter-annual atmospheric radon concentration percentile distributions for May associated with CPO, CGO and MLO.

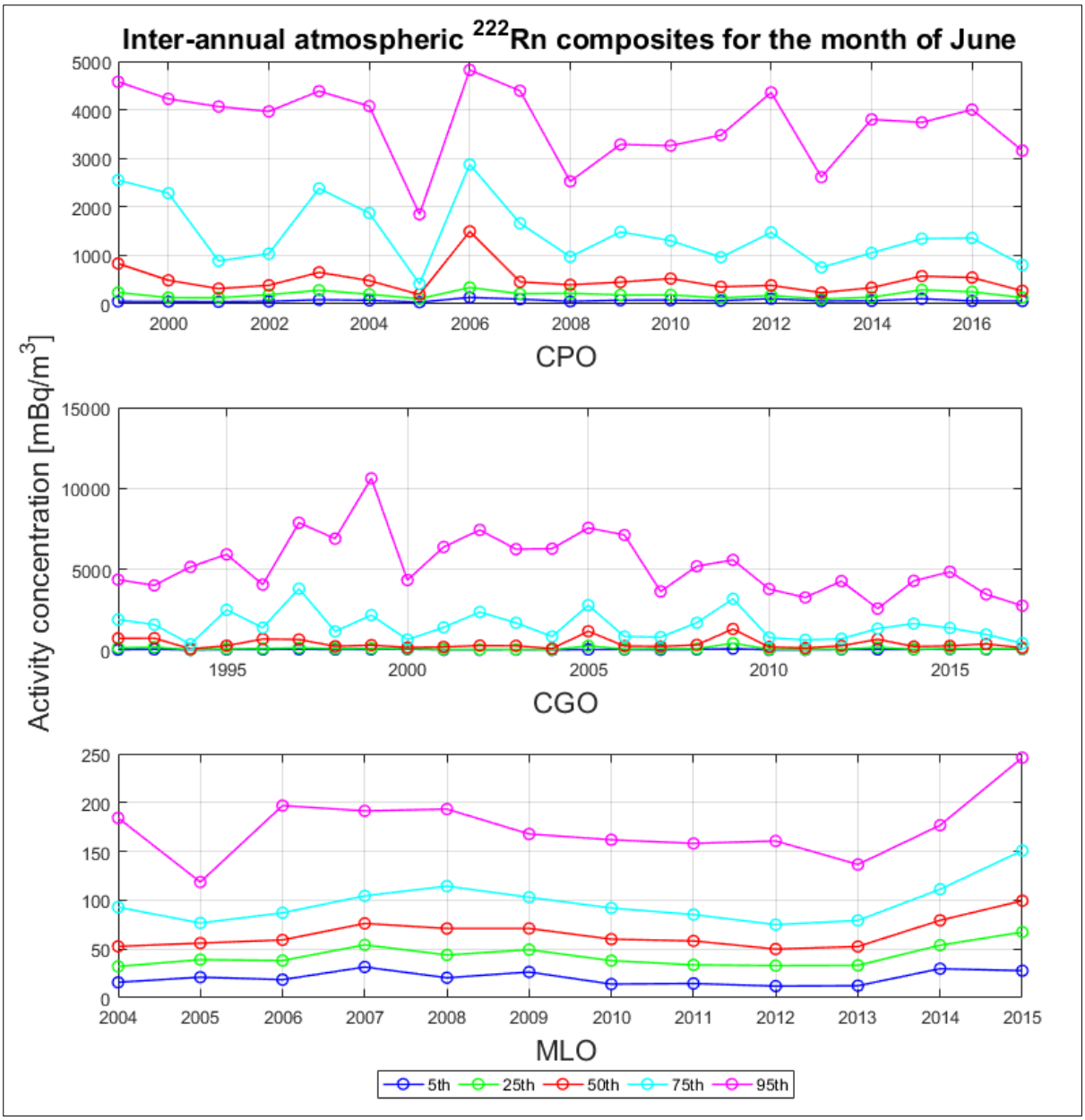

Appendix Figure - 13: Long-term inter-annual atmospheric radon concentration percentile distributions for June associated with CPO, CGO and MLO.

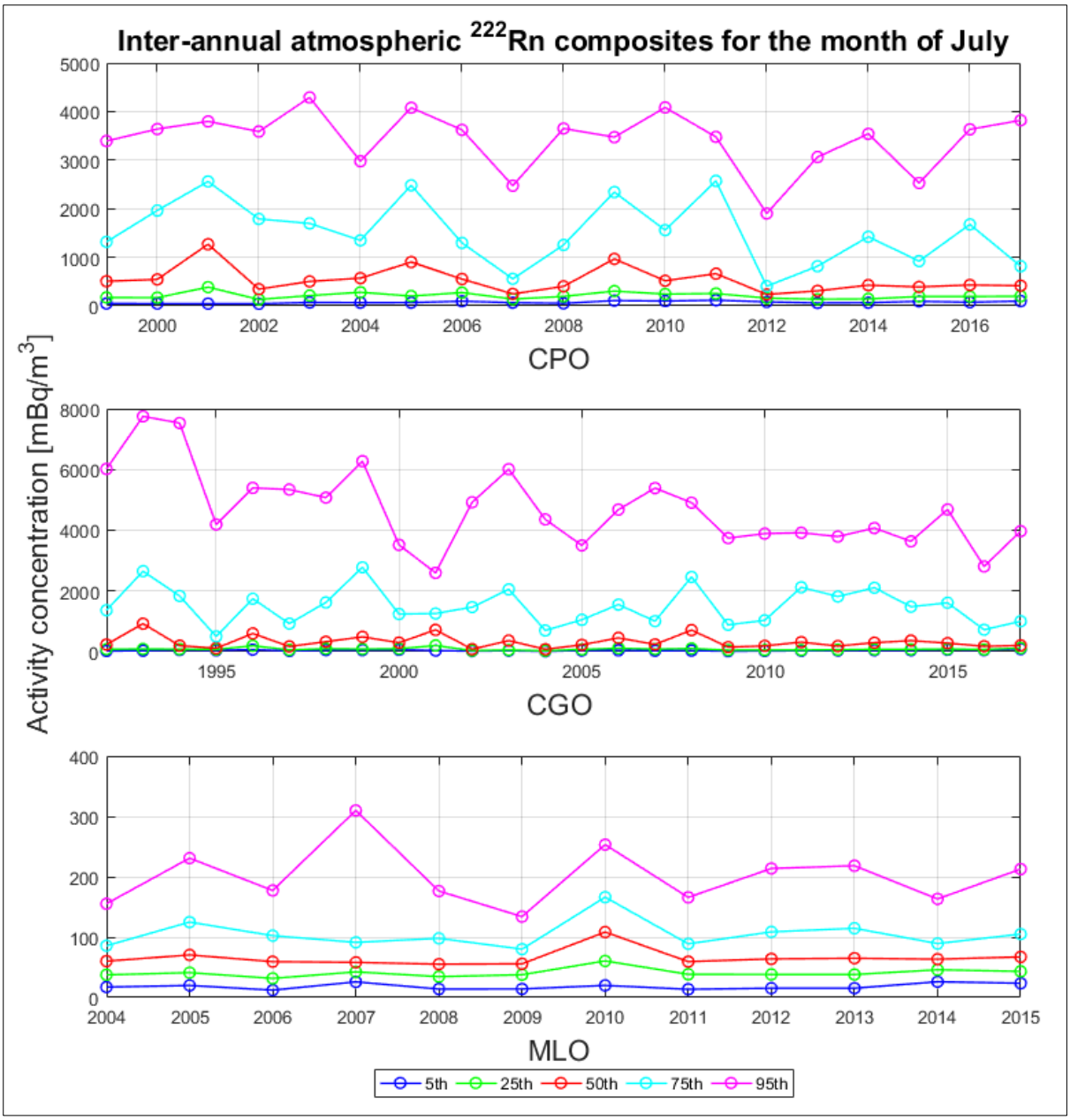

Appendix Figure - 14: Long-term inter-annual atmospheric radon concentration percentile distributions for July associated with CPO, CGO and MLO.

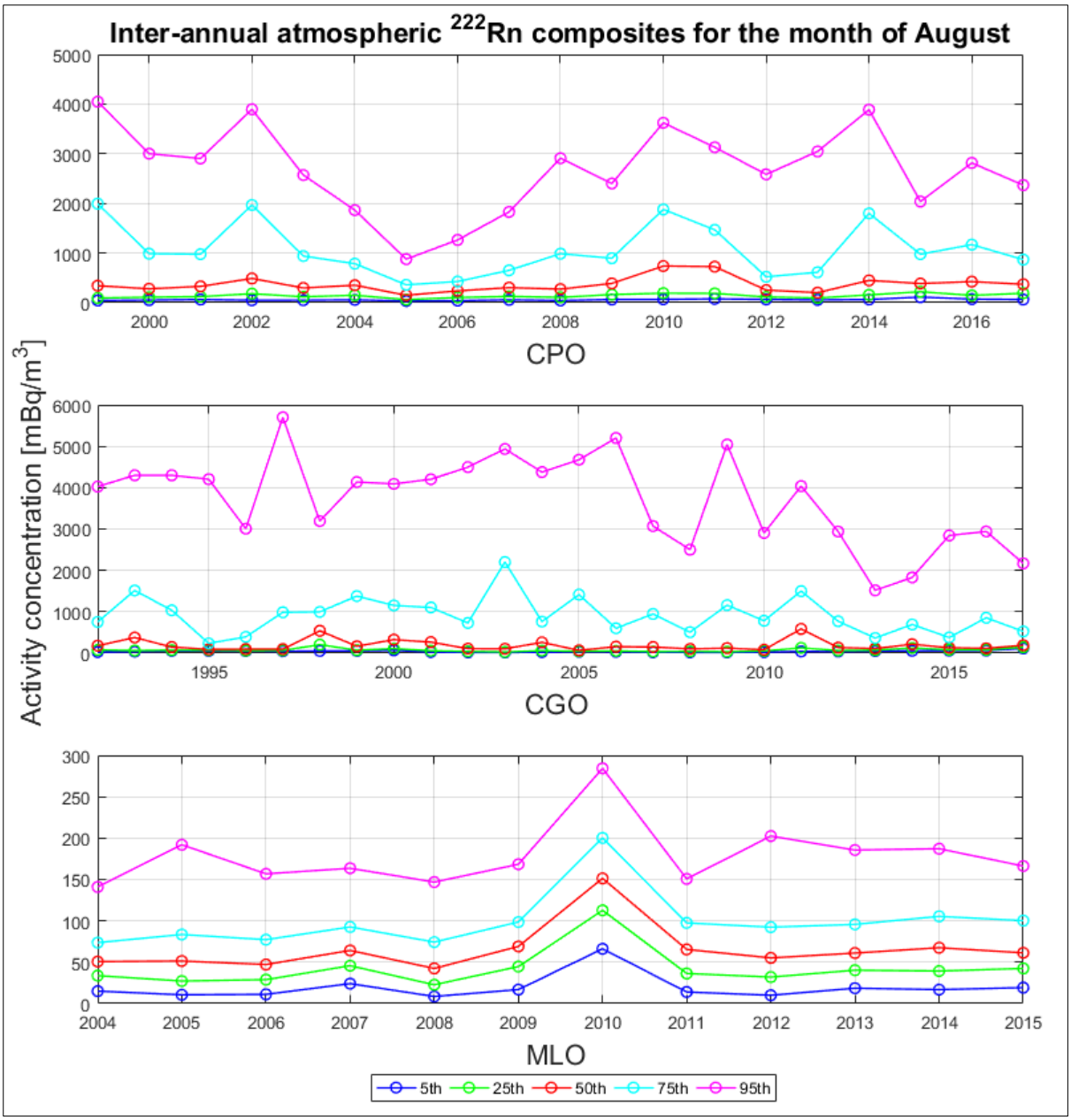

Appendix Figure - 15: Long-term inter-annual atmospheric radon concentration percentile distributions for August associated with CPO, CGO and MLO.

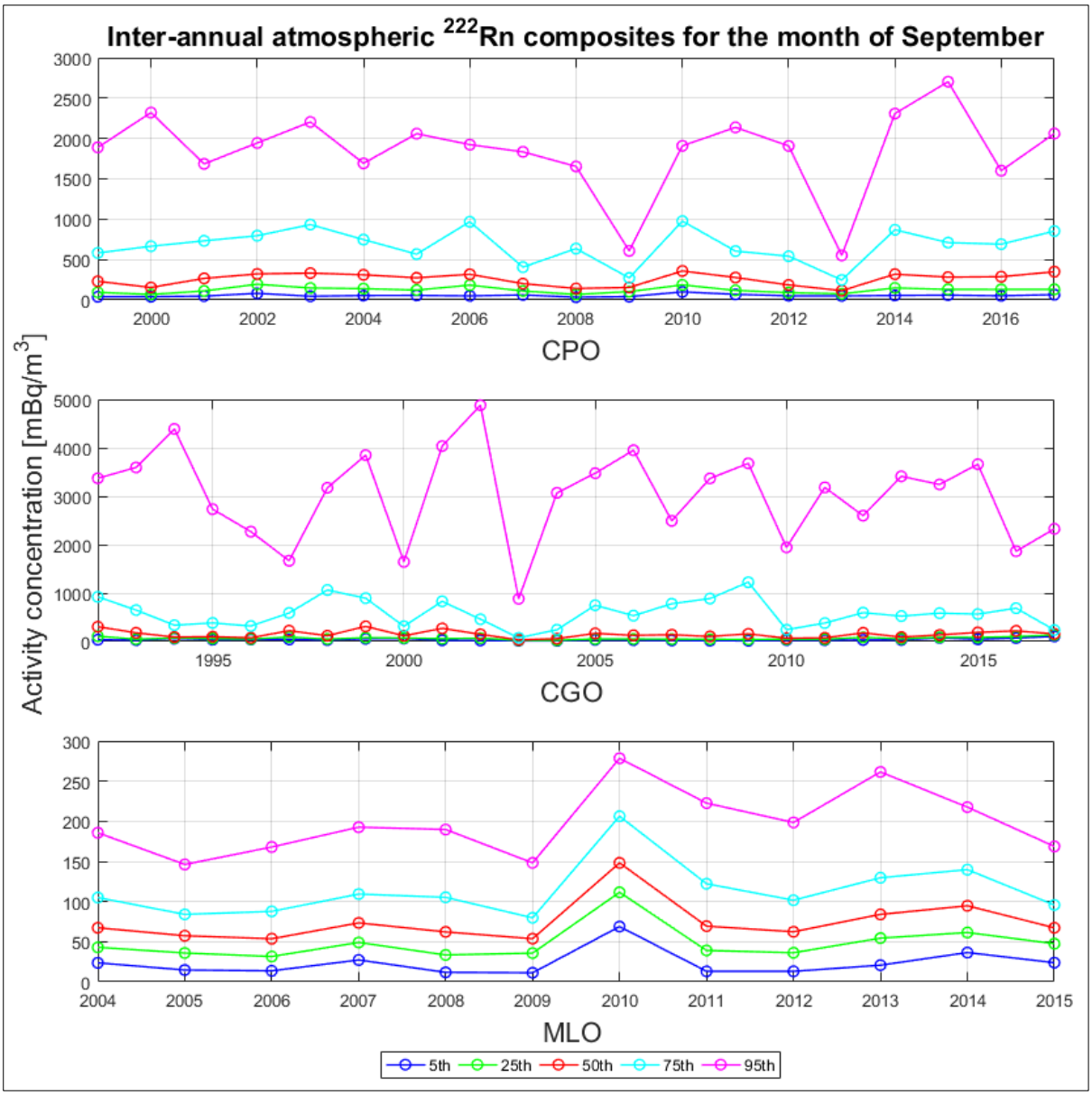

Appendix Figure - 16: Long-term inter-annual atmospheric radon concentration percentile distributions for September associated with CPO, CGO and MLO.

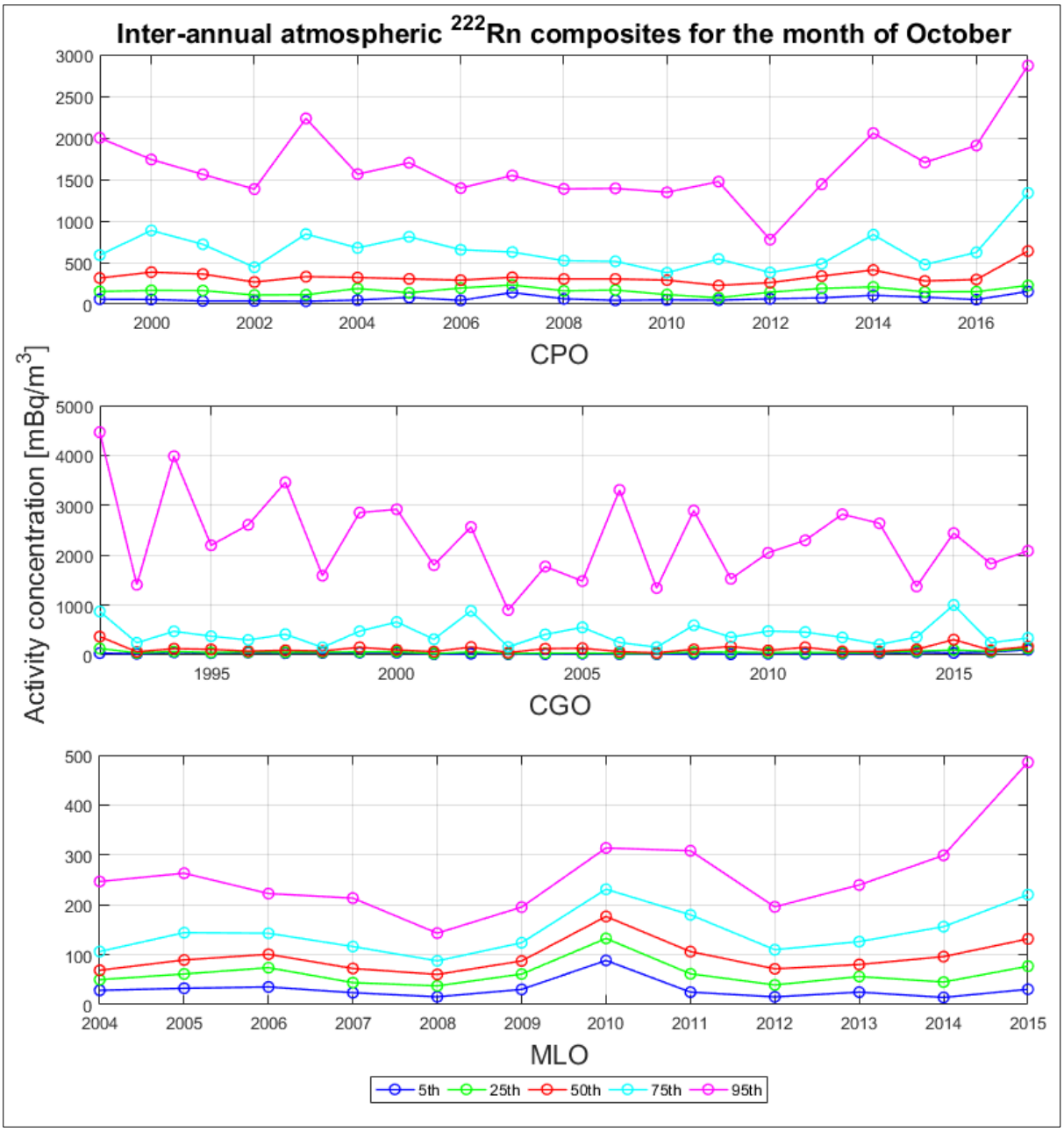

Appendix Figure - 17: Long-term inter-annual atmospheric radon concentration percentile distributions for October associated with CPO, CGO and MLO.

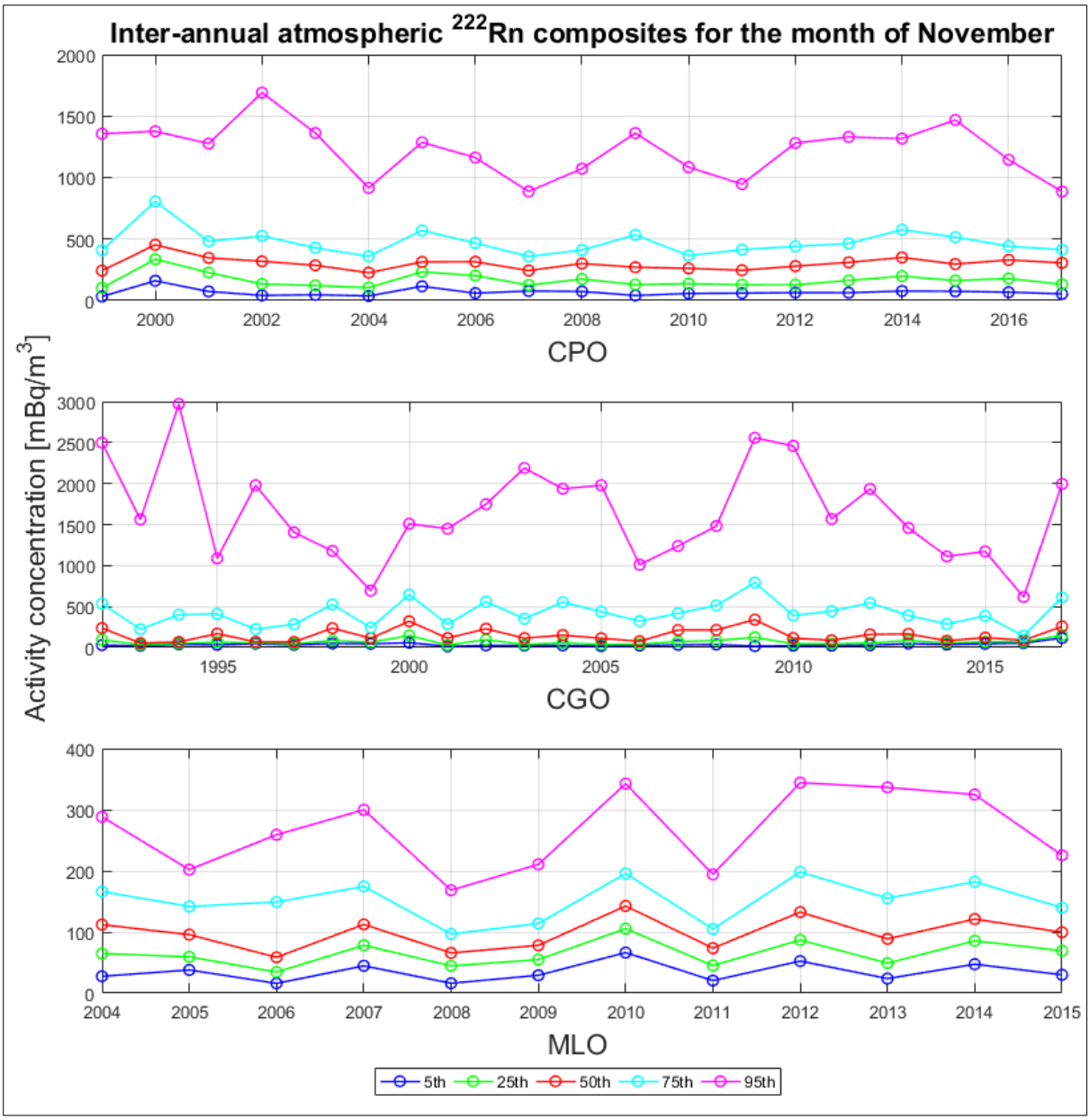

Appendix Figure - 18: Long-term inter-annual atmospheric radon concentration percentile distributions for November associated with CPO, CGO and MLO.

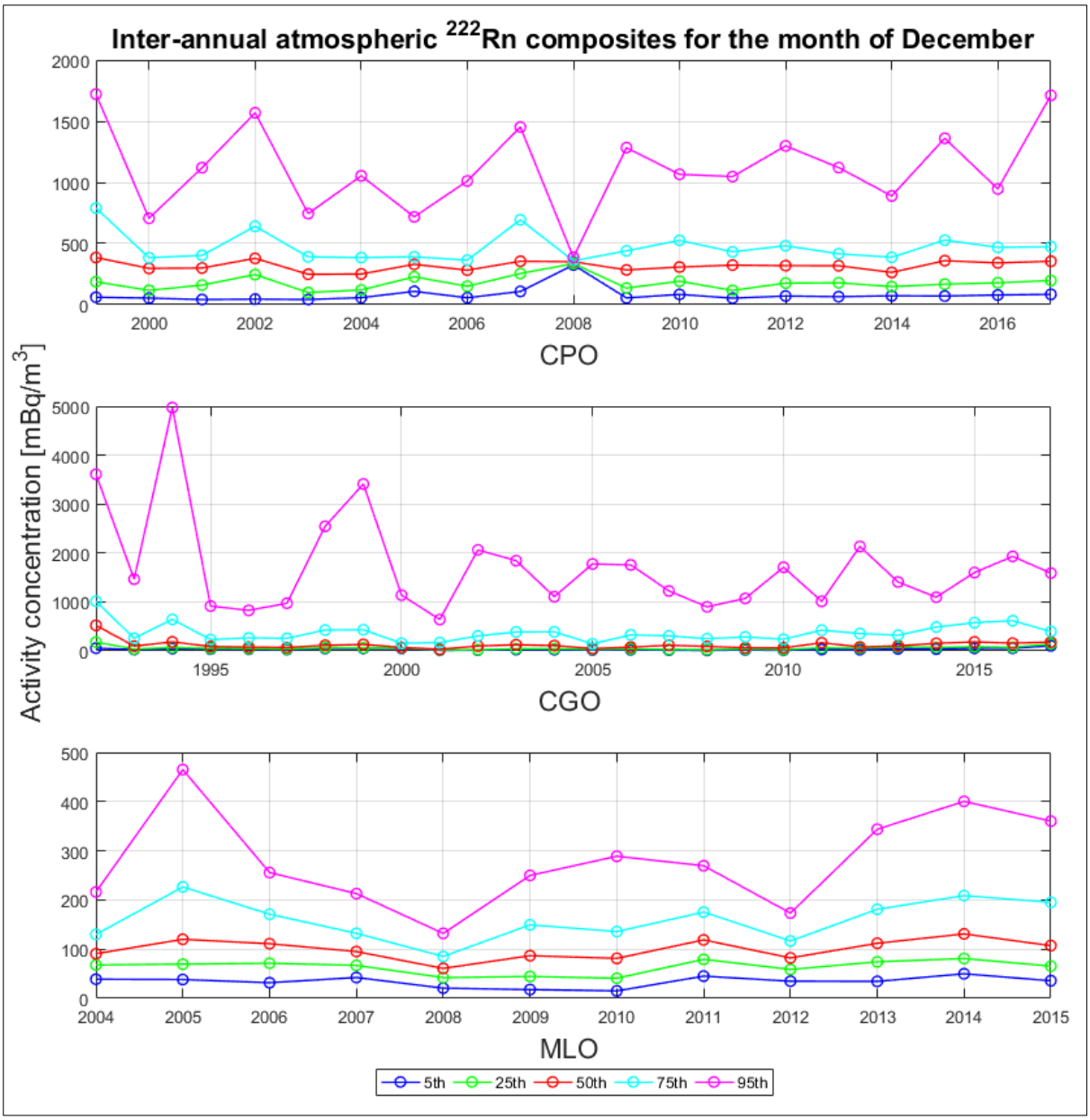

Appendix Figure - 19: Long-term inter-annual atmospheric radon concentration percentile distributions for December associated with CPO, CGO and MLO.

Appendix Table 5: Linear trend analysis results to determine the gradient associated with the radon composites of selected WD-sectors

WD-sectors linear trendline analysis p1 coefficients, f(x) = p1*x + p2				
Station	**Air Mass Sector**	**95th Pctl**	**75th Pctl**	**50th Pctl**
CGO	Continental C1 (275° - 54°)	-91	-42	-17
	Continental C2 (90° - 167°)	-37	-4	0
	Marine O1 (167° - 275°)	-6	1	3
	Marine O2 (54° -90°)	-44	-11	3
	Mixed M3 (60° - 110°)	-36	-1	4
	Mixed M4 (195° -205°)	-1	2	3
	Mixed M5 (265° - 275°)	-5	1	2
	Deep Baseline DD (120° -150°)	-5	2	-3
CPO	Continental C3 (339° -115°)	-58	-35	-7
	Marine O3 (115° - 339°)	32	4	-2
	Mixed M1 (100° - 150°)	9	9	2
	Mixed M2 (250° - 339°)	-3	12	4
	Deep Baseline D (180° -273°)	30	8	2

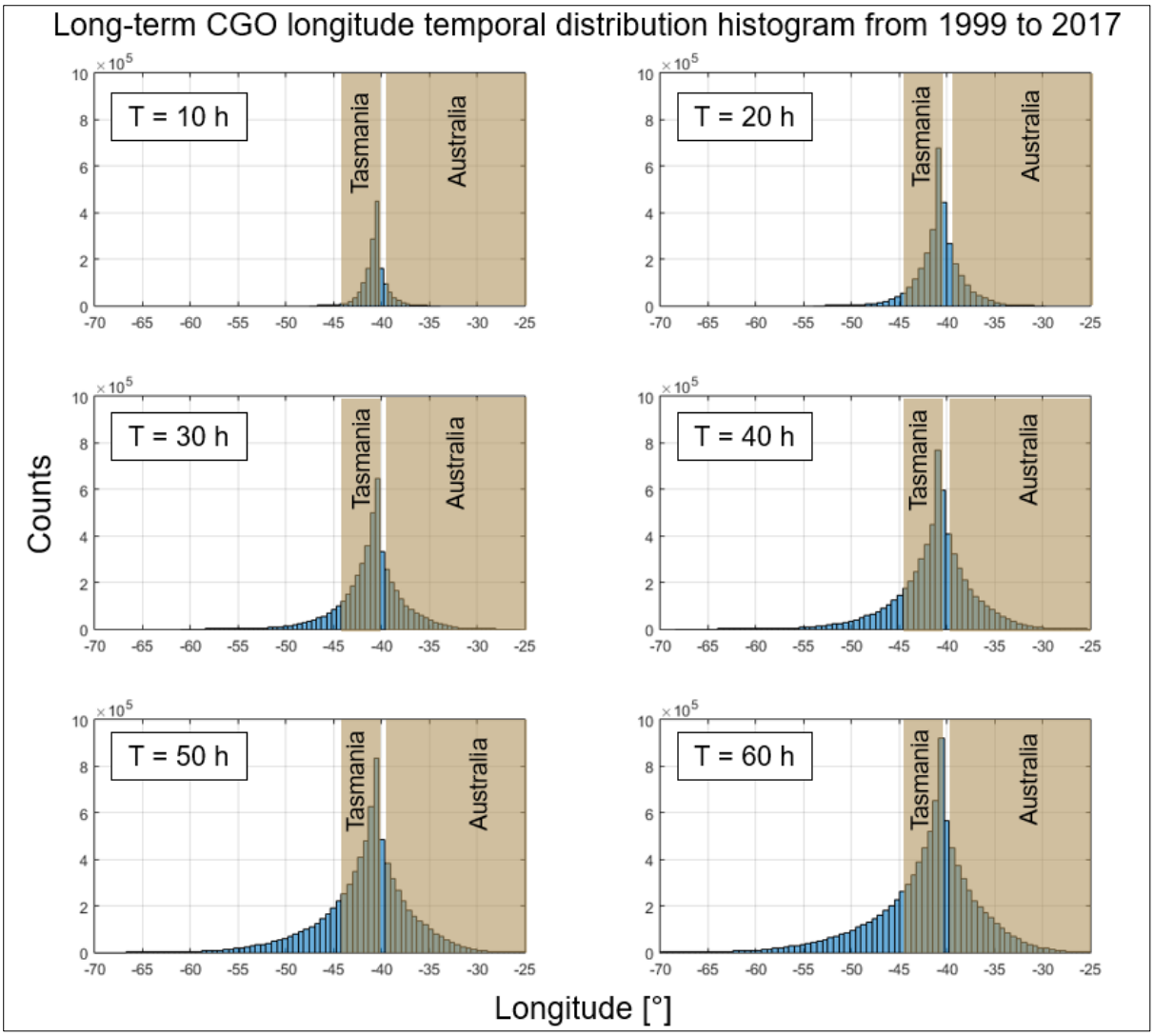

Appendix Figure - 20: CGO long-term back-trajectory longitude histogram computed for a duration from T = 10 h to 60 h back in time. The continental air-masses fetch sectors are illustrated in brown while the remaining will be marine.

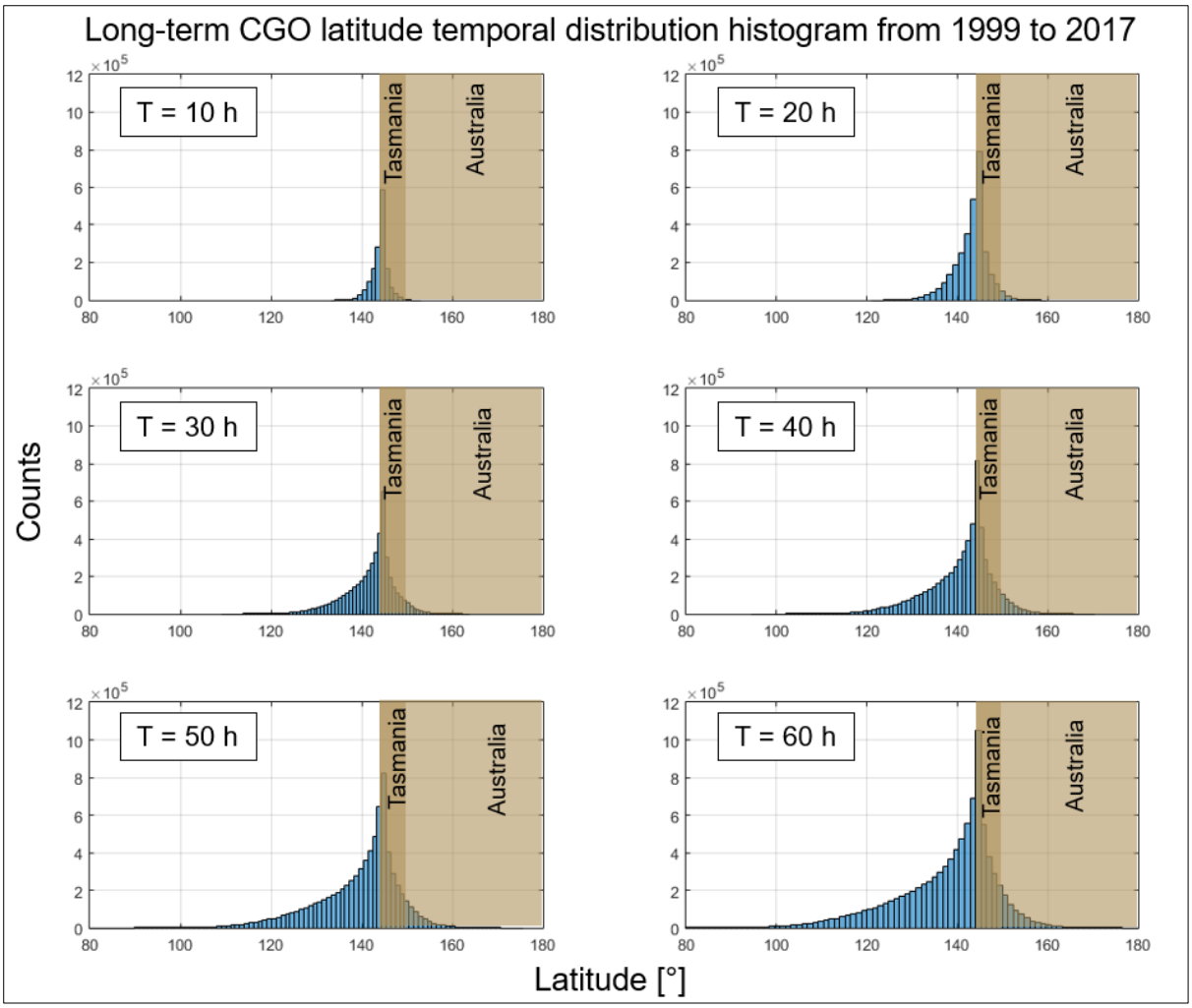

Appendix Figure - 21: CGO long-term back-trajectory latitude histogram computed for a duration from T = 10 h to 60 h back in time. The continental sectors are illustrated in brown.

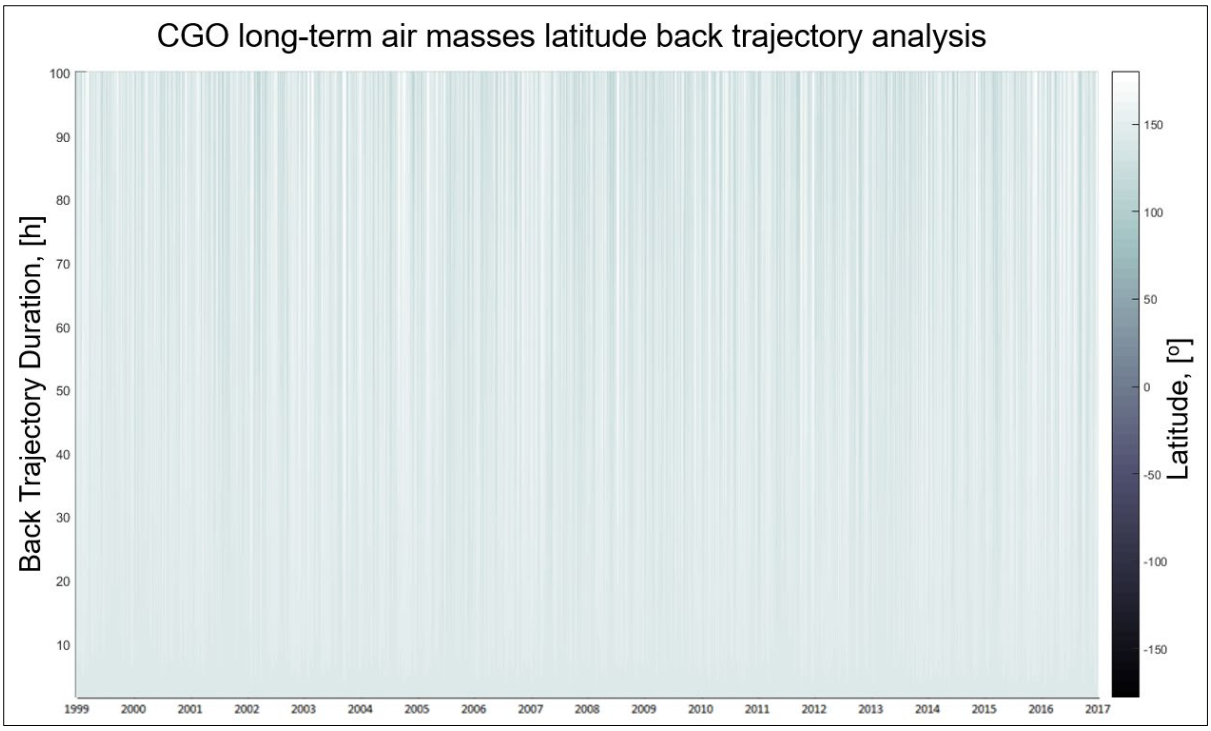

Appendix Figure - 22: CGO long-term back-trajectory latitude density analysis from 1999 to 2017.

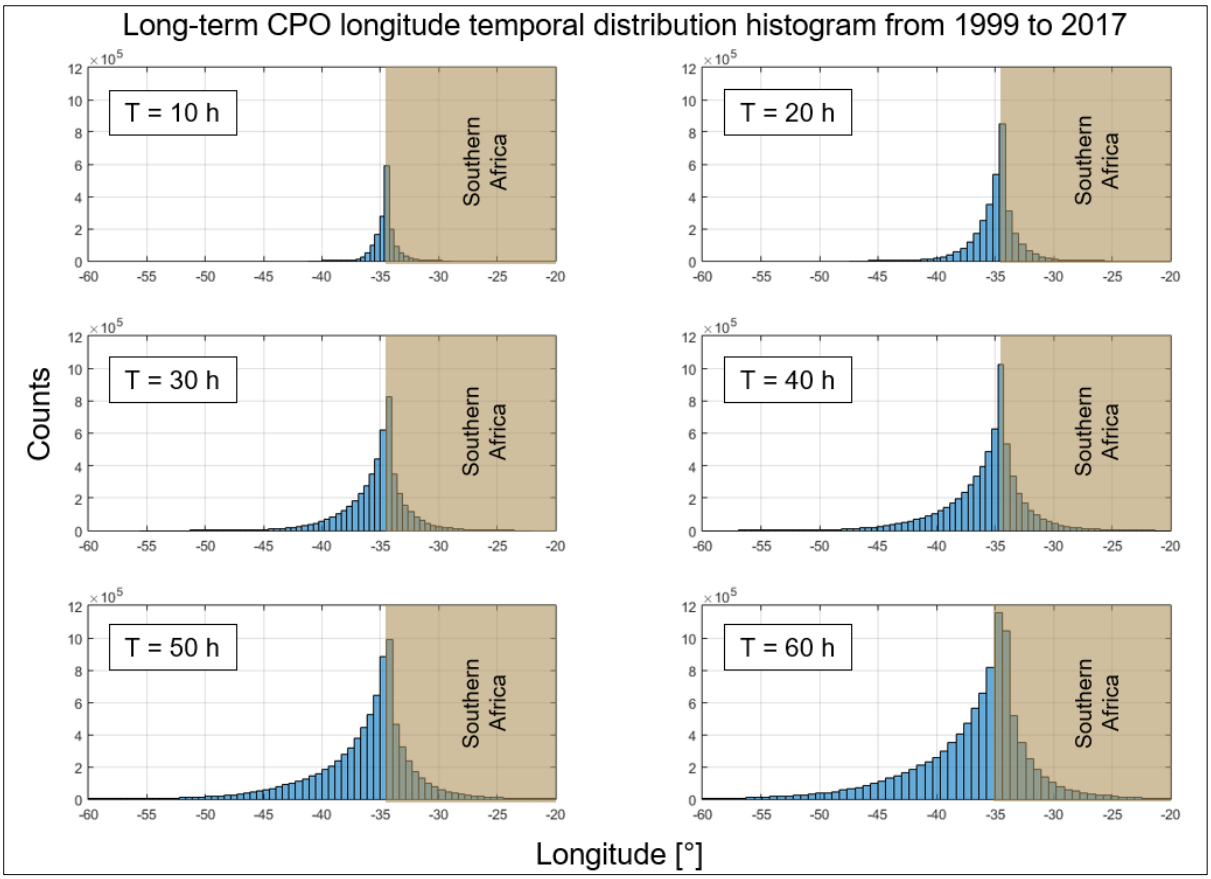

Appendix Figure - 23: CPO long-term back-trajectory longitude histogram computed for a duration from T = 10 h to 60 h back in time. The continental sectors are illustrated in brown.

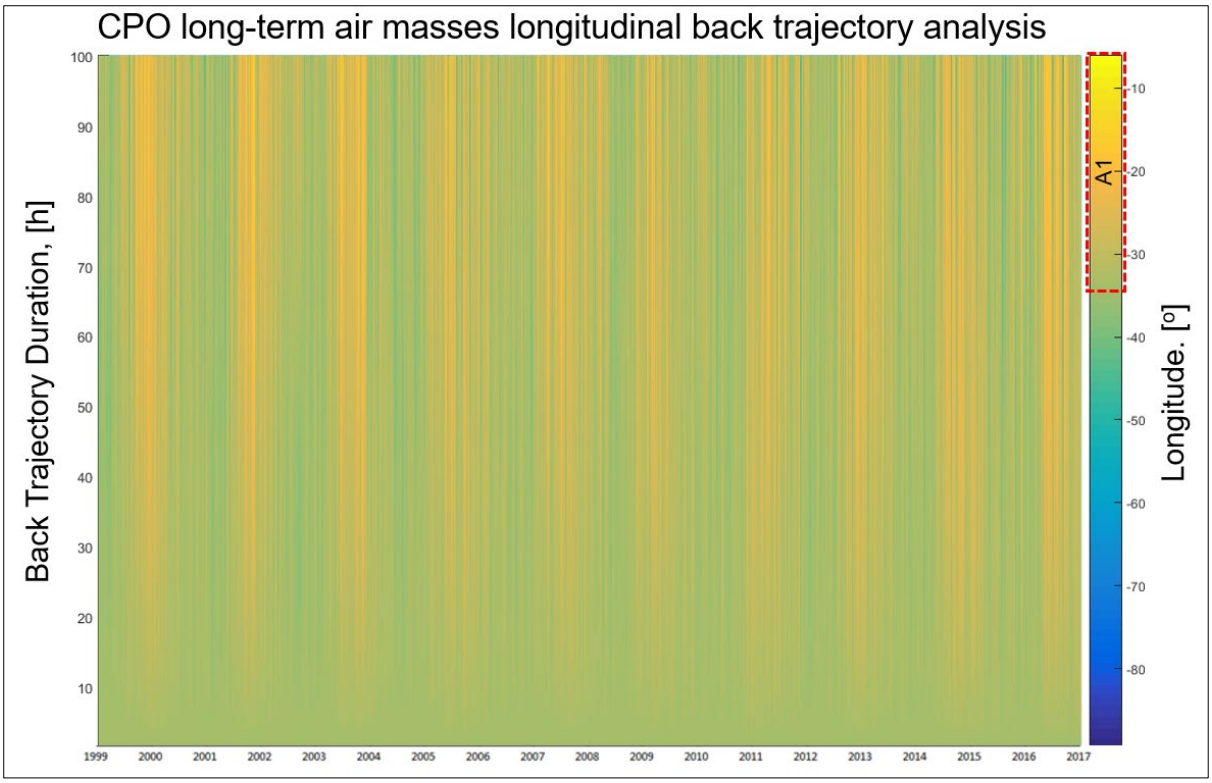

Appendix Figure - 24: CPO long-term back-trajectory longitude density analysis from 1999 to 2017. The colorbar region A1 represents the continental region of Southern Africa.

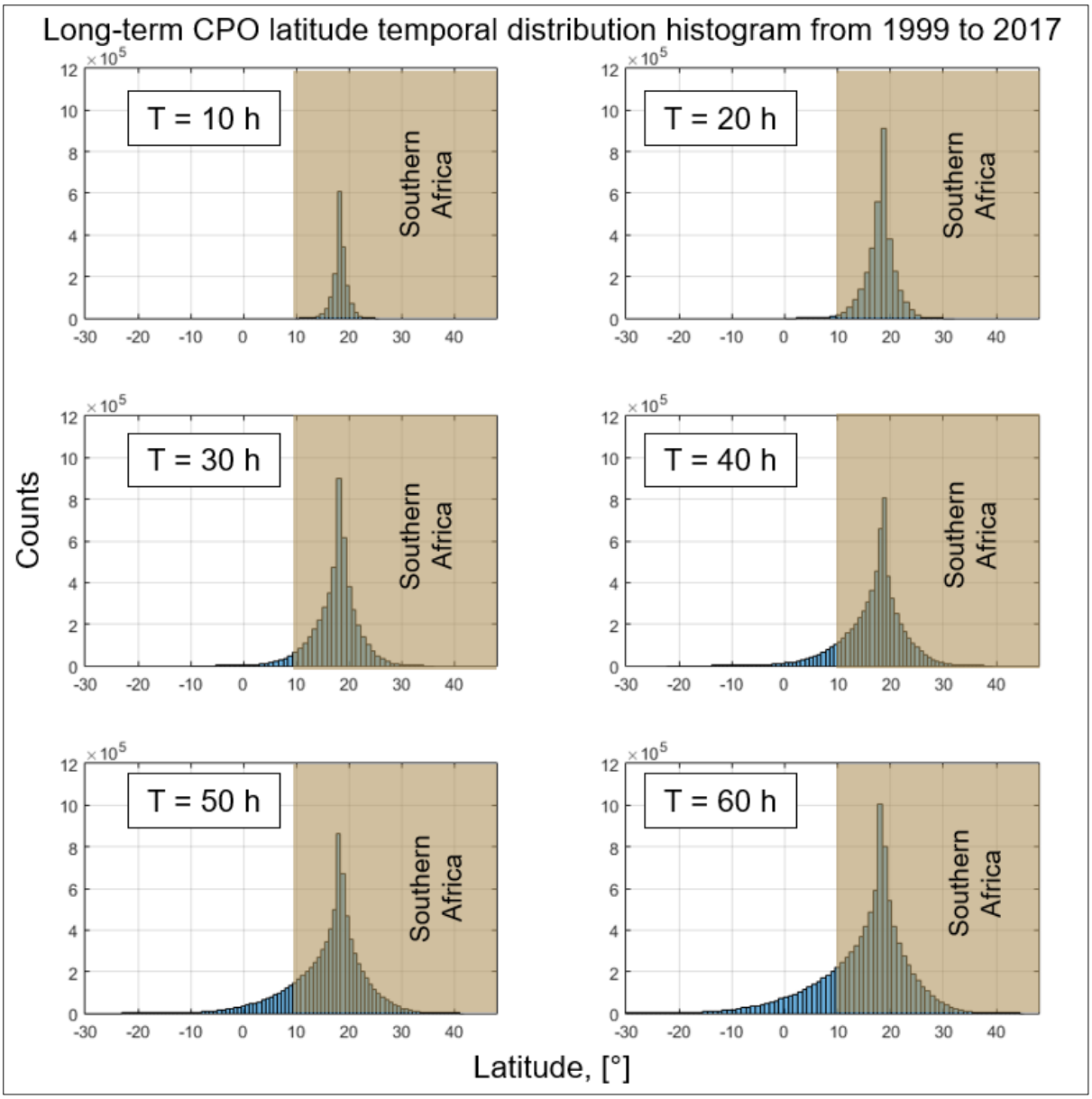

Appendix Figure - 25: CPO long-term back-trajectory latitude histogram computed for a duration from T = 10 h to 60 h back in time. The continental sectors are illustrated in brown.

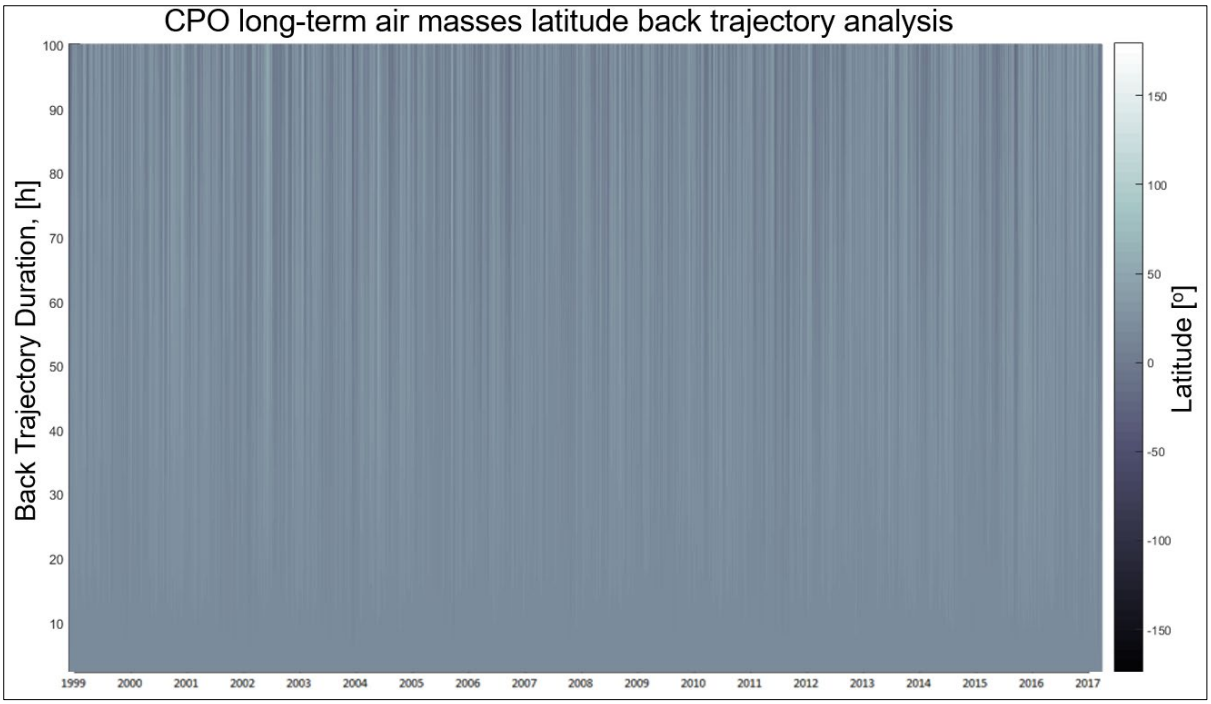

Appendix Figure - 26: CGO long-term back-trajectory latitude density analysis from 1999 to 2017.

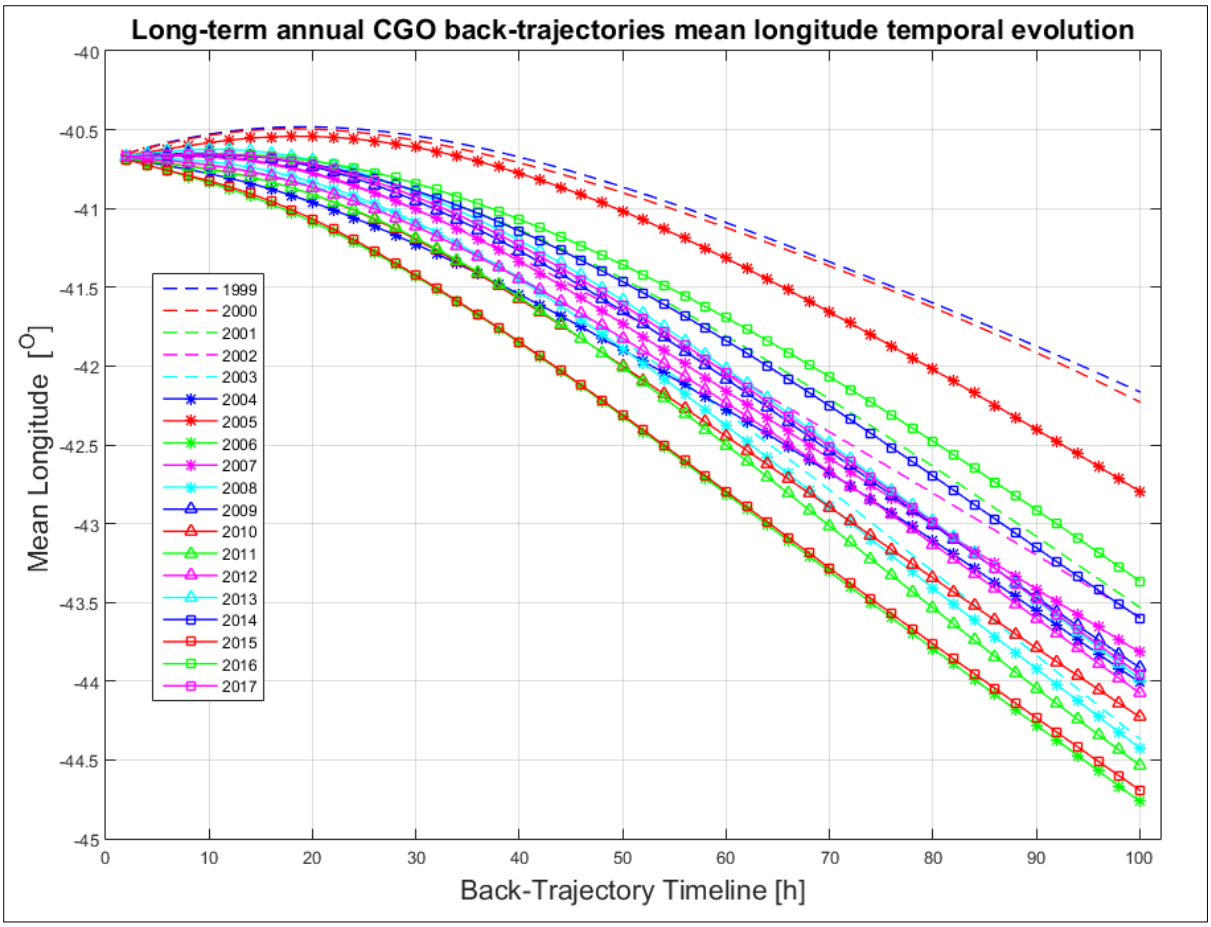

Appendix Figure - 27: Long-term inter-annual CGO air-masses back-trajectories mean longitude temporal evolution from 1999 to 2017.

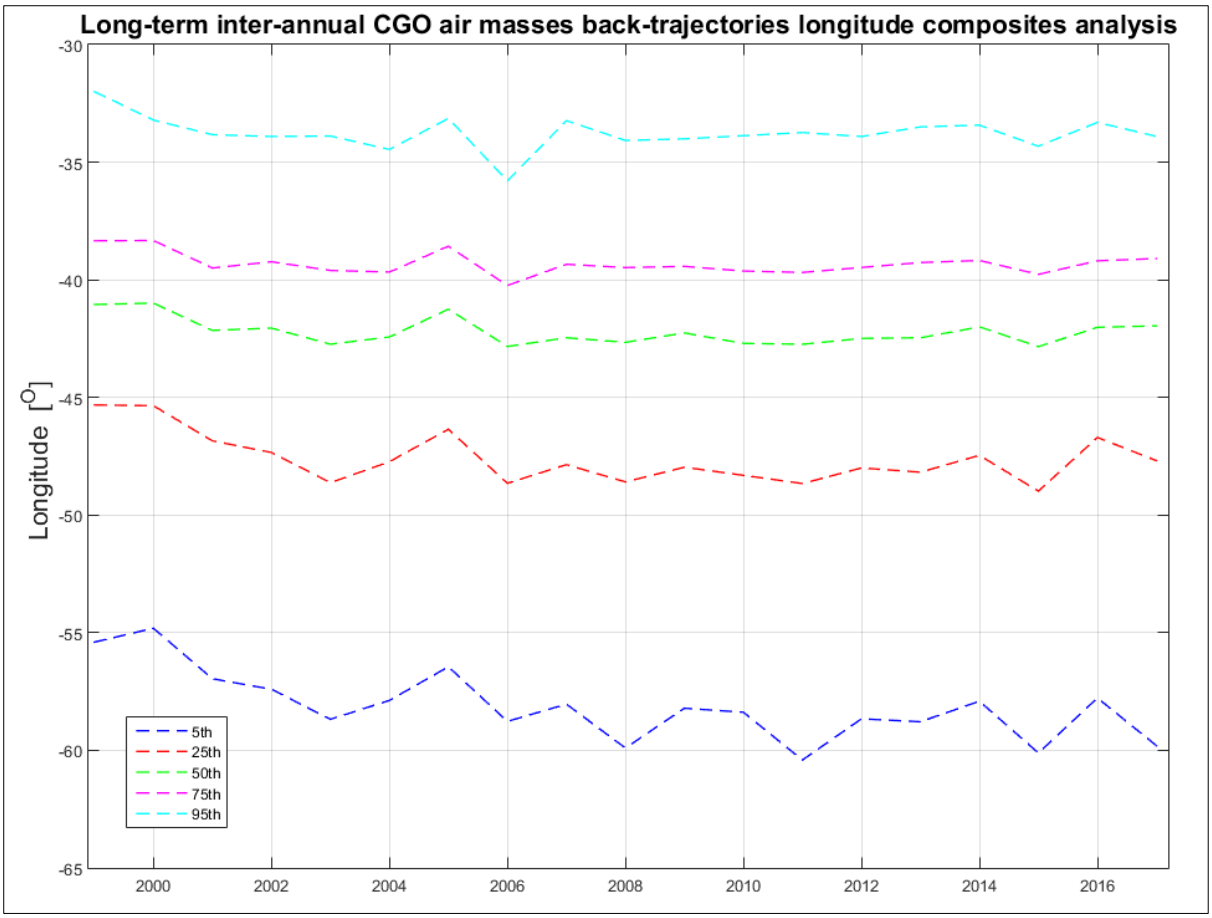

Appendix Figure – 28: Long-term inter-annual CGO air-masses back-trajectories longitude composite analysis (T = 60 h) characterised by 5th, 25th, 50th (median), 75th and 95th percentiles from 1999 to 2017.

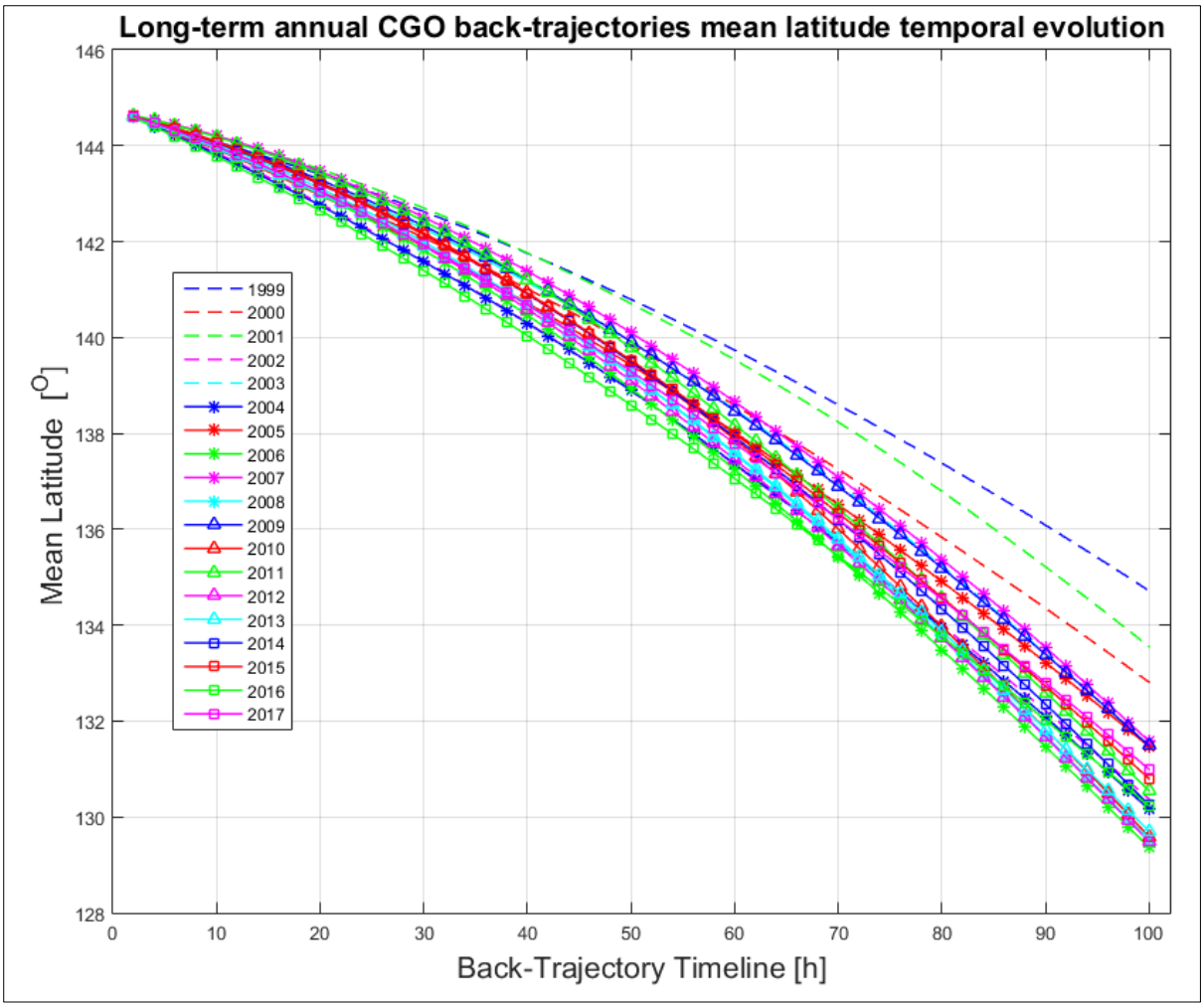

Appendix Figure – 29: Long-term inter-annual CGO air-masses back-trajectories mean latitude temporal evolution from 1999 to 2017.

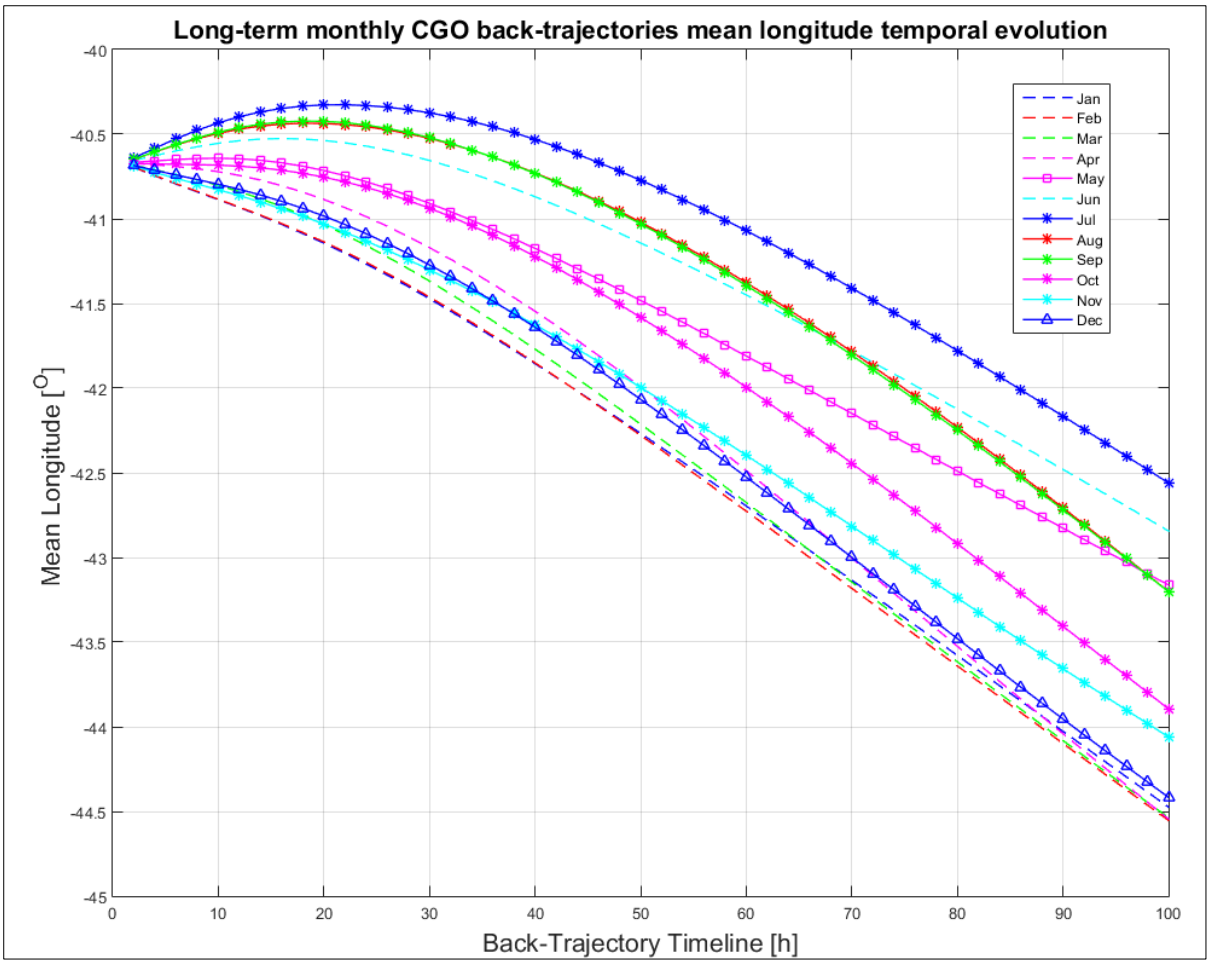

Appendix Figure – 29: Long-term monthly CGO air-masses longitude temporal evolution from 1999 to 2017.

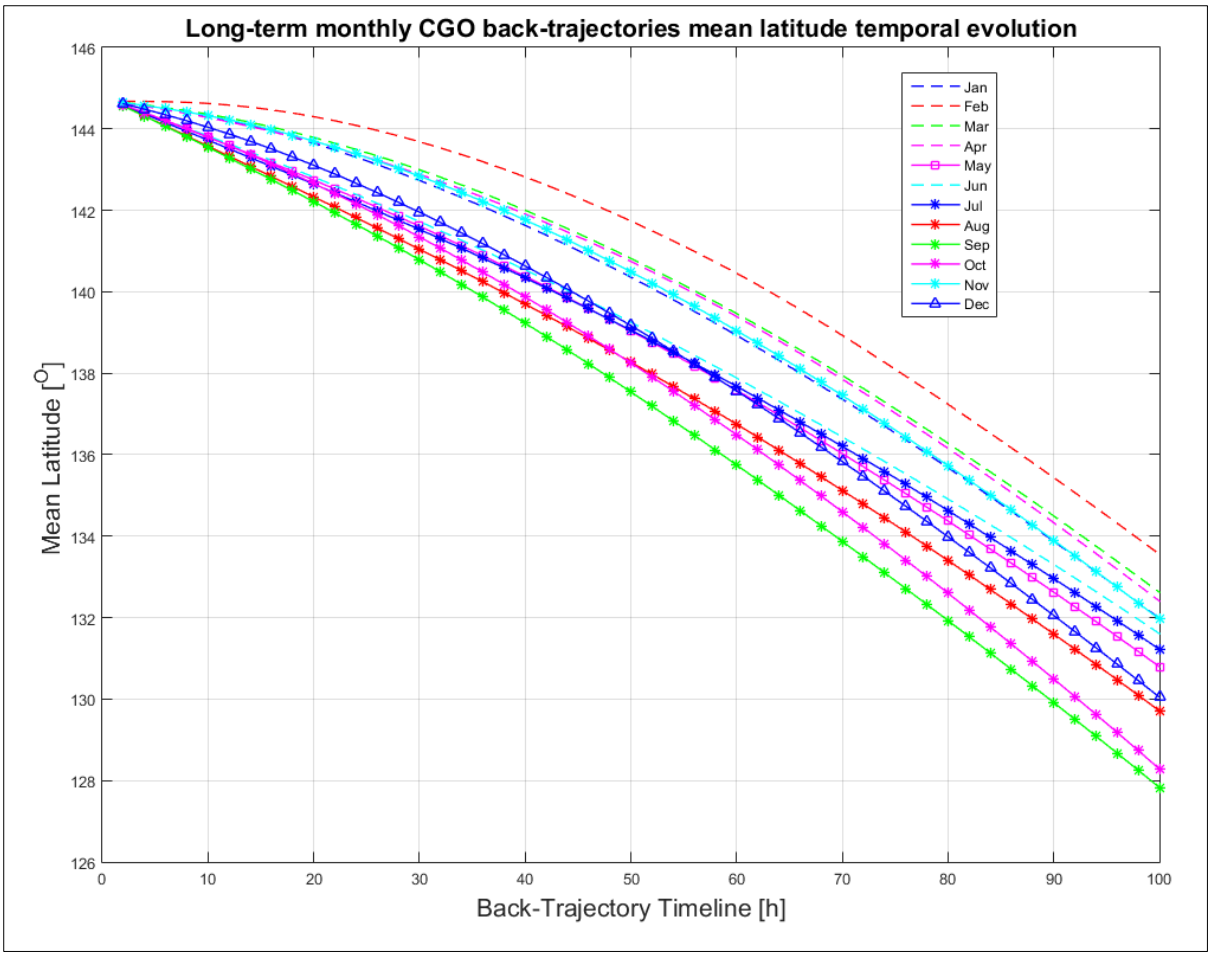

Appendix Figure – 30: Long-term monthly CGO air-masses latitude temporal evolution from 1999 to 2017.

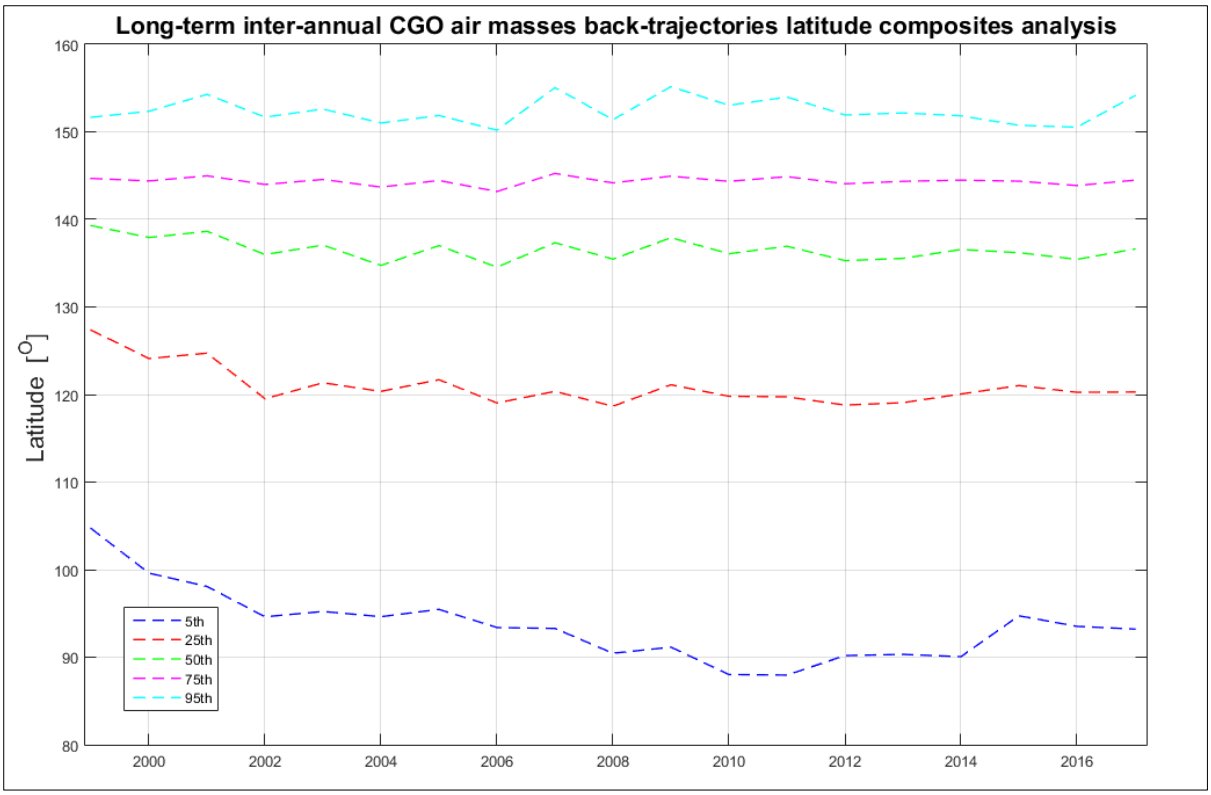

Appendix Figure – 31: Long-term inter-annual CGO air-masses back-trajectories latitude composite analysis (T = 60 h) characterised by 5th, 25th, 50th (median), 75th and 95th percentiles from 1999 to 2017.

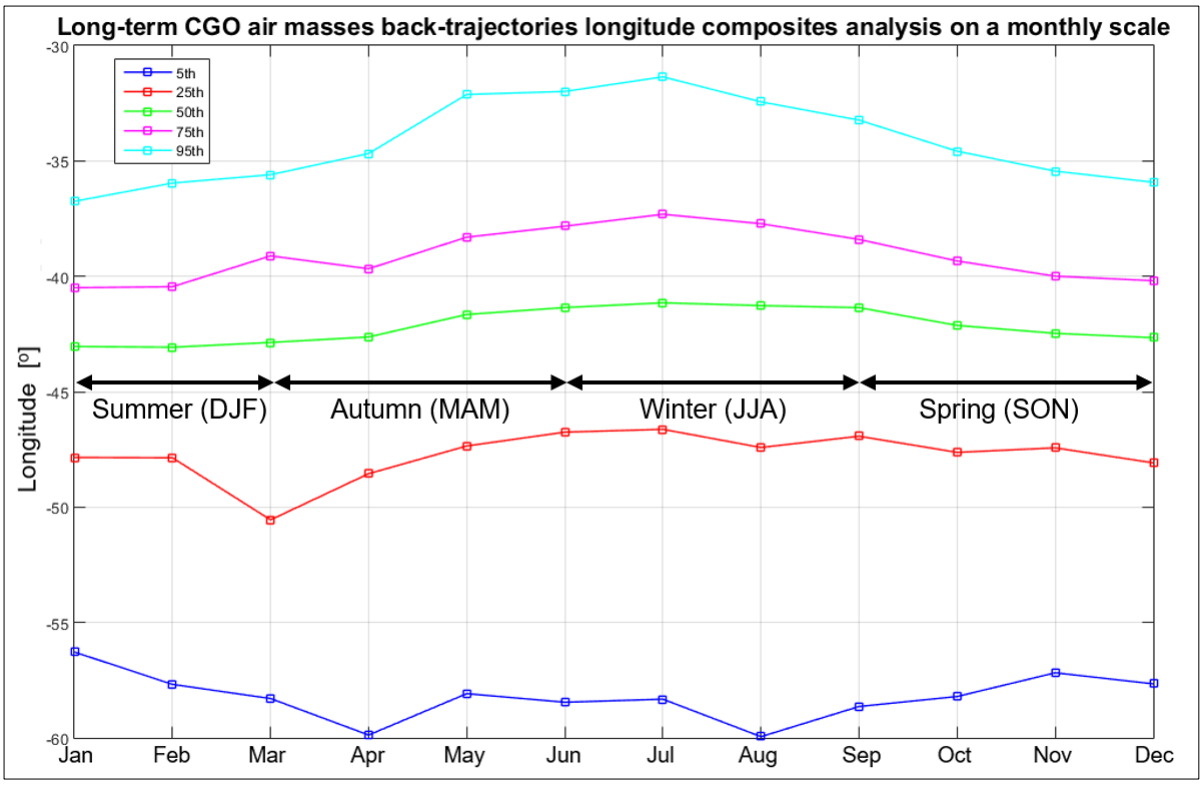

Appendix Figure – 32: Long-term monthly CGO air-masses back-trajectories longitude composite analysis (T = 60) characterised by 5th, 25th, 50th (median), 75th and 95th percentiles computed up to 60 h back in time from 1999 to 2017.

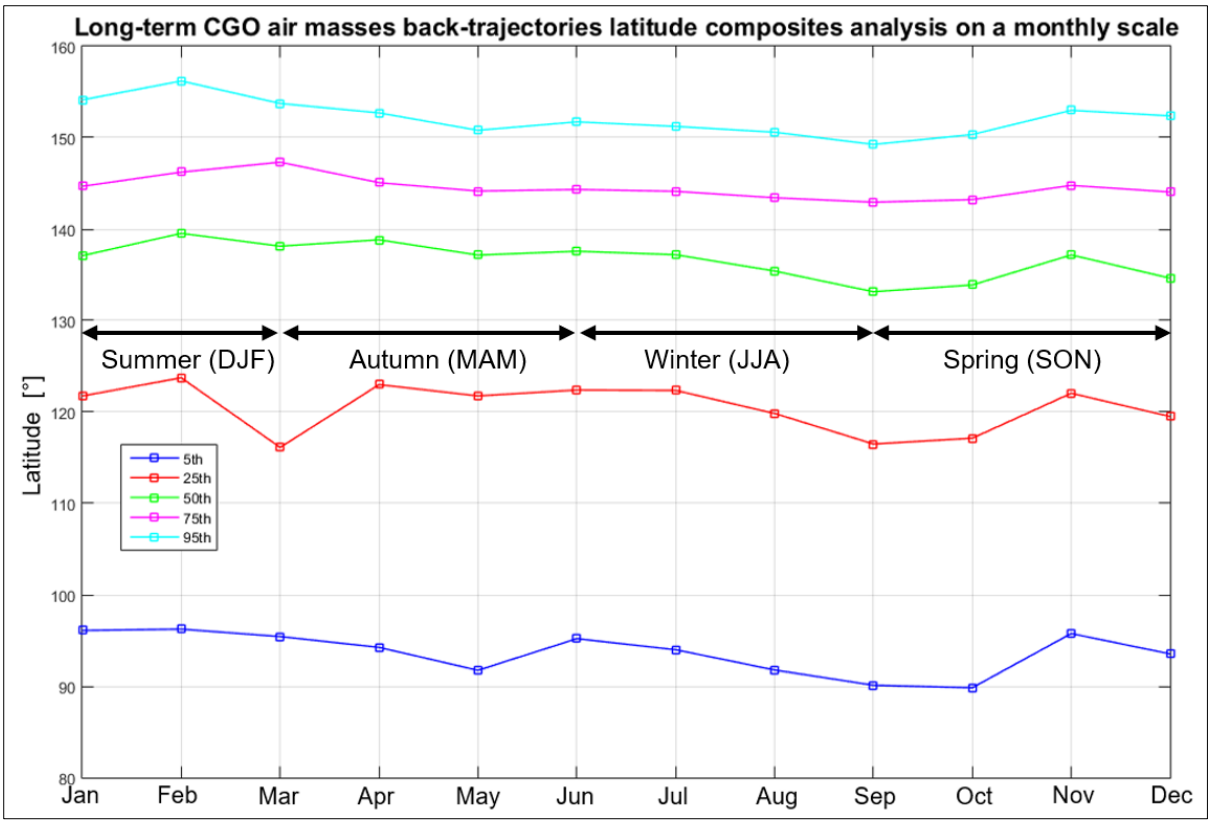

Appendix Figure – 33: Long-term monthly CGO air-masses back-trajectories latitude composite analysis (T = 60) characterised by 5th, 25th, 50th (median), 75th and 95th percentiles from 1999 to 2017.

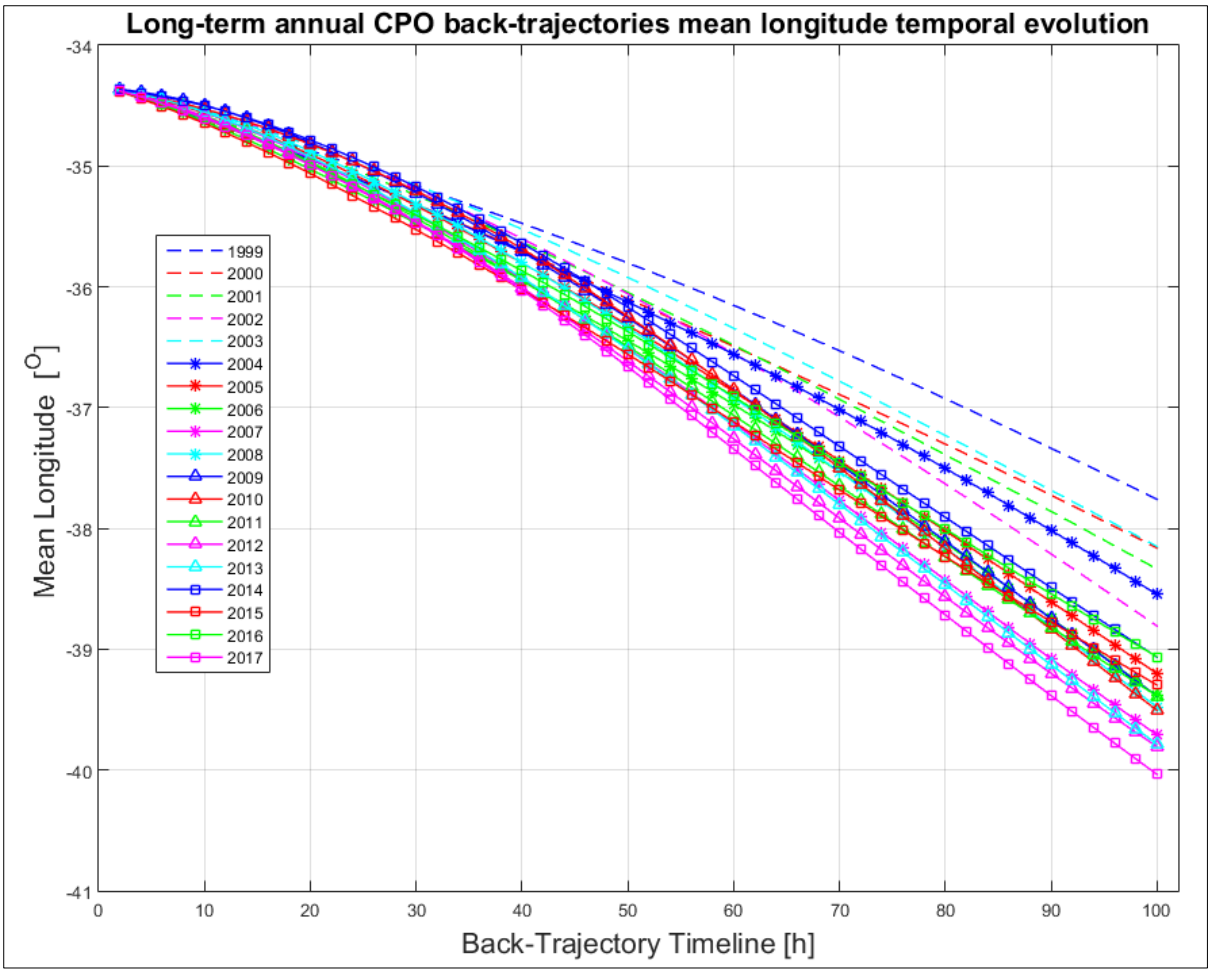

Appendix Figure – 34: Long-term inter-annual CPO air-masses back-trajectories mean longitude temporal evolution from 1999 to 2017.

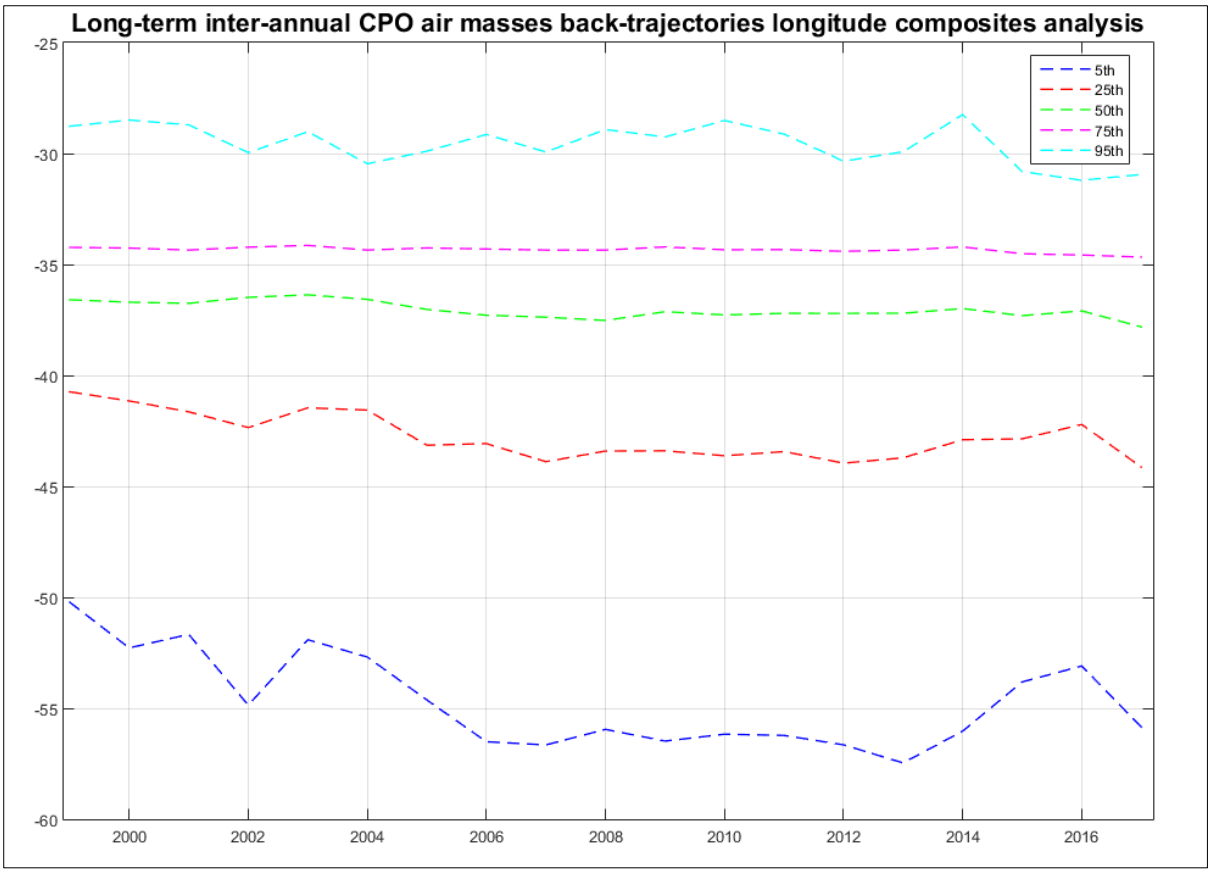

Appendix Figure – 35: Long-term inter-annual CPO air-masses back-trajectories longitude composite analysis (T = 60 h) characterised by 5th, 25th, 50th (median), 75th and 95th percentiles from 1999 to 2017.

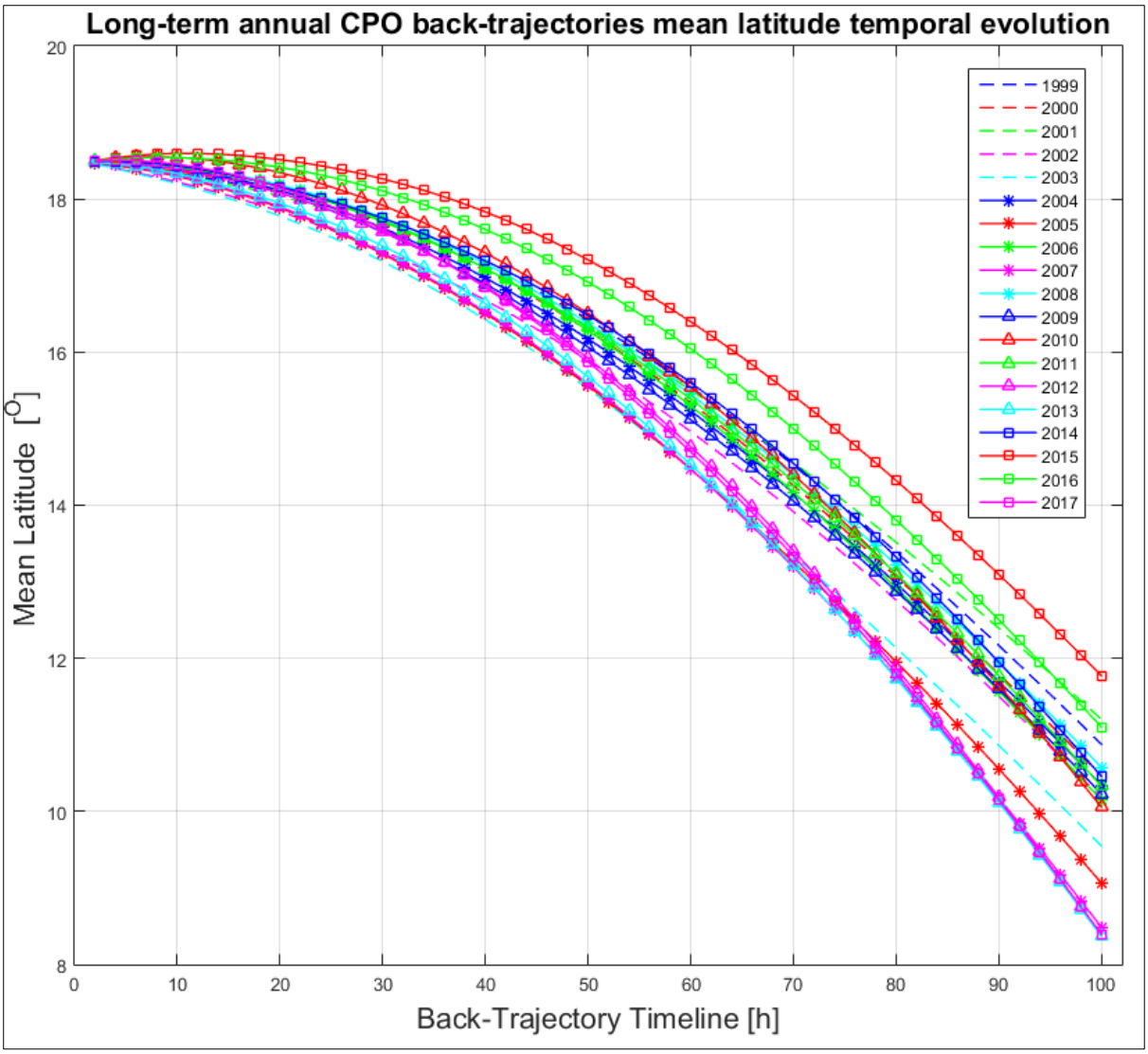

Appendix Figure – 36: Long-term inter-annual CPO air-masses back-trajectories mean latitude temporal evolution from 1999 to 2017.

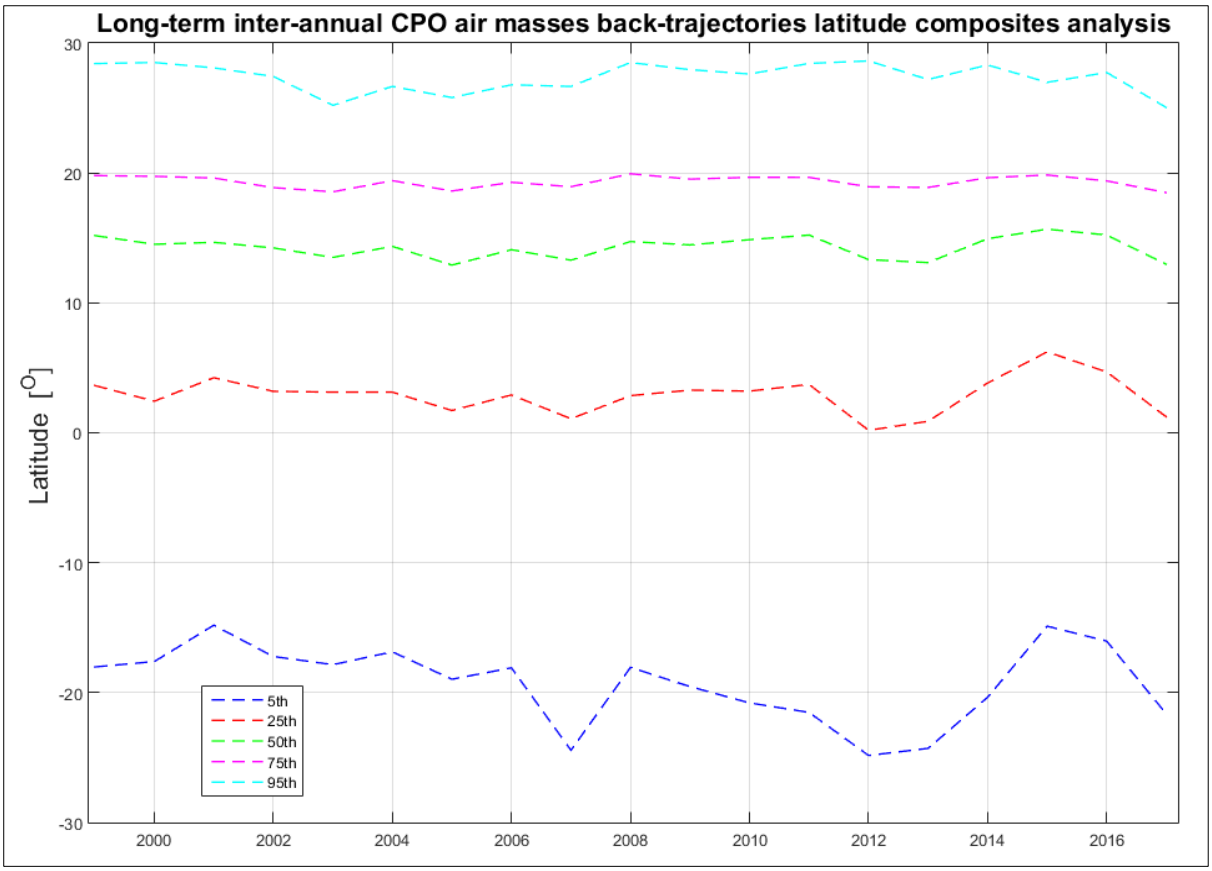

Appendix Figure – 37: Long-term inter-annual CPO air-masses back-trajectories latitude composite analysis (T = 60 h) characterised by 5th, 25th, 50th (median), 75th and 95th percentiles from 1999 to 2017.

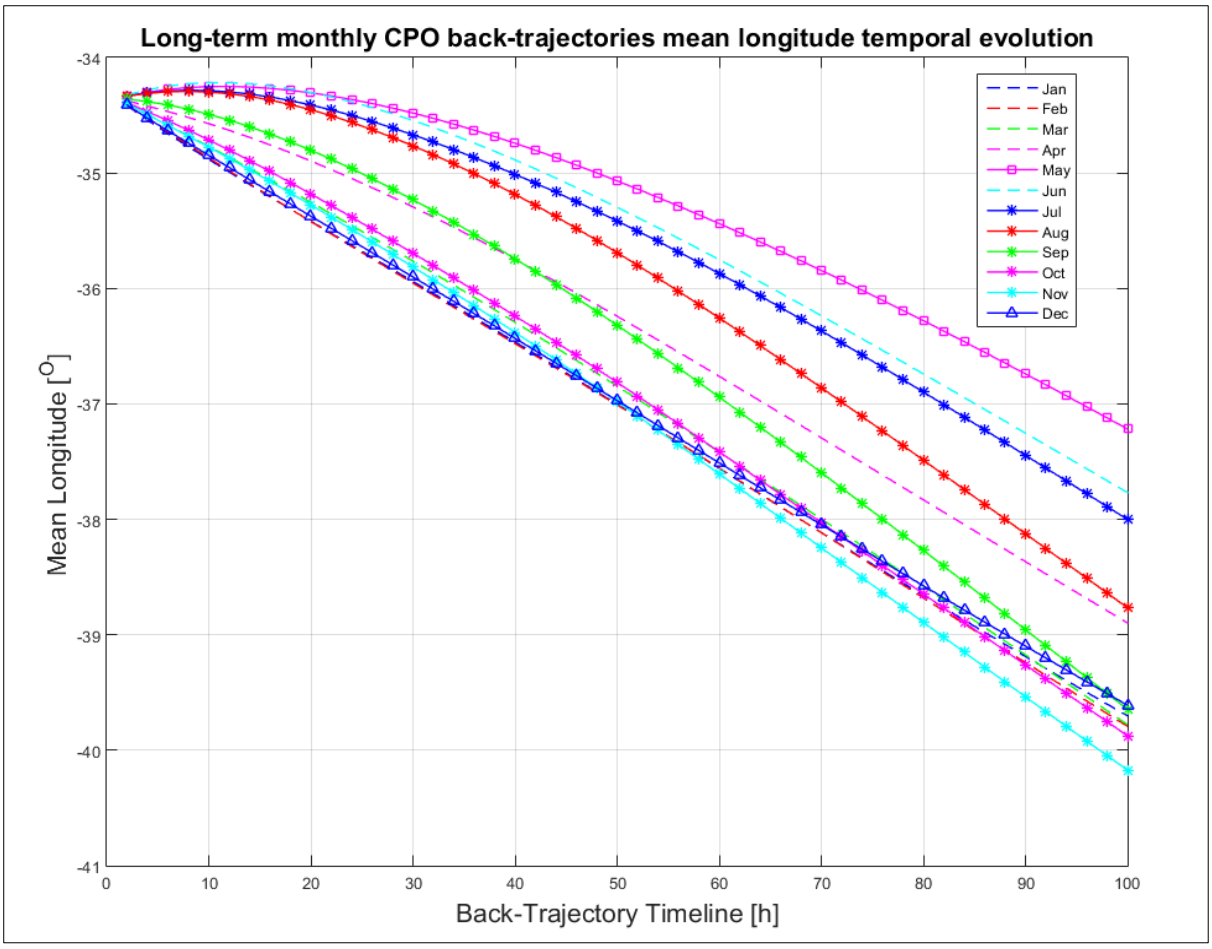

Appendix Figure – 38: Long-term monthly CPO air-masses back-trajectories mean longitude temporal evolution from 1999 to 2017.

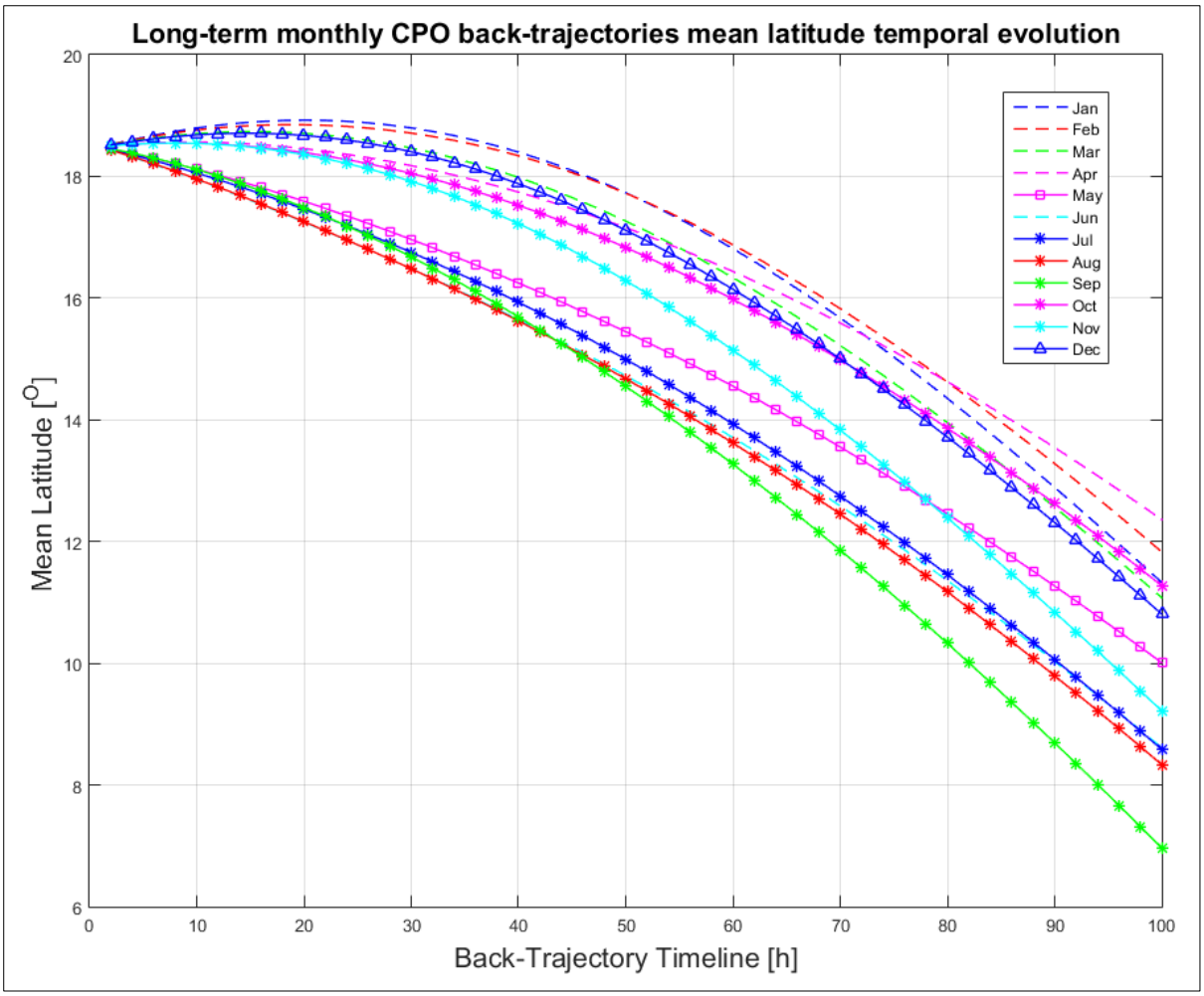

Appendix Figure – 39: Long-term monthly CPO air-masses back-trajectories mean latitude temporal evolution from 1999 to 2017.

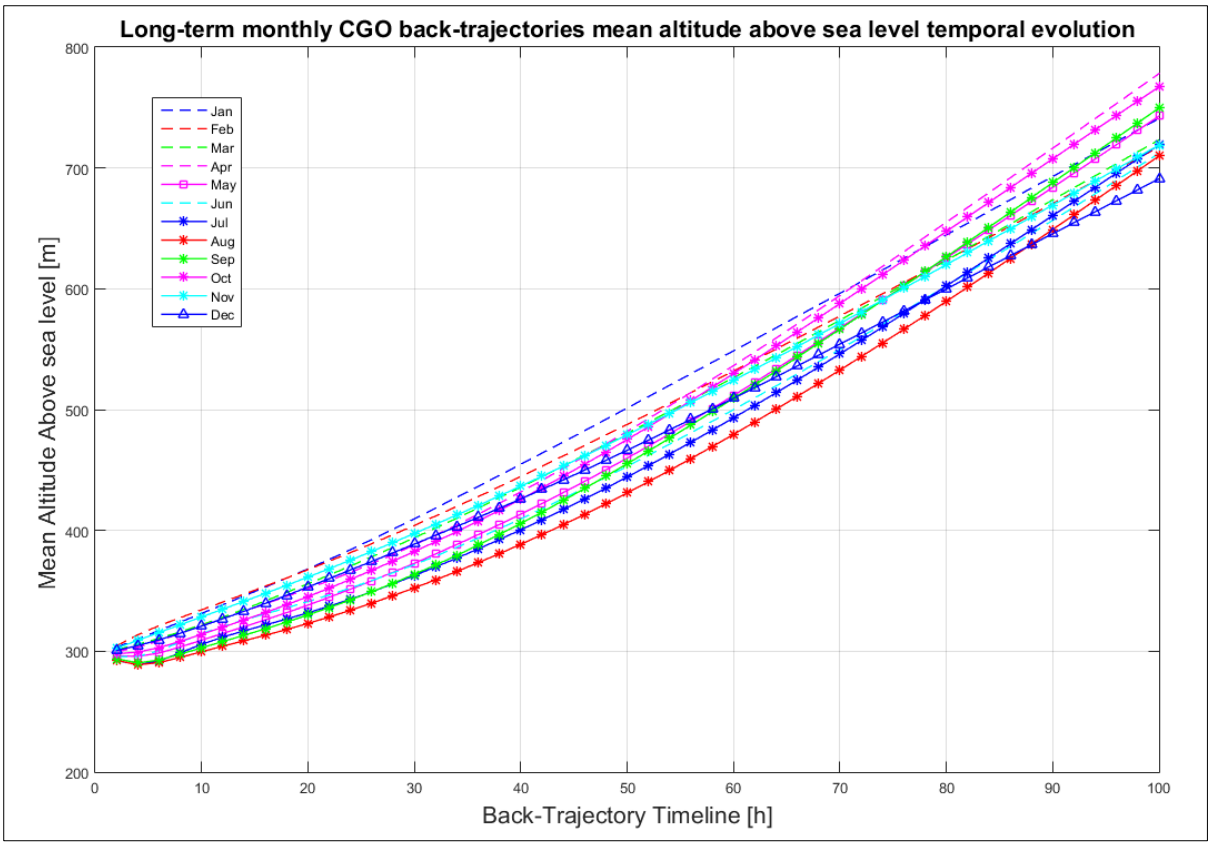

Appendix Figure – 40: Long-term monthly CGO air-masses back-trajectories mean altitude above sea level temporal evolution from 1999 to 2017.

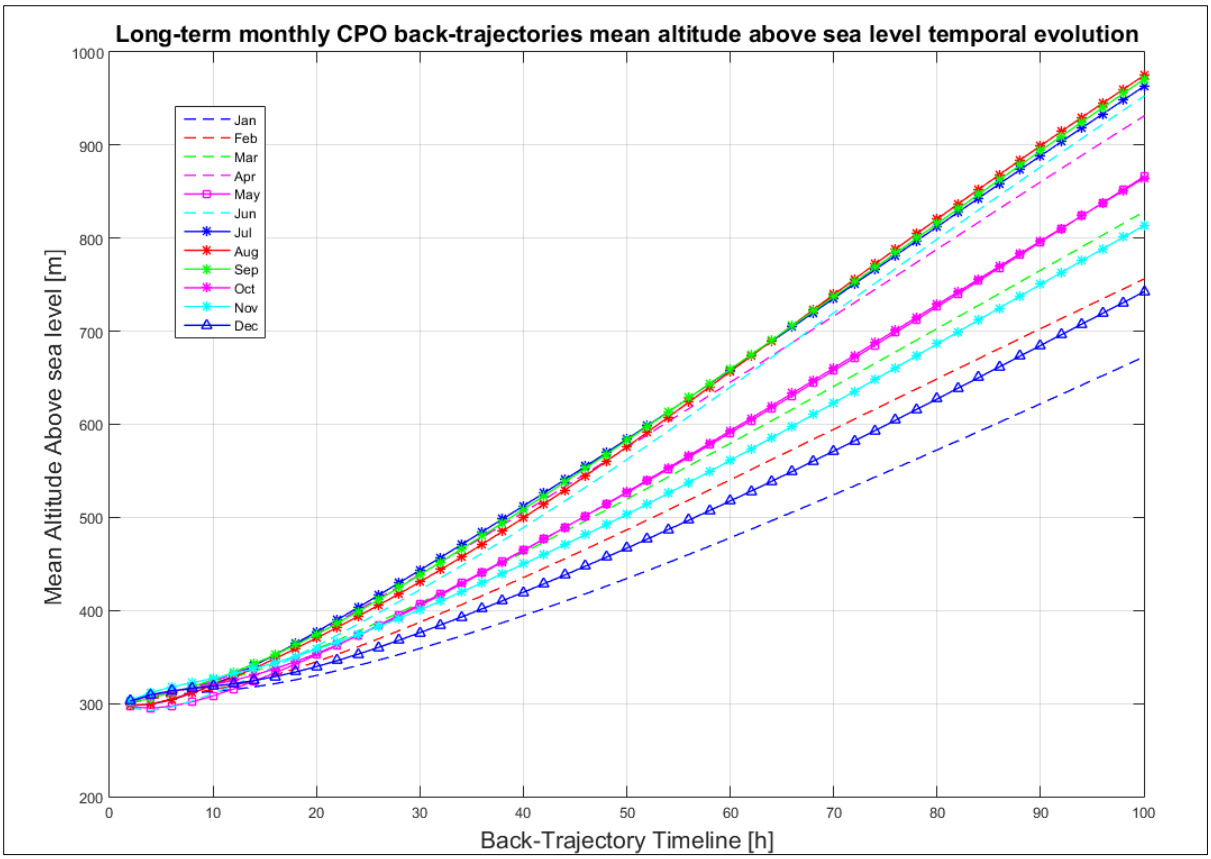

Appendix Figure – 41: Long-term monthly CPO air-masses back-trajectories mean altitude above sea level temporal evolution from 1999 to 2017.

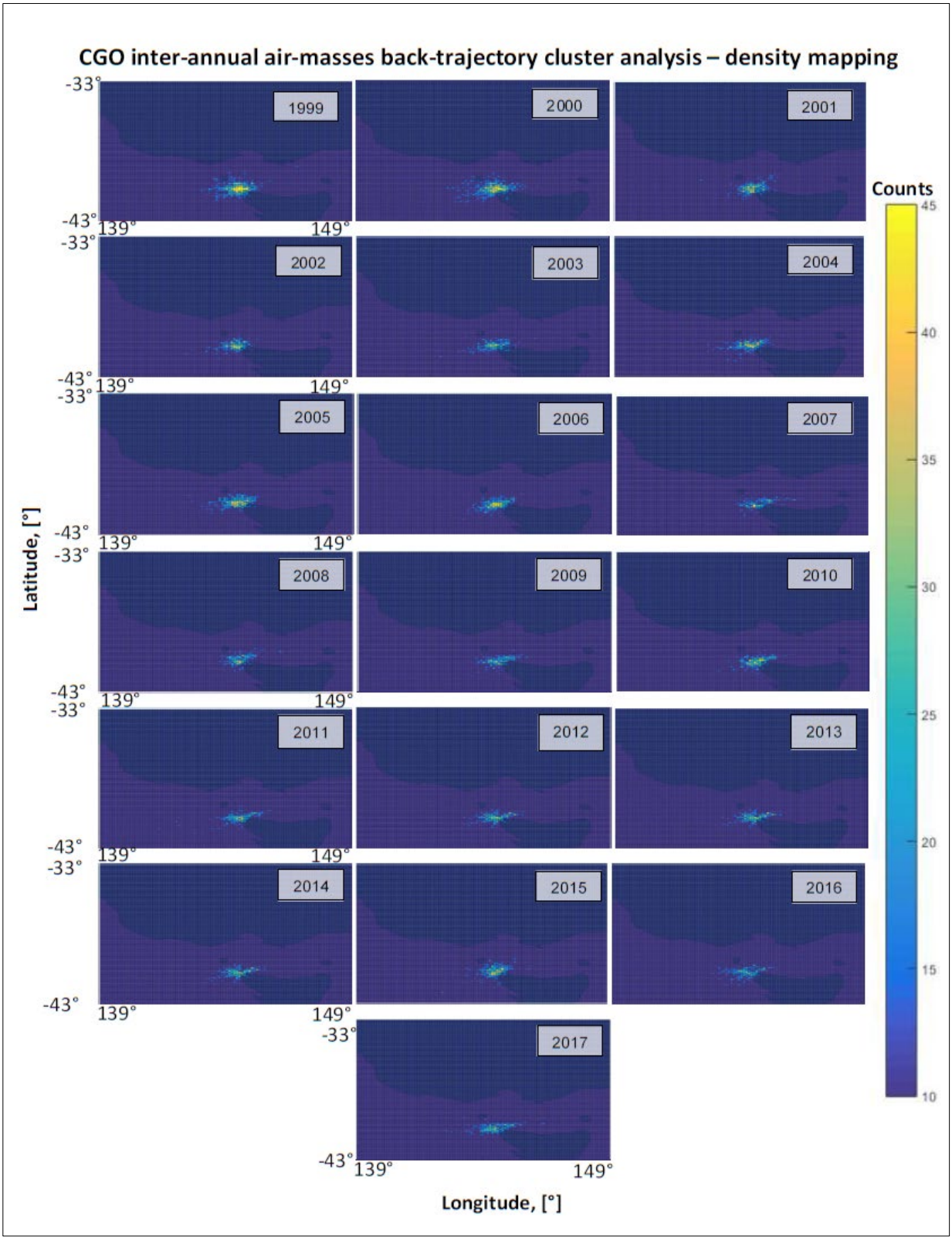

Appendix Figure – 42: CGO inter-annual cluster analysis results for air-masses back-trajectories up to T = 60 h. The upper land mass represents the southern tip of Australia and the lower land mass Tasmania. The plots are zoomed in to emphasize the higher density region (> 25 counts).

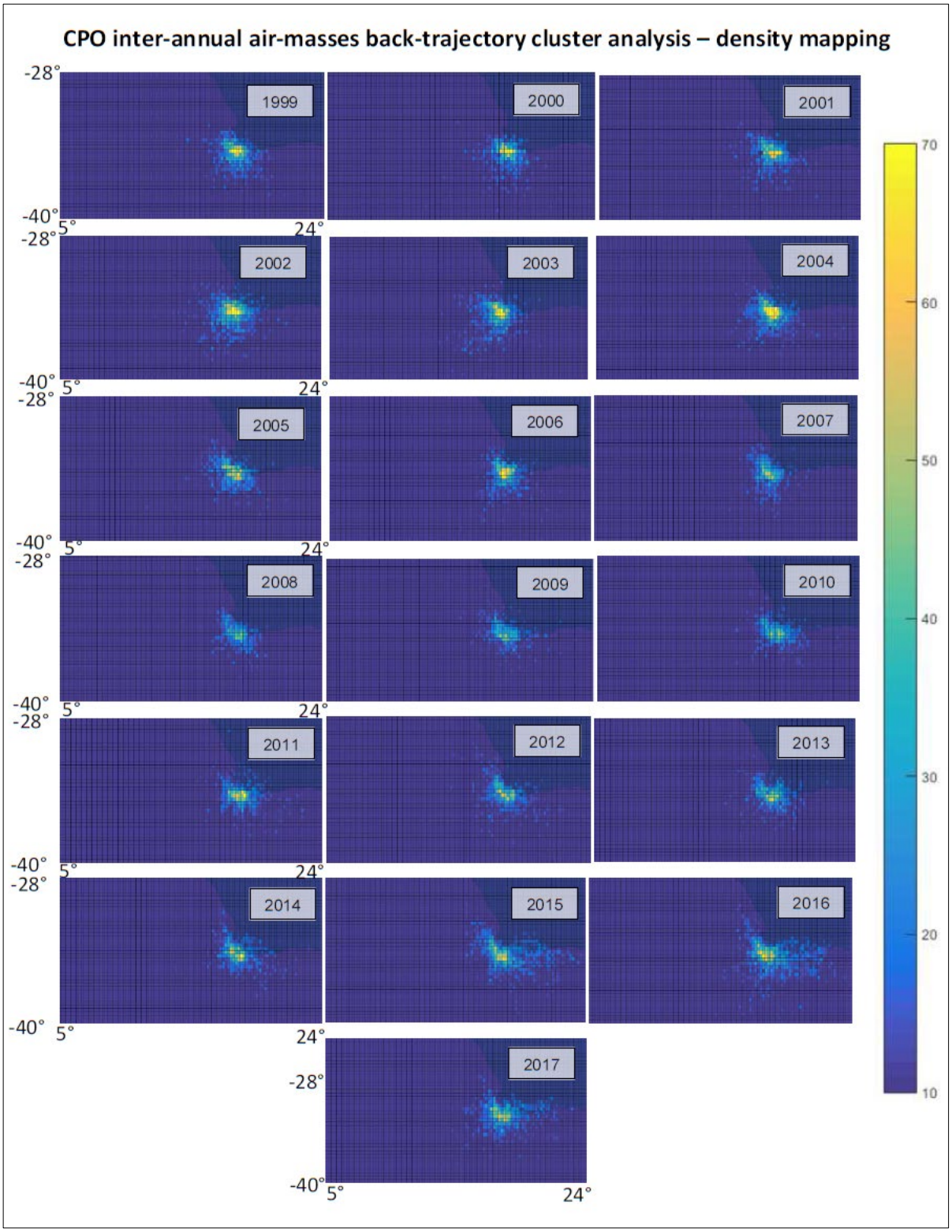

Appendix Figure – 43: CPO inter-annual cluster analysis results for air-masses back-trajectories up to T = 60 h. The upper land mass represents the southern tip of Africa. The plots are zoomed in to emphasize the higher density region (> 25 counts).